N° d'ordre : 41654

Thèse

Présentée à

L'université de Lille 1 - Sciences et Technologies

par

Giuliano MIGNARDI

en vue d'obtenir le grade de

Docteur de l'Université Lille 1 Sciences et Technologies
Spécialité : molécules et matière condensée

$Ca_3Co_4O_{9+\delta}$, cathodes innovantes : optimisation de la microstructure et de la composition

(Innovative $Ca_3Co_4O_{9+\delta}$ cathodes: optimisation of microstructure and composition)

Présentée le 18 décembre 2014 devant le jury :

Rapporteur	M. Pascal Briois	Maître de conférences à l'Université de Technologie de Belfort Montbéliard
Rapporteur	Mme. Mona Bahout	Maître de conférences à l'Université de Rennes
Examinateur	M. Olivier Mentré	Directeur de recherche CNRS
Examinateur	Mme. Elisabeth Djurado	Professeur à Grenoble INP
Co-encadrante	Mme. Aurélie Rolle	Maître de Conférences à l'Ecole Nationale Supérieure de Chimie de Lille
Directeur de thèse	Mme Rose-Noëlle Vannier	Professeur à l'Ecole Nationale Supérieure de Chimie de Lille

Thèse préparée au sein du laboratoire UCCS - UMR CNRS 8181
École doctorale Sciences de la Matière, du Rayonnement et de l'Environnement

© 2014 Tous droits réservés.

doc.univ-lille1.fr

Acknowledgements

I want to particularly thank my thesis director Professor Rose-Noëlle Vannier whose help and guidance have always been a reference for all of us. Even despite her many responsibilities sometimes kept her busy she always found a moment for us.

Another sincere acknowledgement goes to my supervisor Caroline Pirovano, *maître de conférences*, who supervised and assisted me in the long and hard effort of the redaction of this PhD thesis. Indeed not much would have been possible without her.

I would also want to thank my supervisor Aurélie Rolle, *maître de conférence*s for her dedication and insight which provided countless discussion cues amongst us students.

Many thanks to Professor Sylvie Daviero-Minau who assisted me in the exploitation of data fitting and spectra analysis for the electrochemical section. Her precious insight and expertise are an esteemed asset for the laboratory.

A great acknowledgement is directed to engineer Edouard Capoen and Romain Jooris, who supervised the technical part of the experimental setup. They often performed small miracles with the equipment allowing me and my colleagues to work efficiently.

A heartfelt thanks goes to the whole personnel of the UCCS-CS laboratory for their indispensible role: to Laurence Burylo and Fréderic Capet, in charge of the XRD analyses, to Nora Djelal, responsible of thermal and SEM analyses, to Maxence Vandewalle and Véronique Alaimo, who managed the chemical and material stocks; to Catherine Renard, Christophe Volkringer, Murielle Rivenet, Marie Colmont, Nathalie Tancret, whom I assisted during my TA and were very friendly with me.

A particular thank you is directed to my colleagues with whom I always shared work and worries: Vincent, Ibtissam, Xavier, Chloe, Da and Hussien. Their fundamental contribution to the present work has had a key role in the success of this study.

Also, I want to thank my friends who shared so many nice moments with me during these three years: Aline, Almaz, Blaise, Clément, Christian, Diana, Edward, Esperanza, Florent, Florence, Freddy, Giullaume, Ignacio, Jacob, Leticia, Manon, Margot, Marine, Mónica, Nathalie, Nicolas, Prashant, Rénald, Sandra, Tanguy, Thibauld, Vadim.

Last but not least I really want to thank my family (Luigina, Giampaolo and Anna Rita) and my lovely girlfriend Olga for supporting me over all these long years.

© 2014 Tous droits réservés.

Table of contents

© 2014 Tous droits réservés.

© 2014 Tous droits réservés.

© 2014 Tous droits réservés.

List of abbreviations

AC	Alternated current
AFC	Alkaline fuel cells
ASR	Area specific resistance
BLNF	Baryum-lanthanum nickel-ferrates
BSCF	Baryum-strontium cobalt-ferrates
CCD	Charge-coupled device
CCO	Calcium cobaltites
CGO	Cerium gadolinum oxide
CPE	Constant phase element
CSO	Cerium scandium oxide
DP	Depth profile
EDS	Energy dispersion spectroscopy
EIS	Electrical impedance spectroscopy
ESD	Electrostatic spray deposition
FIB	Focused ion beam
FWHM	Full width at half maximum
HRTEM	High-resolution transmission electronic microscopy
IEDP	Isotopic exchange depth profiling
IT-SOFC	Intermediate temperature solid oxide fuel cells
LEPMI	*Laboratoire d'électrochimie et de physicochimie des matériaux et des interfaces*
LS	Line scan
LSCF	Lanthanum-strontium cobalt-ferrites
LSCM	Lanthanum-strontium chrome-manganites
LSGM	Lanthanum-strontium gallium-manganites
LSM	Lanthanum-strontium manganites
MCFC	Moletn carbonates fuel cells
MIEC	Mixed ionic/electronic conductors
NOx	Nitrogen oxides
OCV	Open circuit voltage
ORR	Oxygen reduction reaction
PAFC	Phosphoric acid fuel cells
PDF	Powder diffraction file
PEMFC	Proton exchange membrane fuel cells
PIE	Pulsed isotopic exchange
PLD	Pulsed LASER deposition
PMMA	Poly(methyl methacrilate)
PS	Polystyrene
PS-b-PEO	Polystyrene-b-polyethylene oxide
RC	Resistance-capacitor
RP	Ruddlesen-Popper
rpm	rounds per minute
RT	Room temperature
SBC	Samarium baryium cobaltites
SDC	Samarium doped ceria

© 2014 Tous droits réservés.

SEM	Scanning electronic microscopy
SOFC	Solid oxide fuel cells
TEC	Thermal expansion coefficient
TEM	Transmission electronic microscopy
TGA	Thermo-gravimetric analysis
THF	Tetrahydrofurane
ToF-SIMS	Time of flight secondary ion mass spectroscopy
TPB	Triple point boundary
UCCS	*Unité de Catalyse et Chimie du Solide*
UCCS-CH	*Unité de Catalyse et Chimie du Solide - Catalyse Hétérogène*
UMET	*Unité Matériaux et Transformation*
XRD	*X-Rays diffraction*
YSZ	Yttrium stabilised zirconia
ΔE	Delta of the difference of potential
ΔG	Delta of the Gibbs' energy
ΔH	Delta of the enthalpy

© 2014 Tous droits réservés.

Foreword

The whole energy demand of a colossus like China lies on coal and the direct (carbon particles, dusts, ashes) and indirect (CO, CO_2, NOx, photo-smog) pollution, which has already reached dramatic levels (see Fig. 1.1.1), cannot but increase if the trend is maintained.

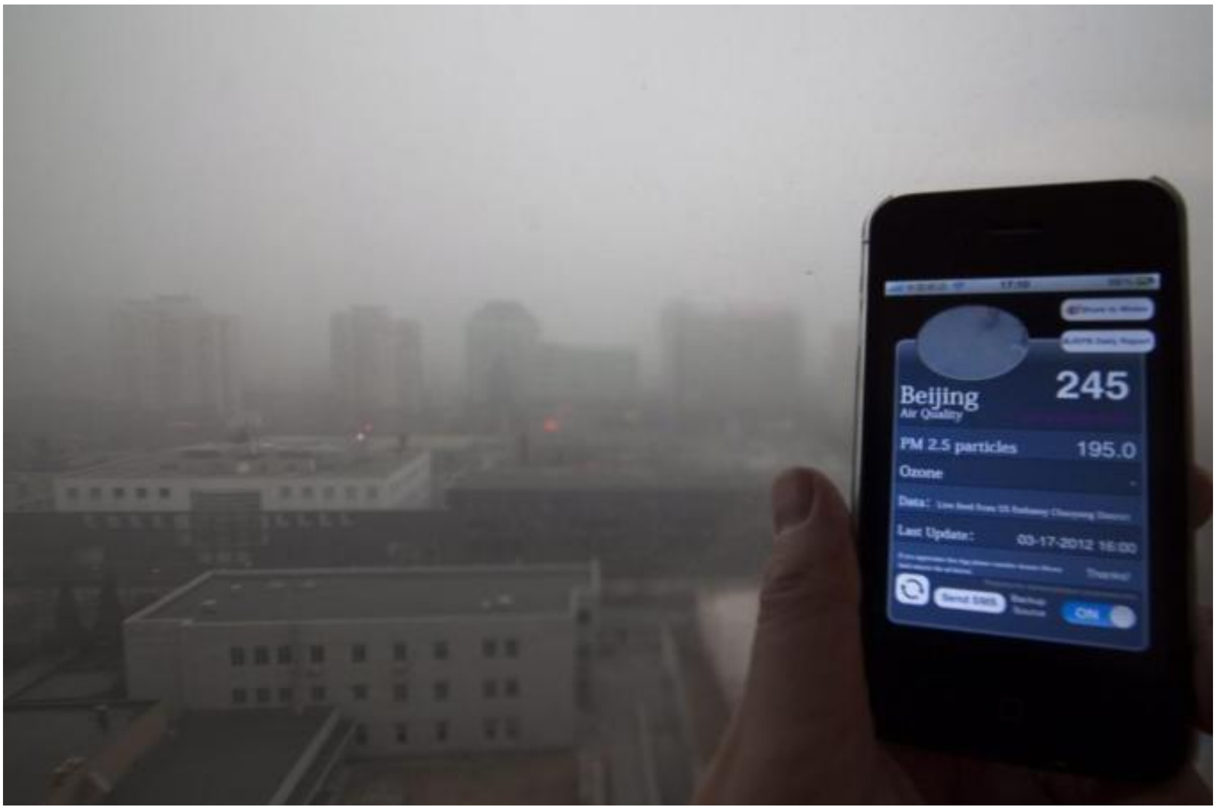

Fig. 1.1.1 - Consequences of pollution in Beijing (China)

Moreover, the great majority of smog and greenhouse gases comes from the automotive industry. In this matter, the introduction of “alternative” fuels, derived from biomasses or bio-refinery, won’t solve the problem. Burning bio-diesel instead of oil-diesel will produce the same CO_2 and NOx. In addition, electricity production is but the “tip of the iceberg”.

The solution that many analysts envision to face this dramatic situation is the shift to the “hydrogen-economy”, but the problems related to the H_2 stocking and distribution will delay its advancement until new, better materials are discovered [1].

More concretely, fuel cells could already overcome the inconvenience of photo-smog and NOx production from automobile industry, as they convert energy directly into electricity, thus making electric cars a valid and robust alternative. Moreover, their superior yield (up to three times higher than the best diesel engines) would drastically decrease fuel consumption thus lowering the dependency from oil and fuel price.

The applications could range from static energy generation for buildings, facilities and factory, to cars and portable devices. The increase in the energy production efficiency would

© 2014 Tous droits réservés.

lower the cost for energy by at least 50%. It would also mark the turning point in the fight against pollution and green-house effect [2].

In this field, Solid Oxide Fuel Cell (SOFC) is a promising technology. Its main advantage is its capability to work with hydrocarbons as fuels. As the distribution network of hydrocarbons is already very well spread, the transition from “classic” fossil fuel energy to “modern” fuel cell energy could be eased by the development of the SOFC technology.

Unfortunately, the elaboration of this scenario is strongly limited by the current performances of the SOFCs. The good yield and resistance to coking depend on the very high working temperature (> 800°C). Also, on the cathode side, the ionic/electronic conduction strongly depends on temperature, with dramatic ohmic losses when decreasing the temperature to 600-700°C.

The consequences of operating at 800-1000°C are fast aging and delamination of the fuel cell, with subsequent quick loss of functionality. Therefore, a great scientific effort is going on to develop materials for the next “generation” of Solid Oxide Fuel Cells, able to operate at lower temperature (600°C) with the same performances (the so-called Intermediate Temperature (IT)-SOFCs). If anode materials with better stability under hydrocarbons and better sulphur tolerance must be developed, resistance losses at the cathode remain still too high. Good progresses have been made with the introduction of Mixed Ionic Electronic Conductors. Among these, cobaltites display the best electrochemical performances but suffer of high thermal expansion coefficients which are not compatible with the commonly used electrolyte as yttrium-stabilized zirconia (YSZ) ($10{\cdot}10^{-6}$ K^{-1}) and gadolinium-doped ceria (CGO) ($12{\cdot}10^{-6}$ K^{-1}) [3].

However, recently, promising electrochemical performances were evidenced at UCCS on the well-known thermoelectric $Ca_3Co_4O_{9+\delta}$ [4–6] which, due to its layered structure, exhibits a thermal expansion coefficient of $9\text{-}10.10^{-6}$ K^{-1}, *i.e.*, in the same range as YSZ and CGO [4]. For a 70 wt% CCO - 30 wt% CGO composite electrode, an area specific resistance (ASR) of 1 $\Omega.cm^2$ was measured at 700°C [5]. This promising performance was confirmed by Samson *et al.* [7], who reported a polarization resistance of 0.64 $\Omega.cm^2$ at 600°C for the composite cathode consisting of 50 vol% CCO - 50 vol% CGO, which corresponds to about 40 wt% CCO - 60 wt% CGO. In addition, using a samarium-doped ceria electrolyte, Zou *et al*. [8] measured a maximum power density of 430 $mW.cm^{-2}$ at 700°C for a 70 wt% $Ca_{2.9}Bi_{0.1}Co_4O_{9+\delta}$ - 30 wt% $Ce_{1.8}Sm_{0.2}O_{1.95}$ | $Ce_{1.8}Sm_{0.2}O_{1.95}$ | $Ce_{1.8}Sm_{0.2}O_{1.95}$-Ni button cell.

For such application, not only the intrinsic properties of the material are of first importance but also its microstructure. Indeed, whereas dense thin films are needed for the electrolyte, porous electrodes with controlled microstructure are preferred to allow the reaction to occur at the Triple Point Boundary (TPB), meeting place of the electron, the ionic species and the gas molecule.

© 2014 Tous droits réservés.

In the first papers published by the UCCS research group, the electrode was deposited by brush without any possible control over the microstructure. Moreover, only the sole CCO and a 70 wt% CCO - 30 wt% CGO composite cathodes were investigated.

Here, after an introduction on fuel cell in chapter one, the optimisation of this electrode's composition and microstructure is presented, which embodies the aim of this manuscript.

With the aim to improve the performances of this promising compound, by means of the screen printing technique, parameters such as electrode layer thickness and composition were adjusted to reach the optimum in chapter two.

Taking inspiration from the work of Hildelbrand [9] in which was reported the beneficial effect of adding a very thin interlayer between the electrode and the electrolyte, a few microstructural modifications were envisioned and are reported in the third chapter. A few deposition methods were investigated. Pulse laser deposition was carried out in collaboration with Marie-Hélène Chambrier at UCCS-Lens. Electrodes samples were obtained by ESD (Electrostatic Spray Deposition) from a collaboration with Elisabeth Djurado of the LEPMI laboratory in Grenoble. Spin-coating of an aqueous solution containing the precursors of CCO on CGO pellets (acting as the electrolyte) was also studied in cooperation with Jean-Philippe Dacquin of the UCCS-CH of Lille and David Fournier of the UMET of Lille.

Lastly, in chapter 4, the influence of substitution of calcium by strontium, lead, bismuth and lanthanum on the electrochemical and transport properties of CCO were empirically studied.

© 2014 Tous droits réservés.

1. Introduction on Fuel Cells

1.1. What is a fuel cell?

A Fuel Cell is an electrochemical device dedicated to the conversion of the chemical energy, contained in a generic fuel, directly into electricity. Thus, as the Fuel Cell is independent from the Carnot limitation, very high theoretical efficiencies can be obtained. This highly valuable energy conversion process is made possible by the intrinsic characteristics of the Fuel Cell itself as the fuel reacts with an oxidizer to form an energetically more stable molecule. The ΔE of the process, instead of being lost as heat, is channelled through the electronic collectors of the Cell and sent to an external circuit, thus generating an electronic stream or electric current [10]. Such a reaction can be schematically represented by the model of the reversed water electrolysis reaction:

$$H_2 + \frac{1}{2} O_2 \rightarrow H_2O + iV\ (E^{\circ} = 1.23V) \qquad (1.1.1)$$

Thermodynamically, this reaction has a specific heat ΔH^0 which is given by:

$$\Delta H^0 = \Delta H_{H2O} - \Delta H_{(H2)} - \frac{1}{2}\Delta H_{(O2)} \qquad (1.1.2)$$

ΔH^0 for equation (1.1.1) is <0.

The Gibbs' free energy (G^0) for the reaction (1) is given by:

$$\Delta G^0 = \Delta H^0 - T\Delta S^0 \qquad (1.1.3)$$

It can be calculated that the variation in the Gibbs' free energy in reaction (1) is negative [11]. The reaction is therefore exothermic, implying that the consumption of a fuel (in this case molecular hydrogen) generates energy plus water as by-product. This energy, if not controlled, normally dissipates as heat which, in the frame of our industrial society, is a lowly valuable form of energy for it is scarcely versatile.

Conversely, the energy coming from the process (1.1.1) expressed in equation (1.1.3), if used in a controlled manner, as for example in a Fuel Cell, can be directly converted into an electronic stream (namely an electric current) which is a highly valuable form of energy, as it is used in many aspects of our advanced society (communications, transport, research, production and so on).

This reaction requires a good separation of the fuel and the oxidizer at the two sides of the fuel cell. Then, according to the type of Fuel Cells, one of the two species will migrate through the electrolytic membrane, reach the opposite side and react with the counterpart.

The difference of potential associated to this equation is given by the Nernst equation:

© 2014 Tous droits réservés.

$$\Delta E_{th} = \Delta E^0 + \frac{RT}{2F} ln\left(\frac{pH_2 \cdot pO_2^{\frac{1}{2}}}{pH_2O}\right) \qquad (1.1.4)$$

Being:

ΔE_{th} the thermodynamic potential at equilibrium;

ΔE^0 the difference of standard potentials at the electrodes;

R the Boltzmann constant;

T the temperature;

2 the number of exchanged electrons in the reaction;

F the Faraday constant.

However, in operating conditions the potential is lower than the theoretical one due to irreversible losses and polarization effects. The actual potential is given by the following equation:

$$\Delta E_{cell} = \Delta E_{th} - |\eta_{cathode}| - \eta_{anode} - Ri \qquad (1.1.5)$$

With: $R = R_{electrolyte} + R_{contact}$ (1.1.6)

Being

$\eta_{cathode}$ the cathodic overpotential

η_{anode} the anodic overpotential

Ri the ohmic losses due to the electrolyte and the contacts.

Contrariwise, Fuel Cells can be used to split water into molecular hydrogen and oxygen, being given enough energy (in the form of electricity). When they are in such a configuration they are called Electrolysers or Electrolysis Cells.

1.2.Concerning Fuel Cell types

There exist a few types of Fuel Cells. Each one differs mostly on the nature of the mobile species, which migrates through the membrane. Table 1.1 sums up the different kinds of Fuel Cells existing to present days.

© 2014 Tous droits réservés.

Table 1.1 - Fuel Cell's technologies and types

FC type	Anode reaction	Transferred species	Cathode reaction	Working T
AFC	$2H_2 + 4OH^- \rightarrow 4H_2O + 4e^-$	$\leftarrow OH^-$	$O_2 + 2H_2O + 4e^- \rightarrow 4OH^-$	80°C
PEMFC	$2H_2 \rightarrow 4H^+ + 4e^-$	$H^+ \rightarrow$	$O_2 + 4H^+ + 4e^- \rightarrow 2H_2O$	90–200°C
PAFC	$2H_2 \rightarrow 4H^+ + 4e^-$	$H^+ \rightarrow$	$O_2 + 4H^+ + 4e^- \rightarrow 2H_2O$	90–200°C
MCFC	$2H_2 + 2CO_3^{2-} \rightarrow 2H_2O + 2CO_2 + 4e^-$	$\leftarrow CO_3^{2-}$	$O_2 + 2CO_2 + 4e^- \rightarrow 2CO_3^{2-}$	650°C
SOFC	$4H_2 + 2O^{2-} \rightarrow 2H_2O + 4e^-$	$\leftarrow O^{2-}$	$O_2 + 4e^- \rightarrow 2O^{2-}$	800–1000°C

All those Fuel Cells have their advantages and drawbacks.

1.2.1. PEM-type: Proton Exchange Membrane

PEMFC (Proton Exchange Membrane – Fuel Cells) is a class of fuel cells capable of transporting the hydrogen as a proton in a Lewis-type solid state acid membrane. The molecular hydrogen (H_2) is split into protons (H^+) at the anode, which is composed of finely dispersed particles of platinum over a graphite support [12]. Then, the protons move towards the membrane whereas the collected electrons are sent to an external electric circuit and end up reducing molecular oxygen (O_2) into water (H_2O) at the cathode. The most advanced membrane nowadays consists of a dense polymer (NafION©). This fluorinated alkane is rich in sulphonil groups ($R\text{-}SO_2OH \Leftrightarrow R\text{-}SO_2O^-$), which enable the proton to hop from one group to another, thus transporting the hydrogen as H^+ [13].

Then, at the cathode (made in the same way as the cathode), four protons ($4H^+$) react with one oxygen molecule (O_2) to form two water molecules ($2\ H_2O$). The energy gain is recovered as electric current (~40%), while the remaining (~60%) is lost as heat [14].

1.2.2. PA-type: Phosphoric Acid

PAFC (Phosphoric Acid Fuel Cells) uses the same mechanistic principle, consisting in transport of one proton from the anode to the cathode. On the other hand, it changes the nature of the membrane, which in this case is semi-liquid or fluid and made of a polyfunctional acid (usually pyro-phosphoric acid). The transport mechanism is no longer a proton-hopping, but a proper transfer of matter by a medium [15].

1.2.3. A-type: Alkaline

AFC (Alkaline Fuel Cells), instead, transport one hydroxyl group (OH^-) from the cathode to the anode. The molecular oxygen (O_2) reacts with water at the cathode to form alkaline OH^- groups. Those groups, once again properly transferred by a medium, react with molecular hydrogen (H_2) to form water molecules (H_2O), and the energy is again collected as an electric current.

© 2014 Tous droits réservés.

The yields of those two latter types of Fuel Cell are higher than PEM's yield (η≈50-60%), but the liquid and corrosive nature of the membrane limits greatly their use and the possible developments [16].

1.2.4. MC-type: Molten Carbonate

MCFC (Molten Carbonate Fuel Cell) bases their membrane technology on a liquid carbonate electrode. The membrane is a composite made of lithium aluminate matrix (nonconductive) supporting the molten carbonates. These mixtures can be either eutectic lithium-potassium carbonate or eutectic lithium-sodium carbonate.

MCFC usually operates at 600-650°C. Although this technology is quite mature, with a long lifetime (in the prototypes it reached a lifespan higher than 35000 hours), it suffers from carbonate corrosive effects [17]. This results in a slow dissolution of the Ni-based cathode and in its deposition on the Ni-based anode, thus inducing short-circuits. Also, the lithium carbonate electrolyte tends to evaporate thus making necessary lithium carbonate addition during operation.

1.2.5. SO-type: Solid Oxide

Lastly, the SOFC (Solid Oxide Fuel Cell) again transfers an ion from the cathode to the anode. In this case the transported species is an oxide ion (O^{2-}), coming from the splitting and subsequent reduction of a molecular oxygen over the cathode. In a SOFC, both the electrodes and the membrane are ceramic-based. The oxide ion reacts with two hydrogen ions over the anode to form water and produce energy, which is collected as an electric current flux. The most known material for SOFC anode is the Ni-cermet, a mixture of metallic Nickel and oxide ceramics, mainly Yttrium Stabilized Zirconia (YSZ).

For the membrane YSZ or CGO (Cerium Gadolinium Oxide) are usually employed. At the cathode side, ABO_3 perovskite-based materials, such as LSM or LSCF, are used. These materials will be detailed later.

The overall cell efficiency is very high, with a yield approaching 60-70% [18].

Amongst all, the two types of Fuel Cells which are draining the greatest attention nowadays are the Proton Exchange Membrane Fuel Cells (PEMFCs) and the Solid Oxide Fuel Cells (SOFCs) since they display solid components which are easier to handle.

1.3. A brief history on Fuel Cells

Since the evidence by Grove of the principle of a fuel cell in 1839 [10, 11], the fuel cell technology was really investigated only in the late 1950s. SOFCs were amongst the first prototypes to be developed as their fully-solid composition allowed several different building geometries. Also, the solid ceramic construction of the unit cell alleviates corrosion issues in the cell granting a moderate cost.

© 2014 Tous droits réservés.

Nevertheless, its very high working temperature made the SOFC challenging to be fully exploitable. Because of corrosion risks, usually coming from the metallic interconnects and other auxiliary elements and thermal expansion mismatch, chosen materials were very expensive and the montage was generally fragile and difficult to stack.

Which is why, during the ‘60s, the AFC were largely developed and used instead, even for the Apollo Program, which made the success of this type of Fuel Cell. However, corrosion and safety issues remain a challenge for terrestrial application of this type of technology. Also, as they need a very pure source of H_2, due to the high sensitivity to CO_2, these cells represent less an alternative than other types of cells.

Later on, following the increase of the oil price, the other types of Fuel Cells were developed. At first, PAFC conquered a large slice of the market for stationary applications. Even nowadays PAFCs are one of the few commercially available Fuel Cells and many tests, demonstrations and pilots are set up all over the world, although in the past two decades this technology has declined in favour of the PEMFC as the latter promises better cost potentials.

In the same period (‘80s) MCFC were also manufactured and sold, again for stationary as well as for marine applications. In these two fields, in fact, the long warm-up time and heavy weight were not a limitation, and as the MCFC tolerate much better than PAFC carbon monoxide and dioxide content in the fuel, they were also thought to be usable for Direct Feeding with Ethanol or Methane.

The last part of the ’90 and the beginning of the new millennium saw the sky-rocketing research and improvement of the PEMFCs, for which many samples and demonstration kits are purchasable. This kind of Fuel Cell combines good performances with light weight, making it perfect for automotive and/or portable applications. On the other hand, its large scale commercialisation is still limited because of two main drawbacks: high price, mainly due to the important amount of platinum and NafION© polymer in the electrodes and the need for very pure hydrogen source since carbon monoxide is a poison.

In this context, SOFCs are nowadays becoming again more attractive, since they have the advantage to be directly fuelled with either methane or CO which is not a poison for them. For instance, Combined Heat Power units based on this technology are currently being developed in Japan. As said before, SOFCs are made by ceramic materials which make them more fragile than other cell types but solve the corrosion and safety problems.

However, they still display a few drawbacks which have to be to overcome:

1. Catalytic activity towards carbon-coking at the anode;
2. Low or no resistance to sulphur poisoning at the anode;
3. High working temperature;
4. Too high resistance losses at the cathode.

© 2014 Tous droits réservés.

The activity towards coking complicates the possibility of hydrocarbon-direct feed. Carbon coking provokes the formation of thick C-layers over the surface of the electrodes. The carbon layers are not removed because of the reducing atmosphere, therefore they tend to pile up rather than being fired away. This prevents the molecular hydrogen from being split over the catalytically active surface, thus stopping any further process.

This is worsen by the fact that commercially available hydrocarbons contain up to 1000ppm of sulphur-based molecules, which provoke poisoning. Sulphur poisoning is a serious threat for the anode as it contains nickel, a highly sulphur-sensitive metal. Nickel, under acidic sulphur conditions (as is the case for sulphureted molecules under hydrogen) tends to be quickly oxidized to Ni^{2+}, thus forming nickel sulphides (Ni_3S_2) that are catalytically inactive towards H_2 splitting.

On top of that, the temperature required to make the system catalytically active for the splitting of the O_2 molecule (on the cathode) and its transfer through the electrolyte as an O^{2-} ion is very high (800°C). This results in a fast aging of the cell with consequent delamination of the electrodes and the electrolyte.

Nevertheless, coking issue can be relatively easily solved by adding traces of ceria or vanadia, while delamination is an engineering minor issue. On the other hand, since approximately 1987 [21], the resistance to sulphur was investigated deeply in order to fabricate new resistant anodes. Much work has been done in the past three decades to overcome these problems, but in the present day we are still far from finding the definitive solution.

1.4.Solid Oxide Fuel Cell Materials

Although pure oxide ion conductors with high relative density are required for the electrolyte, porous electrodes with mixed conductivity are necessary to allow the reactions to occur at the Triple Point Boundary (TPB) where the electrons, ions and molecular species meet.

1.4.1. Electrolyte

The main role of a SOFC electrolyte is to allow the conduction of the oxide ions (O^{2-}) from the cathode to the anode while preventing any electron migration to avoid short circuits. The requirements for the electrolyte are many:

- Good ionic conduction;
- Good electronic insulation (< 0.01 S/cm);
- High density and thinness to minimize ohmic losses;
- Stability under reducing and oxidizing conditions;
- Good mechanical properties;

© 2014 Tous droits réservés.

- Chemical and mechanical compatibility with the other components of the cell (similar Thermal Expansion Coefficient (TEC), no reactivity);

This set of conditions strongly limits the choice for possible materials for SOFC's electrolyte.

The most common ones are zirconias, cerias and gallates. Brownmillerites, pyrochlores or apatites have also been studied as alternative materials. Fig. 1.4.1 sums up the conductivity of most of typical SOFC electolyte materials.

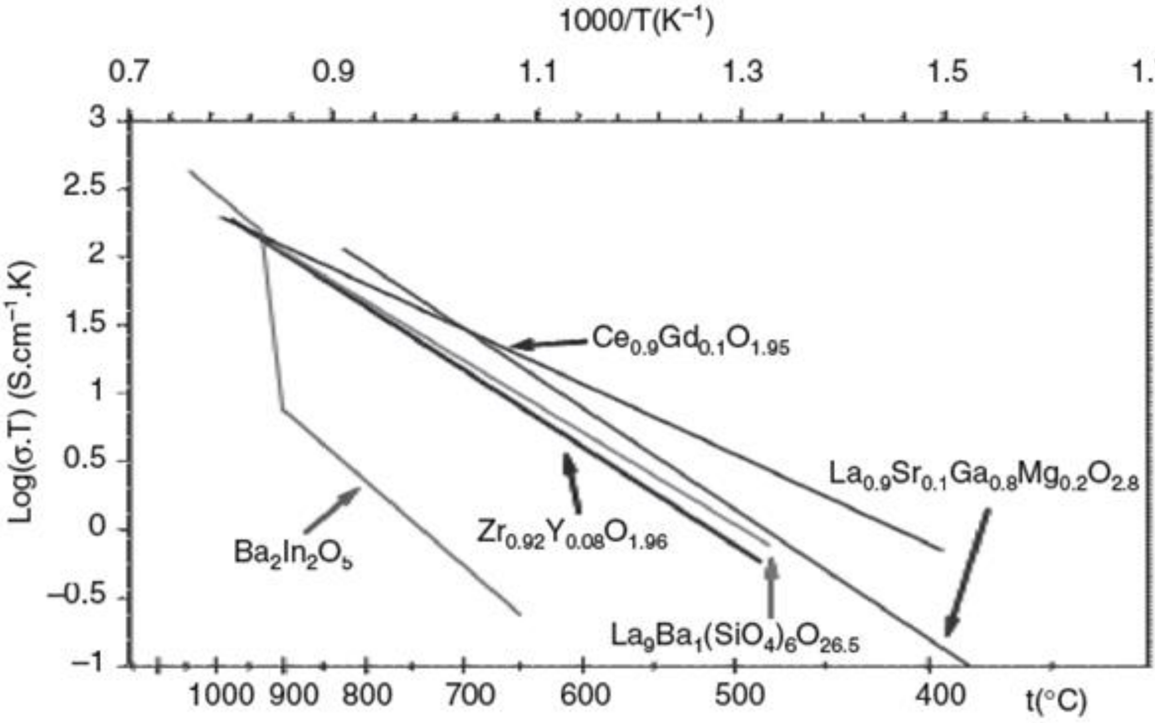

Fig. 1.4.1 - Arrhenius plot of the conductivity of some SOFC's electrolytes

1.4.1.1. Yttrium stabilised Zirconia (YSZ)

The most common electrolyte material for Solid Oxide Fuels Cell is the YSZ: Yttrium Stabilized Zirconia. While pure ZrO_2 is not an ionic conductor, the substitution of Zr(IV) by Y(III) enables the oxide ion conduction by introduction of oxygen vacancies in the structure.

YSZ has general formula $(ZrO_2)_{1-x}(Y_2O_3)_x$, where x can vary from 0.03 (partly stabilised Zirconia) to 0.10 (fully stabilised Zirconia). YSZ-8 ($Zr_{0.92}Y_{0.08}O_{1.96}$ or $(ZrO_2)_{0.96}(Y_2O_3)_{0.04}$) is the most studied composition, as it features the best conductivity (0.2 S/cm at 1000°C [22]). In spite of this, tetragonal zirconia (which contains lower amount of yttria) is sometimes preferred due to its better mechanical properties.

Superior performances were reported for Scandia stabilised zirconia. The stabilisation operated by scandium oxide (Sc_2O_3) allows a temperature decrease by 50-100°C (0.3 S/cm at 1000°C [23], but the development of this electrolyte is limited by the price of Scandia [24]–[29] and poor mechanical stability [30].

© 2014 Tous droits réservés.

1.4.1.2. Ceria

Other materials displaying the same fluorite structure are the doped ceria, which are also widely used. Amongst these, Cerium Gadolinium Oxide (CGO), with general formula $Ce_{1-x}Gd_xO_{2-\delta}$ (0.1 ≤ x ≤ 0.4), is a reference [31]–[33]. Unlike ZrO_2, CeO_2 is cubic already at room temperature. Doping is done to increase the otherwise poor ionic conductivity of the oxide [34].

CGO generally shows a quite good conductivity, which is even higher than that of YSZ ($7.3\cdot10^{-2}$ S/cm at 700°C). Other dopants, such as yttrium and calcium, lead to generally lower values of conductivity ($2.0\cdot10^{-2}$ and $1.3\cdot10^{-2}$ S/cm respectively) [35].

Nevertheless, above 600°C and under reducing hydrogen atmosphere, Ce^{3+} is formed making the electrolyte electronically conductive, with the risk of short-circuiting the cell. Also, reduction induces an increase in the unit cell volume thus generating micro-cracks [36].

1.4.1.3. Lanthanum Gallates

Perovskites with general formula $LnBO_3$ (Ln=Al, Ga, In, Sc, Y) have been extensively studied. Amongst those, lanthanum gallates, having general formula $La_{1-x}Sr_xGa_{1-y}Mg_yO_3$ (x=0.10-0.20 and y=0.15-0.20), were evidenced by Ishihara [37] and further studied by the group of Goodenough [38], [39]. These ABO_3 perovskite are quite promising, as their conductivity can reach down to 0.1S/cm at 700°C. They are more stable under reducing atmosphere than ceria, but suffer from the price of gallium oxide which also volatizes at low oxygen partial pressure. Also, the LSGM synthesis temperature is quite high and they show chemical reactivity towards many electrode materials which may lead to the formation of $SrLaGaO_7$ and $La_4Ga_2O_9$ as secondary phases [40], [41].

1.4.1.4. Other phases

Brownmillerites, which structures are derived from the perovskite one, also attracted some attention in the past decades. $Ba_2In_2O_5$ oxide ion conduction was evidenced in 1990 by Goodenough et al. [42], [43]. The structure is orthorhombic, with BO_6 octahedra layers alternated by chains of BO_4 tetrahedra, which create monodimensional channels along which the ionic conduction is supposed to take place. Upon heating, $Ba_2In_2O_5$ changes symmetry to tetragonal (925°C) and then to cubic (>1040°C). In order to stabilize at lower temperatures the tetragonal and cubic forms, several doping were attempted on either the Ba-site or the In-site.

However, while the conductivity is purely ionic up to 700°C (in dry atmospheres), above that temperature the material becomes a mixed conductor, exhibiting a p-type electronic conductivity. Moreover, the structure is sensitive to water and the same 1-D channels can display protonic conduction below 600°C in wet atmospheres. Because of their instability in wet conditions, high reactivity to CO_2 and easy reducibility, Brownmillerites are unlike to be used as SOFCs electrolytes.

© 2014 Tous droits réservés.

Pyrochlores, whose structure derives from the fluorite one, have general formula $A_2B_2O_7$. They were studied in the 1990s by the group of Tuller [38]–[43]. In comparison to fluorite (ZrO_2), they display intrinsic oxygen vacancies. Best conductivities were measured for $Gd_2Ti_2O_7$ and $Gd_2Zr_2O_7$. However, although the conductivity is almost purely ionic under air, it becomes more and more mixed upon lowering the oxygen partial pressure, due to a partial reduction of Ti^{4+} into Ti^{3+}.

Lanthanum silicates have the apatite structure, which is not derived from the fluorite or the perovskite one ([50], [51]). They have been studied as a possible alternative for SOFC electrolyte membrane during the past decade. Their conductivity is in the same order of magnitude as YSZ [52]. Moreover, their very flexible structure can tolerate a wide range of partial substitution on both Si and Ca site: plenty solid solutions (with Ca, Sr, Mg, Ba, Al, Mg and Ge) are reported in literature [53]–[56]. Nevertheless, due to great difficulties in sintering these materials will be difficult to develop.

1.4.2. Anode

The SOFC's anode is the place where the oxidation takes place. It usually operates under very reducing conditions (e.g. pure hydrogen) thus high tolerance to reduction is one of the prerequisites.

Other requirements of a good SOFC anode are electronic conductivity superior to, ideally, 10 S/cm, ionic conductivity and, according to the fuel used, resistance to corrosion, coking or sulphuring.

Also chemical and mechanical compatibility with the electrolyte and with the interconnects is necessary. On the other hand, in order to ensure good adhesion on the electrolyte support, the anode should not be completely inert [57].

Lastly, also catalytic activity towards, for example, hydrogen oxidation or splitting should be as high as possible.

Therefore, not many materials are suited to this task due to the large set of the requirements. Typically, either single phase metal oxides or cermets are employed as SOFC's anodes [58].

1.4.2.1. Nickel cermets

The most studied material for SOFC's anode material is the Ni-YSZ cermet, a composite material obtained mixing Nickel oxide particles and YSZ ceramic (hence the name cermet). Ni-YSZ cermets are produced by blending YSZ and NiO, followed by firing under hydrogen to reduce nickel oxide into metallic nickel.

This material accounts for most of the requirements mentioned above: the YSZ itself provides the good mechanical and chemical stability, while the excellent catalytic and electronic properties of Nickel ensure high cell performances [59], [60].

© 2014 Tous droits réservés.

Despite its success, this material suffers of many drawbacks which limit its exploitation, namely:

- Sensitivity to sulphur and other contaminants [61];
- Redox cycling intolerance [62];
- TEC notably higher than electrolyte and cathode ones;
- Segregation of Nickel in the pores with consequent reduction of the number of TPB points [63];
- Poor activity for complete carbon oxidation with fossil fuels which leads to coke formation [64].

Those limitations together are an overwhelming handicap for SOFC industrialization. The greatest scientific and technologic challenge, currently, is to find new anode materials having the same performances and activity towards hydrogen dissociation and oxidation, but stable under methane and sulphur tolerant.

Alternatively, the replacement of YSZ with other ceramics was evaluated. When realising CGO ($Ce_{0.9}Gd_{0.1}O_3$) or CSO ($Ce_{0.9}Sc_{0.1}O_3$) nickel cermets the performances of the cells operating under methane were found to be superior [65], [66].

Moreover, cerates were found to promote the catalytic activity towards hydrocarbon oxidation without coking [67], [68].

1.4.2.2. Other cermets

Other anode materials can be obtained by changing either the metal or the ceramic or both components.

In general, different cermets with Cu, Ag or metal alloys instead of Ni proved to have very good performances and a higher tolerance to carbon deposition.

An example is the Cu-YSZ cermets where the lower catalytic activity of Cu towards the C-H bond cracking makes it more stable to coke poisoning.

Copper cermets were applied to a cell fed with ethanol and no degradation nor any carbon deposition were found after 200 hours of operation [58].

Such long-lasting working time was even increased to 250 hours by replacing the ceramic from YSZ to either CGO or CSO [70]. However, the lower melting temperature of copper (1103°C) lowers the temperature range available for practical application in order to minimize segregations.

Also Ag-CSO cermets were tested as SOFC's anode but despite the outstanding performances, their large scale distribution is unlike due to their very high cost.

© 2014 Tous droits réservés.

1.4.2.3. Perovskite-structure based materials

In addition to cermet, much of the research for new anode materials has focused on the production of perovskite-type compounds [71], [72].

$La_{0.75}Sr_{0.25}Cr_{0.5}Mn_{0.5}O_3$ (LSCM) is an ABO_3-type perovskite which first was proven to be redox-stable. LSCM is a p-type conductor with a conductivity of approximately 38 S/cm in air and 1.5 S/cm in 5% H_2/Ar at 900°C. It also displays high resistance to coking when fed with hydrocarbons, while a minor loss in cell performances was noticed when switching to 2:1 mixture of ethanol and water [73].

Substitution of nickel or ruthenium into LSCM was found to introduce metal nanoparticles onto the surface of the oxide which could improve the catalytic performances. A maximum of 2.4 S/cm was measured for $La_{0.75}Sr_{0.25}Cr_{0.5}Mn_{0.44}Ni_{0.06}O_3$ in 5% H_2/Ar at 800°C [74].

LSCM was even used for composite anodes, mixed with CGO, giving acceptable catalytic activity and no carbon deposition when feeding with hydrocarbons.

Strontium and lanthanum titanate are other perovskites which attracted some attention recently [75].

$SrTiO_3$ features remarkable magnetic and conducting properties. However, because of its negligible non-stoichiometry in oxygen, the electronic properties of the pure material are either bad or limited to a very narrow range of temperature.

To overcome this problem, a few different approaches were tried: Nb substitution on the Ti site or formulation of the $LaTiO_3$-$SrTiO_3$ solid solution. In both cases the aim was to create a charge difference on the Ti site to induce oxygen sub-stoichiometry [76]–[78].

1.4.3. Cathode

The very first cathode materials for fuel cells were noble metals (in particular gold and platinum) which excessive cost pushed the researchers to find cheaper valid alternatives.

Amongst the properties that a good SOFC’s cathode must possess are:

- High electronic conductivity under air (>100S/cm);
- High anionic conductivity;
- Chemical and mechanical compatibility with the electrolyte and the interconnects;
- Thermal stability during sintering;
- High catalytic activity for ORR (Oxygen Reduction Reaction);
- Adequate porosity and easily modellable microstructure.

Hence, the first materials to be studied were, in the mid-1960s, the perovskites, which combine the possibility of a mixed metal valence to a sub-stoichiometry in oxygen. There exists a large literature on lanthanum-based ABO_3 perovskites [79].

© 2014 Tous droits réservés.

1.4.3.1. Perovskites

Among the first ones, the LSM ($La_{1-x}Sr_xMnO_3$) dragged large attention for its high catalytic activity [80]. However, its electrical conductivity is mainly electronic which restrains the oxygen reduction reaction to the triple point boundary at the interface between the gas phase, the electrode and the electrolyte. Blends of LSM and YSZ were tried to overcome this problem, but it was found that the two phases react to form the insulating phase $La_2Zr_2O_7$ [81].

Alternatively, doping on both the A and B sites are quite common in order to improve the electrochemical properties or to improve the thermal expansion coefficient to match the electrolyte one. Nevertheless, manganites were abandoned due to their intrinsic scarce capability of inserting interstitial oxygen.

This feature led to the introduction of Mixed Ionic-Electronic Conductors (MIECs), which nowadays are usually preferred.

MIECs are usually obtained by partial substitution of La^{3+} with Sr^{2+} or Ba^{2+}. Also, the Mn site is usually doped with many transition metals such as, Fe, Co, Ni, Cu up to the point of completely exclude manganese from its original site. Amongst the others, cobaltites exhibit the highest conductivity, but suffer of high TEC thus being incompatible with the electrolyte ($23 \cdot 10^{-6}$ K^{-1} for $La_{0.6}Sr_{0.4}CoO_3$ [3]), which is twice the thermal expansion of YSZ ($10 \cdot 10^{-6}$ K^{-1}) or CGO ($12 \cdot 10^{-6}$ K^{-1}) [80].

A good compromise was obtained by partial substitution of cobalt with iron. One of the LSCF composition ($La_{0.6}Sr_{0.4}Co_{0.2}Fe_{0.8}O_{3-\delta}$) is draining large attention [82], [83].

It has shown good electrochemical performances and a lower thermal expansion mismatch ($14\text{-}15 \cdot 10^{-6}$ K^{-1} from 500 to 700°C [84]). After optimisation of the electrode microstructure, with a CGO electrolyte, Marinha et al. managed to obtain an area specific resistance (ASR) of only 0.13 Ωcm^2 at 603°C [85]), far lower than the target which is fixed below 0.15 Ωcm^2 at 700°C. Additionally, Hidelbrand [9] showed that the ASR could be divided by 3 when an interfacial layer was added between the porous electrode and the dense electrolyte, emphasizing the importance of the electrode microstructure on its performances.

The barium cobaltite $Ba_{0.5}Sr_{0.5}Co_{0.8}Fe_{0.2}O_{3-\delta}$ (BSCF), studied by Shao and Haile [86] is also promising. It has very low ASR (only 0.055-0.071 Ωcm^2 and 0.51-0.60 Ωcm^2 at 600°C and 500°C respectively) with $Sm_{0.2}Ce_{0.8}O_{1.9}$ as electrolyte [87], [88]. However, it suffers from risking carbonatation due to the barium content.

Ferro-nickelates are also highly appealing because some compositions are strontium-free, which prevents the chromium poisoning coming from the interconnects.

© 2014 Tous droits réservés.

BLNF (barium, lanthanum, ferro-nickelates) even surpass the previous compounds in terms of catalytic activity, but they pay the price of a much larger TEC and strong sensitivity to CO_2 leading to quick performance losses [89], [90].

Other structures were alternatively studied, to pass from oxygen-deficient oxides to oxygen-interstitial ones. An example of a class of compounds with such a characteristic is the double perovskite. Others are the brownmillerites and the Ruddlesden-Popper layered oxides.

1.4.3.2. Double perovskites

The general formula of the double perovskites is $AA'M_2O_5$ where A is usually a lanthanide, A' an alkaline-earth element and M a 3d metal (typically Mn or Co).

Unlike the other perovskites, where the two A and A' cations are statistically disordered and the compounds are conventionally labelled $A_{0.5}A'_{0.5}MO_{3-x}$, in the double perovskites A and A' are ordered. This occurrence often induces peculiar structural and electronic properties (giant magnetoresistance and superconductivity).

The ordering typically arises for cations having a large difference in their radii, for instance barium and a small lanthanide.

The first report on these phases dates back to 1999, thanks to the work of Maignan et al. [91], for a series of cobaltites with general formula $LnBaCo_2O_{5+\delta}$ (Ln=Pr-Ho). Their structures derive from the '112' type structure of $YBaFeCuO_5$, while HRTEM revealed the existence of two main structural features: first, the lanthanide and the barium ions order in alternate (001) planes; second, oxygen vacancies tend to accumulate in the lanthanide planes [92].

Also, it was shown that the value of δ could be easily tuned by heat treatment under appropriate atmospheres (variable pO_2) and is directly related to the Ln^{3+} ionic radius (δ increases with increasing radius). In the work by Frontera et al. [93], the key role of temperature and annealing time for oxygen vacancy was proven.

The great improvement in the double perovskites, in comparison to the simple ones, is their intrinsically high kinetic of the oxygen transport. Because of this, the oxygen is fast exchanged at the surface thus resulting in a high catalytic activity.

For instance, $SmBaCo_2O_{5+\delta}$ (SBC) electrical conductivity ranges between 434 and 815 S/cm (500-800°C). Moreover its polarisation resistance upon SDC and LSGM is 0.098 and $0.054 \Omega cm^2$ respectively.

While, the oxygen ionic conductivity of this class of materials still remains quite uncertain and debated. Taskin [94] and Kim [95] obtained quite remarkable values of the transport parameters, which were then disproved by Tarancon [96] and Choi [97].

© 2014 Tous droits réservés.

1.4.3.3. Brownmillerites

Brownmillerites represent a particular case of oxygen-vacancies ordering in oxygen-deficient perovskite structures. With a general formula $A_nM_nO_{3n}$, their structure consist of (n-1) layers of corner-sharing MO_6 octahedra and one layer of MO_4 tetrahedra rows [98], [99].

For the most typical $n\neq1$ composition, $A_2M_2O_6$ (for which n=2) the oxygen vacancies are ordered along the (010) planes, forming a 1D diffusion pathways for oxygen ion migration. The unit cell is orthorhombic and is related to the basic cubic perovskite ABO_3 (n=1) by the following relations: $a\approx\sqrt{2}a_c$, $b\approx4a_c$, $c\approx\sqrt{2}a_c$, where a_c is the dimension of the unit cell of the cubic perovskite.

Some Brownmillerites show relatively high electronic conductivity, promising oxygen permeability and compatible TEC ($\approx$11.3-13.6 x $10^{-6}K^{-1}$)[100]–[102]. Polarization resistance was found to be as low as 0.23 Ωcm^2 at 700°C ($Ca_2Fe_{1.6}Co_{0.4}O_5$ [103]), making the Brownmillerites very good candidates for IT-SOFC's application. A scarce literature, though, is available on this class of compounds and the most recent studies date back to 2006.

1.4.3.4. Ruddlesden-Popper layered oxides

Ruddlesden-Popper (RP) compounds are well known and studied since 1958 [104]. Having the general formula $A_{n+1}M_nO_{3n+1}$, the most known family is the one with n=1 to which belongs the highly promising $La_2NiO_{4+\delta}$, which crystalizes in the very well-known K_2NiF_4 structure. A few studies upon RP compounds with $n\geq2$ exist, in which the electrochemical performances were evaluated [105], [106]. The compounds with n=2, 3 displayed very good results, even superior to the ones of $La_2NiO_{4+\delta}$ (ASR ~ 1 Ωcm^2 at 700°C for both $La_3Ni_2O_7$ and $La_4Ni_2O_{10}$ [106]).

In RP compounds belonging to the n=1 series, A is usually a rare earth and M a transition metal. These oxides show T/O-type symmetry (space group I4/mmm, Bmab or Fmmm) although, upon increasing temperature, the orthorhombic cell tends to transform into the higher symmetry tetragonal one (I4/mmm).

The phase transition occurs over a broad range of temperatures (150-650°C) but is not accompanied by a strong change in the cell volume. The transition temperature depends both on the metal ion and on the oxygen stoichiometry, namely on the oxygen partial pressure.

On the other hand, the oxygen stoichiometry also depends on the substitution on the lanthanide site and it can be modulated by substitution of higher or lower valence ions even down to zero (perfect stoichiometry).

1.5.Conclusions

A Fuel Cell is defined as an electronic device capable of converting the chemical energy of a fuel directly into electricity. Its functioning is based on the reversed water electrolysis reaction. The chemical potential, instead of being wasted as heat, is used to create a

© 2014 Tous droits réservés.

difference of potential at the two poles of the battery. The electrolyte membrane, permeable to ionic conduction, is electronically insulating thus forcing the electrons outside the cell and creating a current.

While a few types of Fuel Cell (for instance PEM or PA) already possess a mature technology, their large-scale diffusion keeps being limited by price or safety reasons. Many studies to reduce the amount of noble metals (Pt) and expensive NafION® membrane to lower the cost of the cell are currently carried out.

Conversely, because it can be directly fed with hydrocarbons (methane) and other organic compounds (ethanol) and it is not sensitive to carbon monoxide, the SOFC's technology is very promising.

Nevertheless, its development requires novel performing and durable materials to be found. Also, the future of the SOFC technology depends on the ability to lower the working temperature from approximately 1000°C to 700°C (the so called intermediate temperature (IT) SOFC).

Concerning the electrolyte, despite many researches, the reference materials still remain the yttrium stabilized zirconia (YSZ) and the gadolinium doped ceria (CGO).

For the anode, the crucial point still remains the materials' stability, meant as sulphur tolerance and resistance to coking when working with hydrocarbons. Even though a large set of materials resistant to even high levels of H_2S already exists, their performances are not comparable with the traditional SOFC's materials.

For the cathode, the main point is reducing the working temperature without losing the performances. A big number of possible alternatives (perovskites, Ruddlesden-Popper materials, double perovskites) are already under study. Amongst them, cobaltites look the most promising though they display dilatation coefficients way too high thus damaging the durability of the systems. Therefore, the need for novel SOFC electrode materials is still great and represents a major scientific and technological challenge.

Recently, good performances were evidenced at the UCCS laboratory of the University of Lille 1 for the well-known thermoelectric compound $Ca_3Co_4O_{9+\delta}$ (CCO). With a TEC in the same range of magnitude than the commonly developed electrolytes, this material is promising. With an oxygen transfer coefficient of only $1.6 \cdot 10^{-7}$ $cm \cdot s^{-1}$ at 700°C [107], high catalytic performances towards the oxygen reduction reaction should be expected. As said in introduction, the first electrodes studied at UCCS were prepared by brushing. K. Nagasawa obtained an ASR of 4.00 Ωcm^2 at 700°C under air for pure CCO electrode, which was decreased to 1.42 Ωcm^2 by addition of $30\%_{w/w}$ of ceria to the electrode [4]. This value was greatly reduced by subsequent optimisation of the cathode composition and thickness. Using screen printing, we manage to improve the electrode's performances by optimising its composition and its thickness. This is the aim of the second chapter.

© 2014 Tous droits réservés.

2. Optimisation of CCO electrode prepared by screen printing

As already mentioned in the introduction (see §1.5), the calcium cobaltite $Ca_3Co_4O_{9+\delta}$ belongs to a class of compound of great interest. These misfit layered oxides feature adequate electronic conduction, interesting ionic conductivity, high thermoelectric properties as well as great magnetic susceptibility. They were first studied for their thermoelectric properties with, as reported by Li *et al* [108], a figure of merit of $0.67 \cdot 10^{-4}$ K^{-1} for CCO at 700°C. These outstanding properties are related to their crystal structure.

In fact, the crystal structure of CCO is rather particular. Earliest attempts to describe its structure date back to 2000 – 2001, with the works of Masset and Grebille [109], [110], in which occasion the definition of “misfit layer compound” was attributed to the CCO.

Misfit layer compounds, as a class of oxides, are since long known and the Ca-Co-O system greatly mimics other ones such as thallium or bismuth cobaltites [111, 112]. These compounds present a misfit structure similar to the one observed for the chalcogenides [113].

As a matter of fact, the CCO lattice consists of alternate stacks of CaO-CoO-CaO rock salt type layers and CdI_2-type CoO_2 layers along the [0 0 1] direction. These two crystalline domains are monodimensionally incommensurable with a monoclinic symmetry for both sub-lattices [114]. Namely, the values of the *a*, *c* and β moduli are the same for both lattices, while the b_{RS} and b_{hex} are not multiple of each other.

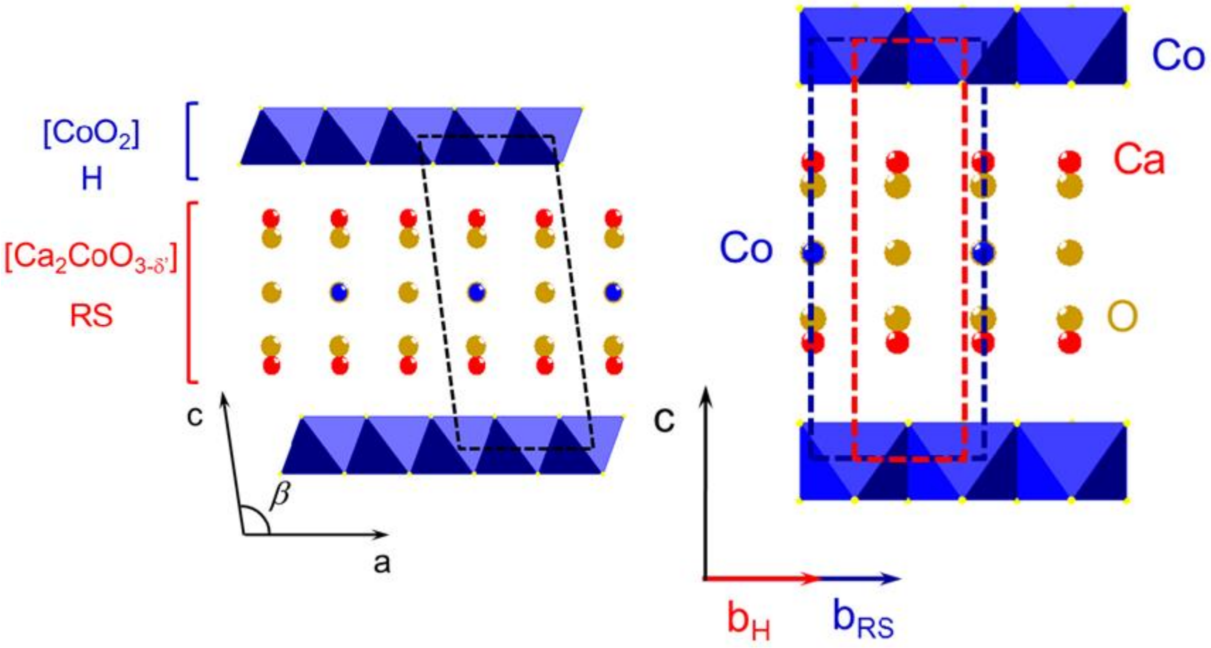

(a) (b)

Fig. 1.5.1 - Crystal structure of $Ca_3Co_4O_{9+\delta}$

© 2014 Tous droits réservés.

The $[Ca_2CoO_3]$ (RS) layer has a strongly distorted arrangement, because the a/b_1 ratio is significantly different from 1 which would correspond to the ideal RS arrangement. Instead, the $[CoO_2]$ sub-lattice is much better correlated to the hexagonal structure CdI_2.

Initially, to resolve the structure (starting from polycrystalline specimens) a commensurate supercell was proposed. Taking into consideration that the ratio b_1/b_2=1.613 is close to 13/8 the deduced cell parameters were a=4.8376 Å, $b \approx 8b_1 \approx 13b_2$=36.479 Å, c=10.833 Å, β=98.06°. According to the stacking sequence (one triple RS stack composed of one CoO and two CaO layers and one single hexagonal layer CoO_2), the ideal supercell should have raw formula $Ca_{32}Co_{42}O_{100}$.

Fig. 1.5.1 reports the crystal structure of CCO on the a-b plane (a) and on the a-c plane (b). The two sub-lattice domains (RS and H) are highlighted with different colours (red and blue, respectively). Also, the b_H and b_{RS} moduli have been evidenced with bold lines. The dashed black line contours the super-cell which was proposed by Masset et al. thus including 13 hexagonal domains (CoO_2) and 8 rock-salt domains (CaO-CoO-CaO). In Table 2.1 are reported the unit cell parameters of the two sub-crystalline domains of $Ca_3Co_4O_{9+\delta}$.

Table 2.1 - Unit cell parameters for $Ca_3Co_4O_{9+}$

Parameter	Value
a	4.83(2) Å
$b_{1\,(RS)}$	4.54(2) Å
$b_{2\,(hex)}$	2.82(1) Å
c	10.76(3) Å
β	98(1) °

Nevertheless, the supercell formalism is questionable because, as it was demonstrated later [109], the two sub-lattices ratio actually differ from the rational 13/8 or 5/8 fractions. Also, the formula would be intermediate between $Ca_{30}Co_{40}O_{90}$ ($10 \cdot Ca_3Co_4O_9$) and $Ca_{33}Co_{44}O_{99}$ ($11 \cdot Ca_3Co_4O_9$) which neglects completely the oxygen non-stoichiometry and cation vacancy. Therefore, the structure is better described in the 5D space group C2/m(1δ0)(α0γ)gm [115]. The composition is then represented by the formula $[Ca_2CoO_3][CoO_2]_{1.62}$. Although this formula gives an approximate composition of $Ca_{3.05}Co_4O_{9+\delta}$, it was decided to refer to CCO as $Ca_3Co_4O_{9+\delta}$. This latter one was also reported as a pure phase, and previous studies were carried out on the basis of this composition.

It was shown that in the hexagonal sub-lattice the valence of cobalt is mixed with a small percentage of Co in 4+ state and the great majority in 3+ state [110]. The mixed oxidation state of cobalt ensures the electronic conduction in the hexagonal $[CoO_2]$ layers and a conductivity of 84 $S \cdot cm^{-1}$ was measured at 700°C [116].

Concerning the rock-salt sub-lattice $[Ca_2CoO_3]$, it should contain both Co in +2 state and the great majority in +3 state [110]. Nonetheless, this hypothesis was disproved by Wakisaka [117] who found no evidences of Co^{2+} in this sub-lattice. This lattice is actually sub-stoichiometric in oxygen. Because of the presence of oxygen vacancies, it has the adequate

© 2014 Tous droits réservés.

characteristics for ionic conduction and oxygen diffusion was recently proven by Thoréton [107], [118] who reported a diffusion coefficient (D*) of $2.7\cdot10^{-10}$ $cm^2\cdot s^{-1}$ at 700°C, associated to a surface exchange coefficient (k*) of $1.6\cdot10^{-7}$ $cm\cdot s^{-1}$.

These two very particular characteristics (good ionic and electronic conduction) make CCO a Mixed Ionic Electronic Conductor (MIEC) and thus a very interesting candidate for SOFC cathode.

Since it reacts with YSZ, the electrochemical performances of this material as a SOFC cathode were first characterised at UCCS with a CGO electrolyte.

Electrochemical Impedance Spectroscopy (EIS) was used to do the measurement. An Area Specific Resistance (ASR) of 4.00 Ωcm^2 at 700°C and a calculated Thermal Expansion Coefficient (TEC) of $9\text{-}10\cdot10^{-6}$ K^{-1} were first reported for the pure compound [4]. By addition of CGO to the CCO electrode, the TEC was increased to $10\text{-}11\cdot10^{-6}$ K^{-1} which better matches the one of CGO ($\sim12\cdot10^{-6}$ K^{-1}) and the ASR was decreased to 1.42 Ωcm^2 at 700°C under air for a $70\%_{w/w}$ $Ca_3Co_4O_{9+\delta}$ – $30\%_{w/w}$ $Ce_{0.9}Gd_{0.1}O_{1.95}$ composite.

The first samples for EIS experiments were prepared by manually brushing a paste (or ink) on a CGO dense pellet without possibly controlling the thickness, the porosity or the distribution. Also, the reproducibility of the deposits was not controlled as the outcome depended only on the human operator.

Thence, it was decided that adopting another technique was required to achieve a better reproducibility of the coating. The chosen one was the screen printing, and it was performed using an automated DEK 248 screen printer.

In the current work, both the electrode thickness and its composition were optimised. In a first step, an ink prepared in the same conditions as Nagasawa was used.

After the synthesis of the CCO powder and its characterisation, the process of optimisation of the CCO cathode will be presented with a focus on the ink preparation, its deposition and the impact of the electrode thickness and composition on the electrochemical performances, evaluated by Electrochemical Impedance Spectroscopy (EIS).

Finally, the evolution of the preparation methodology will be discussed. Having realised that the inks prepared with ethanol were unstable over the time, a new methodology had to be found. To avoid the desiccation of the inks, due to ethanol evaporation, new ethanol-free inks were prepared and tested. Also, along with that, the impact of the granulometry of the CCO powder on the electrochemical performances was evaluated.

2.1.Synthesis and phase identification

The CCO powder was synthesized by solid state reaction from calcium carbonate $CaCO_3$ (Merck, 99.0%) and cobalt oxide, Co_3Co_4. To avoid moisture, $CaCO_3$ was kept in an oven at 100°C before preparation. For the first syntheses we used a Co_3O_4 (Alfa Æsar, 99.7%)

© 2014 Tous droits réservés.

powder. When the Co_3O_4 source was changed, it was found that the precursors (Co_3O_4, Alfa Æsar, 99.7% and $CaCO_3$, Merck, 99.0%) needed to be finely ground by planetary milling for 5 hours in ethanol before the reaction, in order to decrease their granulometry. The alcoholic suspension was then dried under hood without heating until complete drying.

Then, the mixture was collected in alumina crucibles and subsequently fired at 900°C for 12 hours. The thermal treatment was repeated two or three times with intermediate manual grinding in an agate mortar between each thermal cycle. Intermediary XRD analyses were carried out after each second thermal cycle to assess the powder's composition.

A temperature of 900°C was chosen for the synthesis to avoid the formation of the parasitic phase $Ca_3Co_2O_6$ that appears irreversibly above 950°C. $Ca_3Co_2O_6$, in fact, can be seen as the addition product of:

$$3\ CaO + Co_2O_3$$

Whereas $Ca_3Co_4O_{9+\delta}$ can be seen as the addition product of:

$$3\ CaO + 2\ Co_2O_3$$

While the latter phase is a good MIEC, the former is a semi-insulator (poor electronic conduction). The presence of $Ca_3Co_2O_6$ greatly perturbs the electrochemical properties of the $Ca_3Co_4O_{9+\delta}$. Not only, also the TEC coefficient is different ($9\text{-}10\cdot10^{-6}\ K^{-1}$ for CCO versus $15\text{-}16\cdot10^{-6}\ K^{-1}$ of $Ca_3Co_2O_6$ [119]).

To assess the purity of the phase, XRD analyses were carried out on polycrystalline specimens. Analyses were carried out on a D8 advance Bruker-AXS diffractometer equipped with a Cu anode (CuK_α) and a 1D LynxEye PSD detector. The software (EVA, version 13.0.0.2, copyright 1996-2007) was used to process the data. In particular, the $CuK_{\alpha 2}$ radiation was subtracted to help the phase identification.

PDF (Powder Diffraction File) was used as reference database. All spectra were analysed with EVA© and refined with the FullProf Suite tools. The latter software was used to both simulate theoretical CCO spectra and to compare experimental and calculated spectra, in order to ensure a better understanding of the phase composition for every specimen and refine unit cell parameters.

Fig. 2.1.1 (a) shows the experimental spectrum of polycrystalline CCO. Most of the peaks were assigned to the PDF reference #00-021-0139, which lacks, though, a few lines. To ascertain whether those lines belonged to the CCO phase or not, the theoretical diffractogram of CCO was calculated from structural data. As shown in Fig. 2.1.1 (b), a good match with the experimental data was observed and confirmed the purity of the powder.

© 2014 Tous droits réservés.

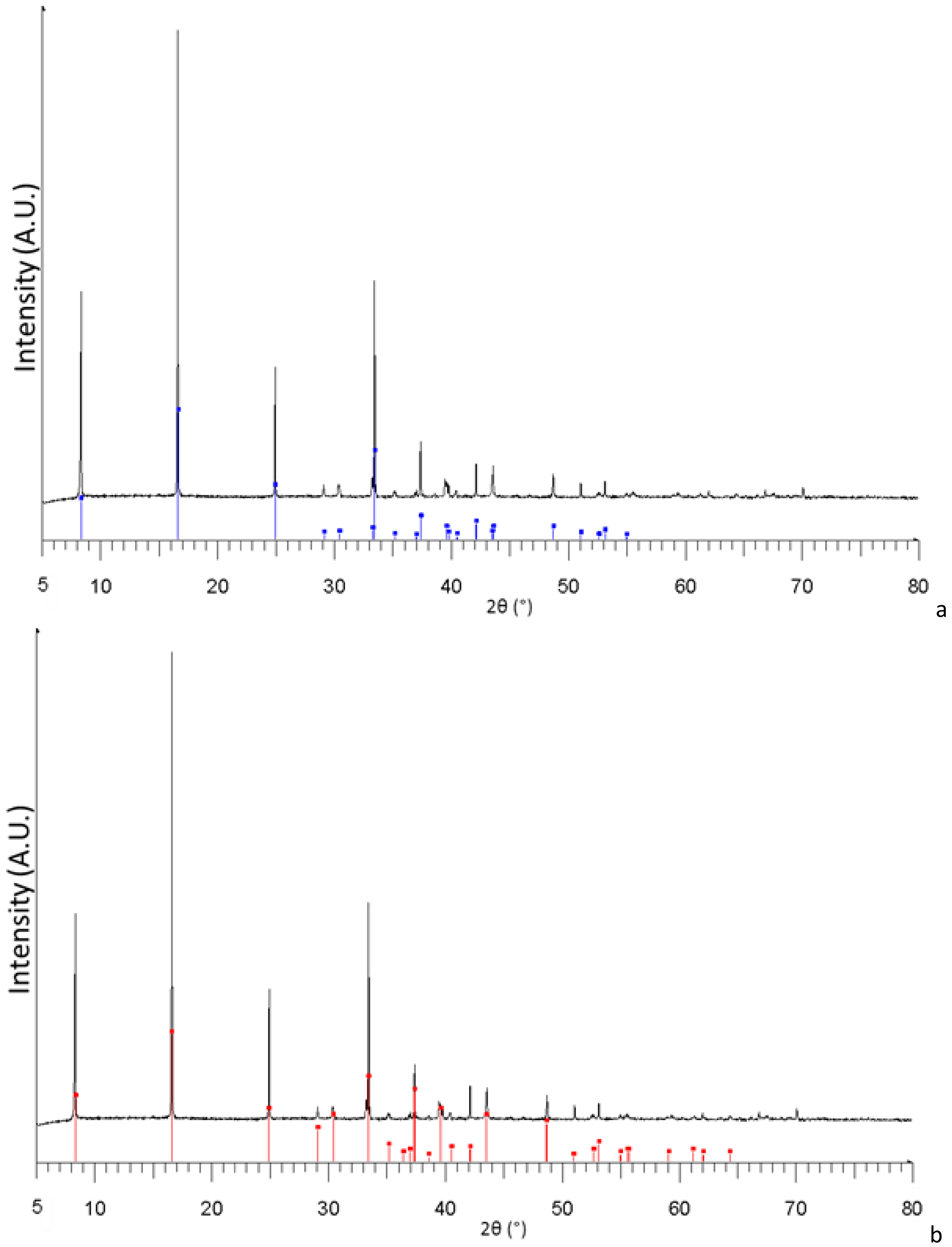

Fig. 2.1.1 - Experimental spectrum of $Ca_3Co_4O_{9+\delta}$ (a) compared to the PDF reference #00-021-0139 (blue bars) and (b) to the theoretical diffractogram calculated from structural data (red bars).

On this base, computer simulation with FullProf Suite tools were performed to further confirm the identity of the phase and to calculate the unit cell parameters of CCO.

© 2014 Tous droits réservés.

The refinements were done starting from a scratch .pcr file, in which the space group and approximate initial unit cell parameters of CCO were inputted. For the background correction was introduced a list of background points derived from the experimental diffractogram. The list was generated manually with the spectrum visualizer's "point selection" tool.

A pseudo-Voigt mathematical function was used to simulate the experimental data, the Full Width at Half Maximum was simulated with the Caglioti function ($FWHM = U \tan^2\theta + V \tan\theta + W$), in which the W-V-U parameters were refined. Due to the specific misfit structure of CCO, it was decided to use a 2-phase approach. Namely, instead of considering the CCO as only one compound it was regarded as a simultaneous contribution of two interdependent phases which shared common (a, c, β) but different b unit cell parameters. During the refinement the former ones were processed simultaneously, with the same constraints on the profile. Conversely, the b_1 and b_2 parameters were set as different and refined at the same time but independently.

The results of the iterated computations are reported in Fig. 2.1.2. The red points represent the experimental diffractogram. The superposed black line is the resulting profile from the simulation. The blue line on the bottom stands for the calculated intensity difference between the experimental (red) and theoretical (black) data.

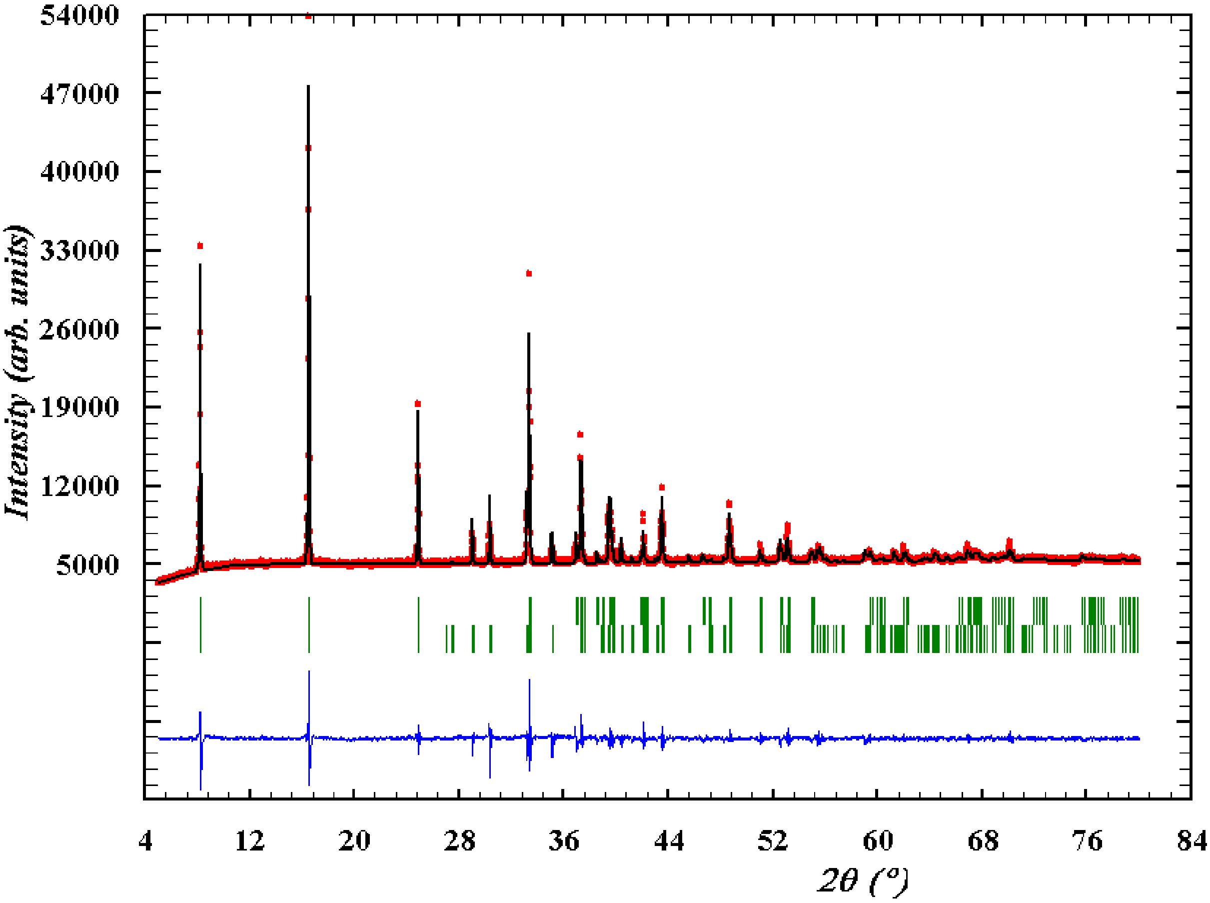

Fig. 2.1.2 - Computer simulations on X-Rays powder diffraction spectrum of CCO

© 2014 Tous droits réservés.

A good agreement was observed between the experimental and calculated data, as it is witnessed by the low intensity of the blue line. In fact, the calculated R-profile non weighted residual (R_p) was about 3%, and the weighted residual (R_{wp}) less than 5%.

Needless to say, the lower this value the better the simulation. Errors may always occur due to zero shift (zero-correction), wrong estimation of the sample's height (S_y-cos or S_y-sin corrections), bad initial unit cell parameters, unaccountable asymmetries affecting the half-width parameters etcetera. Therefore, a standard maximum threshold of 5% for R_{wp} is usually granted.

In Table 2.2 are reported the calculated unit cell parameters of CCO compared with the data from literature reference and the R parameters for the weighted and non-weighted profile residuals.

Table 2.2 - Calculated and reference unit cell parameter for Ca3Co4O9+δ

Parameter	Calculated	Literature [120]
a	4.8305(4)	4.83(2) Å
$b_{1\ (RS)}$	4.5628(4)	4.54(2) Å
$b_{2\ (hex)}$	2.8199(2)	2.82(1) Å
c	10.7653(6)	10.76(3) Å
β	98.143(7)	98(1) °
R_p	2.74 %	
R_{wp}	4.67 %	

Scanning Electron Microscopy (SEM) was also carried out on the powder. An image is given in Fig. 2.1.3. The experiment was carried out on a Hitachi S4700 instrument.

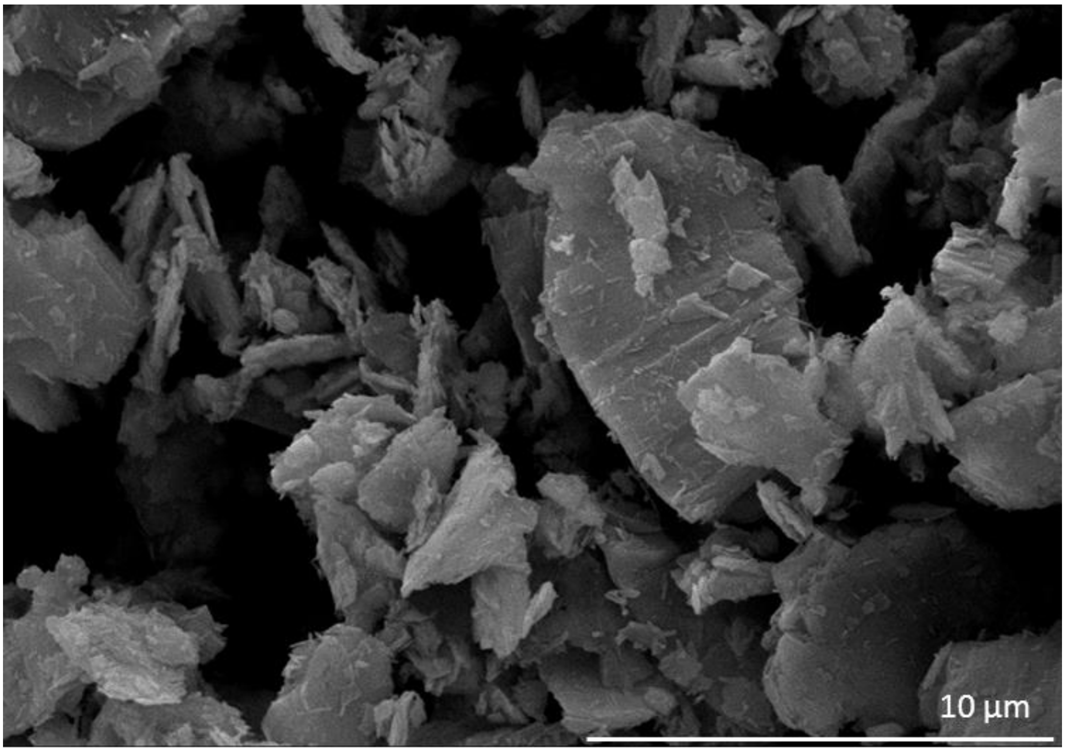

Fig. 2.1.3 - SEM image of a CCO powder (5500X)

© 2014 Tous droits réservés.

The CCO is constituted of flat platelet-like crystals, quite well dispersed allowing to properly recognise the distinctive features of the crystallites. The dimension is not homogenous with the grains sizing from a few (1-2) micrometres to about 10 µm. The shape of the crystallites is not uniform either: some grains tend to an oval form, while others look like broken if not just shapeless.

All in all, the CCO powder reflects the microscopic layered structure of the calcium cobaltite, which has a *c* modulus from 2 to 5 times larger than the b_{1-2} modulus.

2.2.Symmetrical cells prepared with an ink containing ethanol

As said in introduction, a Fuel cell is made of a dense electrolyte and two electrodes. Here, to characterise the performances of CCO as a cathode, symmetrical cells were prepared. Since CCO reacts with YSZ, CGO was chosen as the electrolyte. Since we were only interested in the electrode response, a thick electrolyte with a thickness of 1.8 mm was used. This electrolyte was first prepared before deposition of the electrode by screen printing and impedance spectroscopy.

2.2.1. Preparation of CGO dense electrolytes

Dense CGO pellets, 15 mm in diameter, with $Ce_{0.9}Gd_{0.1}O_{1.95}$ composition, were prepared from commercial Rhodia powder (Rhodia HSA 90/10) according to previously optimised conditions.

The raw powder was die-casted in a circular-holed mould with an applied weight of approximately 1 Mg for 5 minutes. Subsequently, the pellets were recovered and put in a finger glove, evacuated from air and isostatic pressed at 1500 bar for 15 minutes. Finally, the pellets were recovered and heated at 1200°C for 2 hours.

In average, the pellets reached a relative density of 95% after sintering. The last step of preparation was the polishing of the so-obtained pellets. The polishing is necessary for three main reasons. First of all, by polishing it is possible to even out any non-parallelism of the pellet’s faces. Second a smooth surface is more likely to be coated evenly, and grants a higher reproducibility of the specimens for EIS. Third, the shim of the screen printer has a fixed height of 1.80 mm, therefore the thickness of the pellet has to be tuned according to that value.

The polishing of the pellets was done with discs of SiC with increasingly finer grit: P800, which has a particle size of 21.8 µm, and P1200 with a grit size of 15.3 µm.

Finally, upon the pellet has to be deposited the material to be studied. As already mentioned in the introduction (§2), there are many different coating techniques, some of which less reproducible than the others. Here, automatic screen printing was used. This technique will be fully detailed in the following section after the description of the ink preparation.

© 2014 Tous droits réservés.

2.2.2. Ink preparation

The powders that were obtained by solid state reaction and characterised by X-Rays diffraction, were subsequently processed to prepare an ink for screen printing.

For the preparation of the ink, the CCO powder was carefully weighed on an analytic scale (S: 0.0001g) and blended with CGO in the appropriate proportions. $2\%_{w/w}$ of a dispersant (T01) serving to prevent the agglomeration of the crystallites was also added.

To mix the powders, they were put in zirconia pots with a few (from 5 to 8) zirconia spheres and covered with ethanol. The pots containing the mixture were put in a planetary mill to finely grind the powders for 5 hours. Subsequently, the suspension was recovered and a terpene-based ligand (EC3) was added to the suspension in reason of $65\%_{w/w}$ to the mass of the powders (CCO and CGO).

The mixture was then put in a glass container with a small magnetic rod. The suspension was left evaporating under magnetic stirring for a few days until a viscous paste was obtained. At this stage, the viscosity of the ink was not perfectly controlled. It had to be used as quickly as possible due to the volatility of ethanol. If it was needed to be stocked, the glass container was closed with a lid and sealed with a strip of ParaFilm® to minimise the evaporation.

As it was evidenced previously [4], the addition of an electrolyte to the cathode blend greatly increases the electrochemical properties of CCO. In order to further study this effect, a wide range of composition was tried. Inks having the following CCO/CGO proportions were prepared according to the previously mentioned procedure:

- $80\%_{w/w}$ $Ca_3Co_4O_{9+\delta}$ + $20\%_{w/w}$ $Ce_{0.9}Gd_{0.1}O_{1.95}$;
- $70\%_{w/w}$ $Ca_3Co_4O_{9+\delta}$ + $30\%_{w/w}$ $Ce_{0.9}Gd_{0.1}O_{1.95}$;
- $60\%_{w/w}$ $Ca_3Co_4O_{9+\delta}$ + $40\%_{w/w}$ $Ce_{0.9}Gd_{0.1}O_{1.95}$;
- $50\%_{w/w}$ $Ca_3Co_4O_{9+\delta}$ + $50\%_{w/w}$ $Ce_{0.9}Gd_{0.1}O_{1.95}$;
- $30\%_{w/w}$ $Ca_3Co_4O_{9+\delta}$ + $70\%_{w/w}$ $Ce_{0.9}Gd_{0.1}O_{1.95}$.

These inks will be henceforth denoted as, respectively, 80/20-CCO/CGO, 70/30-CCO/CGO, 60/40-CCO/CGO, 50/50-CCO/CGO and 30/70-CCO/CGO.

2.2.3. Deposition by screen printing technique

The screen printing technique is a deposition methodology in which the cathode material has to be prepared in the form of a paste (called "ink"). This paste is then coated on the electrolyte pellet by pressing upon it through a squeegee. Then, the ink is forced through a screen (hence the name screen printing) composed of a fine steel mesh, below which is glued a plastic foil that has a few apertures. This ensemble (steel mesh and plastic foil) is called a "mask". The mask allows depositing perfectly round-shaped layers of material.

Symmetric cells were prepared by screen-printing on CGO pellets (1.8 mm thick) using a DEK 248 screen-printer (Fig. 2.2.1).

© 2014 Tous droits réservés.

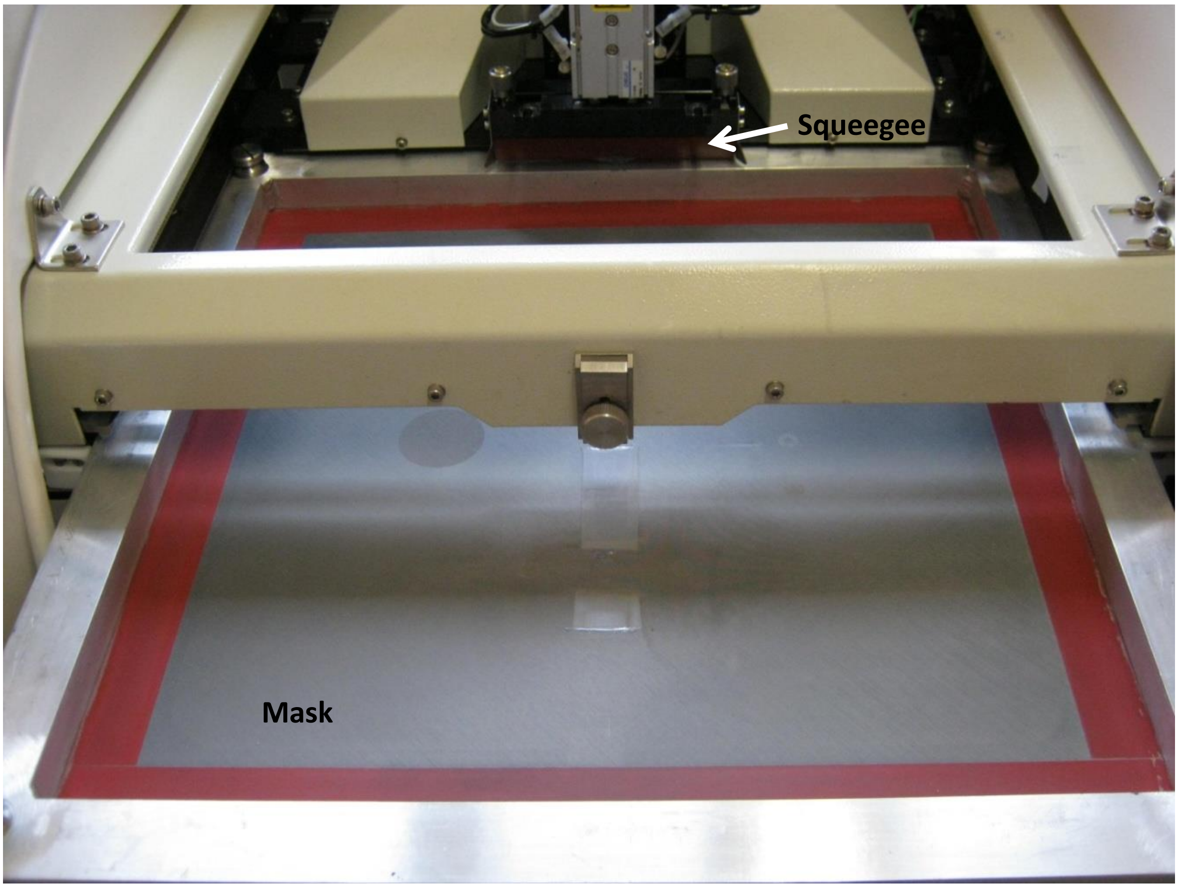

Fig. 2.2.1 - Mask and squeegee of a DEK 248 screen printer

One or several successive depositions with intermediate drying steps at 100°C for 30 minutes were performed to vary the cathode thickness. Subsequently, in order to complete the symmetric cell, an equal deposition was done on the opposite side of the support electrolyte. All the prepared symmetric cells were annealed successively at 500°C for 2h to remove the organics and at 900°C for 1h for sintering. The sintering temperature of 900°C was chosen since, as previously shown [121] and confirmed by Samson *et al.*[7], it leads to the best cathode quality and prevents the CCO decomposition into $Ca_3Co_2O_6$, Co_3O_4 and CoO, which occurs at higher temperature.

The thickness of the deposit is controlled by two main factors:

- Squeegee pressure;
- Brushing speed.

Theoretically, a higher pressure on the squeegee enables more ink to pass through the screen, thus increasing the deposit thickness. Practically, also the mechanical resistance of the CGO support has to be considered in order to avoid fissures, cracks or complete destruction of the pellet.

In fact, as pressure is defined as force over surface ($P = \vec{F} \cdot A^{-1}$), and the surface is constant, to a greater pressure corresponds a greater force. Thus a correct compromise for the applied pressure has to be found in order not to spoil the CGO pellets.

© 2014 Tous droits réservés.

In this case the force is the weight-force ($\vec{F} = m \cdot \vec{g}$), hence from now on when referring to the applied pressure, the surveyed variable parameter will be the weight. In our case, basing on a previous study carried out by Miss D. Huo during her research internship, it was used an applied weight of 4 kg which was the minimum to have uniform deposition without breaking the support.

More often (and also more practically) the brushing speed is the key parameter to control the cathode thickness. Not only, but the deposition's success depends greatly also on the sweeping speed: a too fast passage may leave gaps or uncovered areas. Again basing on the work of Miss D. Huo a speed of 30 $mm \cdot s^{-1}$ was used (for an applied pressure of 4 $kg \cdot m^{-2}$).

Samples with different compositions and thicknesses were prepared. Fig. 2.2.2 shows the Scanning Electron Microscopy (SEM) images of the surface of the corresponding symmetric cells. Because of the grains size's difference between the two phases (CGO grains (~0.2 μm) and CCO grains (~ 1-5 μm)), it appears that the mixed electrodes are not a uniform mix of the phases. Rather, they are more likely an agglomerate mixture of the two components, with CGO particles contouring the CCO grains. This should enhance the catalytic activity of the electrode, although a porosity decrease is evidenced when the amount of CGO increases.

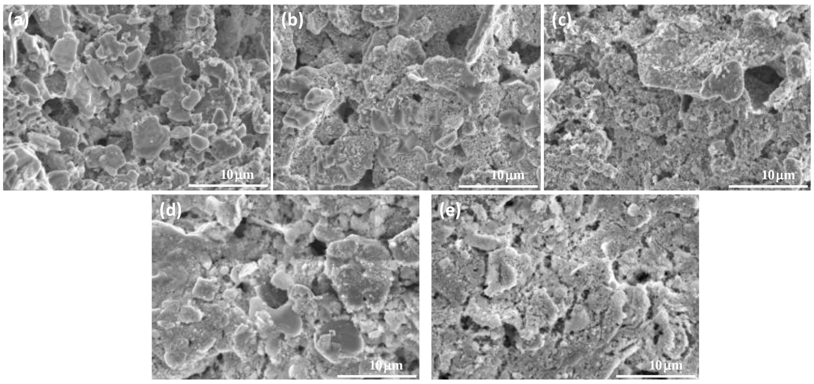

Fig. 2.2.2 - Scanning Electron Microscopy (SEM) micrographs of the symmetric cells surface: (a) 80/20-CCO/CGO, (b) 70/30-CCO/CGO, (c) 60/40-CCO/CGO, (d) 50/50-CCO/CGO, (e) 30/70-CCO/CGO

To study the electrode thickness effect, a series of 50/50-CCO/CGO symmetric cells were prepared with various cathode thicknesses varying in between 9 and 52μm. The SEM micrographs of the cross-sections of 50/50-CCO/CGO cells are shown in Fig. 2.2.3. One can notice that the cathode/CGO interface is uniform, presenting good bonding and continuous contact with the dense electrolyte pellet. As expected, the adhesion of the composite cathode layer on the CGO electrolyte was excellent because of the similar TEC of both materials.

© 2014 Tous droits réservés.

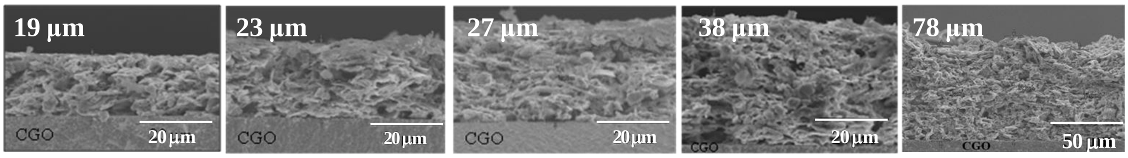

Fig. 2.2.3 - SEM micrographs of the fractured cross-section of CCO50-50 symmetric cells.

Table 2.3 summarises the thicknesses of samples with different compositions and a thickness of about 20 µm (corresponding to the deposition of 2 layers).

Table 2.3 - Studied CCO/CGO mixed compositions for preparation of screen-printing cathodes

Name	Cathode composition	Cathode average thickness (µm)
80/20-CCO/CGO	80wt.% CCO-20wt.% CGO	24
70/30-CCO/CGO	70wt.% CCO-30wt.% CGO	23
60/40-CCO/CGO	60wt.% CCO-40 wt.% CGO	26
50/50-CCO/CGO	50wt.% CCO-50wt.% CGO	21
70/30-CCO/CGO	30wt.% CCO-70wt.% CGO	21

To check the impact of the cathode composition on one hand and the cathode thickness on the other hand, these materials were characterised by Electrochemical Impedance Spectroscopy (EIS).

2.3.Electrochemical properties of the CCO screen printed cathode

Electrochemical Impedance Spectroscopy is a powerful technique for the characterization of electrochemical systems. From impedance spectroscopy not only the area specific resistance of the electrode can be derived but, by modelling the impedance spectra, it should also be possible to go further in the understanding of the mechanisms involved in the oxygen reduction reaction at the cathode.

2.3.1. Principles of Electrochemical Impedance Spectroscopy (EIS)

From an electronic point of view, oxide ion conductive ceramics behave as a capacitor in parallel with a resistance. As a matter of fact, in a pure oxide ion conductor the current flow is carried out by oxygen ions, but the charge transfer at the surface is usually limited (which explains the capacitor behaviour). Therefore, the electrical characterization of such materials cannot be performed with Direct Current. Alternating Current must be applied to derive the impedance Z(ω). EIS is usually measured by applying a sinusoidal potential excitation:

$$E(\omega) = E_0 e^{j\omega t} \tag{2.3.1}$$

where E(ω) is the potential at time t, E_0 is the amplitude of the signal, and ω is the relaxation frequency (ω=2πf). The response signal, I(ω) is shifted in phase (ϕ) and has a different amplitude, I_0.

$$I(\omega) = I_0 e^{j(\omega t+\phi)} \tag{2.3.2}$$

© 2014 Tous droits réservés.

By varying the frequency of the applied signal, the impedance of the system, as a function of frequency, can be recorded.

From equation 2.3.1, in polar coordinate the impedance is given by:

$$Z(\omega) = Z_0 e^{j\phi} \tag{2.3.3}$$

where Z_0 is the magnitude of the impedance and ϕ is the phase shift.

In cartesian coordinate, the impedance is given by:

$$Z(\omega) = Z' + jZ" \tag{2.3.4}$$

where Z' is the real part of the impedance and Z'' is the imaginary part ($j = \sqrt{-1}$). Here below, the two orthogonal coordinate values are explicited.

$$Z' = |Z| cos\phi \,; Z" = |Z| sin\phi \tag{2.3.5}$$

With the phase angle

$$\phi = \tan^{-1}(\frac{Z''}{Z'}) \tag{2.3.6}$$

and the modulus

$$|Z|^2 = (Z')^2 + (Z'')^2 \tag{2.3.7}$$

the plot of the real part of impedance against the opposite imaginary part gives the Nyquist plot.

The advantage of the Nyquist representation is that it gives a quick overview of the data and allows quantitative interpretation. However, when plotting data in the Nyquist format, the real axis must be normal to the imaginary axis, so as not to deform the shape of the curve. The disadvantage of the Nyquist representation is that the frequency dimension of the data is lost, therefore the frequency has to usually be labelled on the diagram.

© 2014 Tous droits réservés.

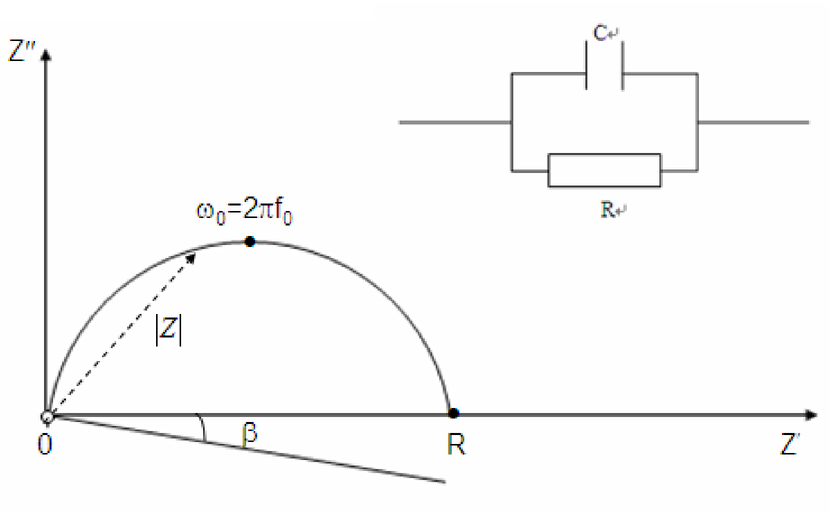

Fig. 2.3.1 - Simple equivalent of a RC parallel circuit and its corresponding Nyquist diagram

In case of a resistor placed in parallel with a capacitor (as shown in Fig. 2.3.1), the impedance of the circuit is given by:

$$\frac{1}{Z} = \frac{1}{R} + jC\omega \quad \Rightarrow \quad Z = \frac{R}{1+R^2C^2\omega^2} - j\frac{R^2C\omega}{1+R^2C^2\omega^2} \tag{2.3.8}$$

One can easily demonstrate the equation of the Nyquist plot in this case, which is that of a circle of radius R/2 with a frequency ω_0=1/RC.

$$z = \frac{R}{1+(\omega/\omega_0)^2} - j\frac{R(\omega/\omega_0)}{1+(\omega/\omega_0)^2} \tag{2.3.9}$$

From these data, the resistance R corresponds to the intercept with the real axis, and the capacitance C is derived from ω_0.

However, in a ceramic, the phenomena are slightly more complicated. In absence of porosity, the ceramic can be described as grains of given size connected to each other by grain boundaries. A response of the electrodes at low frequency is also expected. Using a simple description, the whole can be modelled with serial (R//C) circuits as shown in Fig. 2.3.1.

© 2014 Tous droits réservés.

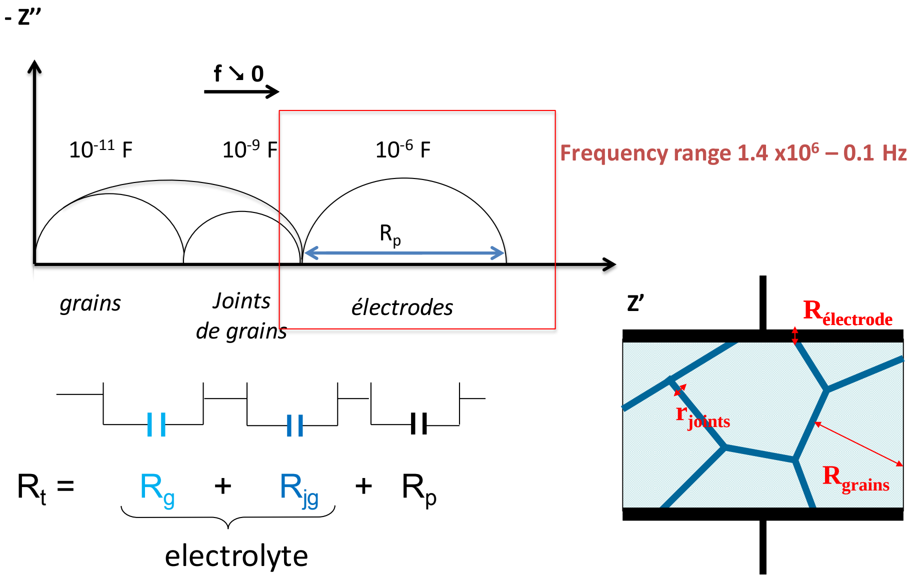

Fig. 2.3.2 - Responses in the frequency domain of the elements of a symmetric EIS cell

Knowing the thickness (e) and surface (S) of sample, the resistance is a function of the conductivity and the capacitance is a function of the dielectric constant of the material as follows:

$$R = \frac{1}{\sigma} \cdot \frac{e}{S} \qquad C = \varepsilon\varepsilon_0 \frac{e}{S} \tag{2.3.10}$$

where ε_0 is the permittivity of vacuum (ε_0=8.8592×10^{-10} F·cm^{-1}).

The capacity of the bulk, which corresponds to the transgranular polarization, is usually in the order of 10^{-12}-10^{-11} F, the one related to the intergranular polarization is in the order of 10^{-9} F and the electrode polarization is around 10^{-5}-10^{-6} F. In Nyquist representation, the bulk response is therefore expected at high frequency, and the electrode response at low frequency. As shown in Fig. 2.3.2, the resistance of polarisation, R_p, corresponding to the electrode response, is given by the difference between the intercepts of the electrode response at high and low frequency. Taking into account the surface of the sample, the Area Specific Resistance can be deduced as follows:

$$ASR=R_p \times S/2$$

Modelling an electrochemical phenomenon with an ideal capacitor implies that the surface under investigation is homogeneous, which is not the case. A CPE (Constant Phase Element) is usually used instead of a capacitance:

$$z = \frac{R}{1+RY_0(j\omega)^n} \tag{2.3.11}$$

where Y_0 is the ideal capacitance and n is an experimental constant, 0≤n≤1. When n=1, CPE acts as an ideal capacitor.

© 2014 Tous droits réservés.

The fitting procedure also leads to the relaxation frequency, f_0, and depression angle, β, according to the following relations:

$$f_0 = \frac{1}{\left[2\pi(RY_0)^{1/n}\right]} \tag{2.3.12}$$

$$\beta = \frac{(1-n)\pi}{2} \tag{2.3.13}$$

The depression angle can be interpreted in terms of the heterogeneity of the examined property. A high β value indicates higher heterogeneity.

To model the diffusion of ionic species at the interface of the electrode, a Warburg Impedance, Z_{war}, is commonly used. Several expressions, based on different assumption of infinite diffusion layer are given:

$$Z = \frac{R\tanh(I\omega T)^P}{(I\omega T)^P} \tag{2.3.14}$$

where R is the diffusion resistance, T the time constant and P the phase constant.

When the temperature increases, a shift towards higher frequency is observed and, due to experimental limitations, only the electrode response may be measured at high temperature. The resistance of the electrolyte, including the grain boundary contribution, corresponds to the intercept of the impedance spectra with the real axis at high frequency.

Instead, the electrode's mechanism is more complicated. To allow the reaction occurring at the Triple Point Boundary, the electrode must be porous or, ideally, a mixed conductor. As shown in Fig. 2.3.3, the oxygen reduction reaction can be dissociated into several steps: the oxygen molecule diffusion into the porous electrode, the oxygen molecule adsorption/dissociation, the charge transfer, and the diffusion of the ionic species. All these contributions will be determined by characteristic frequencies in the impedance spectrum.

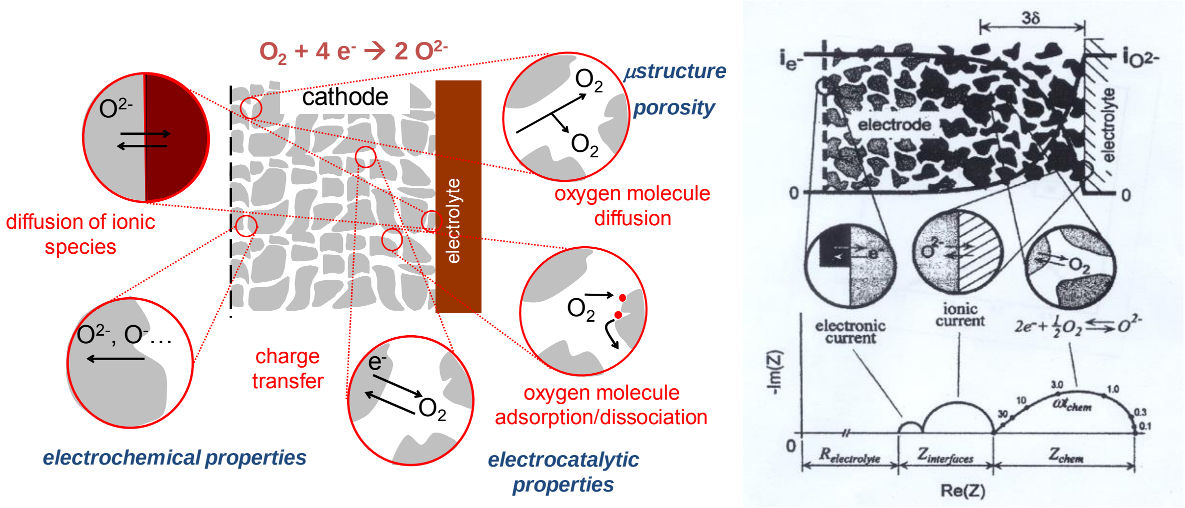

Fig. 2.3.3 - Representations of the contributions from the Adler-Lane-Steele model [122]

© 2014 Tous droits réservés.

The polarisation resistance is not only a function of the intrinsic properties of the studied materials but depends also on the sample microstructure. To describe this response, a good model has been given by Adler *et al.* [122] (Fig. 2.3.3) in which the polarisation resistance is the sum of the resistances of the interface plus a chemical resistance, which is given by:

$$R_{chem} = \frac{RT}{2F^2}\sqrt{\frac{\tau}{(1-\varepsilon)aC_0^2D^*k^*}} \tag{2.3.15}$$

Where D* is the oxygen tracer diffusion coefficient, k* the oxygen surface exchange coefficient, τ the tortuosity, ε the porosity, *a* the internal surface area/unit volume and C_0 the molar concentration of oxygen ions.

2.3.2. Experimental set-up

Here, the set-up shown in Fig. 2.3.4 was used for the experiment. The sample was introduced in between two gold grids used as current collector.

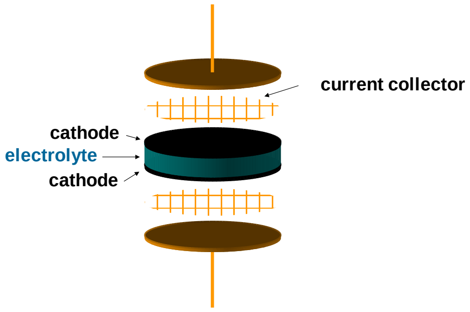

Fig. 2.3.4 - Experimental setup for a symmetric EIS cell

A SI Solartron 1260 frequency response analyser was used for the analysis in the 10^{-1}-10^{6} Hz frequency range. The amplitude of the excitation voltage used was 50mV, with respect to the linearity of the electrical response. Measurements were performed in air, from 600 to 800°C. For sample stabilisation before impedance measurements, the prepared cells were heated at 800°C and two successive heating and cooling cycles were performed. Data were collected every 50°C, with a temperature accuracy of ±1°C and a minimum dwell of 2h for thermal sample stabilisation between each temperature change [4]–[6]. The sample was considered thermally stabilised when the measured global cell resistance varied less than 5%. The measured data were plotted in the complex plane and fitted to an equivalent circuit using the nonlinear least-squares fitting program ZView 3.3a [123]. They were normalized to the geometrical area of the cell and were divided by two to account for the symmetric structure of the cell. The ASR of the cathode layers were deduced from values of the diagram intercept with Z’ axis at low and high frequency.

2.3.3. Influence of the cathode composition

Fig. 2.3.5 (a) reports the stacked Nyquist plot circles for all the composite electrodes at 700°C. Since a zero-shift of the resistance at high frequency was observed from one sample to another due to different contact resistances, for the sake of clarity all the electrode spectra were shifted to the origin. From the depress semi-circles reported below, the ASR

© 2014 Tous droits réservés.

were extracted. The highest value is reported for 80/20-CCO/CGO which shows an ASR of 1.9 Ωcm². The ASR decreases dramatically with increasing CGO content to attain a minimum for 50/50-CCO/CGO (0.5 Ωcm²). Further increasing the amount of CGO has a counterproductive effect on the electrochemical properties of the composite electrode (ASR = 1.5 Ωcm²).

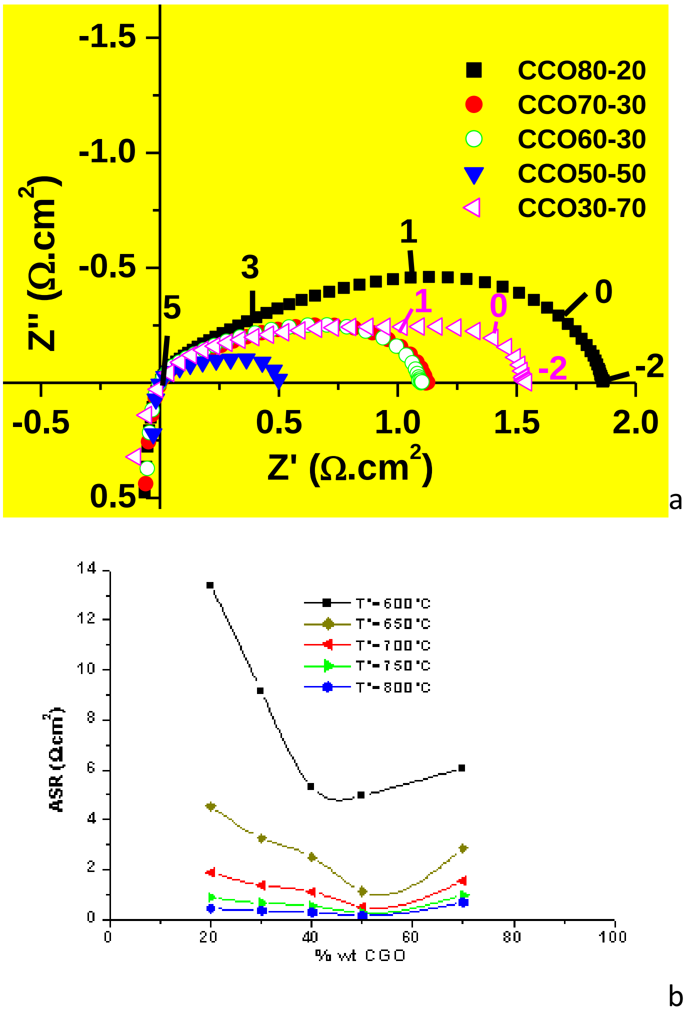

Fig. 2.3.5 - Influence of the cathode composition on the ASR of symmetric CGO-CCO cells: Nyquist plot circles at 700°C (a), ASR at different temperatures (b).

Fig. 2.3.5(b) sums up the EIS results on 80/20, 70/30, 60/40, 50/50 and 30/70-CCO/CGO specimens. The trend seems vaguely parabolic, with ASR decreasing with increasing CGO content until attaining a minimum and then rising up again.

As the CGO content increases, the ASR values decrease to reach a minimum for the 50%$_{w/w}$ CGO composition (ASR = 0.5 Ω.cm^2 at 700°C) and then increases for higher values of CGO content likely because of a lack of CCO percolation, leading to an increase of resistance due to the CGO excess. Thus, the 50/50-CCO/CGO composition can be considered as the optimal weight ratio, with ASR values of about one half of the 80/20-CCO/CGO ones and 10 times smaller than the ones which were previously measured on pure CCO cathodes (ASR= 4 Ω.cm^2 at 700°C) [4]. It was therefore concluded that the optimum composition for the cathode is a blend of $Ca_3Co_4O_{9+\delta}$ and $Ce_{0.9}Gd_{0.1}O_{1.95}$ with a 1 to 1 mass ratio. On this base,

© 2014 Tous droits réservés.

further investigations on the effect of the layer thickness on the electrochemical performances were carried out.

2.3.4. Influence of the cathode thickness

After having found the optimum condition for the cathode's composition, the survey moved towards the investigation of the influence of the cathode's thickness. For this reason, a 50/50-CCO/CGO ink was prepared and screen printed over 4 dense CGO pellets to produce as many symmetric cells. 4 different electrode thicknesses were obtained by single or repeated passages: 9.4 µm (1 deposition, 50 mm·s^{-1}), 13µm (1 deposition, 30 mm·s^{-1}), 20.6 µm (2 depositions, 50 mm·s^{-1}) and 52µm (4 depositions, 30 mm·s^{-1}).

Fig. 2.3.6 (a) reports the stacked Nyquist plot circles for the different thicknesses. The highest value is reported for the 9.4 µm layer which shows an ASR of ~1.9 Ωcm². The ASR decreases dramatically for even small increases of the deposit's thickness (~0.9 Ωcm² at 13 µm) to attain a minimum for the specimen having a 20 µm thick deposit (0.5 Ωcm²). Beyond this point, the effect on the electrochemical properties of the composite electrode is mildly counterproductive: the ASR slightly increases (~0.8 Ωcm²) attaining a value close to the one for 13 µm.

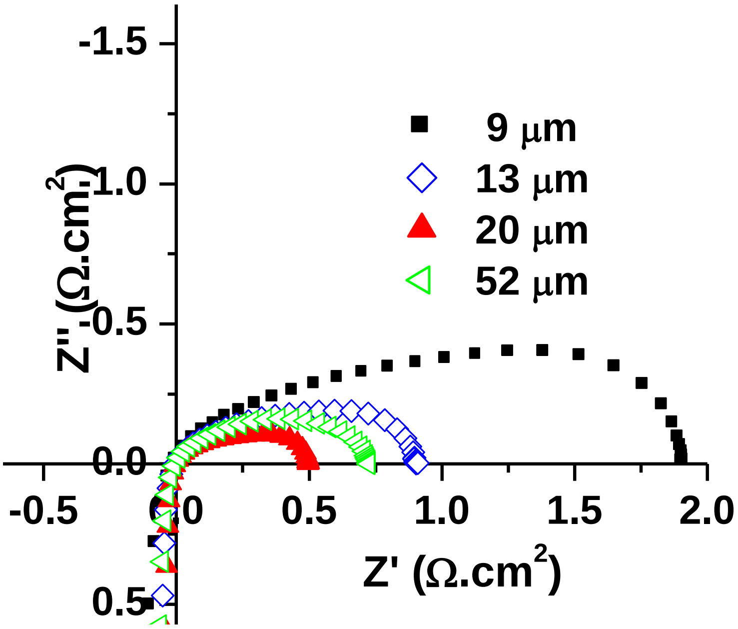

a

© 2014 Tous droits réservés.

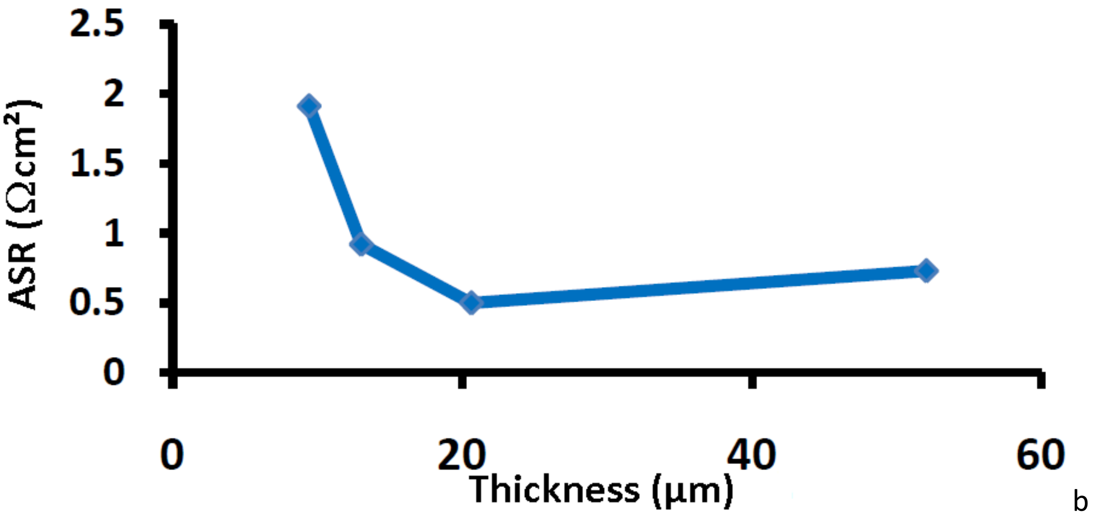

Fig. 2.3.6 – Influence of the electrode thickness for 50/50-CCO/CGO electrodes at 700°C (a) Nyquist plots and (b) trend of the ASR as a function of the electrode thickness.

Fig. 2.3.6 (b) summarizes the obtained results. The value of ASR in Ωcm² is plotted against the cathode layer thickness in µm. After an initial abrupt decrease of ASR with thickness, the value tends to stabilize and the augmentation of the number of deposited layer (4 layers for the 52 µm specimen) has a rather negative effect. The minimum for a thickness of about 20 µm shows that there is a competition between two effects. On one hand, for too thin electrodes, the cathode volume is not sufficient as catalyst for the ORR, leading to an increased ASR. On the other hand, for too thick electrodes, the ASR value increases, due to poor gas diffusion and an enlargement of the electron transport path.

It was therefore concluded that the best value of the thickness of a composite 50/50-CCO/CGO electrode layer is ~20 µm. This value was the one which was always aimed at in all the successive sample preparation for EIS.

2.4.Improvement in ink preparation: tri-cylinder method

The protocol for the ink's preparation described in § 2.2 was considered not reproducible and strongly dependent on the manipulator's impression. In fact, the viscosity of the paste was tuned by evaporating ethanol from the suspension for a longer or a shorter time. Or, in case of overdrying, the suspension was re-fluidified by adding more ethanol. The worst inconvenience was that the thickness of the ink was not measured with a viscometer but only eye-judged. Though this might have been resolved by actually measuring the viscosity, the difficulty stayed in the fact that there are no reference values for this parameter.

Not only: due to the high volatility of ethanol itself, the paste tended to quickly increase its viscosity up to drying out in few weeks. Even during the same day the viscosity changed in a non-negligible way.

Therefore, the protocol was modified by elimination of the alcoholic component in order to make the whole process more reproducible. The contribution of ethanol was taken over by the terpene-based resin only. The inks which were obtained from the modified protocol

© 2014 Tous droits réservés.

proved to be more time-stable: specimens prepared in this fashion kept the same viscosity and texture after several months. Moreover, different cells coated with different inks, which were realized with the new protocol, gave equal results in term of layer thickness and microstructure.

2.4.1. Preparation of the inks with a tri-cylinder crusher machine

To prepare the ethanol-free ink, a blend of 50%$_{w/w}$ CCO and 50%$_{w/w}$ CGO was weighed on an analytic scale (S = 0.001g) and added with 2%$_{w/w}$ of organic dispersant T01. Successively, the blend was put in zirconia pots with a few zirconia balls to be grinded at the planetary miller. The powder was covered in ethanol to minimise the shocks and prevent overheating. The mixture was ground for 5 hours and then recovered in a large beaker. All the components (pots, balls) were washed with fresh ethanol to maximise the recovery.

Successively, the alcoholic suspension was completely evaporated. Then, the resin ligand was added in a ratio of 65%$_{w/w}$ to the mass of CCO and CGO together and manually incorporated into the powder blend with a metallic spatula. Finally, the resulting cream was collected with a paper playing-card and homogenised with a three-cylinder rotating crusher. The paste coming out from the third cylinder was repeatedly recovered with the paper playing-card and put back on the first cylinder to reiterate the homogenisation.

Lastly, the ink was recovered from the third cylinder of the crusher machine and put in a glass pot closed with a lid. Initially, the lid was sealed with a strip of ParaFilm® but subsequent trials showed that this measure was not necessary. The ink kept its aspect and viscosity for a very long time (several months) with or without the ParaFilm® sealing strip.

Therefore, the new methodology for the ink preparation was elected as the new standard procedure for all the following sample preparation. Although it was not systematically studied the effect of layer thickness and cathode composition for the new inks, the previous specifications (20 µm thickness, 50%$_{w/w}$ CCO and 50%$_{w/w}$ CCO, 2 hours at 500°C and 1 hour at 900°C) were kept.

Here below are reported the experimental results of the EIS for a symmetric cell with a 50/50-CGO/CCO cathode prepared with the tri-cylinder method with a thickness of 22 µm. Fig. 2.4.1 reports the spectra at 600°C, 700°C and at 800°C. From these experimental results with the software Z-View the values of the ASR were calculated. Generally speaking, the magnitude of the circles decreases dramatically when the temperature increases. The ASR goes down from 2.9 Ωcm² at 600°C to 0.6 Ωcm² at 700°C and 0.2 Ωcm² at 800°C. The ASR is slightly higher than that obtained with the ethanol based ink but remains still in the same order of magnitude.

© 2014 Tous droits réservés.

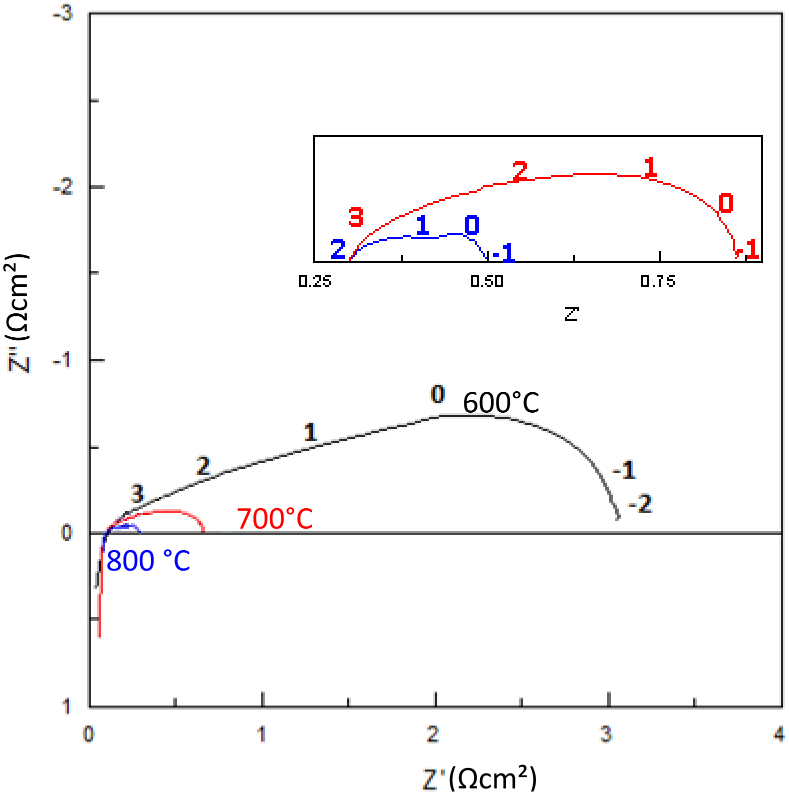

Fig. 2.4.1 – Temperature dependent EIS spectreof a 50/50-CCO/CGO cathode obtained with the ethanol-free ink, in frame zoom of the circles at 700°C (red) and 800°C (blue).

This result mimics exactly the results obtained for the ethanol-based inks. Just as for the previous case, the SEM micrographs, reported in Fig. 2.4.2, show a good uniformity of the layer and a good adhesion. The comparison of the SEM images of the cathodes from the two methods (with or without ethanol) does not reveal any major difference.

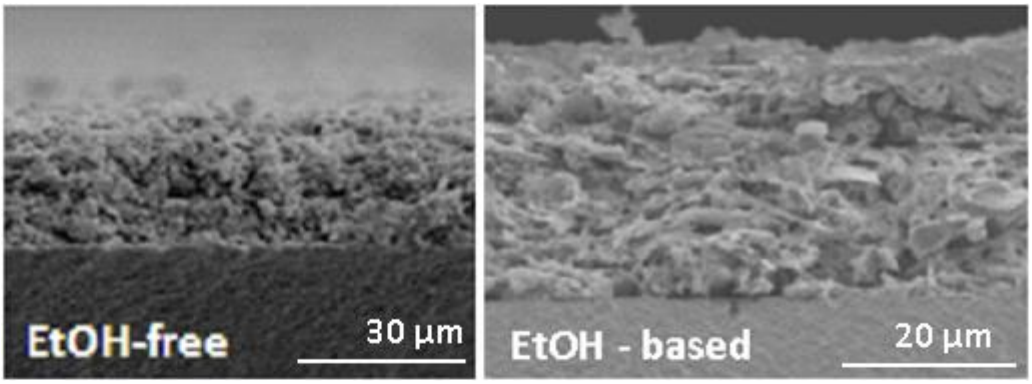

Fig. 2.4.2 - Comparison between the ethanol-based and the ethanol-free 50/50-CCO/CGO cathodes

Having obtained a similar result as to the ethanol-based inks, we can conclude that the optimum conditions (20 µm and 50%$_{w/w}$ CCO plus 50%$_{w/w}$ CGO) are valid also for the new formulation. More importantly, this allows proceeding further in the investigation of the parameters which influence the overall performances of a CCO-based cathode. For this reason, in the next section the effect of the CCO particle size was studied.

© 2014 Tous droits réservés.

2.4.2. Attrition-milled CCO powder for composite 50/50-CGO/CCO electrode

It is at this stage that the influence of the grain size of the starting raw CCO powder on the electrochemical properties is evaluated. Powders with a different particle size were obtained by different methods.

In this case, the CCO powders that were obtained by solid state reaction as described in §2.1 were treated in an attrition miller. The attrition miller is a machine tool that grinds down the powders to the micrometric scale to a few tens of micrometre.

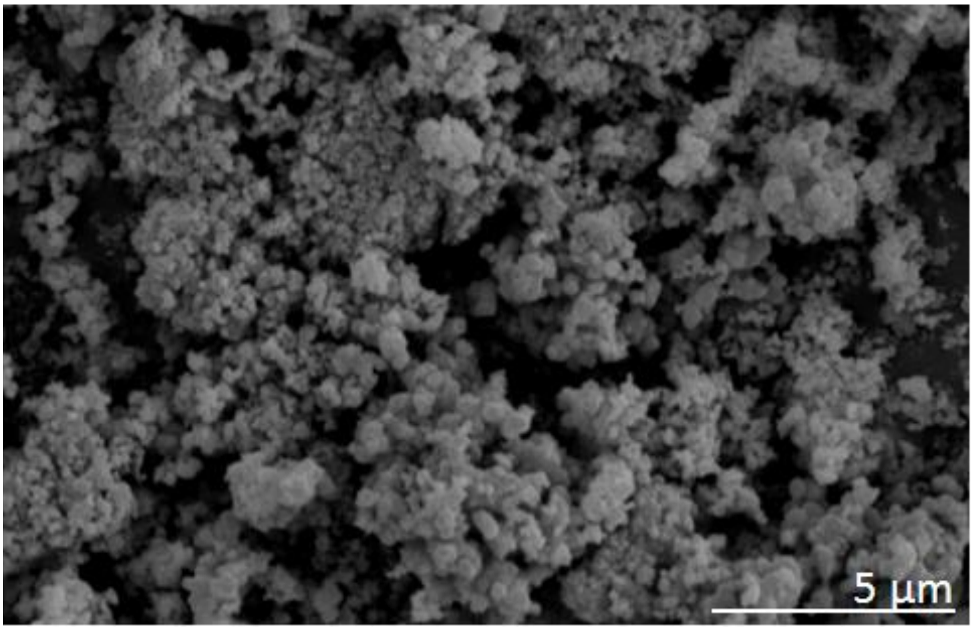

Fig. 2.4.3 - SEM of attrition milled CCO powder

The CCO powder is put in a Teflon bowl with very small zirconia balls (ø = 1 mm) and covered in ethanol. The volume ratio between the powder and the balls has to be quite precise, in order to optimise the grinding. A too big amount of one component or the other results in an insufficient grinding (excess of CCO) or contamination from balls' shock-deterioration (excess of zirconia balls). The proportions used for the preparation were 40 g of powder and 120 mL of zirconia balls.

The amount of ethanol, instead, is not crucial, and is usually added through a small bottle. The effect of ethanol is to improve the fluidity of the mixture and to avoid overheating. Thus, the ethanol has to be enough to moisten and cover fully the CCO/balls mixture. It was found that for 40 g of CCO the least amount of ethanol needed is 40 mL.

The raw CCO was left grinding for 4 hours and then was recovered in a big glass beaker. All the pieces of the attrition grinder were washed with fresh ethanol to maximize the recovery. Also the zirconia balls were washed repeatedly in fresh ethanol and the alcoholic suspension was added into the glass beaker. Finally, the suspension was completely evaporated under hood with no heating and recovered.

© 2014 Tous droits réservés.

The attrition-ground CCO powder was then used to prepare an ink following the procedure described earlier (§2.4) and the ink coated symmetrically on a CGO dense pellet by screen printing. The deposit was grafted with the usual conditions (1 hour at 500°C then 2 hours at 900°C).

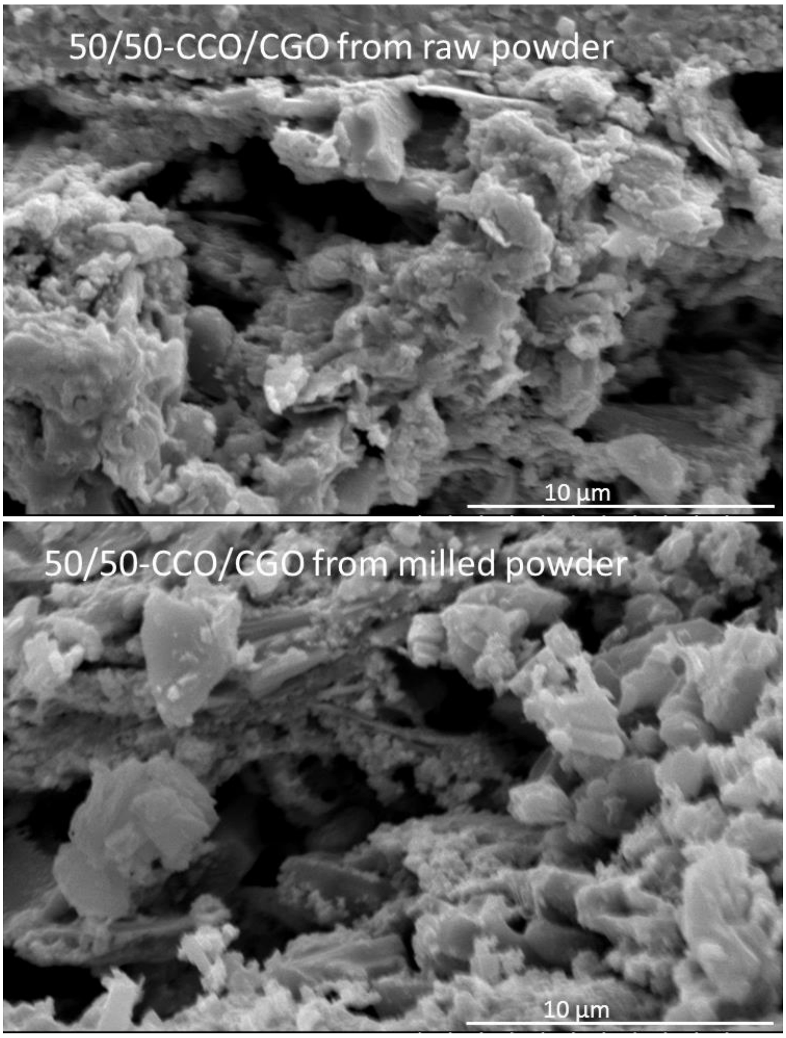

Fig. 2.4.4 - Comparison between the raw and attrition milled CCO cathodes

In Fig. 2.4.4 are reported the SEM images of the microstructure of the already mentioned cathode. To ease comparison, also the SEM image of a screen printed 50/50-CCO/CGO cathode from the raw powder is shown. The microstructures of the two cathodes presented in Fig. 2.4.4 do not display any major difference between the aspect of the two coatings. As a matter of fact, the porosity of the two types of electrodes looks similar and no other specific feature in the morphology can be detected. Subsequently, the symmetric cell was submitted to EIS analysis and the results were treated with the software ZView.

© 2014 Tous droits réservés.

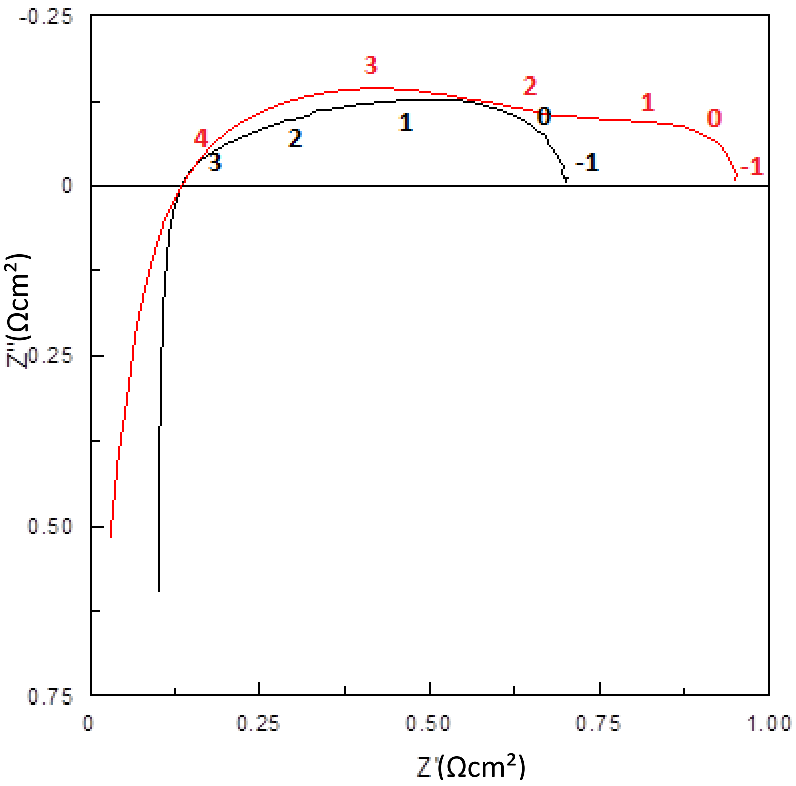

Fig. 2.4.5 - Raw powder (black) and attrition milled (red) 50/50-CCO/CGO EIS spectra at 700°C

Fig. 2.4.5 displays the EIS results on the attrition milled CCO powder (red) in comparison to those of a raw powder cathode (black). Although the microstructure of the two electrodes was rather similar, a higher ASR was clearly observed for the attrition milled powder with an additional contribution at low frequency. This difference is likely due to a slightly denser sample which may affect the oxygen molecule diffusion. An alternative explanation is that thermal treatment subsequent to the deposition (grafting) may induce the grains to regrow, hence losing the benefits from the attrition milling step.

© 2014 Tous droits réservés.

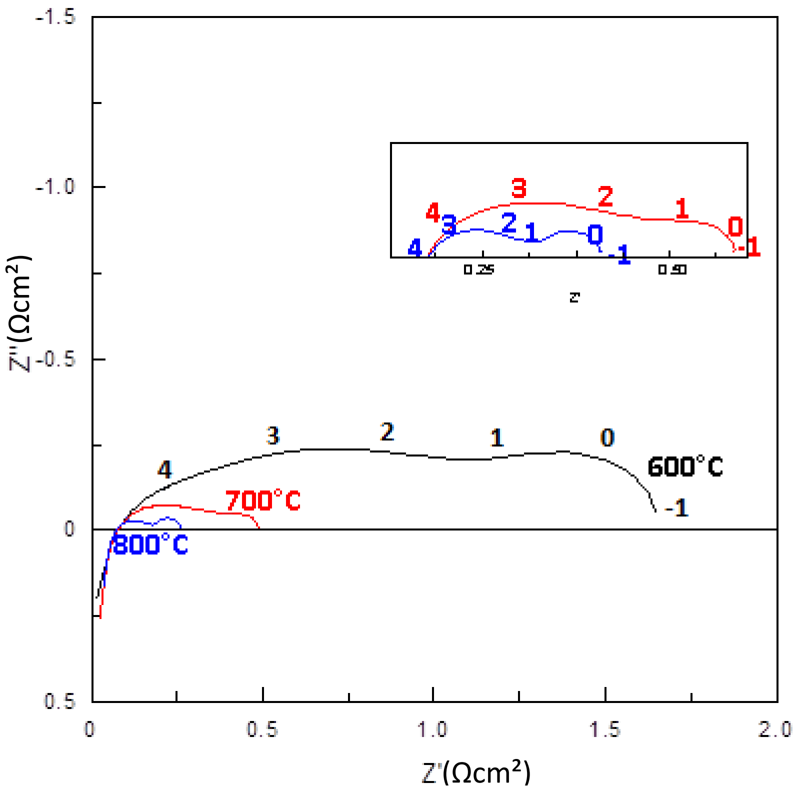

Fig. 2.4.6 - Temperature dependent stacked spectra for attrition milled 50/50-CCO/CGO screen printed cathode, in frame zoom of the circles at 700°C (red) and 800°C (blue).

The stacked spectra at 600°C, 700°C and 800°C of a screen printed 50/50-CCO/CGO cathode from attrition milled powder are shown in Fig. 2.4.6. As expected, a decrease of the ASR with increasing temperature was observed. The evolution of the ln(ASR) against 1000/T in K^{-1} for both the raw powder and the ground powder-based cathodes is reported in Fig. 2.4.7.

© 2014 Tous droits réservés.

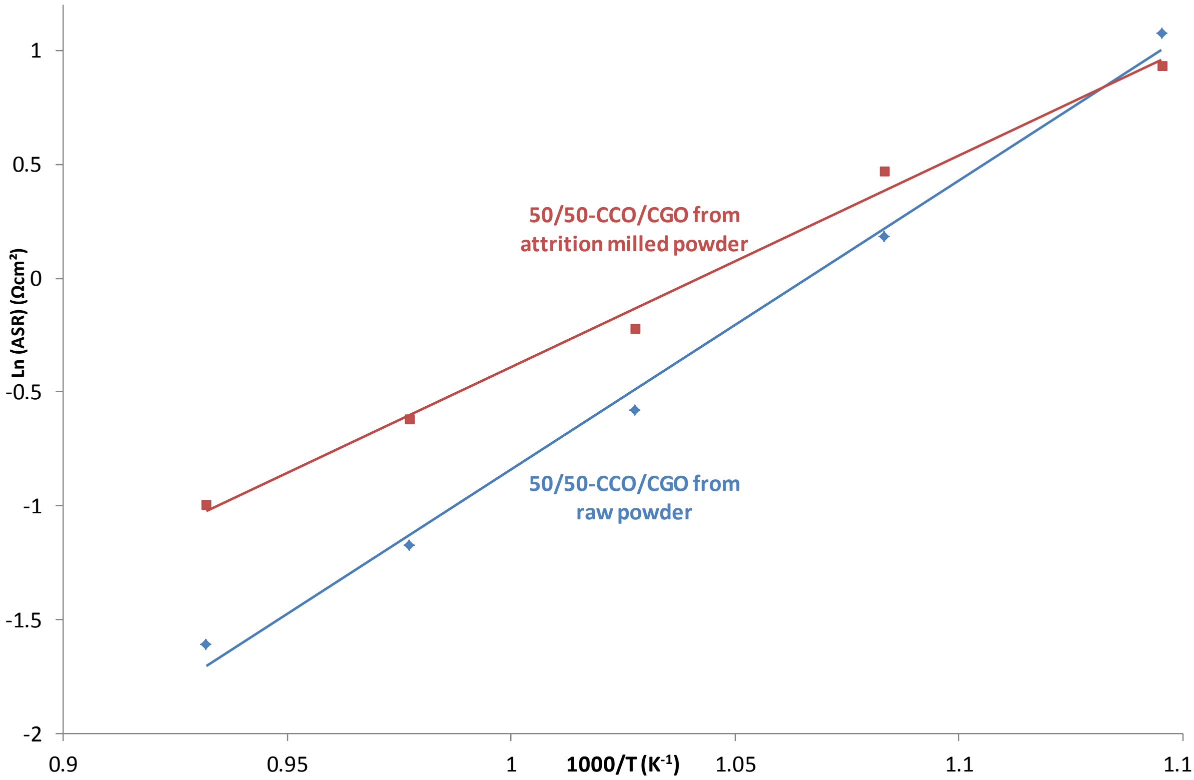

Fig. 2.4.7 - Stacked spectra, SEM images of the microstructure and ASR evolution of 50/50CCO/CGO cathode from ground powder

A good linearity was obtained ($R^2 = 0.99$), which confirms a thermally activated process. It also confirms lower values of ASR for the raw powder 50/50-CCO/CGO cathode for almost the whole temperature range, except at 600°C. Interestingly, a lower activation energy was observed for the 50/50-CCO/CGO cathode from attrition milled powder, 0.97 eV, against 1.33 eV for the 50/50-CCO/CGO cathode from raw powder.

In order to better understand the EIS results, both spectra were modelled using the software Z-View (ver. 3.3d, ©1990 – 2013 [123]) which allows decomposing the overall signal into a sum of multiple compositions.

2.4.3. Equivalent circuits for EIS: results of CCO cathodes from raw and attrition milled powder

As already mentioned (§2.2), the analysis of the electrochemical properties is quite complex. In fact, other than the material's resistance, many additional contributions add themselves to the total. Ohmic losses coming from the grain boundaries contributions, the electrolyte response, the (eventual) contribution of the gold wires and electric collectors are the most frequent causes of interference. Naturally, some are more likely to interfere, while others are very low in magnitude.

Here, a two-electrode setup was used and those "parasitic" contributions cannot be filtered during the experiment so they enter the final spectra. To model the spectra, the equivalent circuit used in previous works of the group was applied (Fig. 2.4.8) [4–6]: $R_1L_1W_s(R_2//CPE_2)$,

© 2014 Tous droits réservés.

where R_1 represents the cell resistance and L_1 the inductance attributed to the high frequency artefact related to the measurement apparatus.

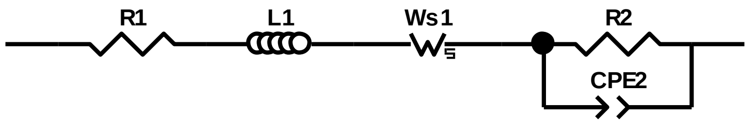

Fig. 2.4.8 - Current equivalent circuit for 50/50-CCO/CGO screen printed electrodes

The short circuit Warburg finite length element gives rise to the 45° slant on the left of the circle. It has to be said that such a feature is typical of supported ionic conductive materials and described by the model of J.R. Macdonald. When, in those materials, the Debye length is comparable to the electrode separation polarization effects may occur, giving rise to the Warburg response.

As reported in [5] and considering an analysis of the frequency ranges for each contribution [124], W_s was associated to the ionic transport of the oxide ions O^{2-} in CCO and CGO through the composite cathode to the CCO-CGO interface, while the (R_2//CPE_2) at low frequency range was related to the Oxygen Reduction Reaction (ORR) itself (adsorption, transfer of species, surface diffusion).

In Fig. 2.4.9 are reported the experimental and calculated spectra of the raw powder cathode (a) and the experimental and calculated spectra of the ground powder cathode (b) at 700°C. The experimental data points are plotted in blue and connected through a red line. The fitting results are traced as green solid lines.

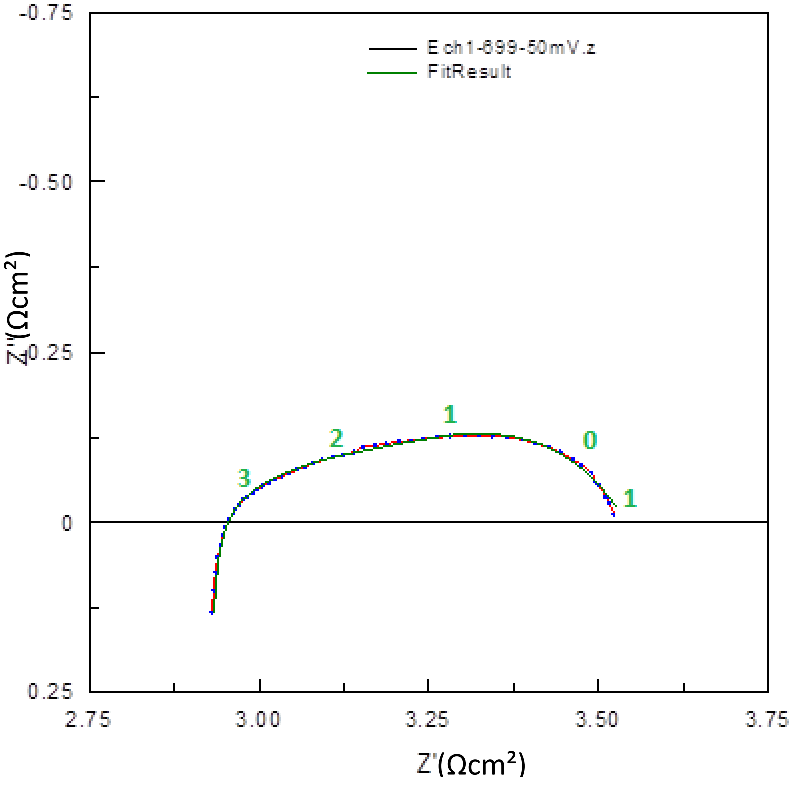

a

© 2014 Tous droits réservés.

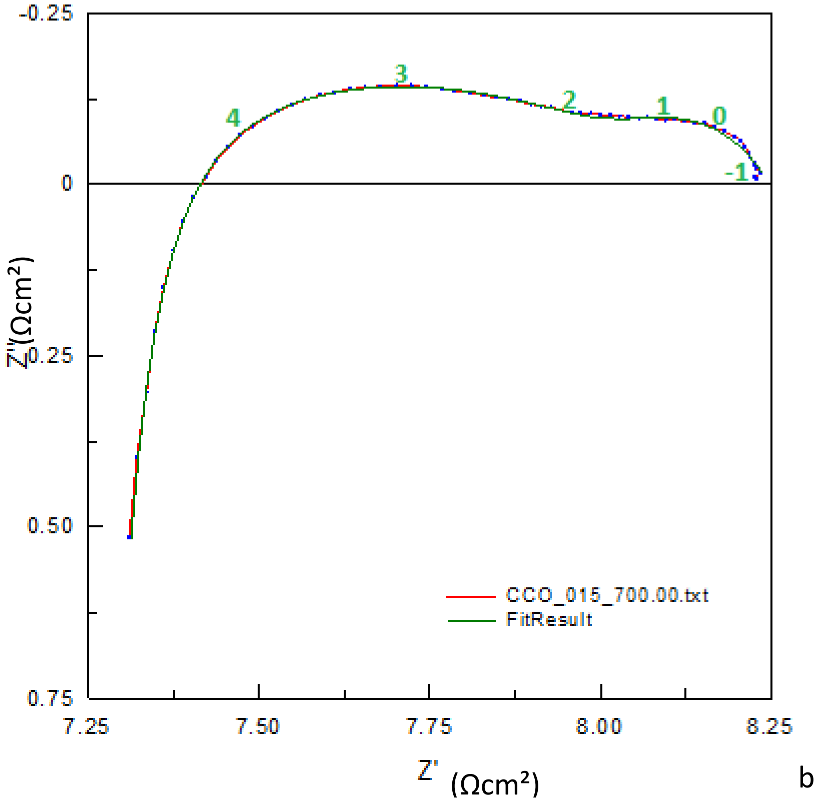

Fig. 2.4.9 - EIS results and fits for a screen printed 50/50-CCO/CGO cathode from raw powder (a) and attrition milled powder (b) symmetric cells

The very fact that is difficult to distinguish between the calculated and the experimental lines is already a good indication of how accurate the equivalent circuit is. Table 2.4 summarises the values of the fitting elements and the overall ASR from the experimental spectra for the screen printed 50/50-CGO/CCO electrodes.

Table 2.4 - Calculated circuit elements of a 50/50-CCO/CGO cathode (raw and attrition milled powders) at 700°C

Element	Raw powder 50/50-CCO/CGO	Attrition milled powder 50/50-CCO/CGO
R1	2.88 Ωcm² [0.1%]	7.07 Ωcm² [0.1%]
L1	1.11·10^{-6} H [1.4%]	7.87·10^{-7} H [0.4%]
W1-R	0.49 [3.6%]	1.04 [1.6%]
W1-T	0.02 [15%]	1·10^{-3} [5.6%]
W1-P	0.28 [1.1%]	0.20 [1.7%]
R2	0.17 Ωcm² [7.4%]	0.14 Ωcm² [6.0%]
CPE_2-T	0.49 [6.5%]	0.65 [4.1%]
CPE_2-P	0.88 [2.6%]	0.84 [2.8%]
ASR (overall)	0.56 Ωcm²	0.80 Ωcm²
χ^2	1.38·10^{-5}	9.82·10^{-6}

The correspondence is very good and thus the calculated values of R1, R2, CPE and-W_s, reported in Table 2.4, are reliable. In both cases, the fitting with two equivalent elements (the short circuit Warburg terminus and the R//CPE component) is matching very well the

© 2014 Tous droits réservés.

experimental data. This is indicative of the presence of two distinct phenomena occurring at two distinct domains of frequency. The first one, at high frequency, simulated by the Warburg terminus is most likely to be related to diffusion process, which may involve the inter-grain electronic-ionic charge. Conversely, the one at low frequency which is simulated by the R//CPE component is more probably related to surface phenomena involving gas phase diffusion within the electrode and oxygen electrochemical dissociation.

The evaluation of the temperature dependency for each element revealed very insightful information (Fig. 2.4.10). The values of the elements resistance (W1-R and R2) decrease quite remarkably with temperature.

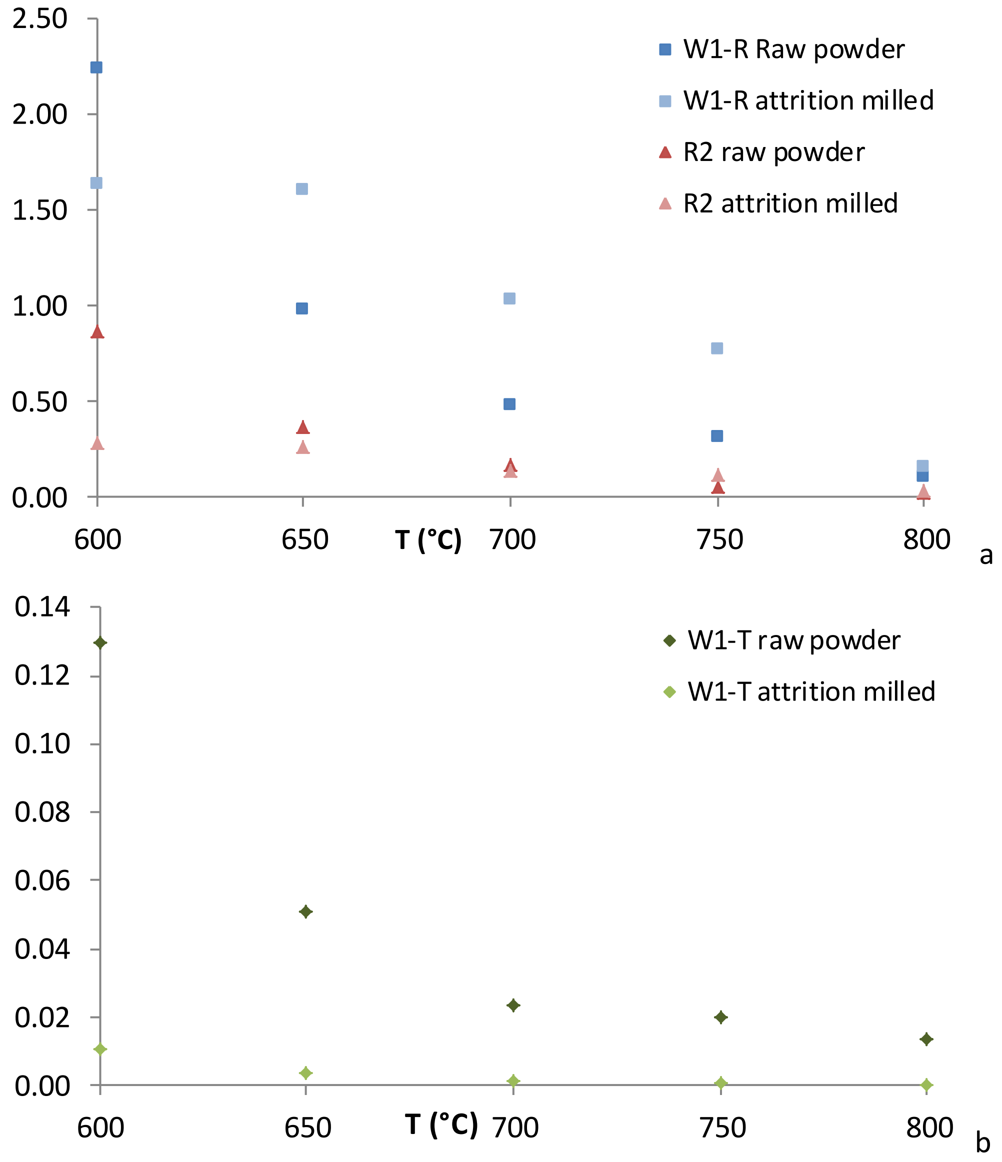

Fig. 2.4.10 - Evolution of the resistance elements (a) and the Warburg's time constant (b) with temperature for a 50/50-CCO/CGO cathode from raw (darker) and attrition milled powder (lighter)

In the case of the raw powder it tends to stabilise above 700°C, while for the other specimen R2 undergoes a further decrease with temperature. This is typical of a thermally activated process. R2 decreases by 75% (raw powder) from 600°C to 800°C and by 95% for the milled

© 2014 Tous droits réservés.

powder. Such an effect may depend on the finer size of the particle, although a direct correlation is difficult to establish. The overall R2 is comparable for both cathodes, in the order of 0.2 Ωcm² at 700°C, meaning that the gas phase diffusion pathway is not really changed by the attrition milling of the CCO.

Also the Warburg's time constant (W1-T) tends to decrease with the temperature increase. This is well explainable by the fact that the electrode/electrolyte transfer is a temperature-dependent phenomenon, and it proceeds faster upon heating. Conversely, the R//CPE's time constant (CPE_2-T) is not changing with temperature.

Lastly, the phase constants indicates that the first element has a very typical Warburg behaviour (W1-P ≈ 0.28), while for the R//CPE the capacitance tends toward the pure capacitor behaviour (CPE_2-P ≈ 0.9). The values of the phase constants, of course, do not change with temperature.

It is very interesting to notice that the cathode from attrition milled powder has Warburg's time constant remarkably lower than the cathode from the raw powder. This effect is clearly visible in the spectra, as the high frequency response is shifted towards the left, meaning that the associated phenomenon occurs quicker. The frequency domain for the cathode/electrode contact of the raw powder is in between 10^4 and 10^2 Hz, while for the attrition milled powder it is shifted to 10^5-10^3 Hz. Namely, the reduction of the grain size appears to favour the electrode/electrolyte contact kinetics.

On the other hand the overall magnitude of the process is higher in the latter case: the W1-R at 700°C for the milled powder is twice bigger than the W1-R of the raw powder. An explanation of this occurrence is not trivial. The two main reasons could be that the reduction of the grain size disfavours the inter-grain charge transfer or that the attrition process introduces an impurity in the powder that is overlapping in the 10^4-10^3 Hz frequency domain. Unfortunately, the Z-View software is not capable of distinguishing between two superimposed contributions, hence a final conclusion is difficult to draw.

After the EIS analyses, the pellets were recovered from the mounting. At naked eye, the cathodes looked unscathed but, in order to confirm their state, SEM images were recorded on the surface and side cut.

Fig. 2.4.11 reports the SEM imaging of a raw powder 50/50-CCO/CGO pellet surface (a) and side cut (b). The analyses confirm that the samples are intact and no remarkable alteration of the cathodes is reported. Also, the layer's thickness was measured with the instrument's measuring tool. Accordingly to what stated in §2.3.4, the thickness of the deposit is 21.5 µm.

© 2014 Tous droits réservés.

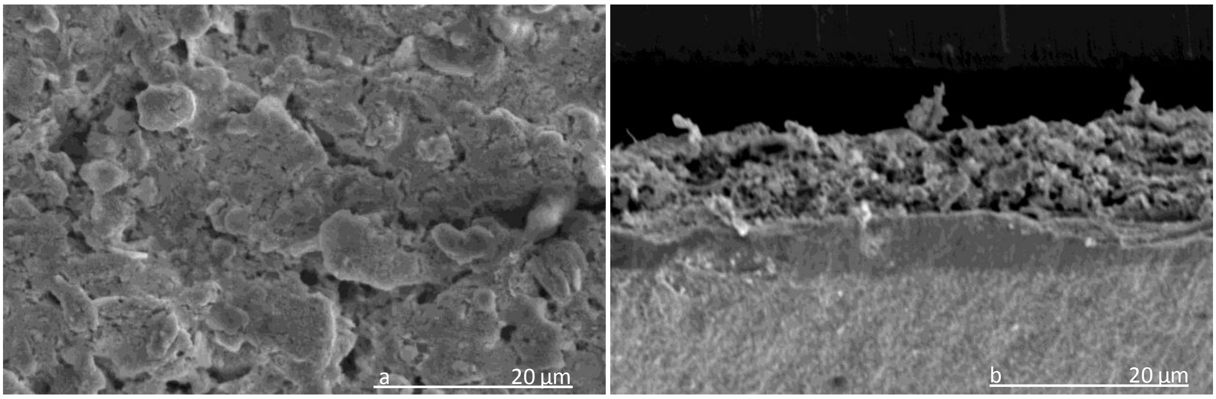

Fig. 2.4.11 - SEM image of a post-EIS analysis 50/50-CCO/CGO cathode from raw powder grafted on CGO pellet, wiev of the surface (a) and of the side cut (b)

2.5.Conclusion

Prior to this study, Dr. K. Nagasawa had obtained an ASR of 4.00 Ωcm^2 at 700°C under air for pure CCO electrode. This was decreased to 1.42 Ωcm^2 by addition of 30%$_{w/w}$ of ceria to the electrode [4]. Here, using screen printing for the electrode deposition, both the thickness and composition of the composite electrode were optimised. The optimisation of a sample for EIS analyses is a high time-consuming process, which requires multiple trials on different samples, as the parameters to vary may be several.

For this novel technique (screen printing), pastes ("inks") with specific rheological characteristics were required. In this study, an ink containing ethanol was used at a first. By optimising both the composition and the thickness, we managed to obtain an ASR of only 0.5 Ωcm^2 at 700°C for a 20 µm electrode composed of 50%$_{w/w}$ CCO plus 50%$_{w/w}$ CGO.

Since the ink was not stable, in a second step the protocol was modified and optimised to meet the same criteria of reproducibility. Stable inks were obtained without an organic solvent (ethanol) but only with the terpene resin to keep the viscosity, the mixtures being homogenised in a tri-cylinder machine ensuring uniform composition and consistence. For a 50%$_{w/w}$ CCO plus 50%$_{w/w}$ CGO composite electrode with a thickness of about 20 µm prepared in these conditions, an ASR of 0.56 Ωcm^2 was obtained, in good agreement with the experiment performed with an ethanol based ink.

The attempt of modifying the microstructure by playing with the particle size (attrition-milled CCO powders) turned out to have a rather negative effect.

Nevertheless, the microstructure is a key factor for the overall cathode's performances and its modification may lead to great improvements in the electrochemical performances of the calcium cobaltite's electrode: the variation of this element constitutes the body of the next chapter.

© 2014 Tous droits réservés.

3. On the effect of textural modification of Calcium Cobaltite's microstructure

Besides the intrinsic properties of the material (mainly ionic and electronic conductivity and surface exchange kinetics towards the oxygen) also the extrinsic properties of the electrode are very important to the overall yield of the Fuel Cell. These extrinsic properties include microstructure (grain size, porosity) interfaces, as well as the shaping of the electrodes (thickness, insertion of interfacial layers, etcetera). They play a fundamental role in the overall cell yield. On this matter, the model proposed by Adler, the so-called Adler-Lane-Steele (ALS) model [122] is a clear demonstration of the impact of the microstructure on the electrochemical performances of a cell (§ 2.3.1 and equation (2.3.15))

The previously mentioned screen printing technique is one example of electrode shaping and formatting: the characteristic porosity and microstructure given by this method is particular and unique. As shown in §2, just by varying the electrode composition and the electrode thickness, we managed to decrease the ASR from 4 Ωcm² for the pure compound deposited by brushing [4] to 0.5-0.6 Ωcm² for a blend composition of 50$\%_{w/w}$ CCO and 50$\%_{w/w}$ CGO and a layer thickness of 20 µm. Of course, the optimisation performed on the technique plays a key role but it is limited by the technique itself. As it was already mentioned, the cathode thickness has an incredible effect on the ASR (§2.3.4) but through screen printing only it was not possible to further modify the distribution of the porosity or the shape.

Fig. 2.5.1 shows the SEM images of a screen printed 50/50-CCO/CGO cathode from the side (a) and from the surface (b). The aspect of the electrode reported in Fig. 2.5.1 is quite stochastic with grains of very different sizes and scarce organisation. The surface of the cathode layer looks uniform from above, with the film well deposited but the porosity is not regular and the crystalline grains have very different sizes. Their shape resembles the one of platelets, but sometimes also big agglomerates are found. The side image reveals the presence of a rather unorganised microstructure.

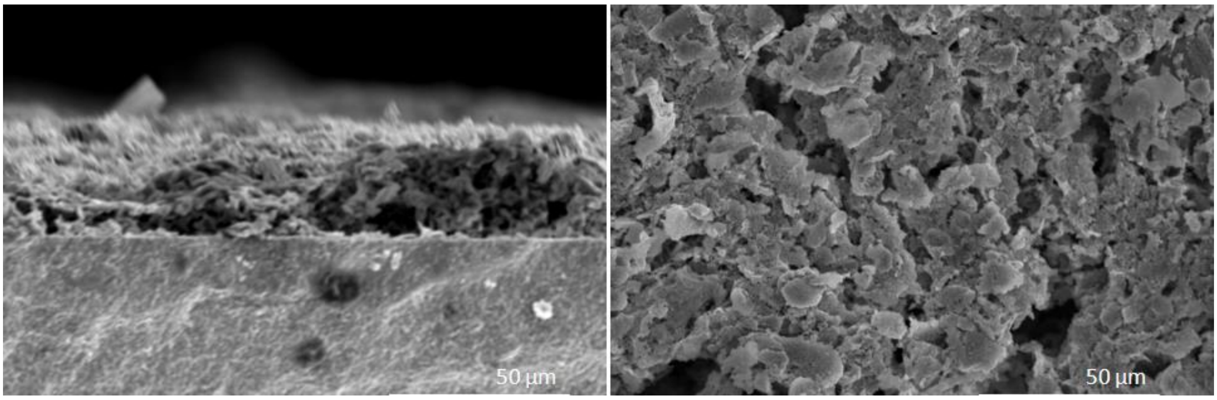

Fig. 2.5.1 - SEM images of a screen printed 50/50-CCO/CGO cathode, side cut and surface

© 2014 Tous droits réservés.

In §2.4.2 a first attempt of microstructural improvement was carried out. The raw CCO powders were attrition-milled and then used to prepare an ink for the composite electrode. However, the reduction of the CCO's grain size resulted in a negative effect on the electrochemical properties, with an increase by 30% of the overall cathode's ASR, although the SEM imaging on the attrition-milled cathode revealed that the microstructure was not very different from the one of a raw CCO's cathode, with the porosity randomly distributed in the layer. Also, the thickness and the general aspect of the two different deposits greatly resembled to each other.

Using other approaches, such as addition of a templating agent to the sol-gel or the Electron Spray Deposition technique, currently developed at the Laboratoire d'Electrochimie et de Physico-chimie des Matériaux et Interfaces (LEPMI) of Grenoble, a better control of the porosity should be expected. Here, in a first moment, in collaboration with Jean-Philippe Dacquin of the Heterogeneous Catalysis group at the UCCS, to produce layered and templated electrodes it was attempted to use the spin-coating technique, starting from a polystyrene template and a sol-gel precursor of the pure CCO electrode. In a second time, in collaboration with Elisabeth Djurado from LEPMI, the Electrostatic Spray Deposition (ESD) technique was also considered to prepare a pure CCO electrode. Lastly, coming back to screen printing, the insertion of a dense nanometric inter-layer of CCO between the electrode and the electrolyte was tried, on the basis of the results obtained by Hildenbrand et al. [9]. This latter study was carried out in collaboration with Marie-Hélène Chambrier at UCCS-Lens.

3.1.Spin-coating technique for deposition of SOFCs layered and templated electrodes

Templating is now considered as the most frequently used method to synthesise materials featuring structural units ranging from nanometres to micrometres. The latest advances in this field are summarised in a special issue of the Journal of Materials Chemistry [125]. Well organised structures can be obtained by using a wide range of templates, such as single organic molecules, dimers, ionic surfactants, block copolymers, carbons, colloids etcetera. As an example, Waterhouse *et al.* reported very nice inverse opal ceria films exhibiting three-dimensional ordered macroporous structures. The macroporous inverse opal was obtained by use of colloidal crystals templates and polymethylmethacrylate (PMMA) spheres of diameter in the order of 325 nm arranged on a face centred cubic (fcc) lattice, impregnated with a ceria sol-gel precursor before calcination at 400°C to remove the polymer template [126]. People at College de France in the group of Clément Sanchez also managed to obtain a nice mesoporous single layer of gadolinium doped cerium oxide (CGO) by addition of PS-b-PEO (polystyrene-b-polyethylene oxide), dissolved in THF to a CGO sol-gel precursor leading to the formation of micelles [127]. They transferred the same technique to prepare a CGO/Ni cermet [128]–[130] and to $La_{0.7}Sr_{0.3}Co_{0.2}Fe_{0.8}O_3$/Gd–$CeO_2$ composite SOFC cathode [131].

© 2014 Tous droits réservés.

Taking inspiration from these previous works, a template of polystyrene spheres was used here to prepare a mesostructured CCO electrode using a sol-gel of CCO precursor and spin-coating was chosen as the deposition technique.

A good schematic of the used technique, for which we used polystyrene spheres as the template, is given in Fig. 3.1.1 [132].

Unlike the screen printing, where the rheological properties of the coating material required a viscous paste, the spin coating demands a rather fluid solution. For this reason, for the CCO synthesis, it was chosen not to proceed through solid state reaction but via sol-gel preparation.

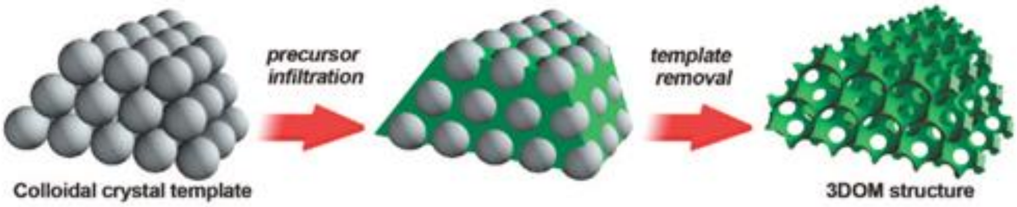

Fig. 3.1.1 - A schematic of the method to prepare a macrocporous structure by colloidal crystal templating from a preformed colloidal crystal template [132]

To optimise the electrode deposition, the polystyrene spheres were characterised by SEM in a first step. Then the sol-gel synthesis was optimised before deposition of the CCO electrode on a CGO substrate and PS template with the consequent characterisation of a symmetrical cell by impedance spectroscopy which was finally compared to a cell with pure CCO electrodes deposited again by spin coating.

3.1.1. Characterisation of the polystyrene spheres as template precursor

The polystyrene spheres, later used as a template, were prepared by Jean-Philippe Dacquin at UCCS from styrene as monomer with divinylbenzen as crosslinker and potassium persulfate as initiator in an aqueous media. They were first characterised by SEM imaging (Fig. 3.1.2) to determine their diameter. It reveals that they were very homogeneous in both size and shape. The average diameter value was assessed at 200 nm.

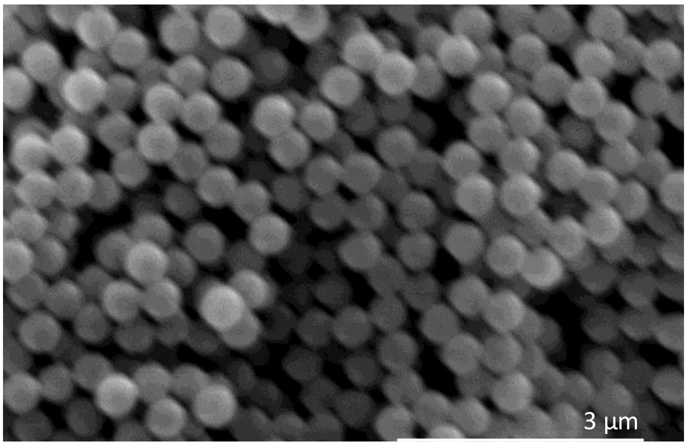

Fig. 3.1.2 - SEM image of polystyrene spheres

© 2014 Tous droits réservés.

3.1.2. Optimisation of the CCO preparation by sol-gel

For the sol-gel preparation, the citrate route, also called the "pseudo sol-gel", in both aqueous and alcoholic media was used. The protocol was kept identical in both cases, changing only the amount of solvent (water or ethanol) in each circumstance, in order to meet complete dissolution of the precursors. Here only the results obtained in an aqueous media will be reported since Co_3O_4 was evidenced as impurity when ethanol was used.

$Ca(NO_3)_2{\cdot}4H_2O$ and $Co(NO_3)_3{\cdot}6H_2O$ were used as precursor, in molar ratio of 3:4 to meet the values of the approximate formula $Ca_3Co_4O_{9+\delta}$. Then, it was added an amount of citric acid equal in moles to the summed moles of Ca^{2+} and Co^{3+} (molar ratio between citric acid and Ca^{2+}+Co^{3+} equal to 1).

The solution was then left mixing under magnetic stirring in an ultrasonic water bath for 30 to 60 minutes, until a homogeneous purple colour was observed.

To derive the temperature of calcination, a TGA was carried out under air from room temperature to 900°C. As shown in Fig. 3.1.3, mainly 3 mass losses were observed at 150°C, 195°C and 630°C likely due to water, NOx and CO/CO_2 releases, respectively.

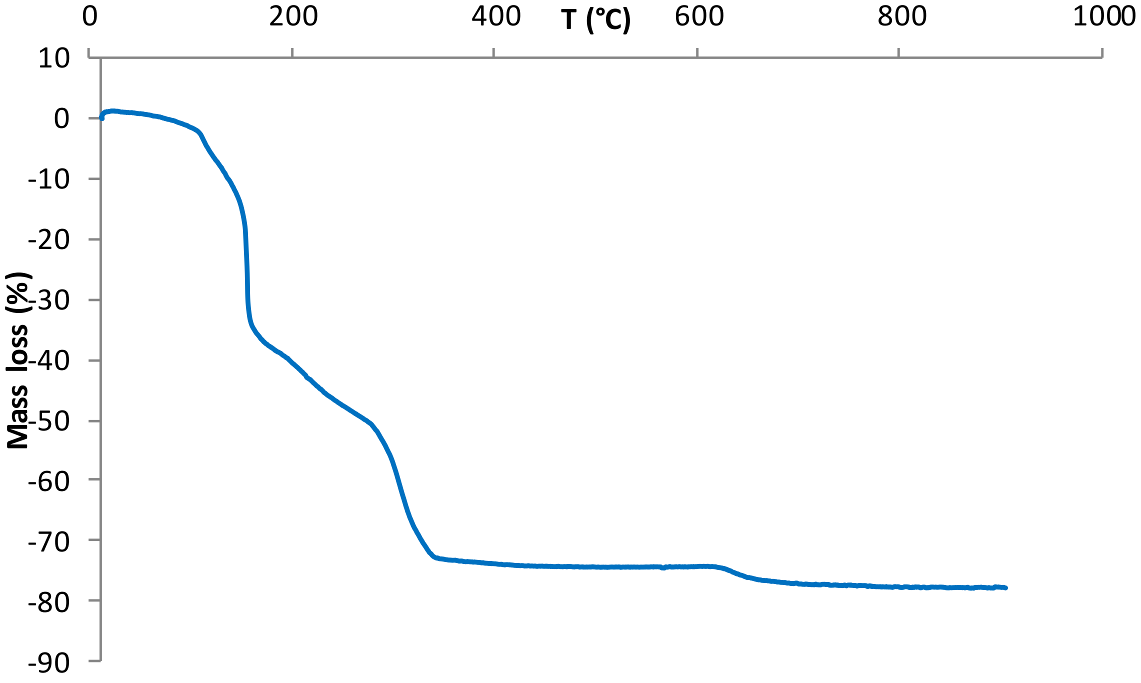

Fig. 3.1.3 - TGA analysis of the CCO sol-gel

It was therefore decided to calcinate the gel at 700°C for 12 hours. After calcination, as confirmed by X-ray diffraction (Fig. 3.1.4) which shows a good agreement between the experimental diffractogram and the reference, a pure phase was obtained.

© 2014 Tous droits réservés.

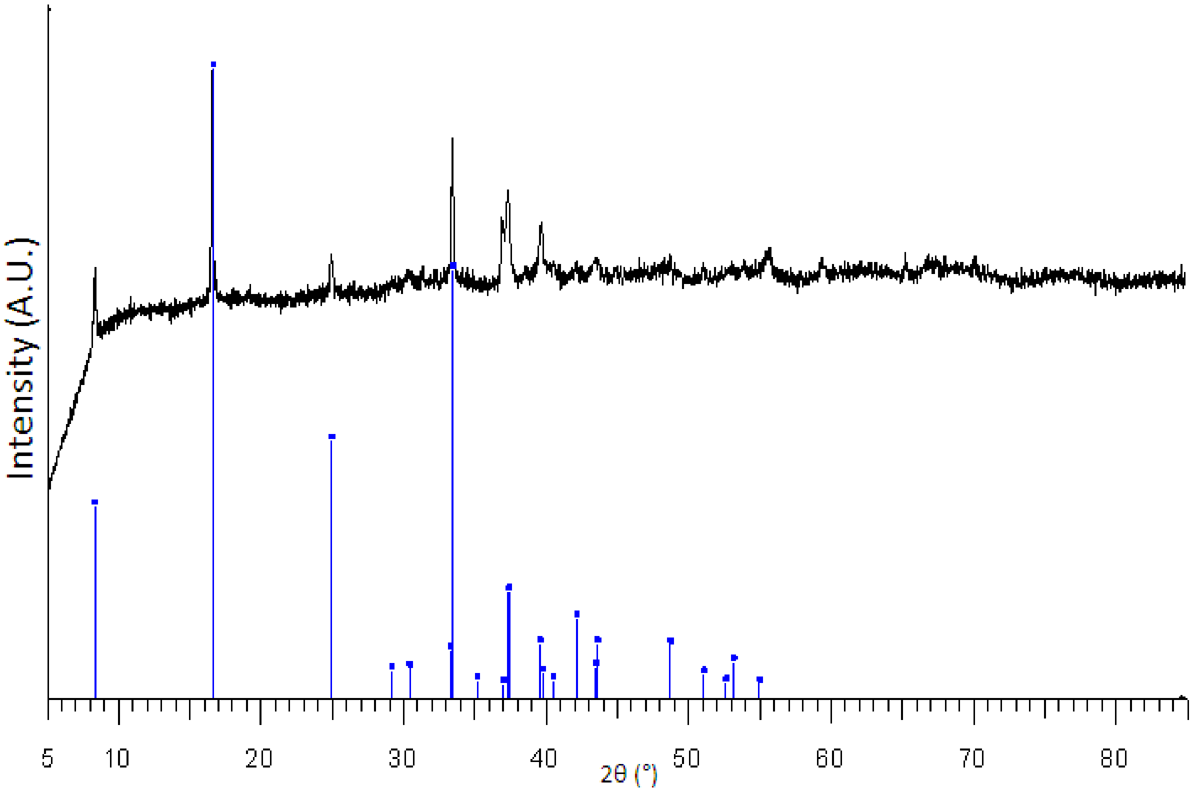

Fig. 3.1.4 - XRD diffractogram for a sol-gel CCO powder calcinated at 700°C with the calculated intensities from structural data (blue bars).

3.1.3. Deposition by spin coating

After the sol gel preparation, with the aim to spin coat a mixture of CCO sol-gel and polystyrene spheres, in a first moment, the polystyrene spheres were added under stirring to the CCO sol-gel solution. A mass ratio of 10g of precursors ($Ca(NO_3)_2{\cdot}4H_2O$ plus $Co(NO_3)_3{\cdot}6H_2O$) to 1g of polystyrene spheres was considered. The solution was left stirring for 15 minutes and then transferred to a Pyrex-glass beaker. The beaker containing the suspension of CCO precursors and spheres was then left dwelling for 4 days in an environmental furnace, set at a temperature of 40°C and relative humidity of 80%. After this treatment, the content of the beaker recovered from the environmental furnace had the aspect of a purple brittle crust. The consistency was nearly vitreous, so it was decided to add a small quantity of solvent (either ethanol or water), drop by drop, until reaching a more fluid texture. Unfortunately, the re-dilution was not the main problem. Because of the great difference in the density the polystyrene spheres tended to sediment on the bottom of the beaker, rather than staying suspended in the solution. This inexorably produced a completely inhomogeneous aspect, as the template concentrated on the bottom part of the gel in a stratified layer of polystyrene which did not produce any organised porosity. The upper part, instead, had crystalized in an airy construction that looked like polyurethane foam.

For as many times as this protocol was tried, never it was possible to achieve an exploitable starting material. Hence, the procedure was abandoned and a different approach was tried.

© 2014 Tous droits réservés.

In a second step, instead of trying to prepare an already microstructured cathode, it was tried to deposit the template first and then cover it with a CCO precursors' gel. For the coating of the organic template a quick survey of the most appropriate solvent was first carried out.

At first, the hydrophilicity of the spheres had to be assessed, to determine whether it was possible depositing on a CGO pellet or not. The chosen support was a P1200-grit polished CGO dense pellet (roughness = 15.2 µm, ρ_{rel} > 95%). 200mg of polystyrene spheres were suspended in 1 mL of deionised water and put dissolving in an ultrasonic water bath for 10 minutes.

The suspension was immediately used for the deposition: 2 or 3 drops were put on a CGO dense pellet. To stick the pellet on the spin coater a strip of bi-adhesive tape was used. The pellet was then made spin at 500 rpm for 30 seconds, then at 1500 rpm for 60 seconds. The sample was then carefully recovered and submitted to SEM imaging.

The recorded microscopy images are reported here below. Fig. 3.1.5 (a, b) shows the surface of a pellet coated with the suspension of water and polystyrene spheres at different magnifications (40 x and 1000 x).

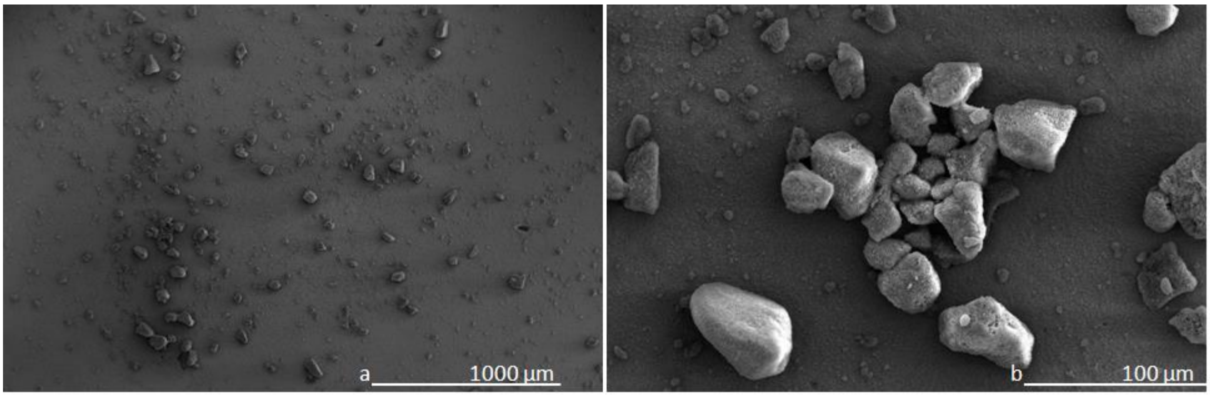

Fig. 3.1.5 - SEM images of a spin coated acqueous suspension of polystyrene spheres magnification at 40X (a) and 300X (b) magnification

The surface looks unevenly covered. Several agglomerates are scattered all around the pellet, while wide areas remained clear. Nevertheless, at larger magnification, the coating appears well deposited and the spheres nicely leaning on the pellet. This proves the hydrophilicity of the polystyrene spheres on dense (ρ_{rel} >95%) polished (roughness = 15.2 µm) CGO pellet.

Because the coating was very inhomogeneous, a different solvent for the template was to be found. The choice was limited to the three most common solvent compatible with polystyrene: acetone, absolute ethanol and tetrahydrofurane (THF).

To obtain each suspension, 200 mg of polystyrene spheres were weighted on an analytical scale (S = 0.0001 g), put in a glass vial and added with 1 mL of solvent (acetone, absolute

© 2014 Tous droits réservés.

ethanol or THF). The vial was finally placed in an ultrasonic water bath and left mixing for 15 minutes.

The three obtained suspensions were used immediately to perform the coating of as many CGO dense (ρ_{rel} > 95%) polished (15.2 µm) pellets. For the coating the same protocol described earlier was used. Also this time, to stick the pellets to the spinner was used a stripe of bi-adhesive tape which was changed after each deposition.

Once coated, the pellets were carefully recovered from the instrument and submitted to SEM imaging.

In Fig. 3.1.6 are reported the SEM images of CGO pellets coated with the suspensions in acetone (a), absolute ethanol (b) and THF (c).

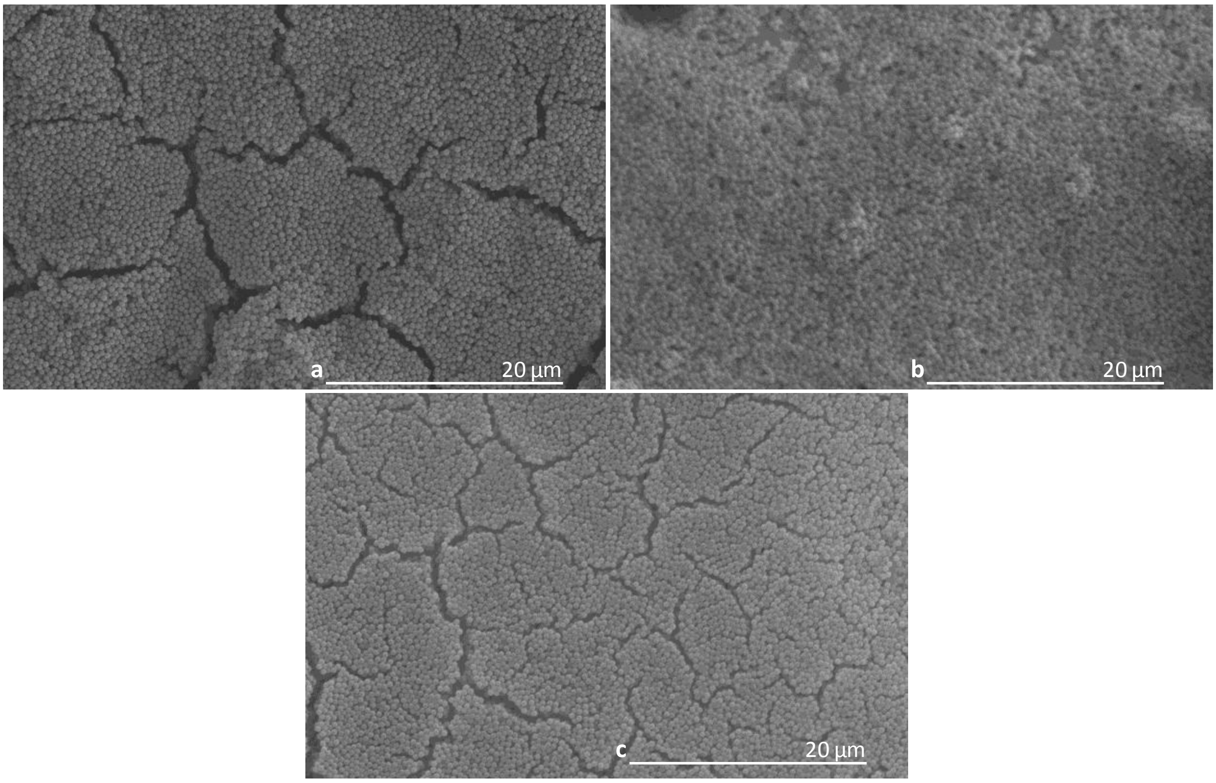

Fig. 3.1.6 - SEM images at 2500X of polystyrene spheres in acetone (a), ethanol (b) and THF (c) solutions deposited by spin coating

The depositions with acetone (a) and with THF (c) share a common feature with the one prepared with water (Fig. 3.1.5): while wide areas are blank in others the polystyrene spheres tend to collect and agglomerate. Which are the causes of this behaviour is still unclear, and it makes not part of the current study.

On the other hand, the aspect of the coating performed with the suspension in ethanol (b) has a much more uniform aspect. The coating is nicely spread all over the surface and there are almost no agglomerates.

© 2014 Tous droits réservés.

The side-cut image (Fig. 3.1.7-b) reveals that the polystyrene spheres are well distributed all over the layer, which has a quite regular thickness. The measure tool of the SEM software indicates that the average thickness is ~3.1 µm. This value is noticeably inferior to the average thickness of the layers prepared with the other suspensions, but the variations are much less significant.

The side cut SEM images of two other deposits are shown in Fig. 3.1.7 (a) and Fig. 3.1.7 (c) for acetone and THF, respectively. With always the measuring tool of the SEM manager software, the thickness of each layer was determined.

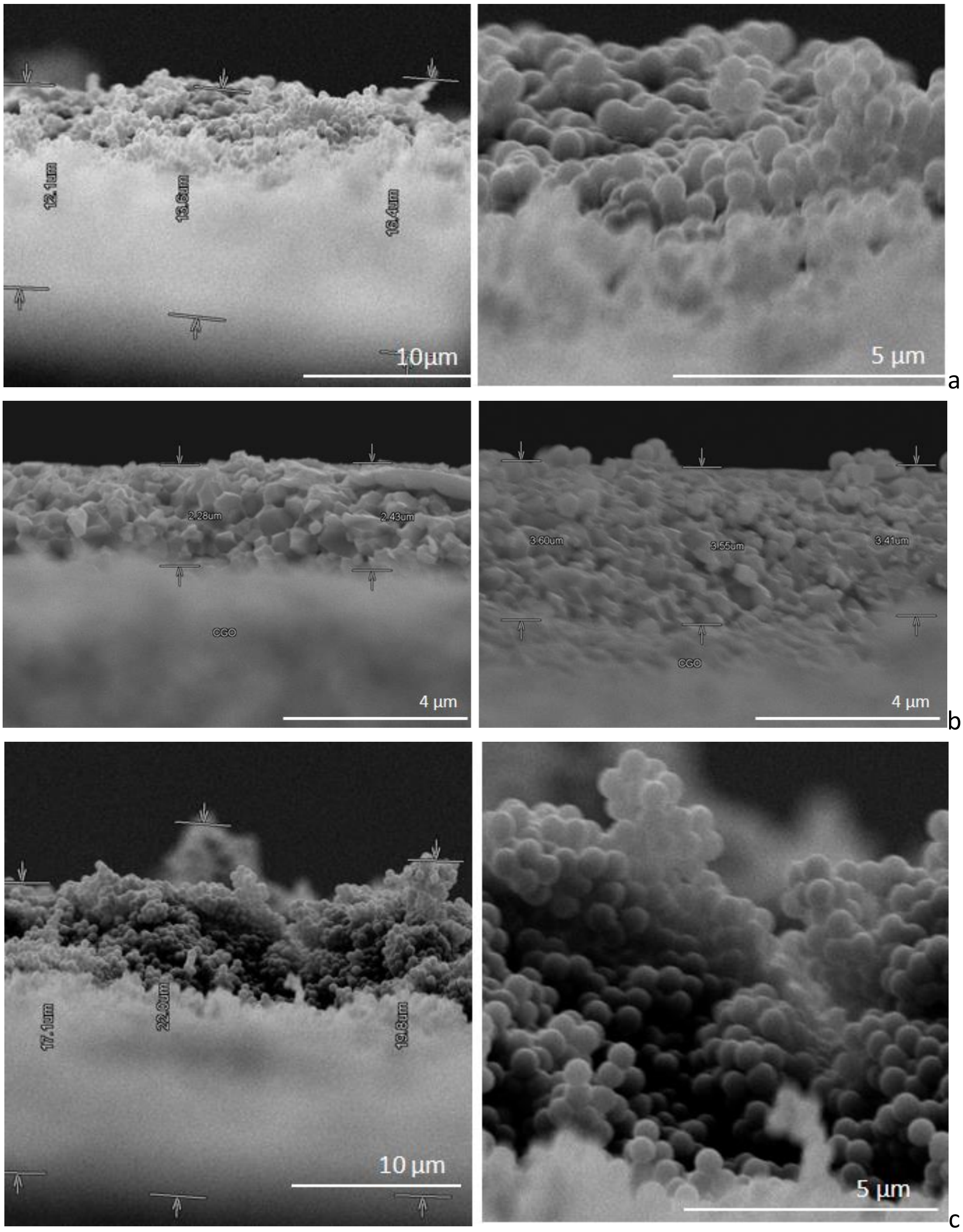

Fig. 3.1.7 - SEM images of the polystyrene spheres coating in acetone (a), absolute ethanol (b) and THF (c)

© 2014 Tous droits réservés.

The values of the thicknesses are ~12.9 µm for the acetone layer and ~19.6 µm for the THF one. These values, other than being remarkably higher than the one for the absolute ethanol deposit, are also affected by a wide distribution.

In fact, for both layers the thickness is variable from a minimum of 9.75 µm to a maximum of 22.1 µm although, of course, these two extreme values are not often encountered.

For all these reasons, the ethanol-based suspension was chosen for the successive preparations.

The following step was verifying if the grafting thermal cycle was suited for this kind of samples. Hence, a pair of pellets was prepared: one coated with the CCO gel only, the other with a layer of polystyrene balls and then covered with the CCO gel. In the latter case, the two spin-coating depositions were done in sequence on the same pellet without touching it after the first part of the procedure.

The coating of the polystyrene sphere layer was done with the usual protocol mentioned above. For the deposition with the CCO gel, instead, the protocol was modified to adapt to the different viscosity of the solution.

From 3 to 5 drops of the CCO gel were taken with a glass Pasteur pipette and dropped on the surface of the CGO pellet. The pellet was fixed to the spinner with a stripe of bi-adhesive tape, and then it was made turning at 500 rpm for 5 seconds and successively at 3000 rpm for 60 seconds. This procedure was used for the deposition of the CCO gel on both pellets, with or without the polystyrene sphere templating layer.

Once coated, the pellets were carefully recovered and thermally treated. The thermal treatment used for the grafting was the same as the one used for the screen printed samples (§2.2.3): after increasing temperature from RT to 500°C the pellets were left dwelling for 1 hour for organic compounds removal. Then the temperature was increased to 900°C and left for 2 hours, then cooled down to RT.

The obtained pellets were submitted to SEM imaging to analyse both the surface and the side cut of the newly obtained samples. The results are reported in Fig. 3.1.8, for the surface of the solely CCO-coated pellet surface (a) and its side cut (b). The other images show the surface of the film obtained by subsequently coating the pellet with polystyrene spheres and CCO (c) and its side (d).

© 2014 Tous droits réservés.

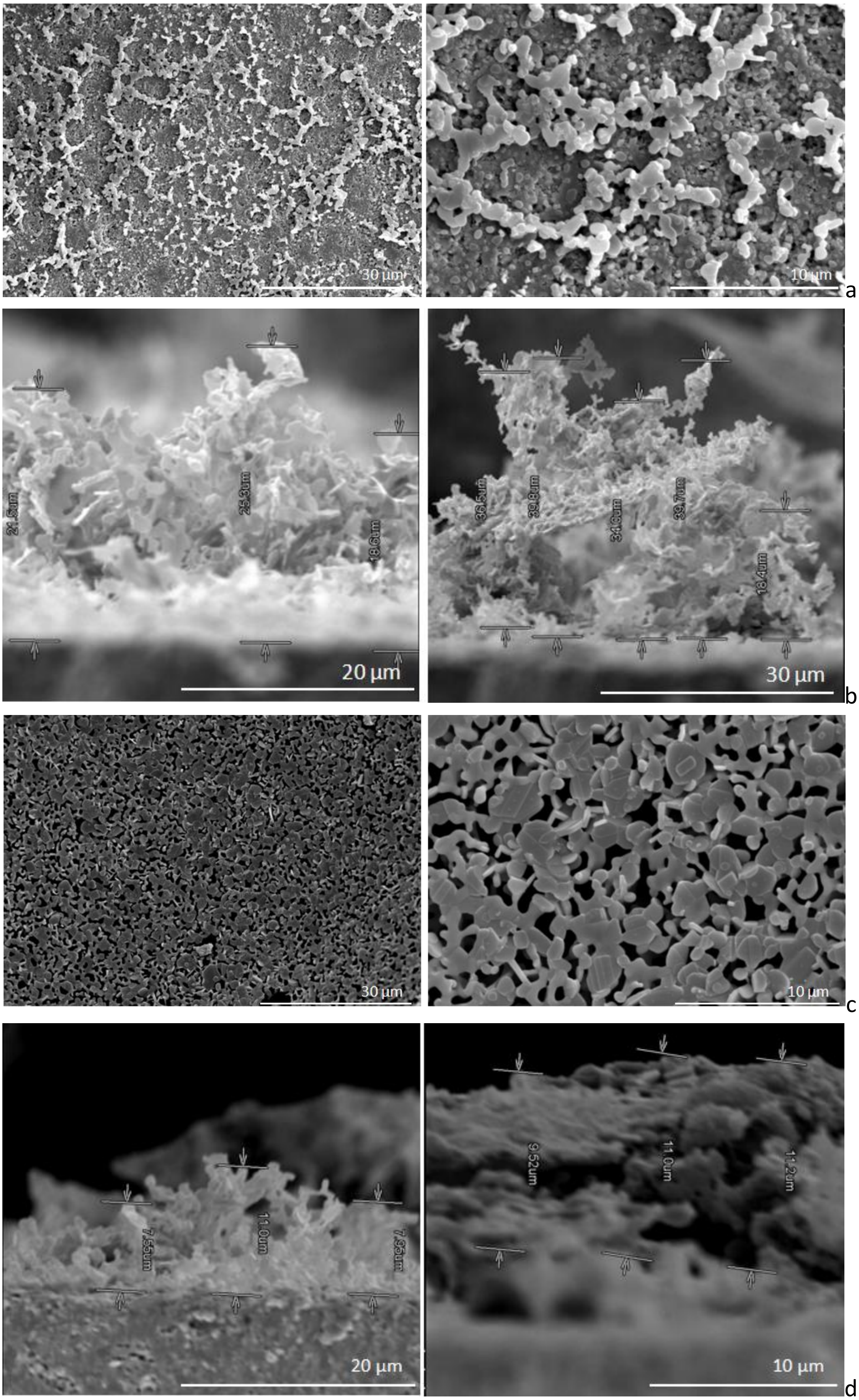

Fig. 3.1.8 - SEM images of the surface of a spin coated CCO cathode after thermal treatment: ball-free cathode's surface (a) and side cut (b) and templated deposit's surface (a) and side cut (b).

© 2014 Tous droits réservés.

Not many differences are noticeable from the images of the surface of the pellets. They both look unevenly covered but agglomerations do not occur. At greater magnification, the first differences in the texture are revealed: the pellet without the templating agent has a broader distribution of the particle size (Fig. 3.1.8-a), while the other one shows smaller and more uniform crystallites (Fig. 3.1.8-c).

Yet, those differences in appearance are secondary. The side cut images (Fig. 3.1.8 b, d), in fact, reveal a much deeper difference lying in the very microstructure of the coating. First of all, the average thickness of the non-templated layer is bigger by ~300% than that of the templated deposit (29 µm against 10 µm).

Also, for the non-templated coating the distribution of the deposit is not uniform, as there are zones where the layer is much thinner (18.4 µm) than others (39.8 µm); the templated deposit, instead, shows a better distributed deposition.

Lastly, the porosity of the templated film seems to be more regular, although far from being perfectly mesoporous, and better distributed.

Here, to ensure the adhesion of the CCO layer on the CGO substrate, the same treatment used for screen printed sample was chosen and thermal treatment was carried out in air. The decomposition of the precursor, on the one hand, and of the polystyrene spheres on the other, together with the high temperature of the thermal treatment may be the reason of such an open structure. These pellets were just for preliminary tests. However, one should expect a better microstructure with a sintering at lower temperature and a first annealing under nitrogen, which should help to maintain the mesoporous structure of the template.

Nevertheless, although the microstructure was rather porous, it was decided to prepare two symmetric cells for impedance spectroscopy measurements to evaluate the difference in performances.

3.1.4. EIS analyses and results on templated and non templated spin coating CCO specimens

The preliminary preparatory work described previously (§3.1.3) was used as a base to prepare another set of samples for subsequent EIS analysis.

Two CGO dense pellets ($\rho_{rel} > 95\%$) were coated symmetrically by spin coating technique. On the first pellet was deposited a single CCO-only film, on both sides, with the protocol mentioned above (5 seconds at 500 rpm plus 60 seconds at 3000 rpm).

For the second pellet, a subsequent coating was performed with the usual protocol. The polystyrene spheres were deposited on the first face of the CGO pellet (5 seconds at 500 rpm plus 60 seconds at 1500 rpm) and then the CCO gel above (5 seconds at 500 rpm plus 60 seconds at 3000 rpm).

© 2014 Tous droits réservés.

In both cases, after the first coating, the pellets were carefully removed from the spinner and put into furnace for the grafting heating treatment (1 hour at 500°C then 2 hours at 900°C).

After the grafting of the first deposit, the pellets were submitted to spin coating the second face. The same procedure just described was repeated for the two pellets which were lastly put into furnace again for grafting the second surface.

The specimens were then submitted to EIS analyses to assess the electrochemical performances of a CCO structured cathode. The samples were heated and then analysed according to the usual procedure described in §2.3.2.

Fig. 3.1.9-a reports the evolution with the temperature of the EIS spectra of the polystyrene spheres-free cathode, while in Fig. 3.1.9-b is shown the temperature evolution for the polystyrene templated specimen.

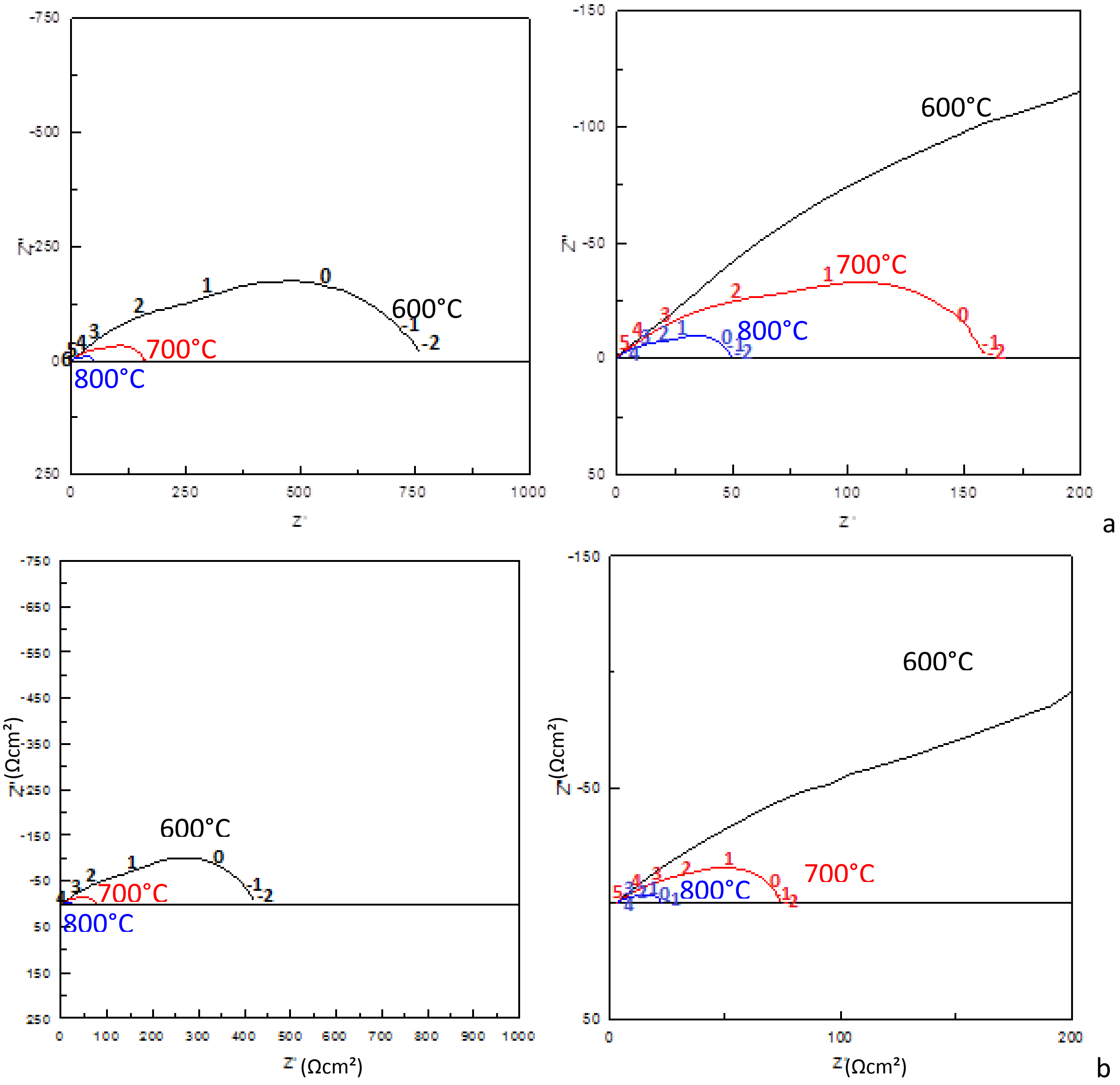

Fig. 3.1.9 - Temperature dependent EIS spectra of spin coated 100% CCO cathodes without (a) and with (b) template

© 2014 Tous droits réservés.

For the sake of comparison, the results of the EIS analyses at 700°C are reported here below in Fig. 3.1.10 (a) for the only CCO-coated pellet (black solid line) and the polystyrene/CCO-coated one (red solid line). The considered spectra were the ones of the last thermal cycle. Those spectra were afterwards used to calculate the fitting parameters starting from the equivalent circuit shown in Fig. 2.4.8. In Fig. 3.1.10 (b) is reported the result of the simulation obtained with Z-View for the only CCO-coated cathode at 700°C, whereas Fig. 3.1.10 (c) shows the fitting results for the cathode obtained by co-impregnation of CCO and the polystyrene template.

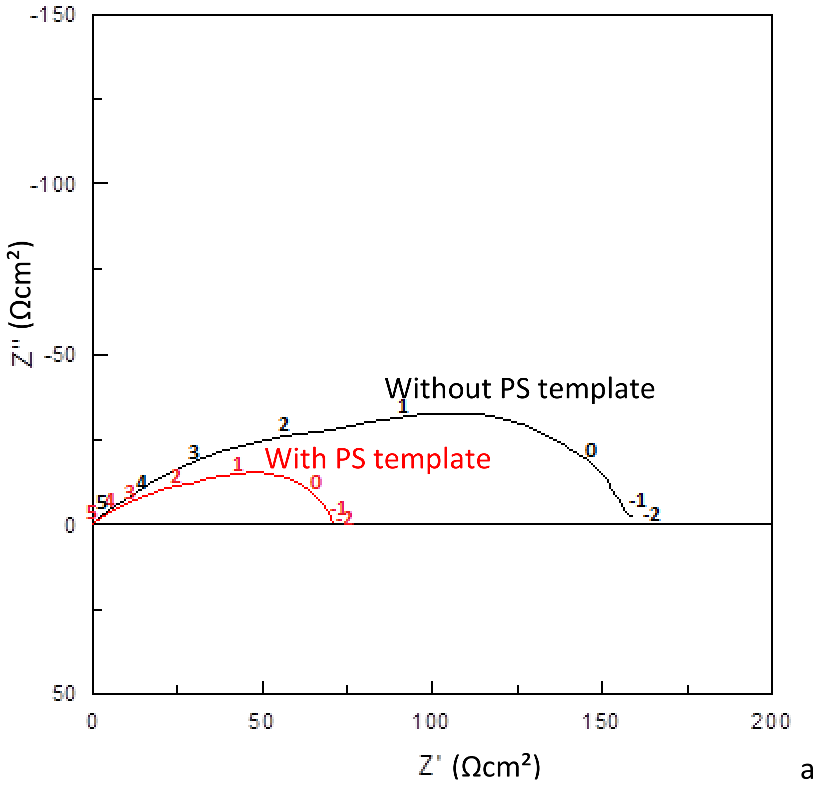

© 2014 Tous droits réservés.

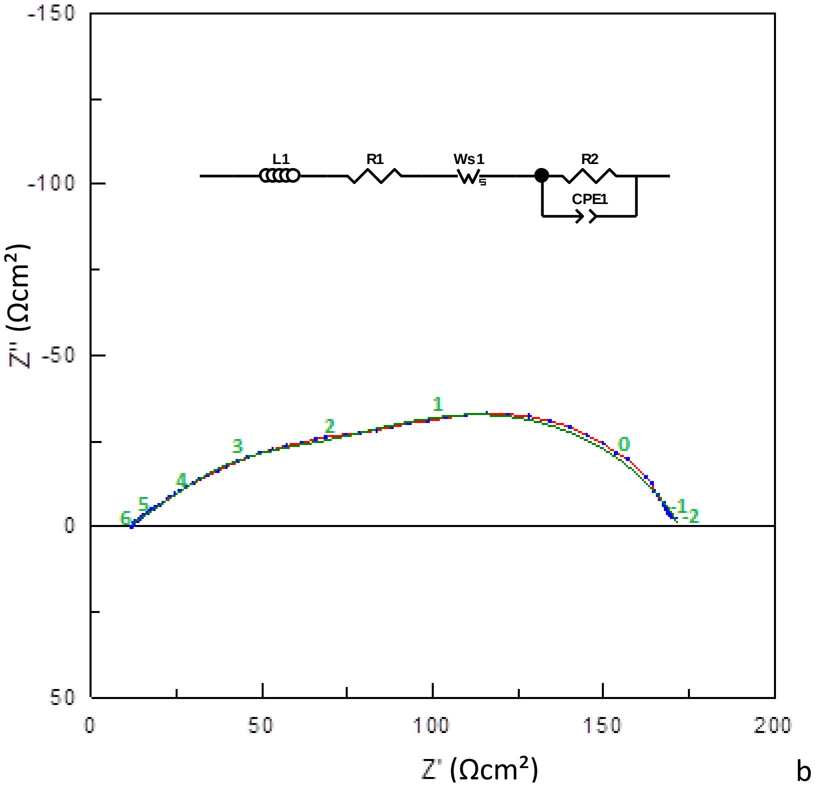

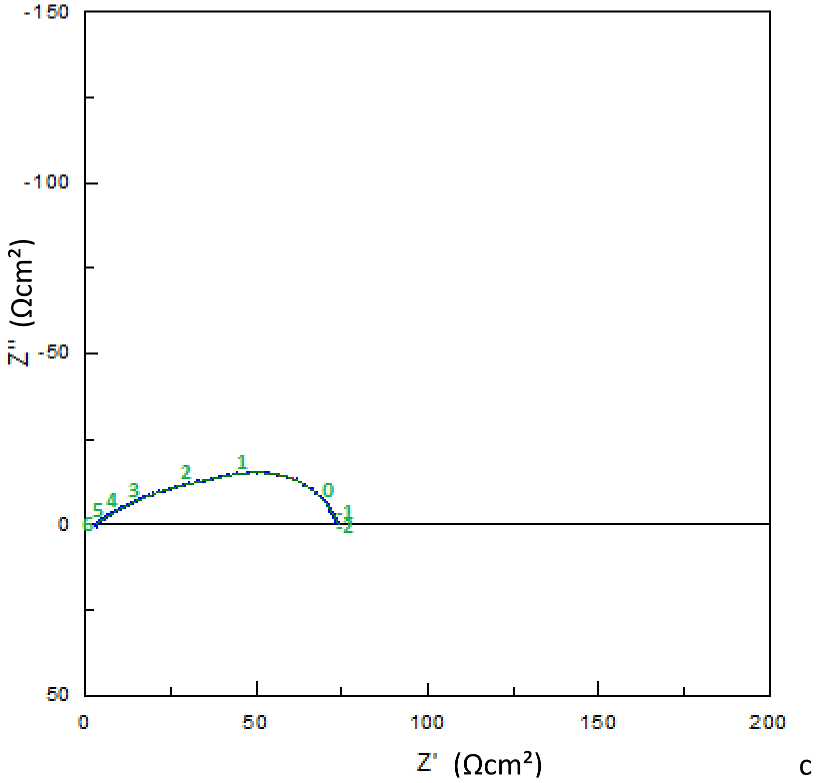

Fig. 3.1.10 - EIS results of spin coated 100% CCO cathodes at 700°C (a: comparison, b: fitting results without template, c: fitting results with PS template)

Interestingly, despite both samples showed high resistances, better performances were observed for the templated sample. However, the spectra display quite big semi-circles, with some slant on the left side and an evident depression angle that compresses the plots. Also, the straight line indicative of inductance phenomena is absent. Whether this depends on an

© 2014 Tous droits réservés.

intrinsic characteristic of the electrodes or on the limited width of the scanning range is still debatable. Last, the circle does not split in multiple components at high temperature (>750°C) although this may depend on the incredibly high magnitude of the cathodes' resistances. Nevertheless, the presence of two contributions is well evidenced on the inflection at about half width in both spectra.

The simulations revealed that the low frequency contribution corresponds to the Warburg elements while the other one, in the right part of the spectrum, is given by the RC element of the circuit.

It is immediately evident that the value of the ASR is two or three orders of magnitude higher than the ones for a screen printed 50/50-CGO/CCO cathode. In comparison to a pure screen printed CCO cathode (4.0 Ωcm²), the increase is by one or two orders of magnitude (70.4 – 152.7 Ωcm²). The incredibly bad performances are to be attributed to the microstructure which is too porous and should be optimised.

The coatings on the pellets were totally inhomogeneous and shapeless. This results in an extremely approximated value of the cathode's specific area which parameter affects the value of the ASR. Nevertheless, the error would not have changed significantly the results and the general considerations on the increases are still valid.

The comparison between the two pellets, instead, reveals some precious information: the polystyrene template seems to have a very positive effect on the overall ASR. In fact the absolute magnitude of the templated cathode is twice smaller than the non-templated one. The estimation on the ASR values confirms this tendency for the whole temperature range.

In Table 3.1 are reported the values of the ASR values for the two cathodes. The results of the fitting are also reported.

Table 3.1 - Values of the simulations on the EIS spectra of spin-coated 100% CCO templated and non-templated cathodes at 700°C

	100% CCO no template Spin Coating	100% CCO PS template Spin Coating
R1	10.13 Ωcm² [1.6%]	4.13 Ωcm² [1.5%]
L1	$1.56 \cdot 10^{-7}$ H [5.2%]	$1.38 \cdot 10^{-7}$ H [7.0%]
W_S-R	60.20 [3.2%]	30.68 [4.2%]
W_S-T	$1.93 \cdot 10^{-3}$ [6.5%]	$1.28 \cdot 10^{-3}$ [11.2%]
W_S-P	0.21 [0.8%]	0.15 [1.1%]
R2	102.00 [2.2%]	41.90 Ωcm² [3.3%]
CPE_2-T	$4.07 \cdot 10^{-4}$ [3.0%]	$3.67 \cdot 10^{-4}$ [4.2%]
CPE_2-P	0.42 [1.7%]	0.36 [2.2%]
ASR (overall)	152.74 Ωcm²	70.42 Ωcm²
χ^2	$4.17 \cdot 10^{-5}$	$5.23 \cdot 10^{-5}$

From the fitting, a strong dependence on the cathode nature for the W_S-R, R2 and ASR for both specimens is revealed. The difference between the Warburg and RC elements is about

© 2014 Tous droits réservés.

a factor of two between the two cells, which confirms the trend given by the overall ASR. Conversely, the time constants (W_s-T and CPE_2-T) follow a different trend. In fact, while the Warburg's time constant is substantially independent from the temperature, the CPE_2-T tends to decrease mildly with increasing temperature. This effect is probably due to the fact that the cathode is composed of CCO only without the CGO contribution. For both the cell with and without the polystyrene template, the time constants are very close each other ($\sim 1\text{-}2 \cdot 10^3$ for the W_s-T and $\sim 4 \cdot 10^{-4}$ for CPE_2-T).

The phase constants (W_s-P and CPE_2-P) are completely independent from the temperature and they settle at about 0.2 for the Warburg terminus and 0.4 for the R//CPE component.

Although these results are preliminary and the correlation with the microstructure is somehow uncertain, the insertion of an organic template has a very beneficial effect on the electrochemical performances of the Spin Coated CCO cathode. This result, while in absolute value is quite bad, reveals that the microstructuration of the CCO cathode by an organic template is able to cut by a factor of two the overall ASR. Further studies will include the improvement of the coating technique, the evaluation of changing the organic template (polydopamine spheres) and the optimisation of the gel composition.

3.2. Electrostatic Spray Deposition procedure of SOFCs structured electrodes

The electrostatic spray deposition is another technique which can lead to given microstructure with controlled porosity. Based on electro-hydrodynamics laws, this technique foresees a precursor solution being pumped through a metallic nozzle at a controlled flow rate. The solution is then atomized into an aerosol by applying a high voltage that generates an electrical field between the nozzle and the substrate. The electrical field generates the aerosol and directs it towards the substrate where the droplets spread, dry and decompose to form the film. The microstructure of the film is a result of the size of the droplets within the spray. ESD is a relatively low-cost process and allows obtaining a large array of different microstructures, some of which quite original. In France it is mainly developed by the group of Prof. E. Djurado of the LEPMI laboratory of the University of Grenoble [133], [134].

Using this technique, Marinha *et al.* managed to get an ASR of only 0.13 Ωcm² at 603°C for a cell made of a CGO electrolyte with a 7 μm thick interfacial layer of LSCF recovered with a 45 μm thick LSCF current collector [85].

CCO ESD-coated samples were prepared at LEPMI by the research group of Prof. E. Djurado on CGO pellet provided by us. The films were prepared from calcium and cobalt nitrates ($Ca(NO_3)_2 \cdot 4\ H_2O$ (calcium(II) nitrate tetrahydrate, Acros Organics, 99%) and $Co(NO_3)_2 \cdot 6\ H_2O$ (cobalt(II) nitrate hexahydrate, Fisher Scientific, 98%) as precursors. The salts were dissolved in ethanol (C_2H_5OH, Prolabo, 99.9%) and/or butyl carbitol (diethylene glycol monobutyl ether $CH_3(CH_2)_3OC_2H_2)_2OH$, Acros Organics, 99+%). Their concentration was 0.02 M. The

© 2014 Tous droits réservés.

microstructure was investigated as a function of the process parameters, such as nozzle-to-substrate distance, solvent composition, substrate temperature, flow rate and deposition time. Films with controlled microstructures were obtained after annealing at 880°C for 2 hours in air with a heating and cooling rate equal to 3°C/min in order to get crystallization. Samples prepared in 100 vol% ethanol, with a 1. 5 mL/h flow rate, a substrate temperature of 450°C and a nozzle to substrate distance of 50 mm were selected for impedance spectroscopy and submitted to X-Rays diffraction and SEM imaging to evaluate the microstructure prior to studying their electrochemical performances.

3.2.1. Characterisation of ESD deposited CCO cathodes over CGO dense pellets

As shown in Fig. 3.2.1, the purity of the CCO phase was confirmed by X-ray diffraction.

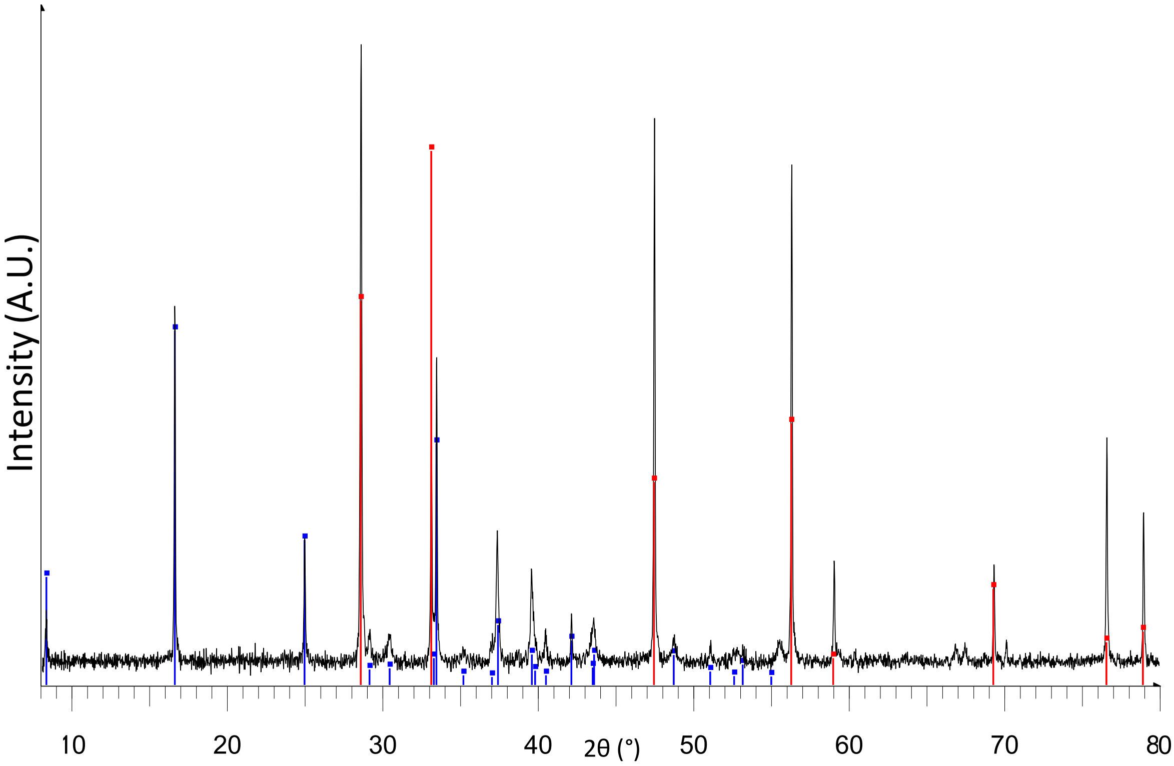

Fig. 3.2.1 - X-ray pattern of the ESD CCO cathode deposited on a CGO dense electrolyte at LEPMI, prior to EIS investigation (only the CCO, blue bars, and CGO, red bars, patterns were evidenced, attesting the sample purity)

It was already stated that the ESD coating technique provides rather interesting microstructures (§3.2). Those structures are often referred to as “cauliflower” assemblies, due to their resemblance to the vegetable.

To see the aspect of the coated film, SEM images were recorded on a Hitachi N3400 instrument equipped with a CCD-camera detector.

Fig. 3.2.2 shows the microstructure of the ESD-deposited CCO layer on CGO dense pellet at different magnifications: 500 x (a), 1500 x (b), 2500 x (c) and 5000 x (d).

© 2014 Tous droits réservés.

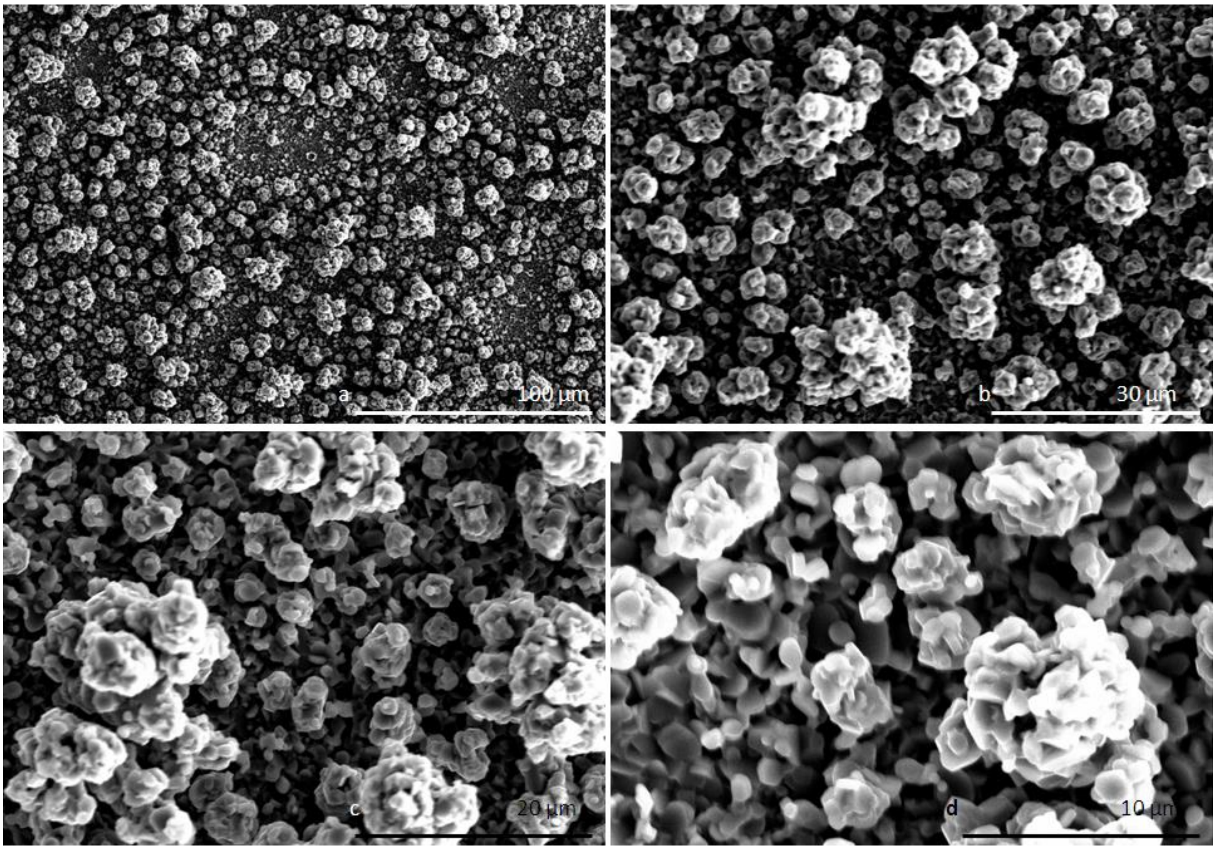

Fig. 3.2.2 - SEM images ad different magnitudes of the ESD deposited CCO layer at 500X (a), 1500X (b), 2500X (c) and 5000X (d) magnification

Indeed the structure of the ESD-coated CCO film resembles to the face of a cauliflower. The image with the smaller zoom (a) reveals an evenly covered surface without noticeable holes or gaps.

Increasing the zoom level (b, c), minor imperfections were noticed: small indents, microscopic holes etcetera. Nevertheless, the overall structure was perfectly regular, with a coverage level and aspect totally homogenous in each part of the film.

For even narrower zooms (d), the “cauliflower” aspect was revealed in more intimate details. Even though it is impossible to see the growth of the structure from the base of the CGO structure, due to the thickness of the deposit, the fine structure of the excrescencies is displayed.

The growths present a fine cylinder-like base that enlarges towards the top like a small pyramid.

Other very interesting information is collected from the side-cut image of the ESD-coated CCO film (Fig. 3.2.3).

© 2014 Tous droits réservés.

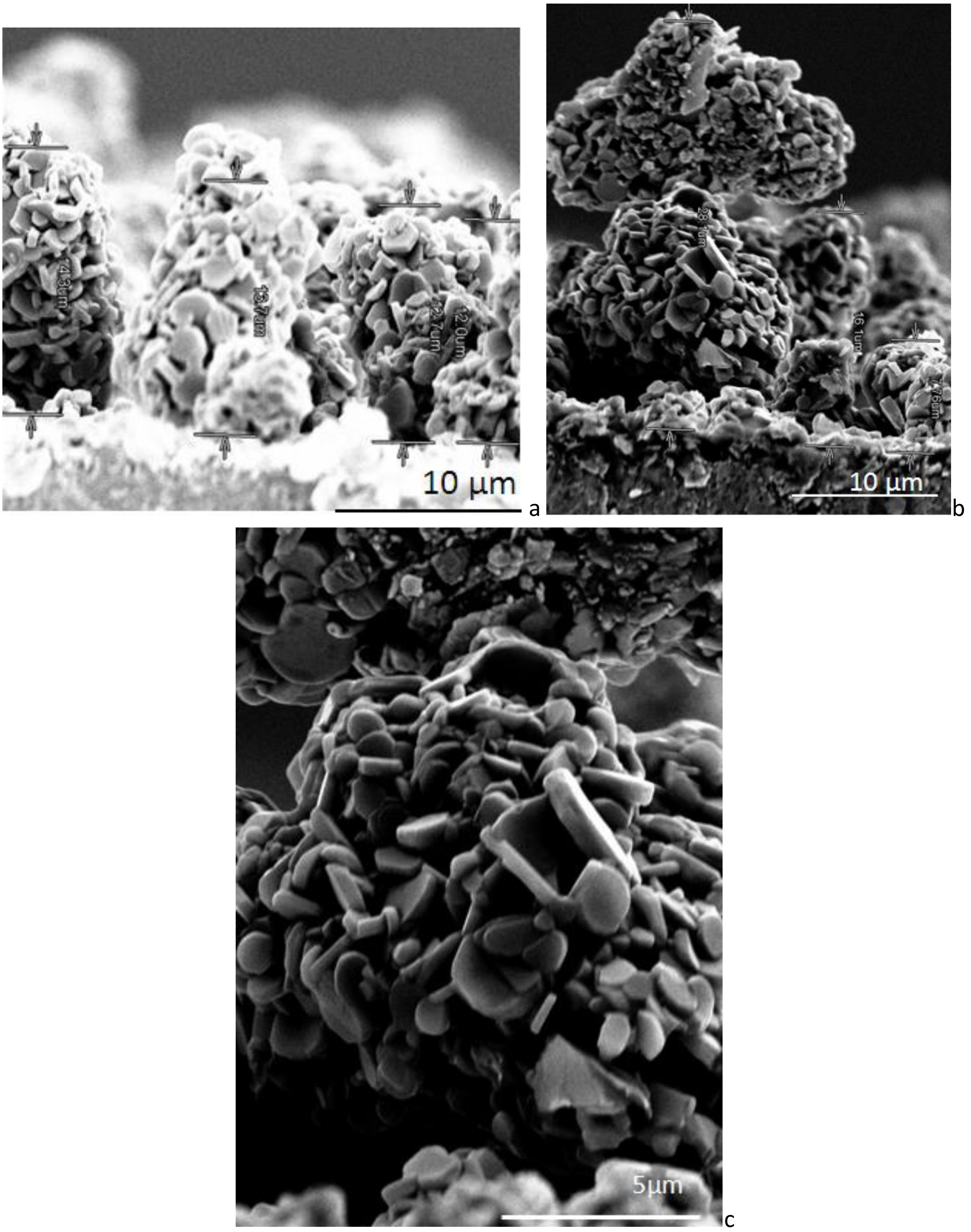

Fig. 3.2.3 - Side cut SEM images of a EDS coated CCO cathode at 3200X (a, b) and 7000X (c) magnification

From these SEM images (Fig. 3.2.3 a, b, c), the average thickness of the CCO layer was estimated to be about 15 µm. The distribution of the layer's thickness is quite homogenous with values ranging within a few micrometres of difference, as it is possible to see from Fig. 3.2.3 (a).

© 2014 Tous droits réservés.

On the other hand, the very typical “cauliflower” formation, with the large pointy tip, has a much bigger size which approaches 28.5 µm, as reported in Fig. 3.2.3 (b). Noteworthy, the excrescence is sided by portions of coating much thinner than the average (7.76 µm), as if the cauliflower formation acted as an umbrella preventing the coating to grow thicker just next to it.

At deeper magnification (7000 X) the intimate nature of the deposit is seen, as well as the layer’s growth. The crystallites are in a platelet form with a widely distributed size, which is not quantified here. Their flat and round shape is clearly visible even though in the layer itself, those crystallites are agglomerated and packed.

Lastly, the set of SEM images reveals that the grafting of the deposit is extremely good, with the ESD growths finely anchored on the CGO support electrolyte.

With a rather different microstructure from the one obtained by screen printing, one could expect a rather different behaviour in impedance.

3.2.2. EIS analyses on ESD deposited CCO cathodes supported on CGO dense pellets

For EIS analysis, the temperature was increased from RT to 800°C with steps of 200°C per hour, and then it was varied in between 600°C and 800°C by steps of 50°C with a stabilization time of 2 hours per step.

The imposed voltage was set at 50 mV, the AC frequency sweep was comprised in between 1.4 MHz and 10 mHZ and, for each decade, 8 data points were collected.

In Fig. 3.2.4 are reported the results of the EIS analyses at 600°C (black line), 700°C (red line) and 800°C (blue line).

© 2014 Tous droits réservés.

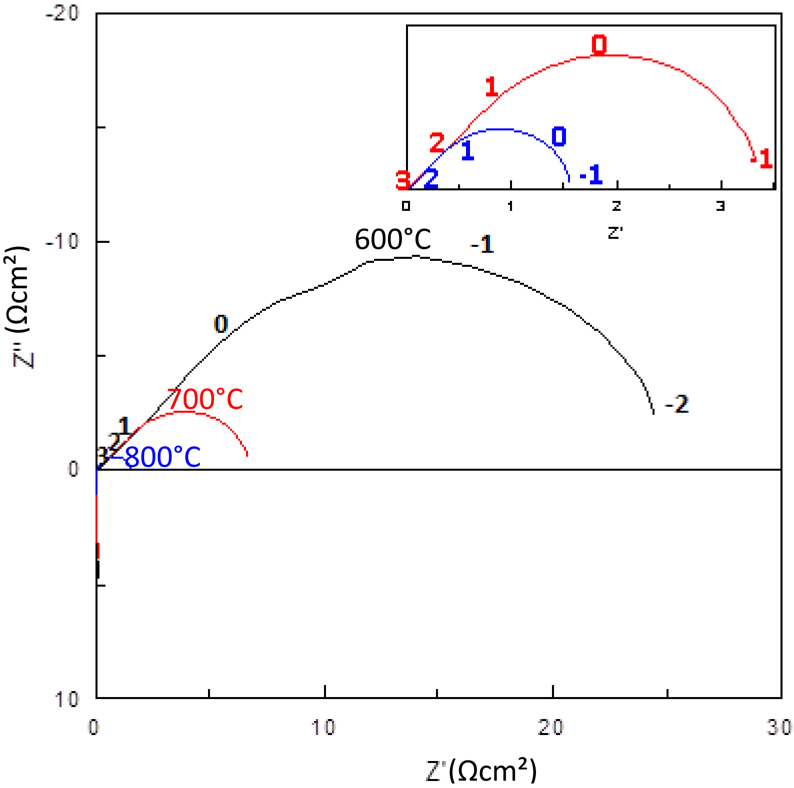

Fig. 3.2.4 - EIS spectra for a symmetric ESD-coated CCO cathode

For the sake of comparison, a screen printed sample made of pure CCO was prepared in the same conditions as in §2.4.1. A SEM of the sample is given in Fig. 3.2.5. Its microstructure was similar to the composite one with a thickness of about 30 µm.

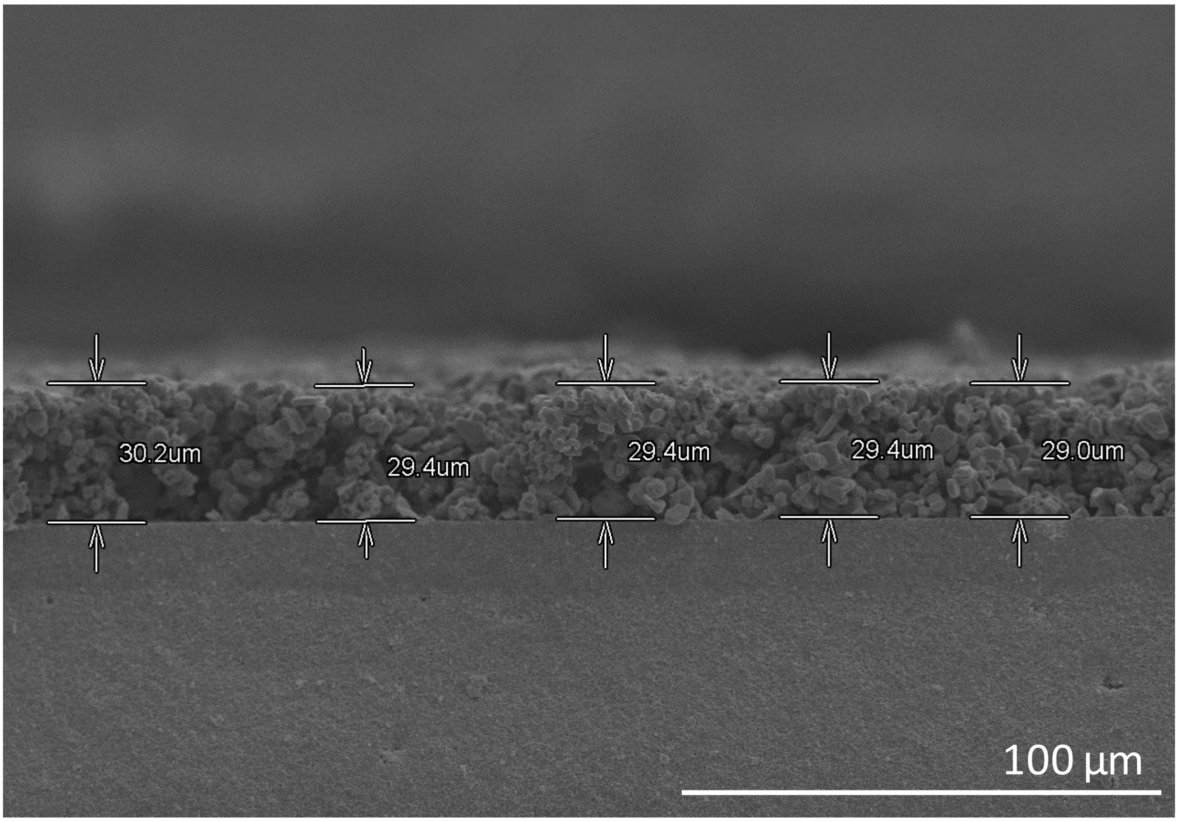

Fig. 3.2.5 - SEM image of a 100% CCO screen printed cathode

© 2014 Tous droits réservés.

In Fig. 3.2.6 are reported the results of the analysis at 600°C (a), 700°C (b) and 800°C (c) for screen printed (black line) and ESD-deposited (red line) CCO cathodes. On the top right corner the microstructures of the two cathodes are recalled (from left to right: the screen printed 100% CCO deposit and the ESD 100% CCO one).

Interestingly, whatever the temperature, better performances were obtained for the ESD coated sample with an ASR of 3.32 Ωcm² at 700°C to be compared to 4.58 Ωcm² for the screen printed sample.

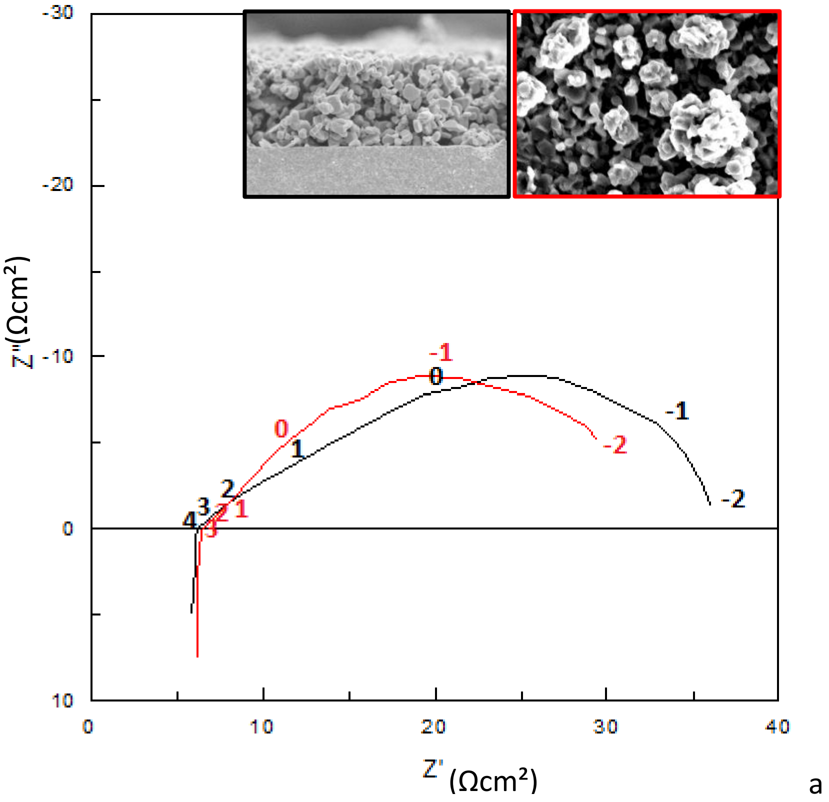

© 2014 Tous droits réservés.

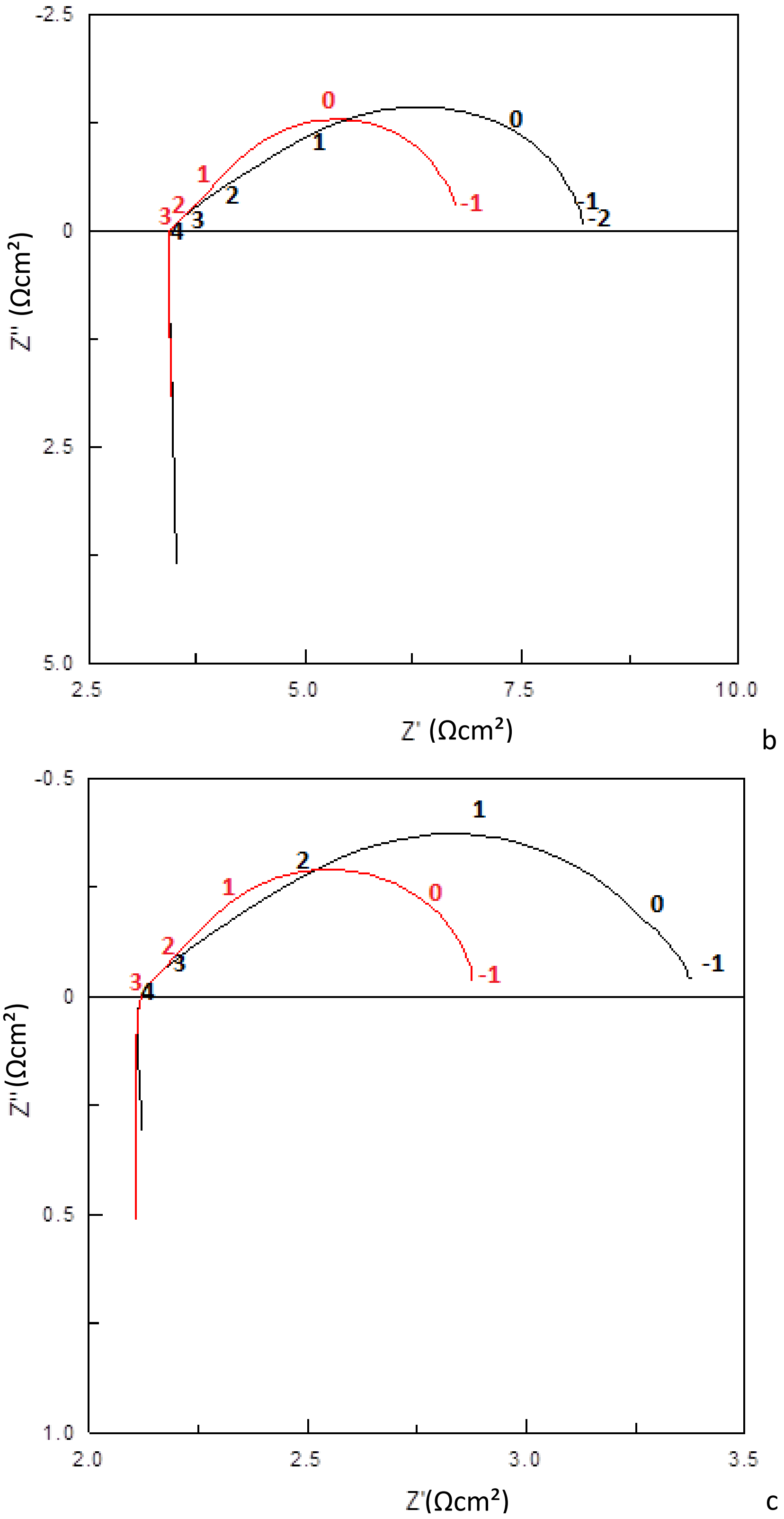

Fig. 3.2.6 - Stacked EIS spectra of 100% CCO symmetric cells by EDS (red) or screen printing (black) (a: 600°C, b: 700°C, c: 800°C)

The spectra of both the ESD and the screen printed cathodes feature the typical 45° slant and a well pronounced circle at low frequency characteristic of a Warburg at high frequency in series with a RC element at low frequency. Although, visually, a third contribution at high frequency would likely be added, for data collected on the screen printed sample at 800°C

© 2014 Tous droits réservés.

both the spectra of the ESD-coated and the screen printing-coated cathodes have been fitted with the equivalent circuit reported in Fig. 2.4.8. The results of the calculations at each temperature are reported in Table 3.2 and in Fig. 3.2.7 are shown the results of the fitting at 700°C for the ESD-coated CCO cathode (a) and for the screen printed CCO cathode (b). Interestingly, a very good fit was obtained for both the ESD and the screen printed sample although, for the screen printed sample, the agreement was lower, possibly due to an additional contribution at low frequency which could be the fingerprint of more difficult oxygen gas diffusion in the screen-printed sample. Nevertheless, the analysis of the fitting results evidenced that the addition of another component to the circuit results in a worse agreement between the experimental and the calculated data. On the other hand, this cannot be taken for granted as the simulation software (Z-View) is not a subtractive one so two different contributions can merge into only one if they're too well superposed.

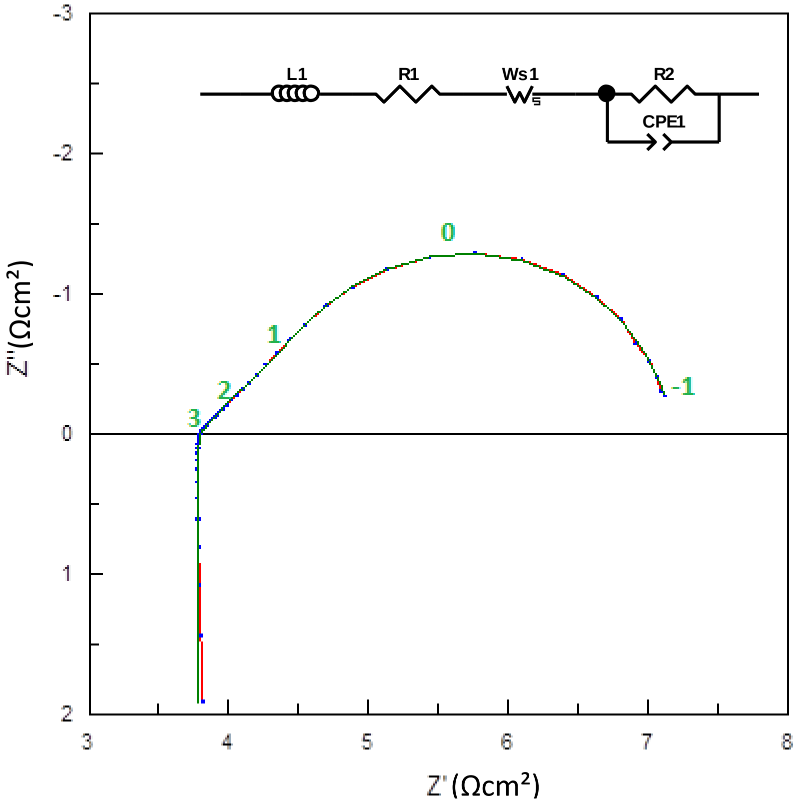

a

© 2014 Tous droits réservés.

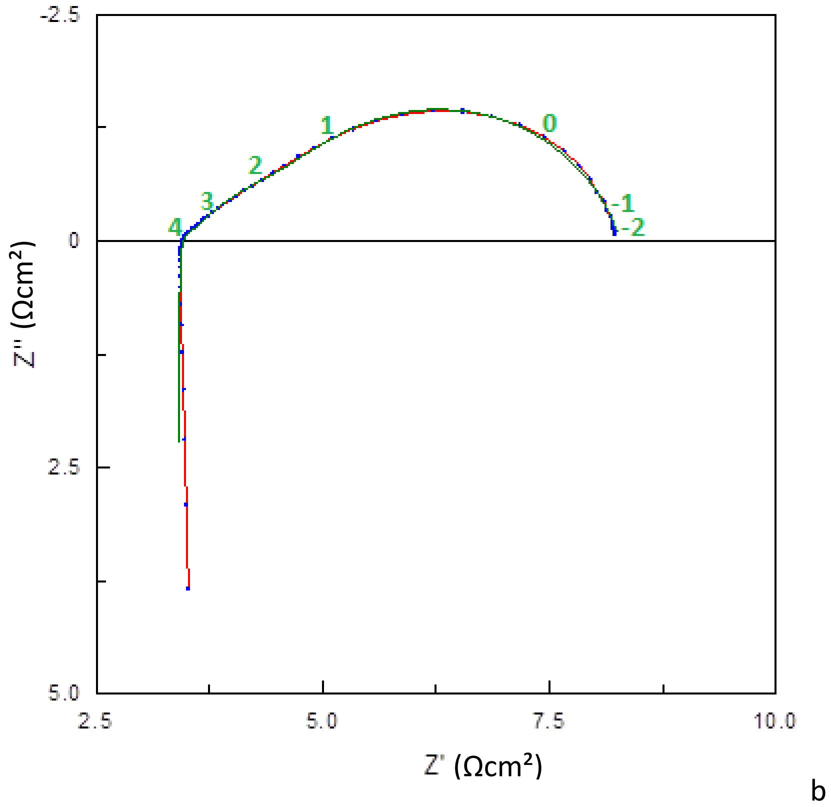

Fig. 3.2.7 – Fitting results on the EIS spectra for the ESD coated (a) and screen printed (b) 100% CCO cathode at 700°C

Table 3.2 - Fitting calculation EIS results for EDS-coated and screen-printed cathodes

	600°C		700°C		800°C	
	ESD	S. P.	*ESD*	S. P.	*ESD*	S. P.
R1	6.39 Ωcm^2 [0.1%]	12.78 Ωcm^2 [0.2%]	3.76 Ωcm^2 [0.1%]	3.40 Ωcm^2 [0.2%]	1.42 Ωcm^2 [0.1%]	2.09 Ωcm^2 [0.1%]
L	$7.26\cdot10^{-7}$ H [0.6%]	$5.59\cdot10^{-7}$ H [2.5%]	$7.77\cdot10^{-7}$ H [5.9%]	$4.49\cdot10^{-7}$ H [0.8%]	$1.45\cdot10^{-6}$ H [2.2%]	$4.86\cdot10^{-7}$ H [0.8%]
W_s-R	3.67 [0.6%]	7.512 [2.7%]	0.65 [5.8%]	1.75 [0.1%]	0.13 [3.4%]	0.22 [8.1%]
W_s-T	0.25 [9.6%]	0.06 [6.2%]	0.06 [5.8%]	0.04 [21.2%]	0.02 [3.4%]	$1.8\cdot10^{-3}$ [1.7%]
W_s-P	0.37 [1.2%]	0.36 [0.8%]	0.38 [0.9%]	0.32 [1.7%]	0.36 [1.6%]	0.36 [3.6%]
R2	21.55 Ωcm^2 [0.9%]	23.36 Ωcm^2 [1.1%]	2.77 Ωcm^2 [0.6%]	2.80 Ωcm^2 [5.4%]	0.63 Ωcm^2 [9.5%]	1.10 Ωcm^2 [1.7%]
CPE_2-T	0.07 [1.6%]	0.03 [1.6%]	0.10 [0.7%]	0.05 [5.8%]	0.13 [17.1%]	0.05 [1.7%]
CPE_2-P	0.89 [0.6%]	0.80 [0.3%]	0.92 [0.3%]	0.85 [1.6%]	0.92 [1.2%]	0.73 [1.0%]
ASR	22.90 Ωcm^2	29.80 Ωcm^2	3.32 Ωcm^2	4.58 Ωcm^2	0.76 Ωcm^2	1.26 Ωcm^2
χ^2	$2.85\cdot10^{-4}$	$2.90\cdot10^{-4}$	$1.97\cdot10^{-5}$	$2.80\cdot10^{-4}$	$1.86\cdot10^{-5}$	$6.53\cdot10^{-5}$

As reported in [5] Ws is associated to the ionic transport of the oxide ions O^{2-} at the CCO-CGO interface and the (R_2//CPE_2) at lower frequency range represents the processes of the oxygen reduction reaction itself (adsorption, transfer of species, surface diffusion). Lower R2

© 2014 Tous droits réservés.

values for the ESD-coated sample showed clearly evidence of an easier oxygen reduction reaction than in case of the screen printed sample.

The comparison of the fitted data confirms the superior performances of the ESD-coated CCO cathode over the screen-printed one. At every temperature the overall ASR of the former is lower than the ASR of the latter (-23% at 600°C, -28% at 700°C and -40% at 800°C). Concerning the values of the time constants (W_S-T and CPE_2-T) the tendency is quite peculiar. In fact, the CPE_2-T is maintained unchanged over the whole temperature range even though for the screen printed sample the absolute value is one order of magnitude higher than for the ESD sample. Instead, the Warburg's time constant (W_S-T) decreases very strongly with the temperature. The dependency of this parameter with the temperature is so strong that below 700°C it surpasses the value of CPE_2-T producing an apparent "inversion" of the time constants. This effect is typical of a very difficult electrode/electrolyte contact charge transfer, as it is the case for a 100% CCO cathode [4].

It is interesting to notice that the superior performances of the ESD coated cathode are reflected in the values of its equivalent circuit's elements. Both the Warburg and the RC temperature dependent components show inferior values for the ESD cell than for the screen printed one. Also in this case, both these two parameters (W_s-R and R2) decrease strongly with the temperature, meaning that the process is thermally activated. Here, the ESD technique of deposition plays a role on all the steps of the physico-chemical process, showing the great importance of the cathode morphology.

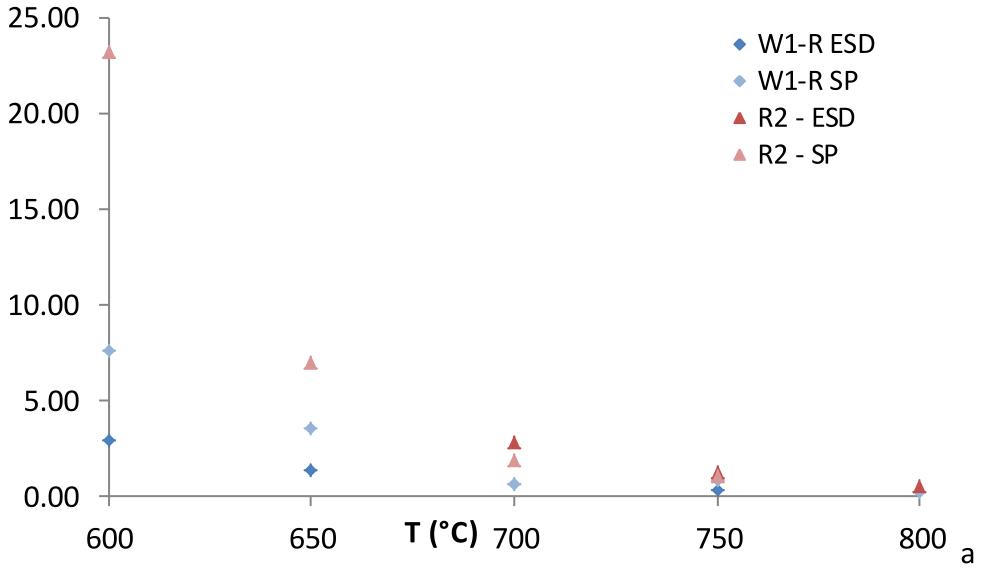

© 2014 Tous droits réservés.

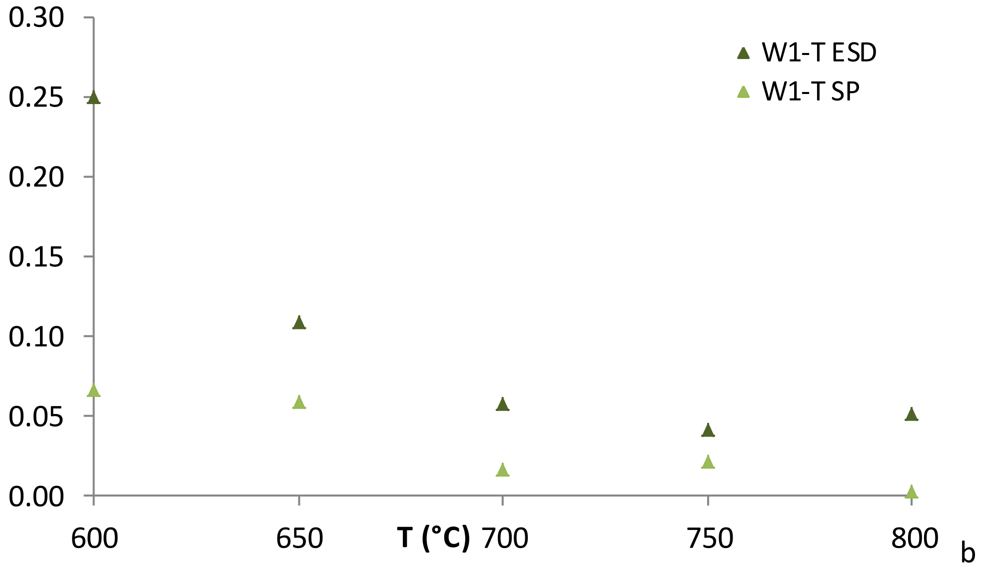

Fig. 3.2.8 - Evolution of the RC and Warburg's resistance (a) and Warburg's time constant (b) as a funciton of temperature for a 100% CCO screen printed (lighter) and 100% CCO ESD coated (darker) cathode

Finally, the phase constant elements (W_S-P and CPE_2-P) remain constant with temperature. The Warburg behaviour is strongly marked (W_S-P ≈ 0.4), while the CPE tends to a perfect capacitance behaviour (CPE_2-P ≈ 0.9).

While it is true that this outstanding result is far higher than the one from the optimised screen printed cathode composition (50/50-CCO/CGO), it is also true that the ESD CCO cathode has not gone under any optimisation survey.

Moreover, not only the contribution from the composition may be improved (blending CCO and CGO), but also the influence of the thickness may play a role. All things considered, this result is very promising and further experiments will have to be carried out on CCO-CGO composite with different thicknesses using the same technique.

3.3. Macroscopic modification of the cathode layer: insertion of a nanometric CCO interlayer between the electrolyte and the electrode

It was recently proved by Hildenbrand et al. [9] that the insertion of a very thin dense layer of LSCF between a YSZ electrolyte and a porous LSCF cathode greatly reduces the ASR of a symmetric cell. It decreases from 0.67 Ωcm² to 0.21 Ωcm² at 600°C in air.

Taking inspiration from this work, the same approach was tried with the 50/50-CCO/CGO cathodes.

In collaboration with Dr. M.H. Chambrier, of the UCCS laboratory of the University of Lens a dense layer of CCO was deposited on dense (ρ_{rel}>95%, roughness = 15.2 µm) CGO pellets by Pulsed LASER Deposition (PLD).

© 2014 Tous droits réservés.

3.3.1. Sample preparation: deposition of a dense CCO nanometric layer by Pulsed Layer Deposition

A compex Pro 102 deposition system using a KrF excimer laser beam (λ= 248 nm) was used for pulsed laser deposition. To optimize the condition of depositions as temperature, pressure, frequency, based on the study reported by Sun *et al.* [135], first experiments were carried out on sapphire Al_2O_3-(0001) oriented single crystals before deposition on dense CGO electrolytes for preliminary electrochemical characterisations. The beam was focused at a 45° angle onto a rotating CCO target inside a vacuum chamber and the laser fluence was adjusted to 2 J/cm^2. The target (1 inch in diameter) was prepared from powders obtained by solid state reaction, by uniaxial pressing and annealing at 900°C for 12 hours. The target-substrate distance was fixed at d= 4.5cm. In a first step, the vacuum in the chamber was decreased to 10^{-5} mbar, consecutively the temperature was increased to 750°C at a 10°C/min rate. In a second step, an oxygen dynamic pressure of 10^{-1} mbar was introduced. All films were deposited for 9000 pulses. After that, they were cooled down to room temperature at a 10°C/min rate. Prior to the deposition, the sapphire substrate was thermally heated at 1400°C for 25 min and then ultrasonically cleaned in ethanol for 5 min.

Best films were obtained at a rate of 3 Hz at 750°C under pO_2 =10^{-1}mbar. As shown by transmission electron microscopy (Fig. 3.3.1), they were well crystallized, exhibiting a preferred orientation along the [0 0 1] directions. The CCO structure was confirmed both by electron and X-ray diffraction.

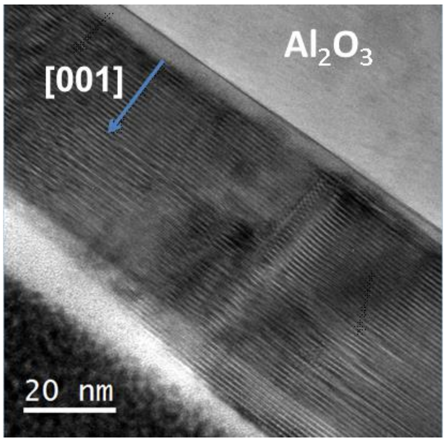

Fig. 3.3.1 - TEM cross-section images of a CCO thin film deposited by PLD on a sapphire Al_2O_3-(0001) oriented single crystals

In a second step, these conditions of deposition were transferred to a CGO electrolyte. However, two films were prepared, one with a LASER shooting frequency set at 2Hz, and a second one with the 3Hz optimal frequency. For the preparation of symmetric cell for impedance spectroscopy, a gold sheet was used as sample holder and mask to allow the thin film deposition on both sides of the sample. It was fixed to the deposition system by mean of a silver paste.

© 2014 Tous droits réservés.

Because of the high intensity of the CGO dense electrolyte, it was difficult to confirm the purity of the film by X-ray diffraction, the peaks corresponding to the film being too low in intensity. TEM on a samples prepared by Focused Ion Beam (FIB) is planned but has not been carried out yet.

Finally, the preparation procedure foresaw the deposition of a screen-printed layer of 50/50-CCO/CGO as a cathode on both sides of the support (symmetric cell) using the same procedure as described in §2.4, with the same heating treatments, 500°C for 2 hours for organic compounds removal and then 900°C for 1 hour. Since the conditions on ink preparation and deposition may strongly influence the sample thickness, a reference sample without interfacial layer was prepared in the same conditions.

In Fig. 3.3.2 is reported a schematic representation of the cell mounting. In the centre is the thick dense electrolyte (CGO). At both sides is coated the cathode (symmetric cell) with the dense PLD deposited CCO film first and the porous screen printed 50/50-CCO/CGO layer after.

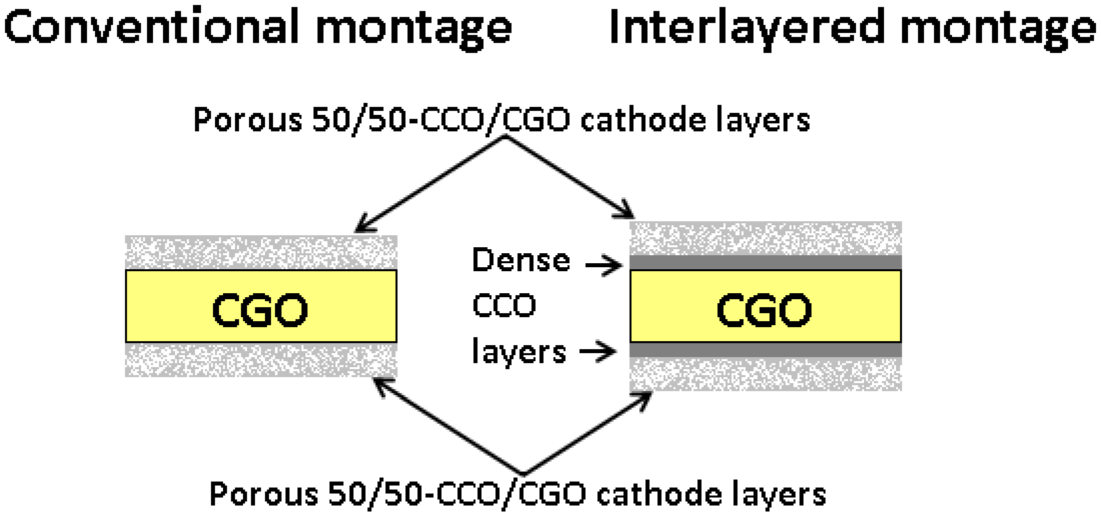

Fig. 3.3.2 - Schematic representation of a conventional and interlayered symmetric cell

The cross-section images of the samples after EIS is given in Fig. 3.3.3, which aim is to show that a thickness of about 16 µm was measured for all samples. Also, in the figure is evidenced the morphology which is again very similar in all the cases.

© 2014 Tous droits réservés.

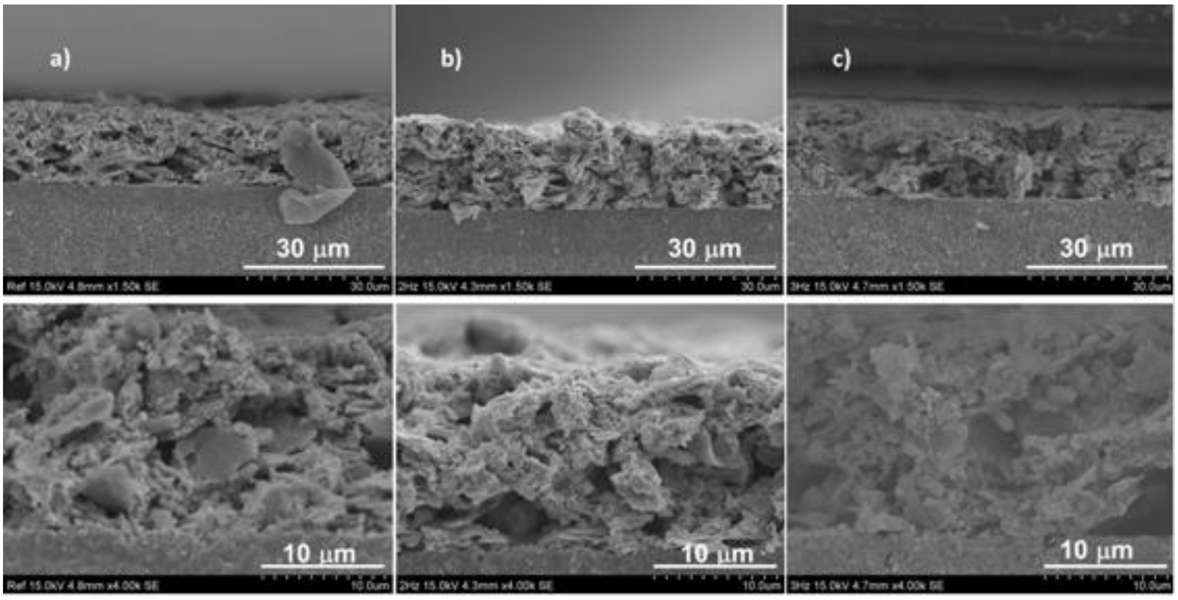

Fig. 3.3.3 - SEM cross section of a 50/50-CCO/CGO screen printed sample without interfacial layer used as reference (a), a 50/50-CCO/CGO screen printed sample with an interfacial layer deposited at 2 Hz (b) and a 50/50-CCO/CGO screen printed sample with an interfacial layer deposited at 3Hz

3.3.2. EIS analysis of electrochemical performances of PLD intercalated dense CCO layer on a screen printed composite 50/50-CCO/CGO electrode

The three cells were submitted to EIS simultaneously. They were put into a furnace under air and heated from room temperature to 800°C by steps of 200°C per hour. The analysis conditions were kept the same as in §2.3.2.

The results of the EIS analyses are reported here below. Fig. 3.3.4-a shows the temperature dependent stacked spectra at 600°C, 700°C and 800°C of the specimen with the 2Hz deposited thin film. In Fig. 3.3.4-b are reported the stacked spectra at 600°C 700°C and 800 °C for the other pellet, with the thin dense CCO layer deposited at 3Hz. The spectra corresponding to the reference sample are given in Fig. 3.3.5

© 2014 Tous droits réservés.

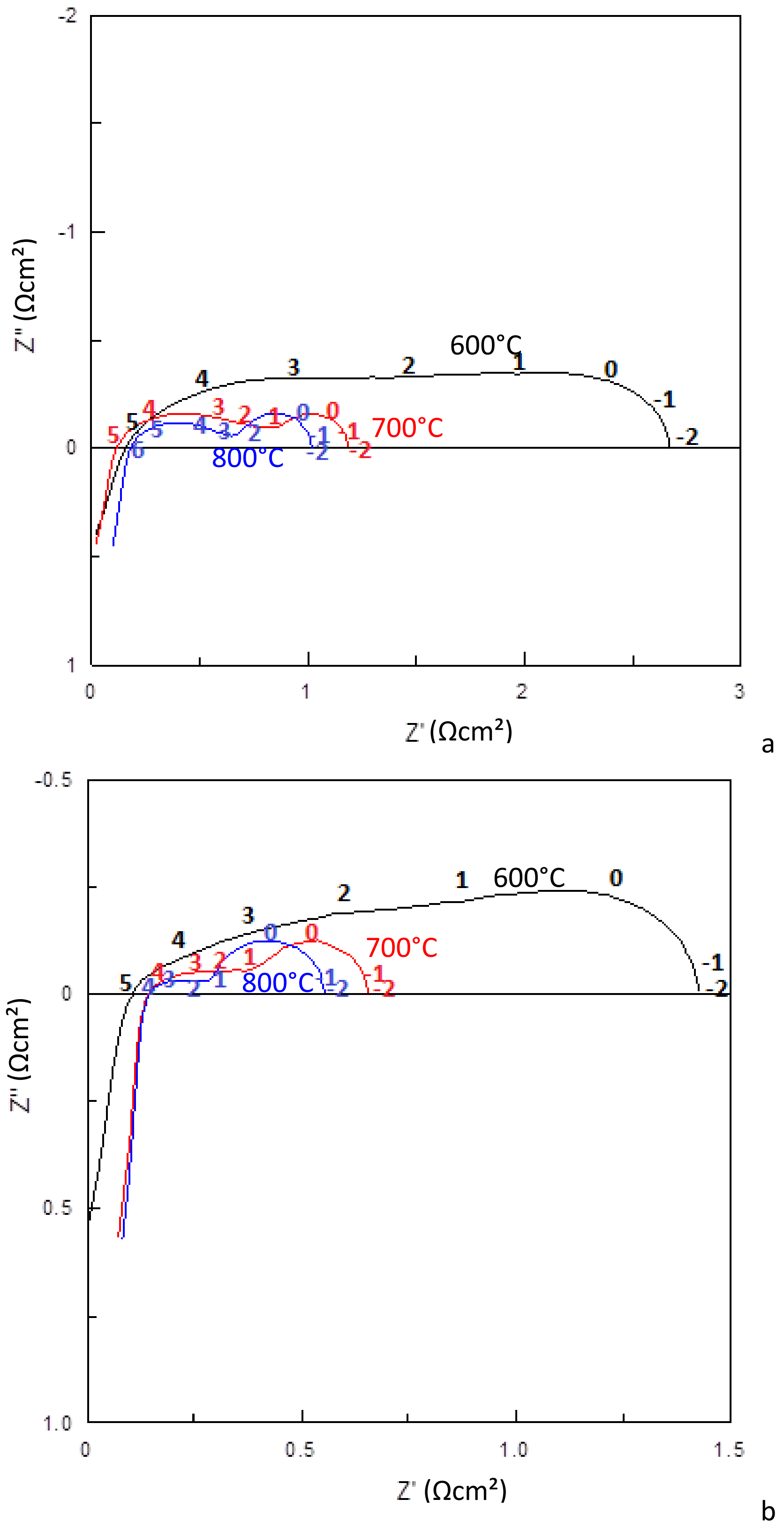

Fig. 3.3.4 - Temperature dependent stacked EIS spectra of 2Hz (a) and 3Hz (b) PLD deposited symmetric cells

© 2014 Tous droits réservés.

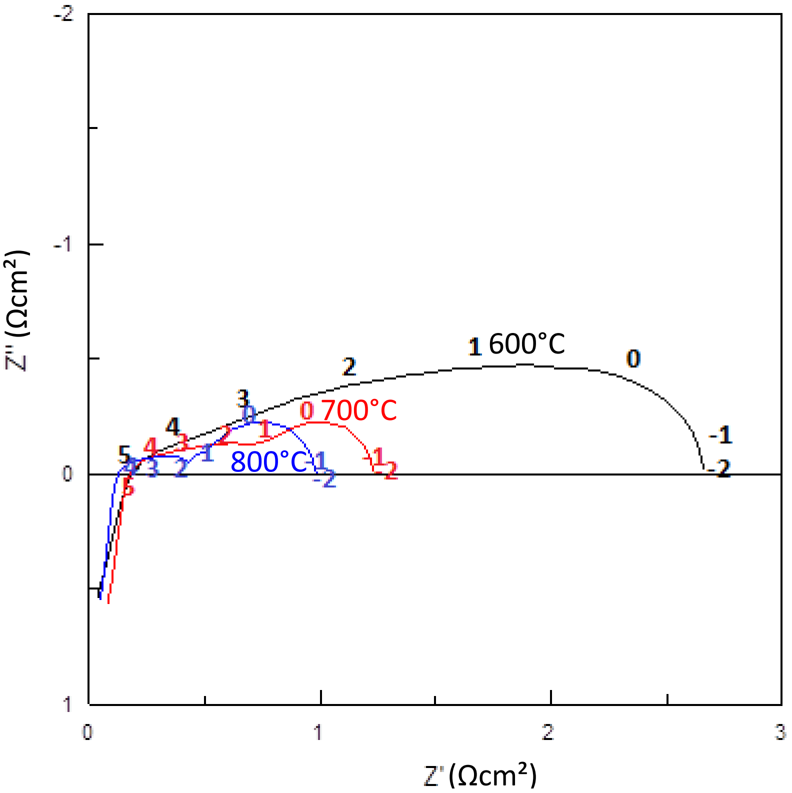

Fig. 3.3.5 - Temperature dependent stacked EIS spectra of interlayer-free symmetric cells at 700°C

Here, for the reference, an ASR value of 1.05 Ωcm² was measured for the dense film-free specimen. Though higher than the optimal value measured and reported in §2.3.4, it is has to be said that the electrode thickness in this case was lower than the optimum, with an ASR similar to what obtained for a 13 µm-thick sample (Fig. 2.3.6). An ASR of 1.17 Ωcm² was measured for the sample with a 2Hz deposited CCO interlayer. In contrast, this value decreased to 0.51 Ωcm² for the 3Hz deposited CCO interlayer sample. The 2Hz frequency was not the optimal one. Without any further characterisation, it is difficult to conclude but, as shown by Sun and co-workers [135], the deposition rate is a key parameter during the thin film growth and Ca_xCoO_2 may be easily obtained as secondary phase. The growth speed of the interlayer may induce either a bad quality of the film or the formation of insulating phases such as $Ca_3Co_2O_6$. Instead, with the optimal deposition frequency (3Hz), ASR decreases by a factor of 2. This decrease was confirmed for the whole temperature range (600-800°C). Although adequate carefulness should be taken for the conclusions, very insightful result seems to reveal that the insertion of a dense film between the electrolyte and the porous electrode has a very beneficial effect.

However, these results are rather preliminary than conclusive. No optimisation was done on the procedure and on the interlayer composition or on the thermal treatment. Still, further experiments like FIB and TEM analyses must be done to determine the microstructure of the PLD coating.

To go further in the understanding of the impact of this interfacial layer on the oxygen reaction reduction, the fitting of the data was successfully attempted. The spectra were

© 2014 Tous droits réservés.

simulated and fitted with software Z-View (ver. 3.3d, ©1990 – 2013 [123]) using the same equivalent circuit proposed in Fig. 2.4.8 at first. Because the first fits gave a value of the phase constant higher than 1 for the R//CPE component, it was decided to modify the circuit by replacing the CPE with a simple capacitor. For the sake of comparison, the modified circuit proposed in Fig. 3.3.6 was used for all the fits reported in this section, including the ones for the reference cathode without an interface.

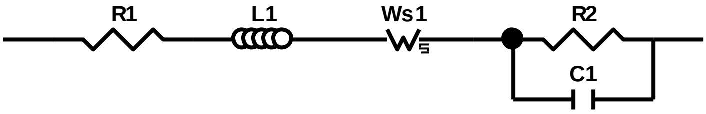

Fig. 3.3.6 - Modified equivalent circuit for the fitting of the 50/50-CCO/CGO cathodes with or without PLD-coated interfacial dense CCO layer

The results of the fitting are reported in Fig. 3.3.7 which shows the spectra of the layer-free specimen (a), the specimen with a 2Hz deposited interlayer (b) and the one with a 3Hz deposited interlayer (c) at 700°C.

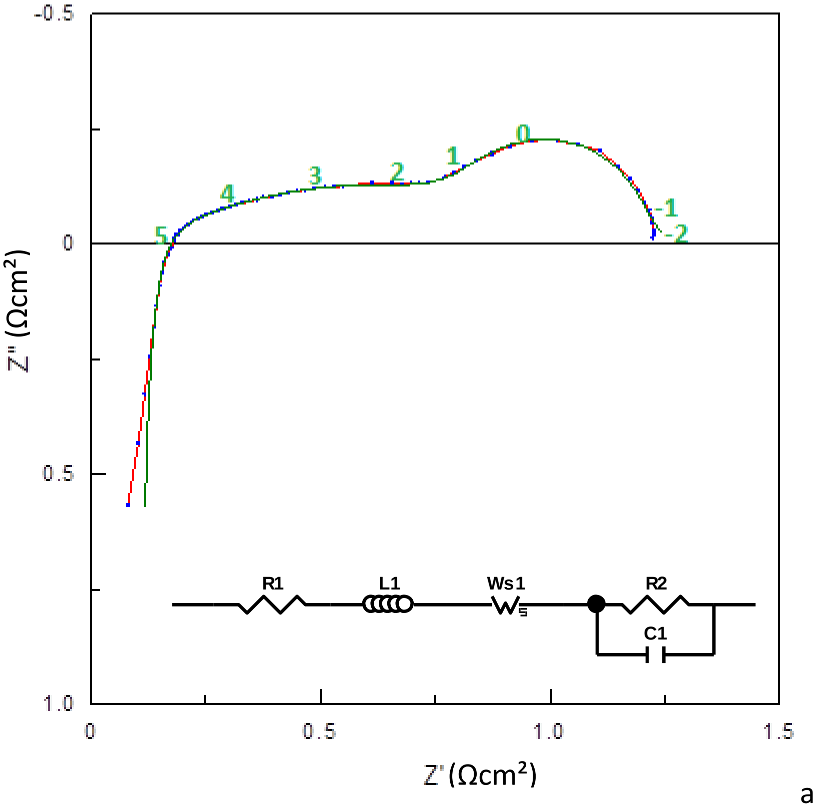

© 2014 Tous droits réservés.

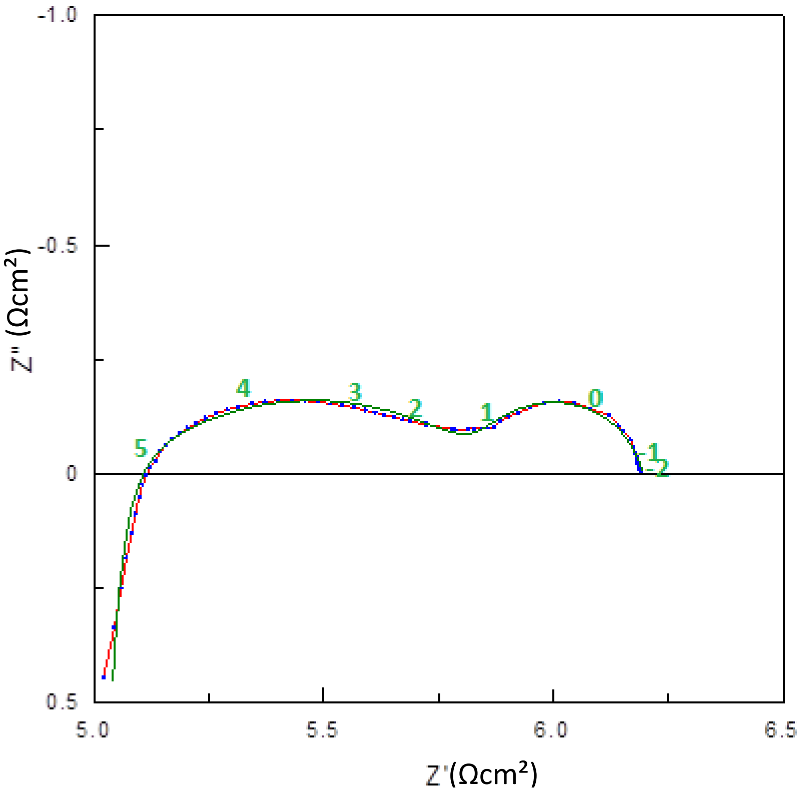

b

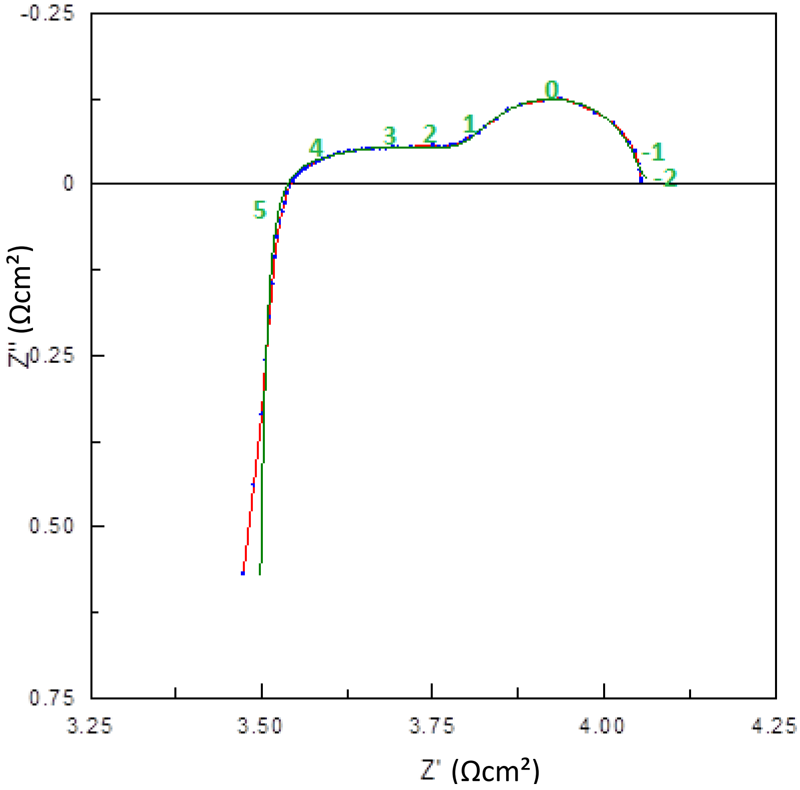

Fig. 3.3.7 - Results of the fitting on a layer-free, 2Hz-PLD coated and 3Hz-PLD coated symmetric EIS cells

The reference spectrum (50/50-CCO/CGO with no interlayer) is remarkably different from the one presented in §2.4.1, especially in the high frequency domain. This difference is rather visual than conceptual, in fact also here two main phenomena appear at two distinct

© 2014 Tous droits réservés.

frequency ranges: the electrode/electrolyte contact (high frequency) and the gas phase diffusion within the electrode (low frequency). The main difference lies in the overall magnitude of the associated phenomenon. In fact, the gas phase diffusion response is fully comparable with what reported in §2.4.3 for a 50/50-CCO/CGO cathode from raw powder. Instead, the electrode/electrolyte contact has a magnitude outstandingly lower despite the fact that the overall ASR for the reference cell in this section is higher. The higher value of the ASR should be depending on the difference in the cathode thickness (~16 µm). The difference in those two contributions' magnitude results in a spectrum with the particular shape reported in Fig. 3.3.5.

Table 3.3 - Fitting parameters of interlayer-free, 2Hz-deposited interlayer and 3Hz-deposited interlayer symmetric cells

Element	No PLD interlayer	2Hz PLD interlayer	3Hz PLD interlayer
R1	4.83 Ωcm^2 [0.1%]	4.93 Ωcm^2 [0.1%]	3.45 Ωcm^2 [0.1%]
L1	$9.5\cdot10^{-8}$ H [0.5%]	$8.0\cdot10^{-8}$ H [0.9%]	$9.4\cdot10^{-8}$ H [1.5%]
W1-R	0.95 [2.2%]	0.94 [1.3%]	0.44 [3.2%]
W1-T	0.02 [15%]	$1\cdot10^{-3}$ [5.6%]	0.01 [2.2%]
W1-P	0.10 [1.9%]	0.12 [1.7%]	0.09 [3.2%]
R2	0.30 Ωcm^2 [4.3%]	0.32 Ωcm^2 [2.4%]	0.19 Ωcm^2 [4.1%]
C1	0.53 $s\cdot C^{-1}$ [2.8%]	0.44 $s\cdot C^{-1}$ [3.4%]	0.88 $s\cdot C^{-1}$ [2.8%]
ASR (overall)	1.05 Ωcm^2	1.17 Ωcm^2	0.51 Ωcm^2
χ^2	$5.78\cdot10^{-5}$	$1.05\cdot10^{-4}$	$1.83\cdot10^{-5}$

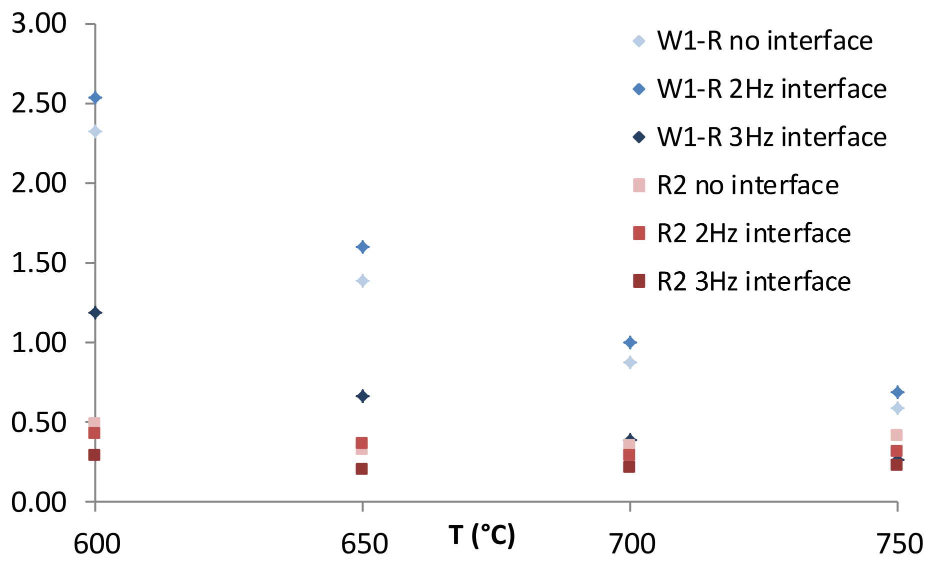

Fig. 3.3.8 - Evolution of the resistances with temperature for the interface-free, the 2Hz LASER interface and 3Hz LASER interface cells

The comparison between the results of the three studied samples (no interlayer, 2Hz interface and 3Hz interface) reveals that the aspect of the spectra is very similar, with two evident distinct contributions at low and high frequency. The former is well represented by the Warburg element, while the latter is perfectly simulated by the RC component. For the first two cells (layer-free and 2Hz deposit) the overall ASR, the values of R2 and W$_s$-R are

© 2014 Tous droits réservés.

very close for the first two cells, while they are significantly lower for the last specimen (3Hz deposited)

Also, the phase constants associated to the phenomena associated to the two part of the circuit confirm the parallelism of this new assembly to the one presented in §2.4.3. The CPE_2-T, which is associated to the surface reaction is in the order of the 10^{-1} ($0.2 \leq CPE_2\text{-}T \leq 0.9$) in the whole range of temperature (600 °C-800 °C).

Instead, the Warburg's time constant W_S-T has a very different behaviour for the three cells. In the case of the specimen without the dense CCO interface, the W_S-T is similar to the one of the 50/50-CCO/CGO powder presented in §2.4.3, with a value in the order of the 10^{-2} ($0.02 \leq W_S\text{-}T \leq 0.06$) constant over the temperature range. When switching to the assemblies featuring a 2Hz-coated interface this constant decreases by one order of magnitude. Also, its value decreases strongly with the temperature. This indicates that the effect of the dense CCO interface is to improve the electrode/electrolyte contact. On the other hand, the LASER deposition at 2Hz is not improving significantly the overall performances, as it is proved by the comparison between the W_S-R and R2 of the interface-free and the 2Hz LASER coated cells. Those two values, in fact, are similar between the two assemblies at every temperature.

When comparing the performances of the interlayer-free and the 3Hz LASER coated cells, the same behaviour of the CPE_2-T is noticed. The value of this constant is one order of magnitude lower for the cell with interface than for the one without the CCO interlayer, and it decreases strongly with the temperature.

Concerning the resistance elements (W_S-R and R2) they both are lower in magnitude (almost twice smaller for every temperature) for the cell with an interface than for the one without. It has to be noticed that the cathode's thickness is almost the same for all samples (17 µm for the interface-free and with 2 Hz LASER coating cells and 18.0 µm for the one with 3 Hz LASER coating), slightly lower from the ideal 21 µm value. Therefore, whether the overall performances may be dependent on the small difference in the cathode thickness, the contribution of the CCO interface cannot be denied for the 3 Hz coating. Further characterisations of the interlayer (TEM, ellipsometry) are envisioned to better understand the role and the morphology of the dense CCO interface.

In Table 3.3 are summarised the fitting parameters's values of the Warburg and R//C circuits for the three different assemblies. The temperature evolution of WS-R and R2 is reported in the graphic in Fig. 3.3.8, in which is displayed also the evolution of the WS-T for the three cells.

This survey reinforces the idea of a beneficial effect of the intercalation of a dense CCO film between the electrode and the electrolyte. Also, it proves another point: the microstructure of the cathode is extremely important for the fuel cell's performances.

© 2014 Tous droits réservés.

3.4.Conclusions

Here the impact of the microstructure of a CCO electrode on the electrochemical performances of a cell was confirmed. In a first step, pure CCO cathodes were deposited by two techniques. A sol-gel route, using a polymer template, was iteratively developed to create a mesoporous structure with controlled porosity, on the one hand, and the electrostatic spray deposition (ESD) was studied, on the other hand.

While the results obtained with the first technique are too preliminary to draw conclusions and additional experiments have to be carried out to optimise the microstructure, the results obtained by ESD are very promising. This technique led to a unique microstructure defined as “cauliflower” assembly. Measurement of the electrochemical properties gave an ASR value of 3.3 Ωcm² for a symmetric cell with this texture to be compared to 4.6 Ωcm² for a pure CCO screen printed sample. Undoubtedly, the superior performances of the ESD-deposited CCO (ASR: -27.5%) depend on its unique structure. Further improvements are expected by optimizing the composition and the thickness of the layer (creation of a 20 µm-thick 50/50-CCO/CGO ESD-coated cathode). This perspective may lead to outstanding results in terms of electrochemical properties of the CCO cathode.

In an attempt to reproduce the results of Hildenbrand et al. on the impact of the addition of an interfacial layer between the electrolyte and the porous electrode, a nanometric dense CCO film was intercalated between the dense CGO electrolyte and the porous 50/50-CCO/CGO electrode. The film was deposited by PLD at 2Hz or 3Hz on two different dense polished CGO pellets. Subsequently a 16 µm thick 50/50-CCO/CGO cathode was screen printed upon the dense PLD-deposited CCO layer on both faces of the two pellets to build as many symmetric cells.

Even though the 2Hz PLD deposit assembly resulted in a ASR value about the size of the compared reference, prepared in the same conditions but without interfacial layer (1.2 Ωcm² against 1.1 Ωcm²), the 3Hz deposited PLD dense CCO interlayer led to a great improvement, with the reduction of the ASR from 1.1 Ωcm² to 0.5 Ωcm² at 700°C. This outcome may be connected to a better quality of the coat at 3Hz in terms of both composition and porosity but further characterisation (pending) are required to verify this hypothesis and go further in the understanding of the impact of the interfacial layer.

Although at a preliminary stage, all these results are encouraging and open the path to improved performances for the CCO cathode.

The experiments carried out so far dealt with the unsubstituted CCO only. However, many studies proved that the doping of $Ca_3Co_4O_{9+\delta}$ on the calcium site had a very beneficial effect on the thermoelectric properties. The modification of the composition may lead to unexpected improvements of the electrochemical properties too. The investigation of the effect of the Ca-site substitution is the objective of the following chapter.

© 2014 Tous droits réservés.

4. Effect of Calcium-site doping on the electrochemical and ionic transport properties: substitution with Sr, Pb, La and Bi

In the previous chapter, it was shown how the microstructure has an important effect on the overall electrochemical performances of a SOFC cathode material. The ASR depends greatly on the many interactions occurring between the cathode elements (gas phase, interfaces, electrode/electrolyte contact, etcetera). The ohmic losses due to these interactions can be significant: for instance, switching from screen printing to EDS reduces the overall ASR by approximately 28% (on non-optimised samples). Nevertheless, also the material itself can be improved to enhance the ionic/electronic conductivity thus making it more performing.

For example, the performances of the LSM perovskites described in the introduction (§1.4.3.1) were greatly increased by partial substitution of lanthanum by other metal ions.

The same idea can be applied to the calcium cobaltite $Ca_3Co_4O_{9+\delta}$. At the earliest stages of the investigation on these materials, the research group of Yamada found that the substitution with bismuth on the calcium site increased the figure of merit of the thermoelectric CCO [108]. Little by little, a large set of substitution on the calcium site were attempted and, more recently, a lesser quantity of trials of Co-site doping were obtained. All these compounds have drained more and more attention on the cobaltite family, for some of them increased the magnetic permeation, others the figure of merit, others the ionic conductivity coefficients.

Generally speaking, for an ideal SOFC cathode, the electronic properties, given probably by the mixed valence state of cobalt in the hexagonal subsystem, should be the highest possible, as well as the ionic conductivity is required to be very fast and efficient. Those properties can be achieved and boosted by doping with elements having a different valence than Ca^{2+}. Doing so, V. Thoréton in his thesis evidenced improved oxygen ion diffusion and kinetics toward oxygen molecule dissociation at the surface of the solid when Ca^{2+} was partly substituted with Sr^2 (Table 4.1).

Table 4.1 - Oxygen ion diffusion parameters for CCO and Sr-doped CCO (10 and 20%)

Compound	T (°C)	pO_2 (mbar)	k* ($cm\cdot s^{-1}$)	D* ($cm^2\cdot s^{-1}$)
$Ca_3Co_4O_{9+\delta}$	700	230	$1.6\cdot10^{-7}$	$3.5\cdot10^{-10}$
$(Ca_{2.9}Sr_{0.1})_3Co_4O_{9+\delta}$	694	219	$3.0\cdot10^{-6}$	$4.1\cdot10^{-10}$
$(Ca_{2.8}Sr_{0.2})_3Co_4O_{9+\delta}$	694	219	$3.6\cdot10^{-6}$	$5.4\cdot10^{-10}$

The improved performances were attributed to the unit cell expansion due to the difference in ionic radius for Ca^{2+} (1.00 Å) and Sr^{2+} (1.18 Å) [136]. In addition, first electrochemical performances characterisation seemed to indicate an improvement of the ASR when calcium was partly doped with strontium.

© 2014 Tous droits réservés.

In the present work, in a first moment, the impact of the strontium substitution on the electrochemical properties was again considered. Then, to study the influence of the dopant valence and of the possible impact of dopant with lone pair, samples doped with Pb^{2+}, La^{3+} and Bi^{3+} were studied. For sake of comparison, the dopant concentration was fixed to the same value for all the samples. However, because of the low solubility of Pb in the Ca site, this concentration was fixed to a rather low value. After X-Ray diffraction analyses, electrochemical measurements were performed by EIS on screen printed symmetric cells prepared in the optimal condition defined in §2.4. Finally, coming back to the strontium doped compound, pulse isotope exchange was carried out to get information on the limiting step of the molecular oxygen's exchange at the surface of the sample.

4.1.EIS characterisation of 10 and 20%$_{molar}$ strontium-doped CCO

Cells assembled in the same fashion as described in §2.4 with $(Ca_{0.9}Sr_{0.1})_3Co_4O_{9+\delta}$ or $(Ca_{0.8}Sr_{0.2})_3Co_4O_{9+\delta}$ were characterised by Electrical Impedance Spectroscopy.

Also for these two doped cobaltites inks were prepared by blending each doped CCO with equal masses of CGO. The obtained inks, which will be henceforth called 50/50-CGO/CCO-Sr_{10} and 50/50-CGO/CCO-Sr_{20}, were screen printed on dense polished CGO pellets (ρ_{rel} >95%, roughness = 15.2 µm). Subsequently, the deposits were grafted on the support by firing under air at 500°C for 1 hour and at 900°C for 2 hours.

The analyses were carried out with a 1260 SI solartron in the temperature range 600°C – 800°C. The acquisition conditions were maintained the same as described in §2.3.2. The results of the EIS analyses are reported in Fig. 4.1.1 that displays the EIS results for $(Ca_{0.9}Sr_{0.1})_3Co_4O_{9+\delta}$ in black and $(Ca_{0.8}Sr_{0.2})_3Co_4O_{9+\delta}$ in red.

© 2014 Tous droits réservés.

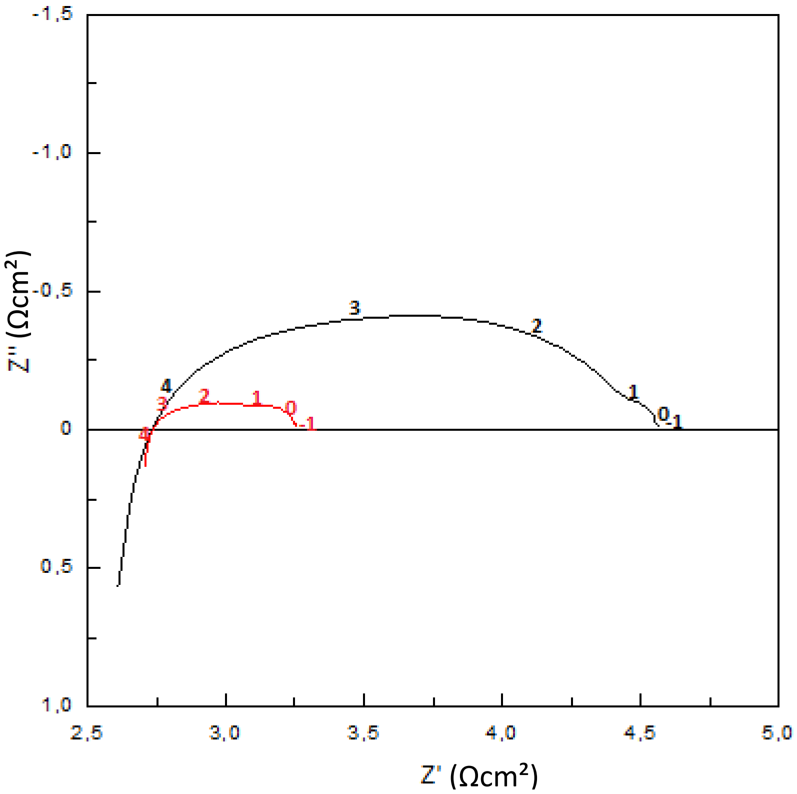

Fig. 4.1.1 - EIS results on 50/50-CGO/CCO-Sr$_{10}$ (black) and 50/50-CGO/CCO-Sr$_{20}$ (red) at 700°C

From these spectra the ASR of each compound was calculated. At 700°C, an ASR of 1.83 Ωcm² was found for the 10%$_{molar}$ strontium-doped CCO and of 0.51 Ωcm² for the 20%$_{molar}$ strontium-doped CCO composition. These two values have to be compared with the 50/50-CCO/CGO reference presented in §2.4.1 which displayed an ASR of 0.56 Ωcm².

In a preliminary study, an ASR of only 0.35 Ωcm² for a 22 µm thick electrode with 10%$_{molar}$ Sr-substitution had been obtained, thus rendering questionable the high value recorded in this case. But, as previously shown, the ASR is strongly dependent on the electrode thickness, therefore SEM was carried out on both samples to determine their thickness and morphology. The images of the side cut are reported in Fig. 4.1.2.

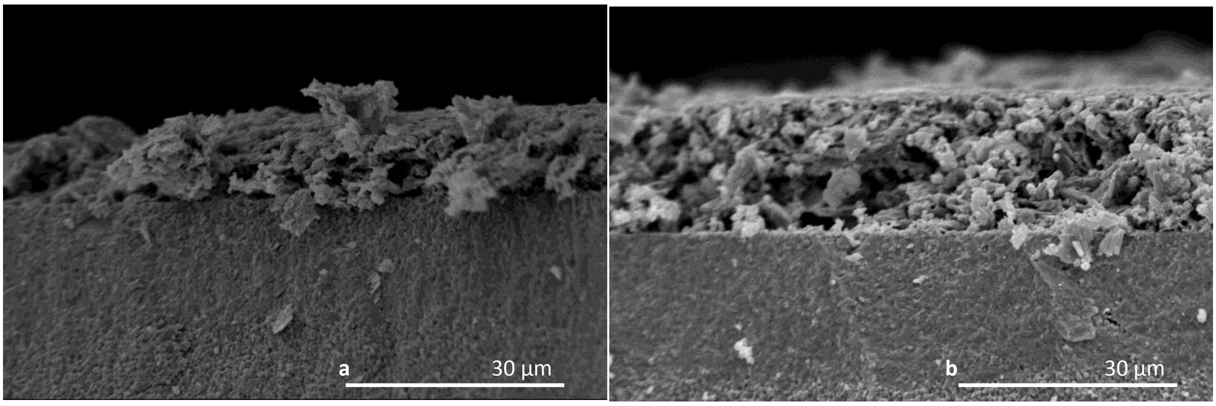

Fig. 4.1.2 - SEM micrographs of the 50/50-CCO/CGO-Sr$_{10}$ (a) and 50/50-CCO/CGO-Sr$_{20}$ (b) cathodes

A rather bad microstructure was observed for the 50/50-CGO/CCO-Sr$_{10}$ sample, moreover, its thickness was only 13 µm which explains in part the higher ASR. However, for the non-

© 2014 Tous droits réservés.

doped compound an ASR of 0.9 Ωcm² was obtained for a 13 µm thick cell. Also, the non-homogeneous microstructure of our 50/50-CGO/CCO-Sr_{10} sample is likely to be the reason for such a high ASR. At this stage, we have no explanation for such a bad microstructure and the preparation of a new cell is already planned but has not been done yet due to a lack of time.

For the 50/50-CGO/CCO-Sr_{20}, a thickness of 16 µm was measured. This remarkable divergence from the optimal value of 21 µm could already account for the limited improvement in the electrochemical performances. Nevertheless, the fact that a very slight lowering of the ASR is noticed means that, with the appropriate thickness, the doping by Sr on the Ca site of the CCO should lower this value. Impedance spectra were also fitted with software Z-View, which results are reported in Table 4.2.

Table 4.2 - Fittingresults on the 50/50-CGO/CCO-$Sr_{10/20}$ at 700°C

Element	50/50-CGO/CCO-Sr_{10}	50/50-CGO/CCO-Sr_{20}
R1	5.94 Ωcm² [0.1%]	2.62 Ωcm² [0.1%]
L1	$1.28 \cdot 10^{-6}$ [0.5%]	$1.19 \cdot 10^{-6}$ [1.1%]
W_S-R	0.21 [12.1%]	0.53 [2.4%]
W_S-T	$3 \cdot 10^{-3}$ [4.5%]	0.01 [9.6%]
W_S-P	0.49 [4.3%]	0.25 [1.7%]
R2	1.97 [1.3%]	0.11 [8.1%]
CPE_2-T	0.01 [2.1%]	0.81 [4.3%]
CPE_2-P	0.46 [0.6%]	0.91 [27.9%]
ASR	1.83 Ωcm²	0.51 Ωcm²
χ^2	$2.34 \cdot 10^{-5}$	$1.51 \cdot 10^{-5}$

Similarly to what was stated for the 50/50-CCO/CGO cathode in §2.4.3, two main phenomena can be identified: a diffusion process at high frequency, simulated by the Warburg terminus, and a surface phenomenon at low frequency which is simulated by the R//CPE component.

These two phenomena are well resolved in the time scale with time-dependent constants (W_S-T and CPE_2-T respectively) not changing significantly with the temperature. Also the phase constants (W_s-P and CPE_2-P) are mostly independent from the temperature, settling at about 0.5 for both the Warburg and the RC elements for the 50/50-CGO/CCO-Sr_{10} cathode. For 50/50-CGO/CCO-Sr_{20}, the behaviour of the time constants is again quite independent of the temperature, although their absolute value is around one order of magnitude higher than in the previous case. Also, the phase constants are remarkably different, settling at 0.25 for the Warburg's terminus and at 0.9 for the other element.

Naturally, the main difference resides in the resistance moduli which decrease accordingly with the increase in temperature, as it is typical of a thermally activated process.

© 2014 Tous droits réservés.

4.2. Influence of dopant in $(Ca_{1-x}M_x)_3Co_4O_{9+\delta}$ (M = La, Pb, Bi, Sr, x = 0.02) on the electrochemical performances and transport parameters

4.2.1. Synthesis of $(Ca_{1-x}M_x)_3Co_4O_{9+\delta}$ doped phases (M = La, Pb, Bi, Sr, x = 0.02)

With the aim to study the impact of the dopant on the electrochemical performances on the one hand and on the transport parameters on the other hand, a few dopants were studied in addition to strontium. Pb^{2+}, Bi^{3+} and La^{3+} were chosen as dopant, the former two because of their specific electronic structure which displays a lone pair and could have an influence on the oxide ion diffusion, and the last one to make comparison between Bi^{3+} and La^{3+}.

Table 4.3 - Known solid solution limits for Sr^{2+}, Pb^{2+}, Bi^{3+} and La^{3+} expressed in molar percentage $(Ca_{1-x}M_x)_3Co_4O_9$

Cation	Radius in Å (coordination)	Solid Solution phase domain	References
Sr^{2+}	1.18 (VI)	0 – 0.33	[137]
Pb^{2+}	1.19 (VI)	0 – 0.03	[138]
Bi^{3+}	1.03 (VI)	0 – 0.25	[8]
La^{3+}	1.03 (VI)	0 – 0.15	[139]

This doping ratio was fixed at x = 0.02 for $(Ca_{1-x}M_x)_3CO_4O_{9+\delta}$. It was chosen to have a homogeneity in the composition and was imposed by the low solubility limit of lead. A strontium doped compound was also prepared.

Similarly to the synthesis of non-doped CCO, the Ca-substituted compounds were prepared by solid state reaction.

The precursors sensitive to moisture were stocked in oven at 100°C ($CaCO_3$, $SrCO_3$ Merck), or under vacuum (Co_3O_4, Alfa Æsar). Other oxides (PbO, Bi_2O_3 and La_2O_3) were rather pre-treated at high temperature for hydroxyl and carbonate removal (600°C for PbO and Bi_2O_3 and 900°C for La_2O_3 overnight). The precursors were examined by X-Ray diffraction to determine their purity. For the synthesis, the protocol presented in §2.1 was followed: the precursors ($CaCO_3$, Merck, 99.0%, Co_3O_4, Alfa Æsar, 99.7% and $SrCO_3$, Aldrich, 99.9%, PbO, Riedel-den-Haën, 99.0%, Bi_2O_3, Aldrich, 99.9% or La_2O_3, Prolabo, rectapur) in stoichiometric ratio were ground by planetary milling for 5 hours in ethanol.

Then, they were dried and put into alumina crucibles. Subsequently, the powders were fired at 500°C for 1 hour to remove any trace of organic compound and at 900°C for 24/36 hours for the synthesis, with intermediate manual grinding in agate mortar every 12 hours of thermal treatment.

The synthesised powders were recovered from the oven, ground manually in an agate mortar and submitted to X-Ray powder diffraction analyses to assess their purity (§4.2.2). For the sake of simplicity, the $(Ca_{0.98}M_{0.02})_3Co_4O_{9+\delta}$ will be henceforward be abbreviatedly referred to as CCO-M_2, M being Sr, Pb, Bi or La.

© 2014 Tous droits réservés.

4.2.2. XRD powder diffraction of doped CCO

The diffractograms of Sr, Pb, Bi and La doped CCO are reported in Fig. 4.2.1 (a-d). The used starting reference was the .dif file used for assignment of non-doped CCO (see §2.1). Such reference was modified to match the x-shift of each peak due to the modification of the unit cell parameters. Already at this stage, every phase is considered to be pure as all peaks are assigned to a standard reference.

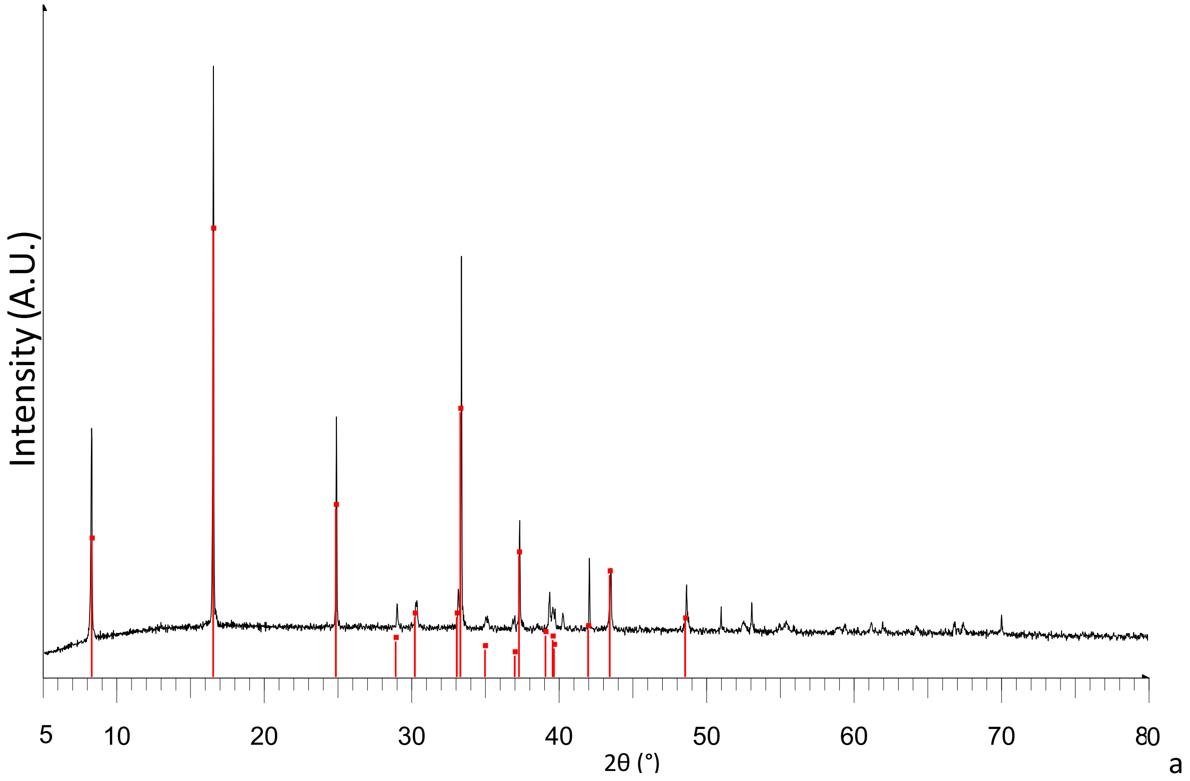

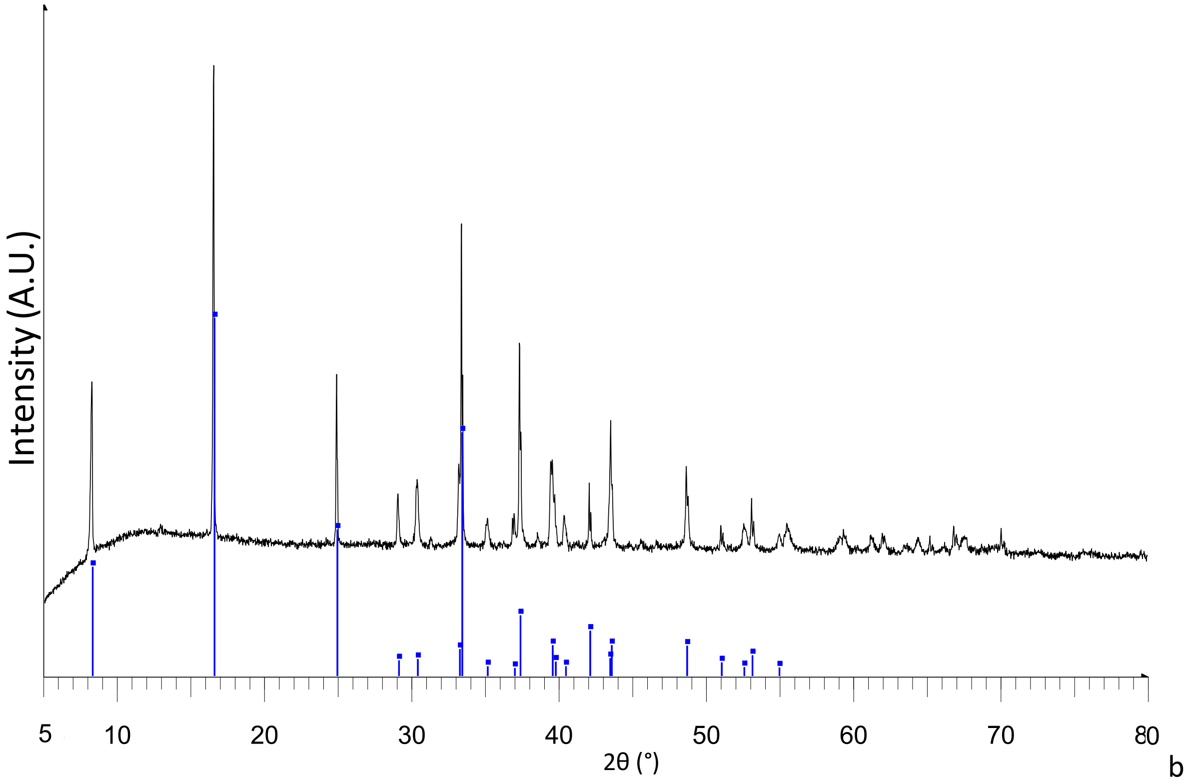

© 2014 Tous droits réservés.

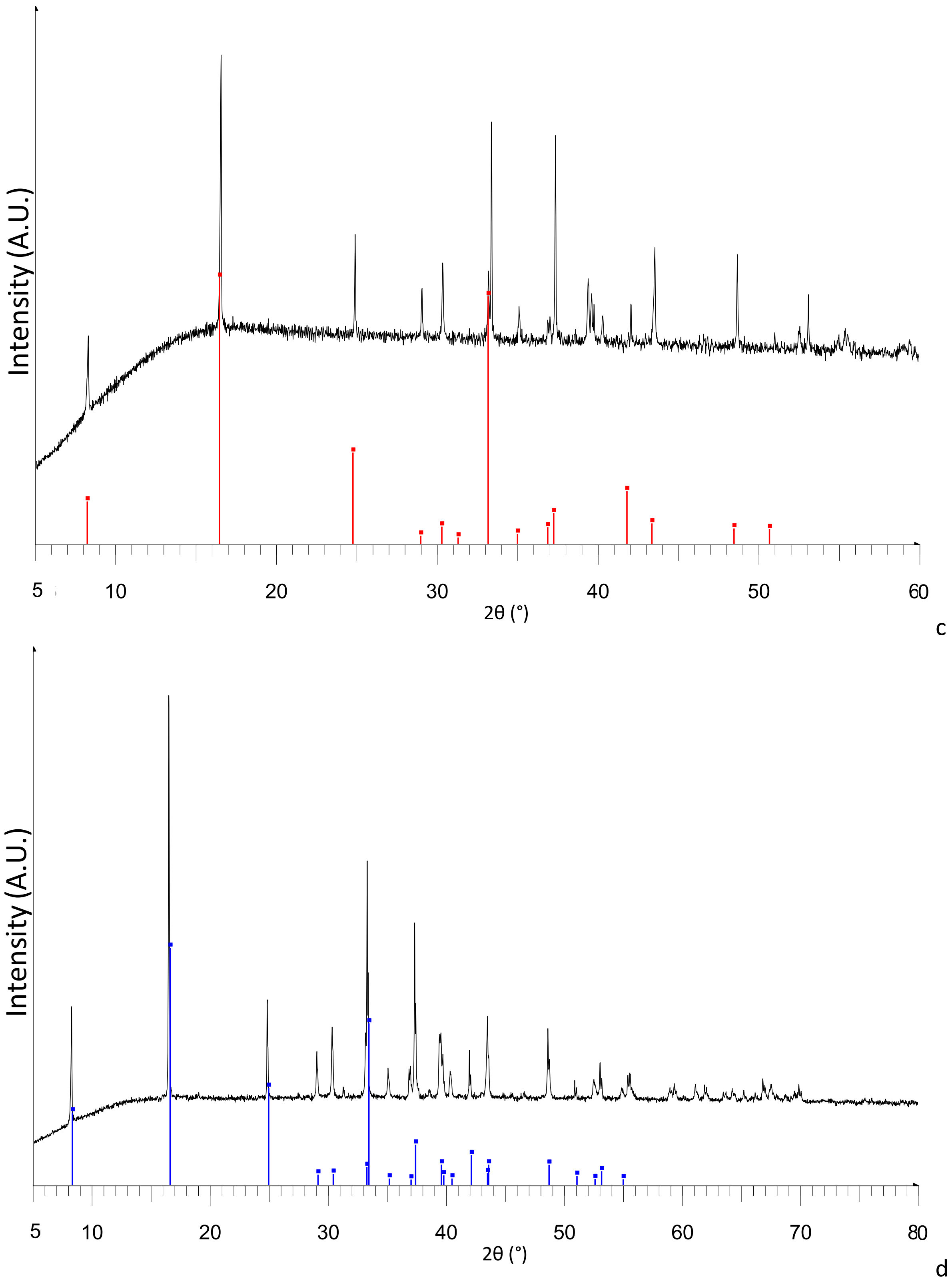

Fig. 4.2.1 - Experimental X-Rays diffraction spectra of CCO-M_2 (M = Sr (a), Pb (b), Bi (c), La (d)) compared to the .dif reference for CCO (red or blue bars)

The unit-cell parameters were also refined with the FullProf Suite (ver. 2.05, July 2011), using two different crystal domains to simulate the misfit structure.

© 2014 Tous droits réservés.

In Fig. 4.2.2 (a-d) are reported the simulated XRD spectra of $(Ca_{1-x}M_x)_3Co_4O_{9-\delta}$: the blue line at the bottom of each simulation represents the difference between the calculated (black line) and the experimental (red line) spectrum.

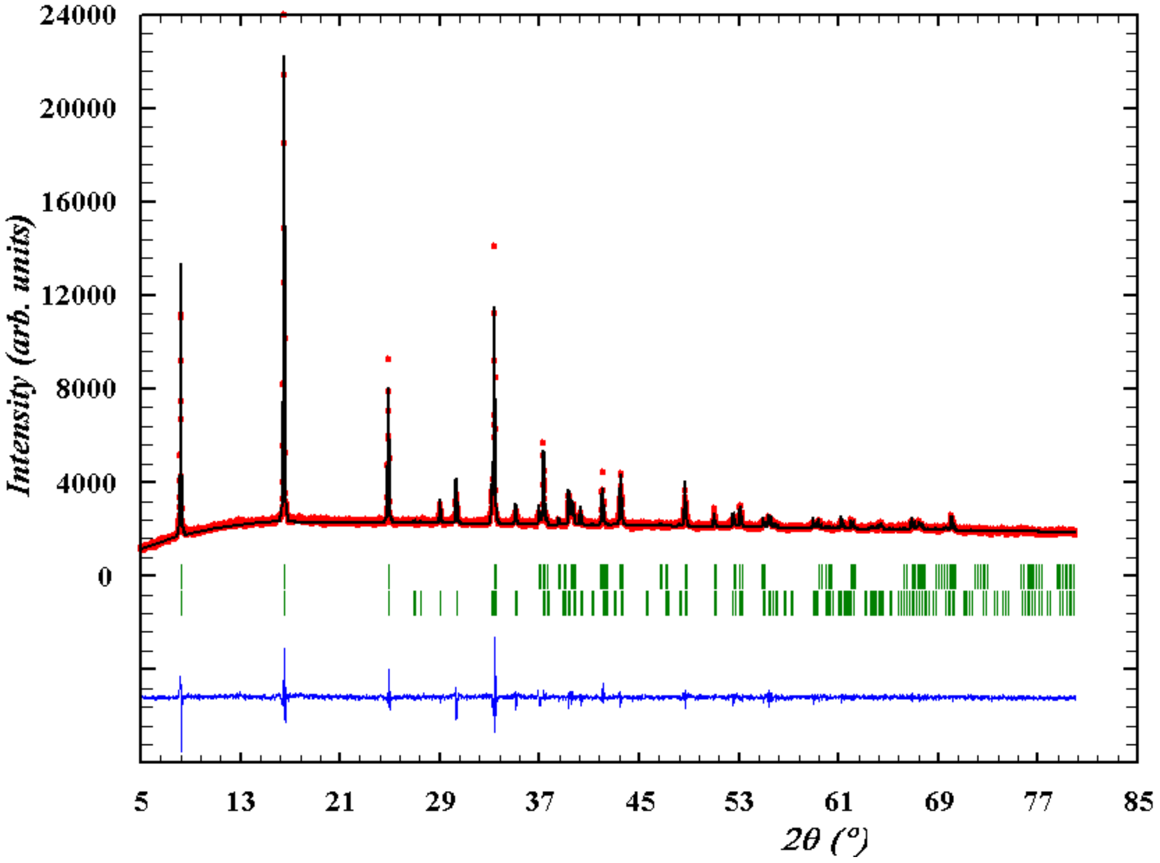

a

© 2014 Tous droits réservés.

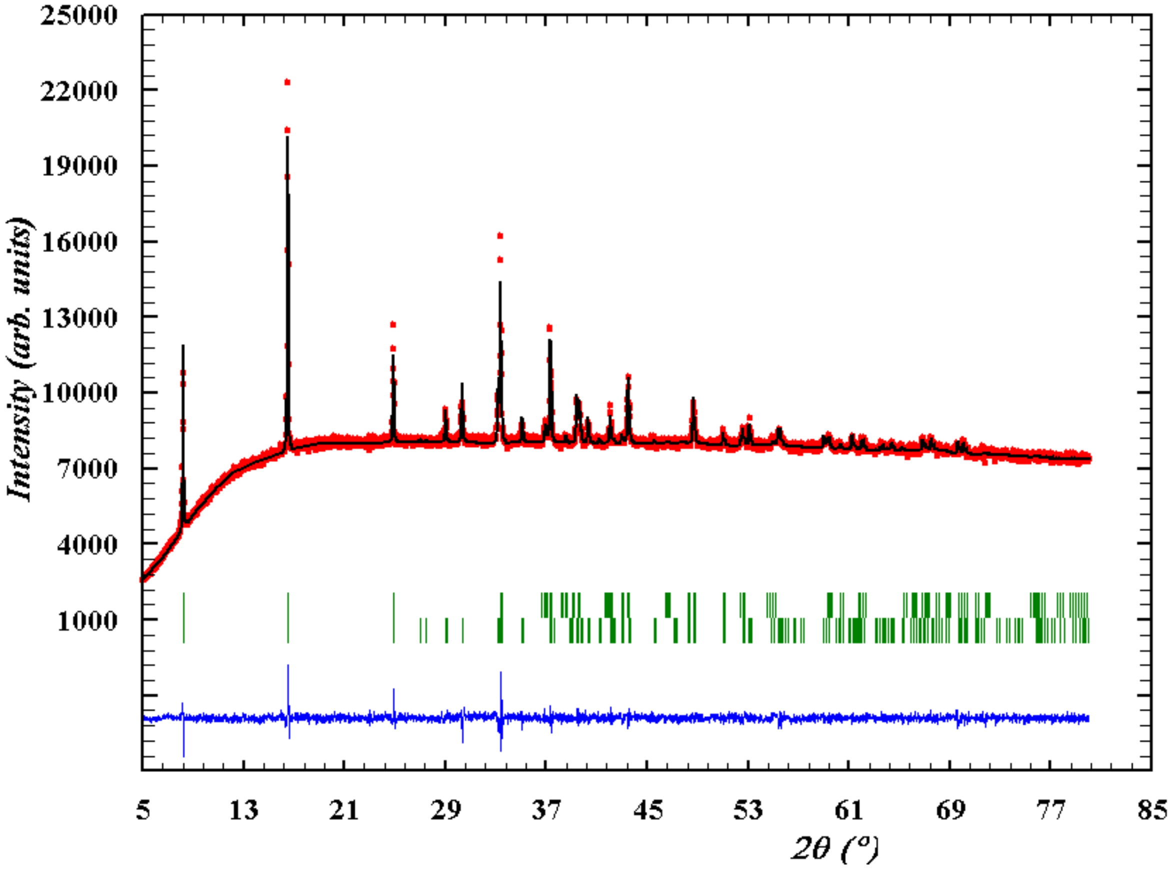

b

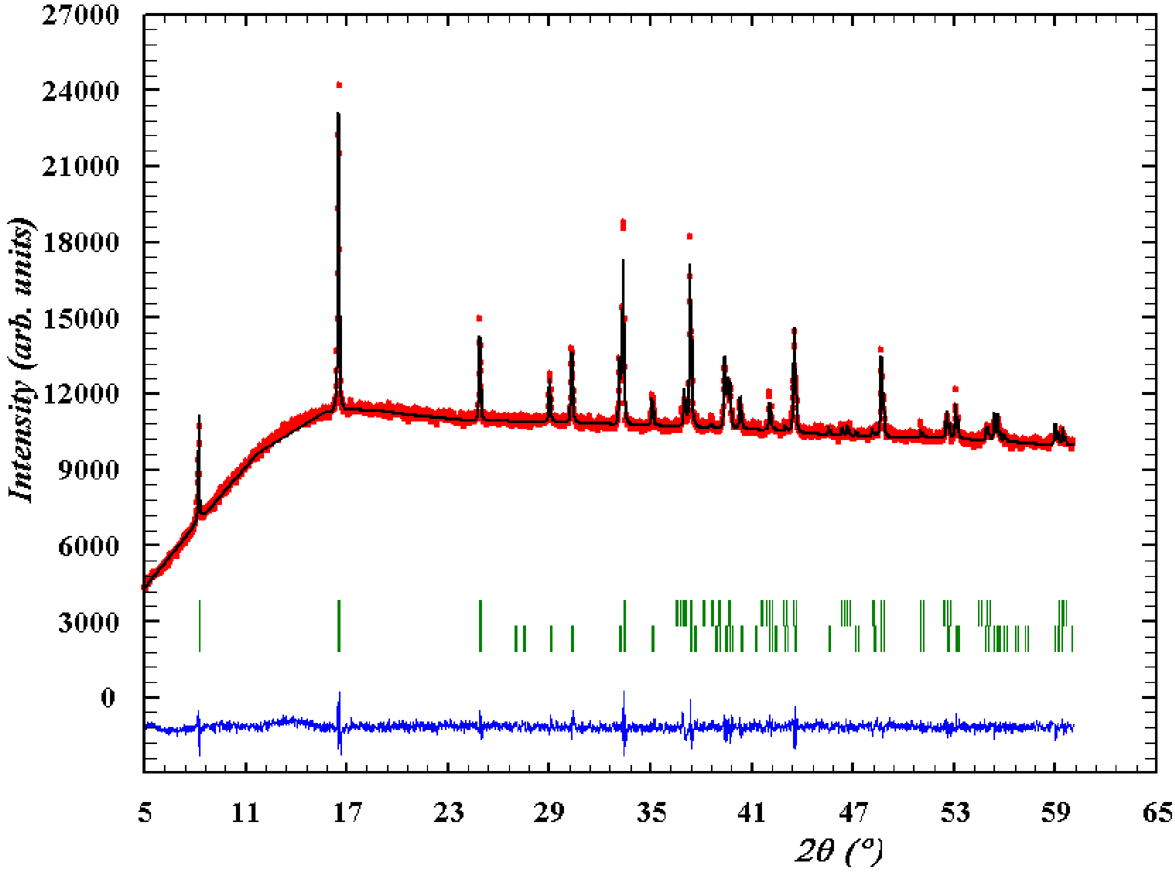

c

© 2014 Tous droits réservés.

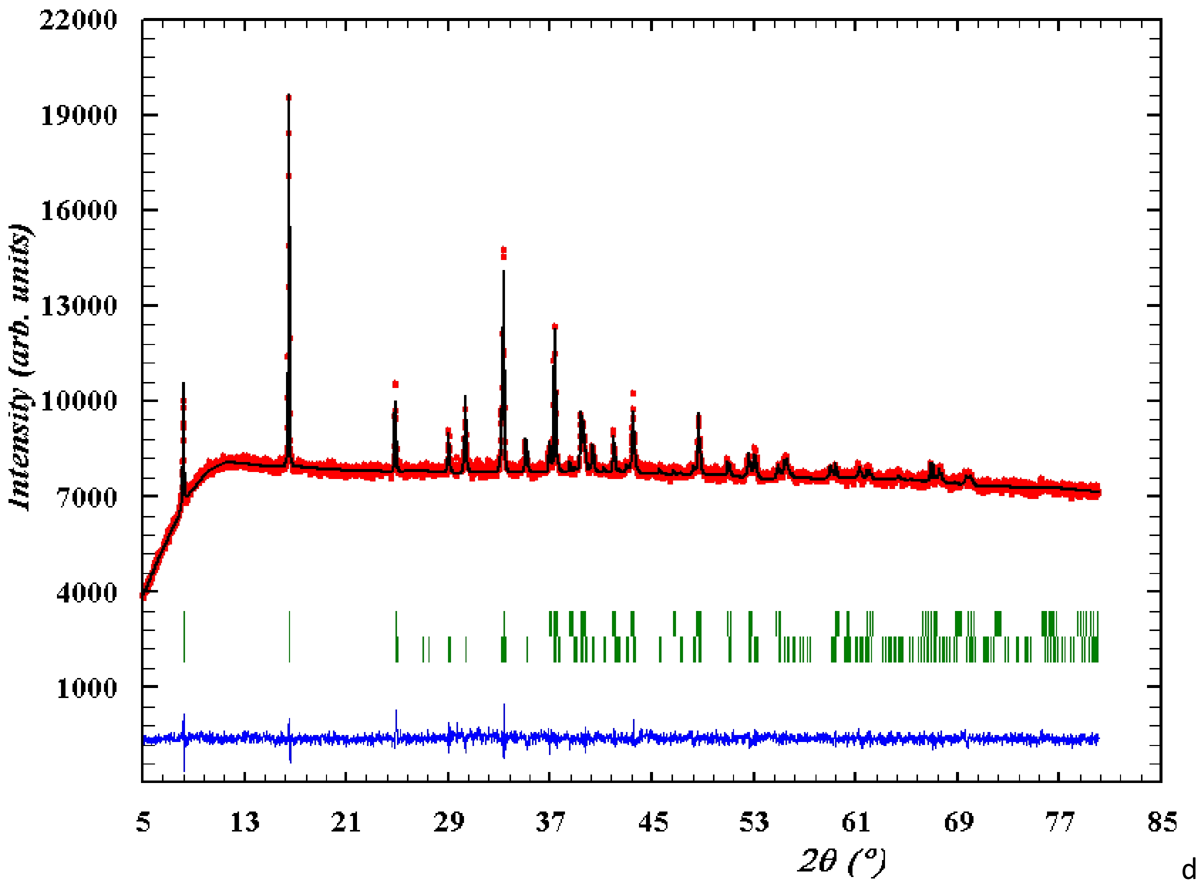

Fig. 4.2.2 - Calculated X-Rays diffraction spectra of CCO-M_2 (M = Sr (a), Pb (b), Bi (c), La (d))

As it is possible to notice, all the peaks are matching. The blue line lies within a confidence interval given by the background noise. Therefore, the assignment for each compound is confirmed and thus the purity of the compounds is verified.

Table 4.4 reports the values of the unit cell parameters (a, b_{RS}, b_{CdI2}, c, β and V) for all the doped compounds. Also, to ease comparison, the unit cell parameters of non-doped $Ca_3Co_4O_{9+\delta}$ are reported.

Table 4.4 - Unit cell parameters of doped and non-doped CCO phases

	a Å	*b*$_{RS}$ Å	*b*$_{CdI2}$ Å	*c* Å	β (°)	V (Å^3)
CCO-Sr_2	4.8313(2)	4.5760(3)	2.8201(3)	10.8433(5)	98.135(5)	237.3
CCO-Pb_2	4.8707(3)	4.5691(3)	2.854(1)	10.8550(6)	98.777(6)	238.7
CCO-Bi_2	4.8672(3)	4.5702(4)	2.865(3)	10.8581(9)	98.776(6)	238.7
CCO-La_2	4.8658(3)	4.5676(4)	2.8194(2)	10.8686(7)	98.731(6)	238.8
CCO	4.8305(4)	4.5628(4)	2.8199(2)	10.7653(6)	98.143(7)	234.9

The replacement of calcium by strontium seems to induce a distinct expansion of the cell volume. Such an expansion is well explained by the difference in the cationic radii between Ca^{2+} (1.00Å) and Sr^{2+} (1.18Å).

Likewise, the substitution of Calcium with Lead, Bismuth or Lanthanum induces an increase in the cell volume, connected to the difference of cationic radii (1.19Å for Pb^{2+}, 1.03Å for Bi^{3+}

© 2014 Tous droits réservés.

and 1.03Å for La^{3+} in contrast to 1.00Å for Ca^{2+}). For each composition, the difference is indubitable, even for such a small doping ratio.

4.2.3. Electrochemical properties: Impedance Spectroscopy

To measure the electrochemical properties of doped calcium cobaltites a symmetric cell was prepared for each composition. Starting from the raw powder of each composition, the whole set of inks was prepared by following the protocol described previously (§2.4.1).

The inks, and thenceforth the deposited cathodes, will be henceforward referred to as 50/50-CGO/CCO-M_2 with M = Sr, Pb, Bi or La.

Once those inks were obtained, they were screen printed on as many CGO pellets according to the screen printing protocol reported earlier (§2.2.3). The pellets were coated with one single layer of doped CCO on each side to produce the symmetric cells required for the EIS experiments.

The obtained pellets were then thermally treated at 500°C for 2 hours to remove any trace of organic compounds and subsequently sintered at 900°C for 1 hour to graft the electrodes on the electrolyte.

The symmetric cells obtained in this way were submitted to Electrical Impedance Spectroscopy to assess their electrochemical properties. The EIS spectra were recorded on a 1260-Solartron instrument, equipped with computer remote control and managing software.

The potential imposed on the specimen was 50 mV, the AC frequency scansion was comprised in between 1.4 MHz and 10 mHz and for each decade 8 data points were acquired. The temperature was increased from room temperature to 800°C by steps of 200°C per hour and then swept in between 600°C and 800°C by steps of 50°C with a stabilization time of 2 hours per step.

After the EIS experiments, the pellets were submitted to SEM imaging to depict the aspect of the cathode's surface. Subsequently, the pellets were fractured and the fragments were submitted to SEM imaging to record pictures of the post-analyses cathodes from the side.

The whole set of data was finally compared to the EIS results and SEM imaging of the optimised 50/50-CCO/CGO cathode. The results were related to the data from the X-Ray diffraction analysis to deduce an explanation. In Fig. 4.2.3 are reported the stacked spectra at 700°C for the 50/50-CCO/CGO symmetric cell in black, for the Sr-doped one in red, for the Pb-doped one in blue, for the Bi-doped one in green and for the La-doped one in ochre. These results were further exploited and fitted by calculations performed on Z-View. The results and interpretations are discussed in §4.2.3.1.

© 2014 Tous droits réservés.

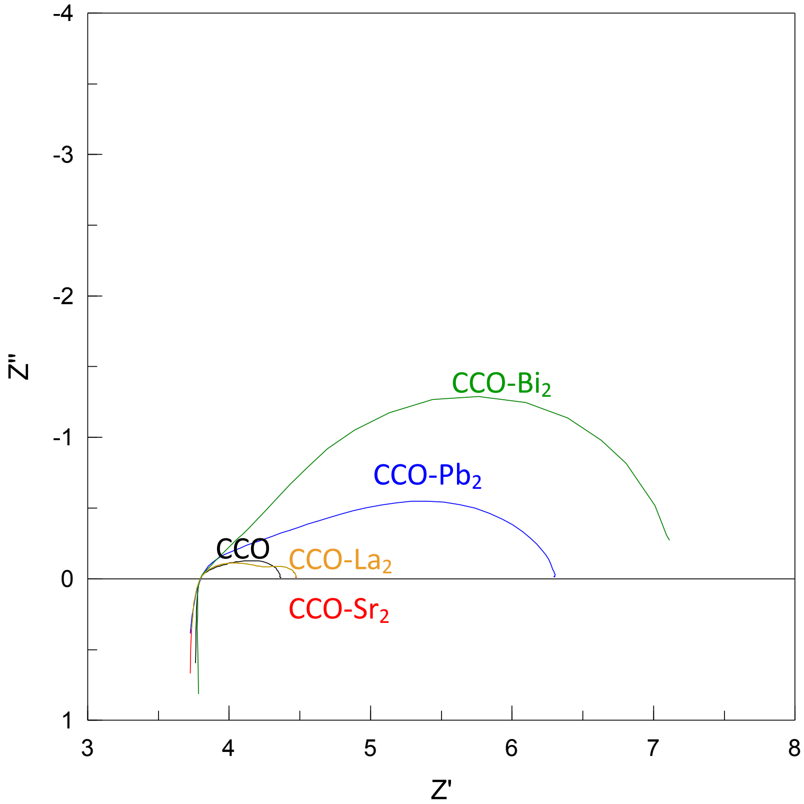

Fig. 4.2.3 - Stacked EIS spectra at 700°C for the doped and non-doped 50/50-CGO/CCO-M cathodes

4.2.3.1. EIS experiments on $(Ca_{0.98}M_{0.02})_3Co_4O_{9+\delta}$ (M = Sr, Pb, Bi, La) symmetric cells

As previously mentioned (§4.2.3) the symmetric cells prepared by screen printing were analysed by EIS to determine their electrochemical properties.

The results of the analyses are reported in Fig. 4.2.4 which shows the stacked impedance spectra at different temperatures for of 50/50-CGO/CCO-Sr$_2$ (a), 50/50-CGO/CCO-Pb$_2$ (b), 50/50-CGO/CCO-Bi$_2$ (c), and 50/50-CGO/CCO-La$_2$ (d). In black are the spectra at 600°C, in red at 700°C and in blue at 800°C. For each composition the global and zoomed view is provided.

The zero-shift and the overall aspect of each specimen are completely different from one to another although, for the sake of clearness, a correction was applied to the spectra in order to rescale them all.

© 2014 Tous droits réservés.

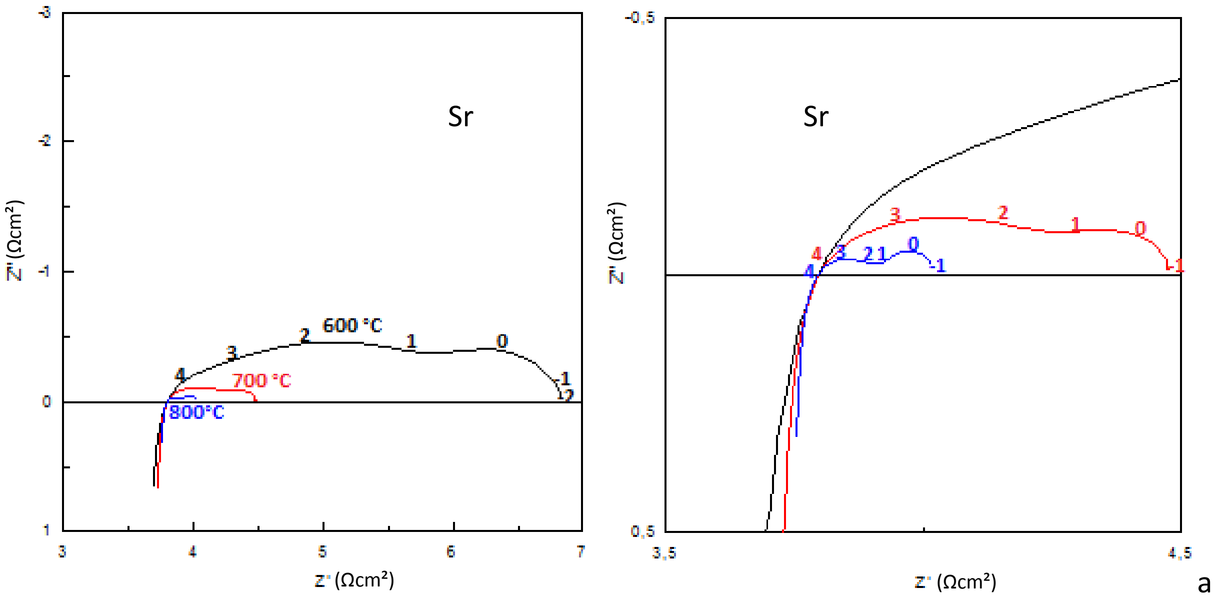

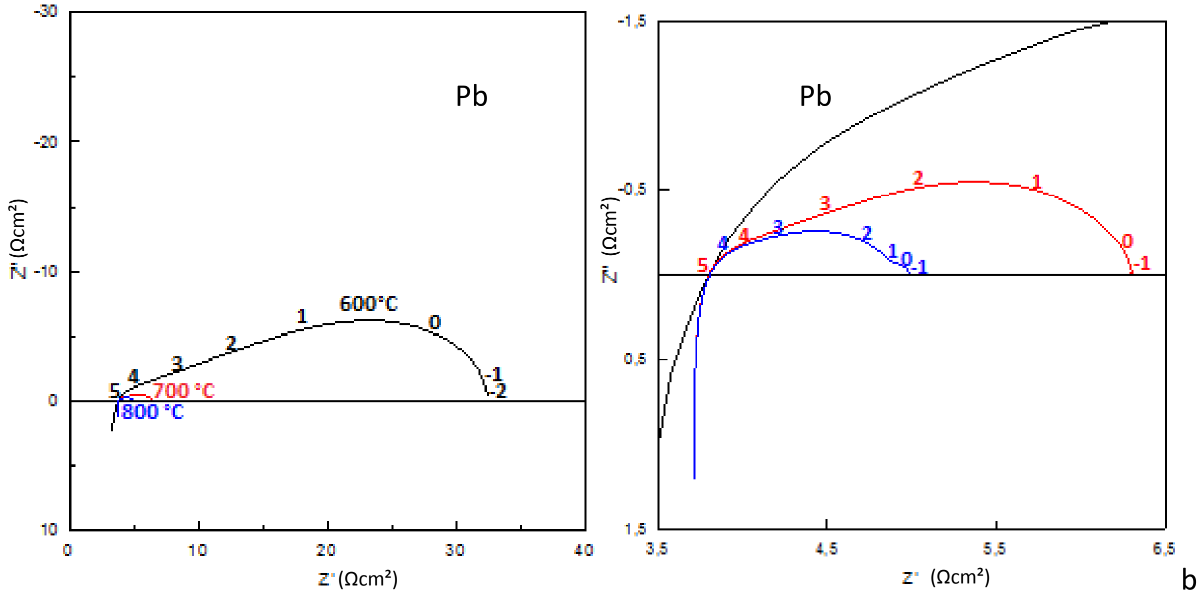

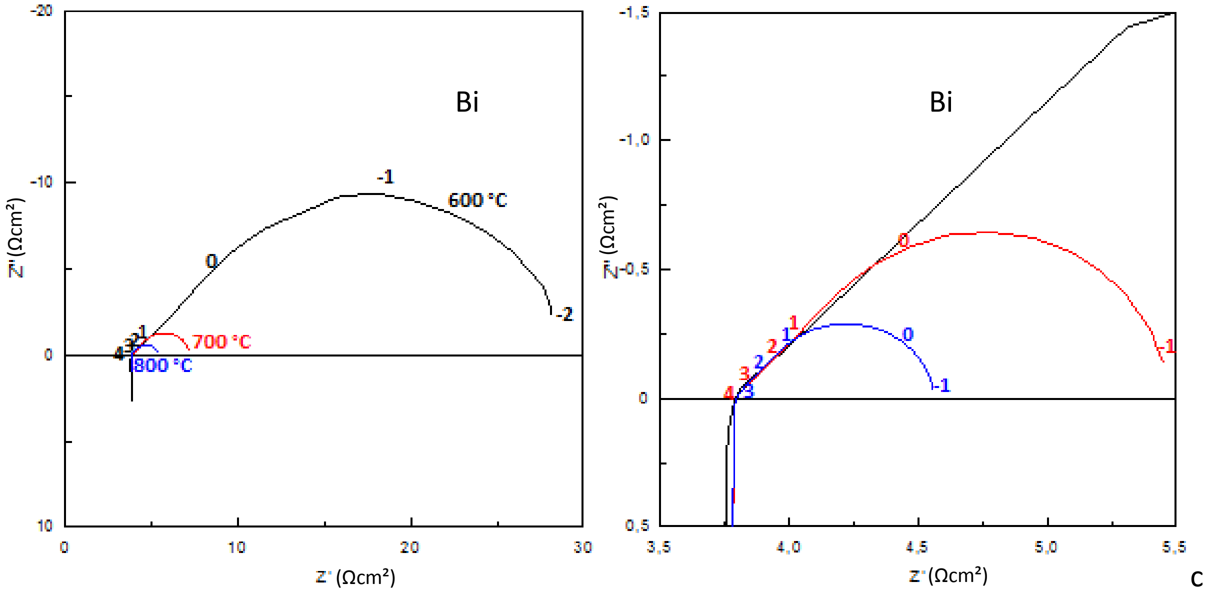

© 2014 Tous droits réservés.

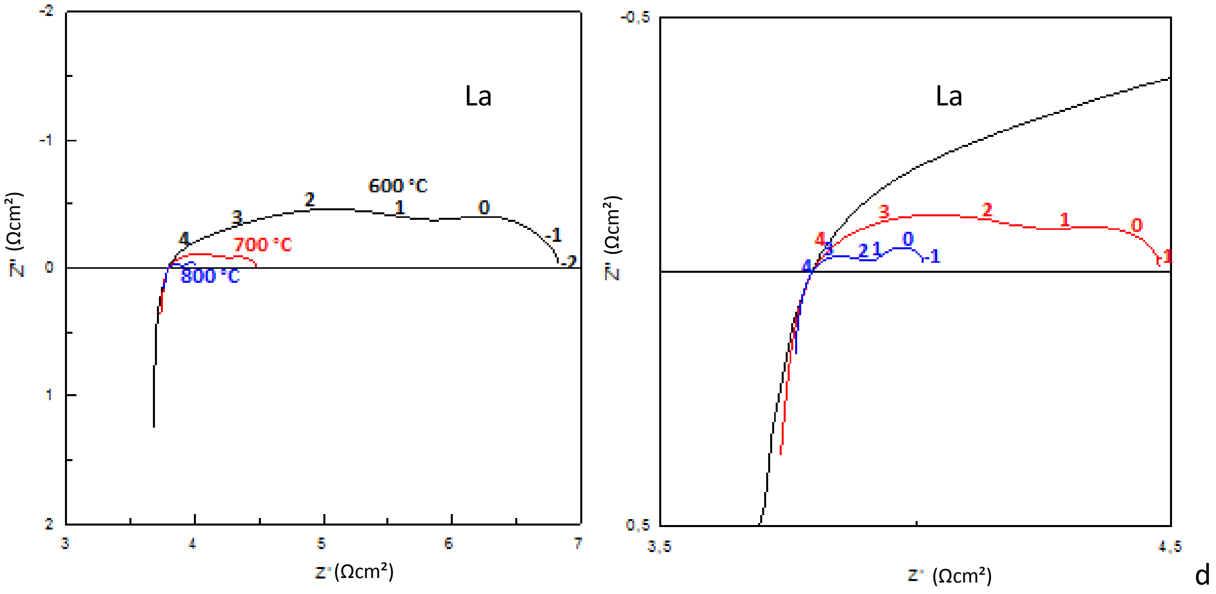

Fig. 4.2.4 - Stacked spectra at 600, 700 and 800°C of 50/50-CGO/CCO-M_2 (M = Sr (a), Pb (b), Bi (c), La (c))

The circles reported in the spectra feature few distinctive characteristics typical of the composite 50/50-CCO/CGO cathode: the presence of two contributions, one at high frequency (typically the Warburg) and another at low frequency usually belonging to the RC element.

If for strontium and lanthanum the two contributions are quite well resolved, for lead they are coalesced into one big circle only. Bismuth has an even more intense effect, with the low frequency contribution greatly increasing and incorporating the high frequency response.

The total ASR of these samples is reported in Table 4.5, in which is reported also the ASR of an optimised 50/50-CCO/CGO cathode for comparison.

Successively, the spectra were fitted with the equivalent circuit shown in Fig. 2.4.8 and the values of the Warburg and RC components were calculated. Those values are reported in Table 4.5 where are also reported the W, R and CPE of 50/50-CCO/CGO to ease comparison.

The results of the simulation and the corresponding measured spectrum are reported in Fig. 4.2.5-a (50/50-CGO/CCO-Sr_2), b (50/50-CGO/CCO-Pb_2), c (50/50-CGO/CCO-Bi_2) and d (50/50-CGO/CCO-La_2).

The black solid lines are the experimental plots, while the red solid lines outline the result of the fitting simulations. The two plots are very close to each other for every composition, which indicates that the fitting is very good in comparison to the experimental data.

© 2014 Tous droits réservés.

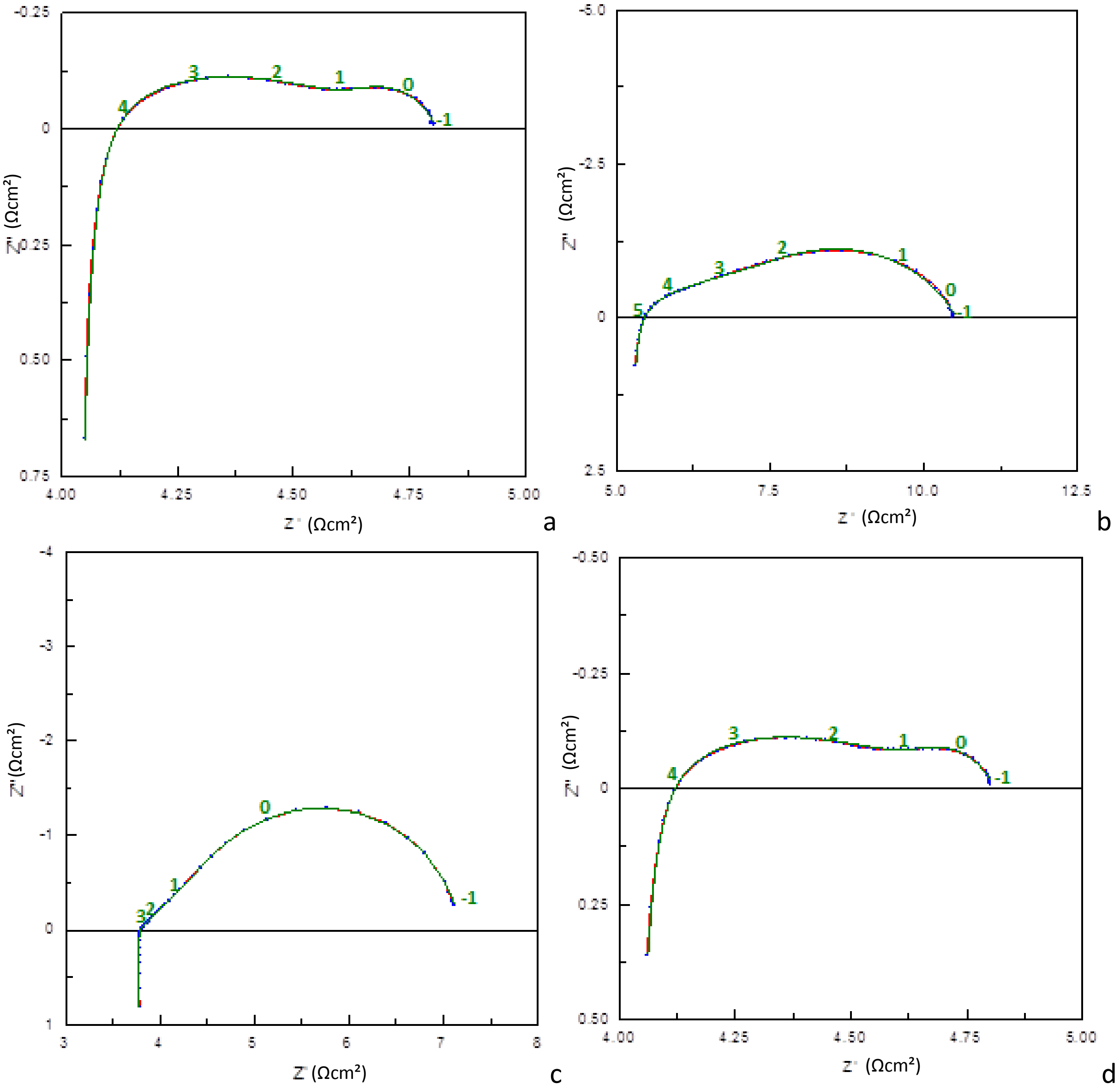

Fig. 4.2.5 - EIS experimental and simulated spectra of 50/50-CGO/CCO-M$_2$ cathodes (M = Sr (a), Pb (b), Bi (c), La (d))

Table 4.5 – Fitting parameters and ASR values for doped and non-doped CCO screen printed cathodes at 700°C

Element	50/50-CGO/CCO-Sr$_2$	50/50-CGO/CCO-Pb$_2$	50/50-CGO/CCO-Bi$_2$	50/50-CGO/CCO-La$_2$	50/50-CGO/CCO
R1	4.00 Ωcm²	5.15 Ωcm²	3.77 Ωcm²	4.00 Ωcm²	2.88 Ωcm²
L1	$6.0\cdot10^{-7}$ H	$4.3\cdot10^{-7}$ H	$7.1\cdot10^{-7}$ H	$6.1\cdot10^{-7}$ H	$1.1\cdot10^{-6}$ H
W_s-R	0.16	3.74	0.61	0.16	0.49
W_s-T	0.27	0.03	0.05	0.28	0.02
W_s-P	0.46	0.35	0.39	0.45	0.28
R2	0.65 Ωcm²	1.65 Ωcm²	2.80 Ωcm²	0.65 Ωcm²	0.27 Ωcm²
CPE_2-T	0.05	0.01	0.10	0.05	0.49
CPE_2-P	0.41	0.44	0.92	0.41	0.88
ASR	0.70 Ωcm²	1.44 Ωcm²	1.56 Ωcm²	0.68 Ωcm²	0.56 Ωcm²
χ^2	$1.98\cdot10^{-5}$	$9.57\cdot10^{-5}$	$1.07\cdot10^{-4}$	$2.34\cdot10^{-5}$	$1.38\cdot10^{-5}$

© 2014 Tous droits réservés.

The first remarkable conclusion is that in this case all the dopants have quite a negative effect on the cathode ASR. The increase of this parameter varies widely for the different doped phases. For instance, strontium and lanthanum substitution have a close result to each other as well as lead and bismuth doping, but the two couples are very far from each other.

When switching to relative values (percentage) the influences are quite remarkable for any doped phase. In fact for 50/50-CGO/CCO-Sr_2 and 50/50-CGO/CCO-La_2 the increase is equal to +20-25% (respectively), while for 50/50-CGO/CCO-Pb_2 and 50/50-CGO/CCO-Bi_2 the augment reaches +155-180% (respectively).

The interpretation of the fitting parameters gives a different perspective on the whole picture: the RC elements, noteworthy R2, CPE_2-T and CPE_2-P, are mirroring the trend described by the ASR values, with the R2 for bismuth and lead much higher than for strontium and lanthanum which have an R2 twice bigger than the non-doped phase. The CPE_2-P values, however, already mark an exception as they are close in size for Sr, Pb and La and they match exactly the reference 50/50-CCO/CGO.

Finally, the CPE_2-T's trend is very surprising as its values are outstandingly lower for the doped phases, in particular for lead, than for the parent compound. This sort of anomaly may be explained by the fact that the doping may induce a faster charge transfer or improve the contact phenomena.

Concerning the contribution of the overall Warburg element, a very particular trend is noticed, dissimilar from any other one. The W_S-R values are remarkably smaller for the strontium and lanthanum doped phases (three times smaller than the parent compound) but then the W_S-R increases dramatically for lead (0.61 vs 0.49) and even more for bismuth (3.74).

Even if it is true that the Warburg and the RC responses are independent from each other, the results of the fitting for the doped phases are nevertheless surprising. Although it would be difficult at this stage to draw a conclusion, it can anyway be stated that the general trend of the doped compositions is towards a worsening of the electrochemical properties, while the interpretation of the contributions and of the fitting results remain still ambiguous and difficult.

4.2.3.2. Post analysis of the $(Ca_{0.98}M_{0.02})_3Co_4O_{9+\delta}$ cathodes

Similarly to what was done for the optimised 50/50-CCO/CGO cathodes, the samples were carefully recovered after EIS analyses for evaluating their aspect after the analyses' thermal cycles. By the light of what was said in §3, the effect of the microstructure on the different cathodes has to be evaluated.

© 2014 Tous droits réservés.

In order to acquire detailed information on the CCO doped cathodes, SEM imaging was performed on both the surface and the side cut of each sample. The images were recorded on a Hitachi N3400 scanning electronic microscope.

The corresponding images are given in Fig. 4.2.6 for the Sr-doped cathode. Similarly, in Fig. 4.2.7, Fig. 4.2.8 and Fig. 4.2.9 are reported the surface images (a-c) and side cut (d) of the Pb-doped, Bi-doped and La-doped cathodes, respectively.

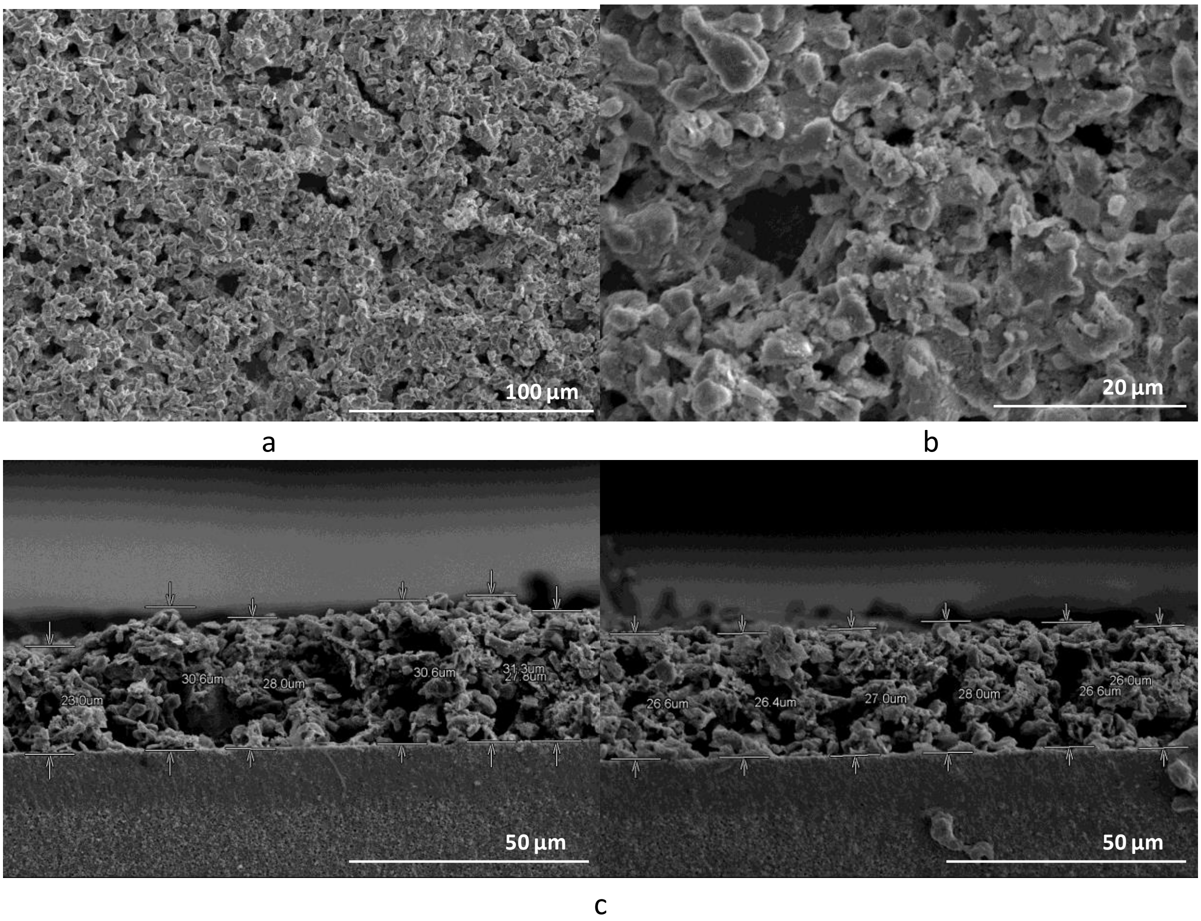

Fig. 4.2.6 - SEM images of the surface (500X a, 200Xb) and side cut (c, 1000X) of the 50/50-CGO/CCO-Sr_2 cathode

© 2014 Tous droits réservés.

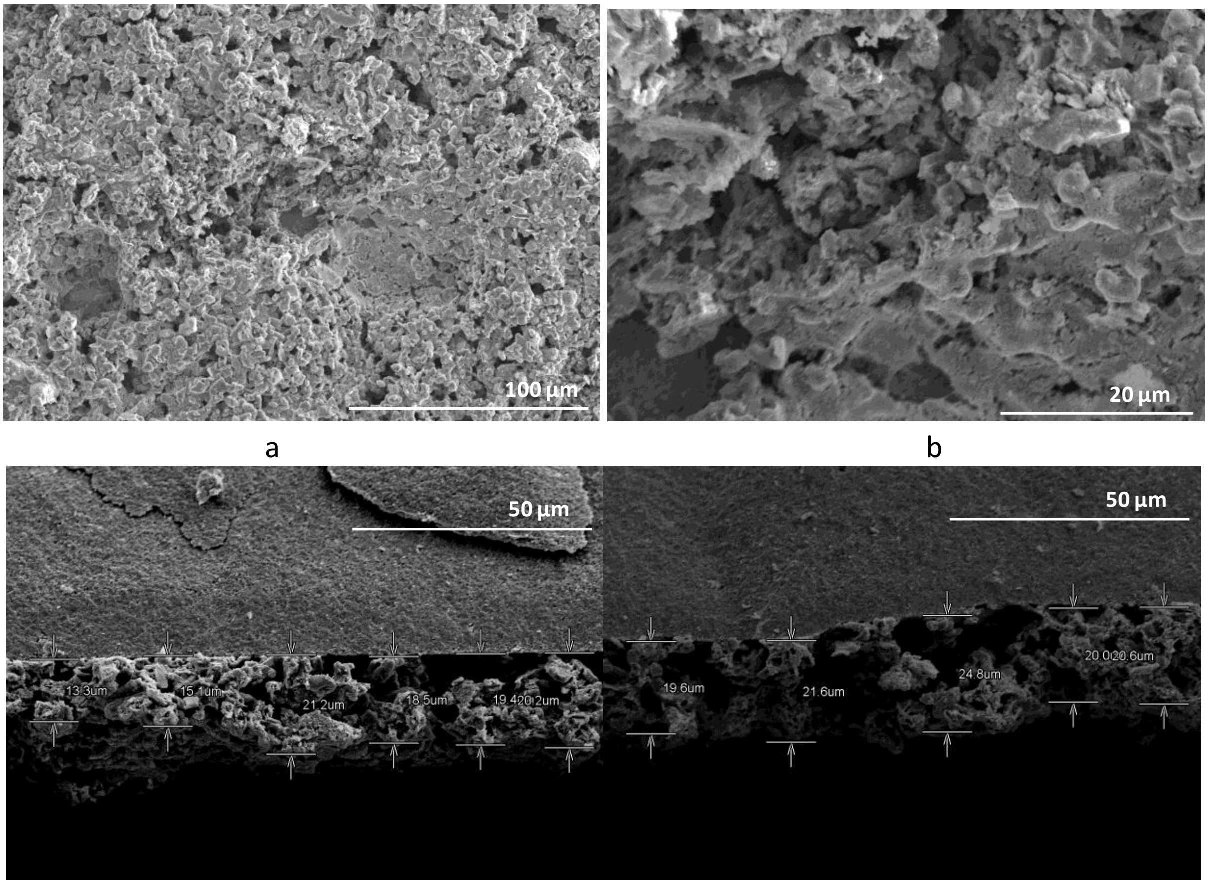

a

b

c

Fig. 4.2.7 - SEM images of the surface (500X a, 200Xb) and side cut (c, 1000X) of the 50/50-CGO/CCO-Pb_2 cathode

© 2014 Tous droits réservés.

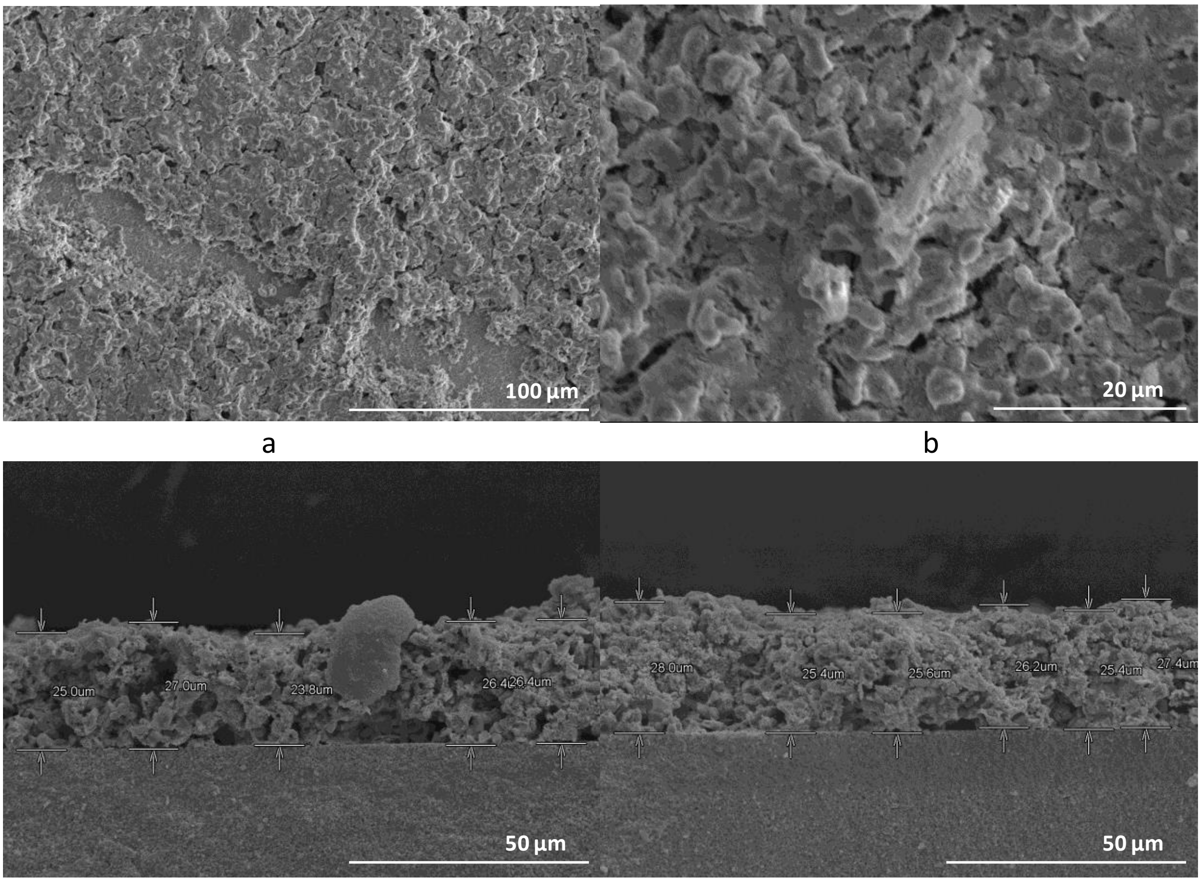

a

b

c

Fig. 4.2.8 - SEM images of the surface (500X a, 200Xb) and side cut (c, 1000X) of the 50/50-CGO/CCO-Bi_2 cathode

© 2014 Tous droits réservés.

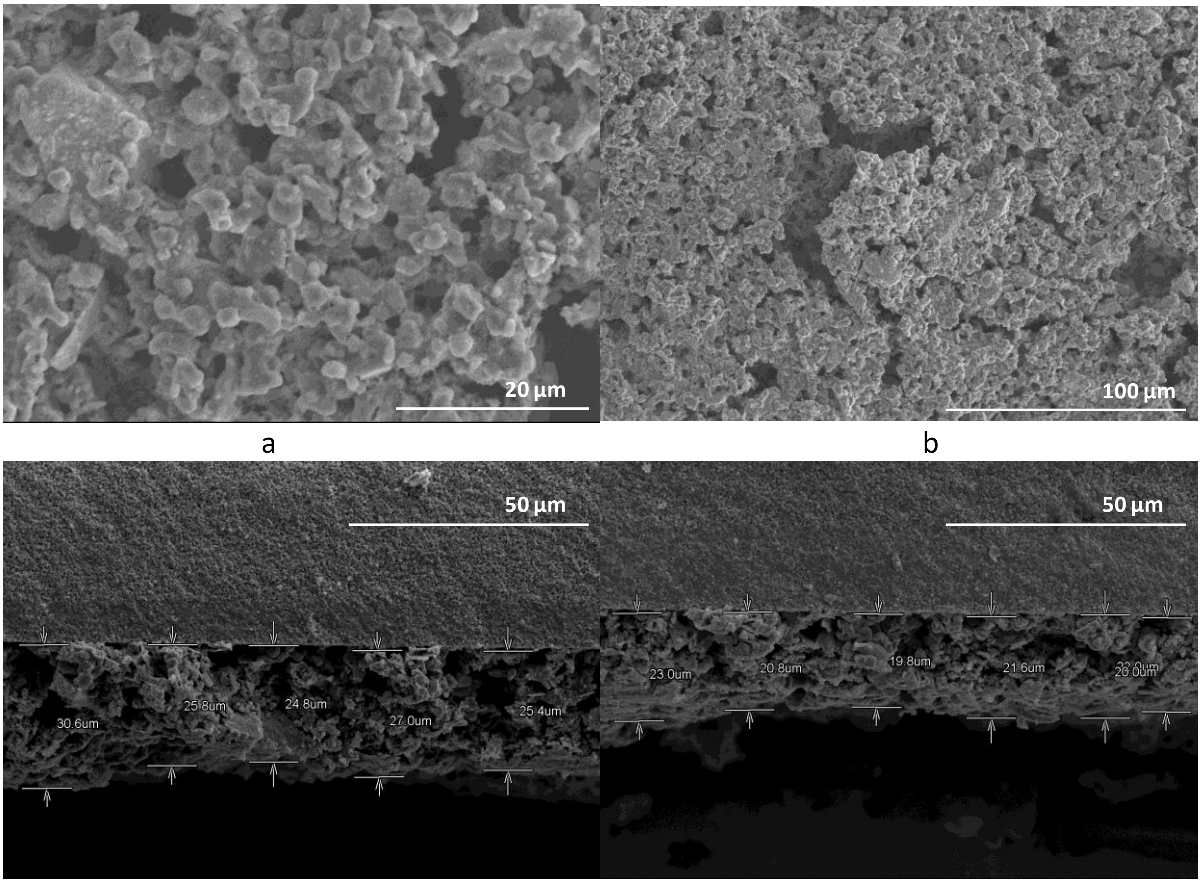

a

b

c

Fig. 4.2.9 - SEM images of the surface (500X a, 200Xb) and side cut (c, 1000X) of the 50/50-CGO/CCO-La$_2$ cathode

It is shown that the degradation is not serious on the analysed surface and that the thermal cycling of the cathode represents neither a serious issue nor causes fast ageing.

Also, from the side cut SEM images of the cathode, it can be told that the microstructure of the cathode is very well matching the one of a 50/50-CCO/CGO screen printed cathode. The porosity is casual and no major organisation is displayed. The deposit appears to be quite well grafted on the support, which is also confirmed by the experimental procedure: when removing the pellet from the analysis' rig, the cathode kept stable at its place.

Another parameter that can be retrieved from the side-cut SEM images of the 50/50-CGO/CCO-Sr$_2$ cathode is the layer's thickness. The average thickness of the deposit is 26.8 µm, which is only about 5 µm higher (+21%) than the optimum one. Even though the difference may be remarkable in percentage, the absolute value is not so great. Not only, but the difference is not disqualifying as the increase in the cathode thickness above 21 µm does not result in a major augmentation of the reference ASR (Fig. 2.3.6-a, b).

By extrapolating the influence of the increased 50/50-CGO/CCO-Sr$_2$ cathode's thickness, an increase by 4% of the ASR would be expected. The fact that experimentally the ASR is 0.70 Ωcm² against 0.56 Ωcm² (+25%) means that this effect is not given by the layer's thickness only.

© 2014 Tous droits réservés.

Another factor could be the blend composition. Once again the inks were prepared with a blend of 50%$_{w/w}$ CCO-M$_2$ and 50%$_{w/w}$ CGO, even though the optimum composition may be different. Lastly, the effect of the substitution could just negatively affect the electrochemical performances of the calcium cobaltite because of microscopic effect (oxygen vacancies filling, steric hindrance, differential charge balance with consequent loss of mixed cobalt valence, etcetera).

Indeed the overall effect of the dopant on the calcium cobaltites' electrochemical properties is quite negative. But whether this depends on the materials themselves or on a degradation of the cathodes is still being debated.

The surprisingly bad performances of the doped compounds are not easily understandable: the comparison of the doped and non-doped microstructure does not reveal any remarkable difference. Neither the difference in thickness, which in some of the cases is negligible, could explain the increase of the overall ASR of the cathodes.

In order to investigate further, post-EIS X-Ray diffraction was also carried out as well as EDS on both faces. As shown in Fig. 4.2.10, no major modifications of the X-Ray diffractograms was to be noticed, with the exception of bismuth for which the background level was higher.

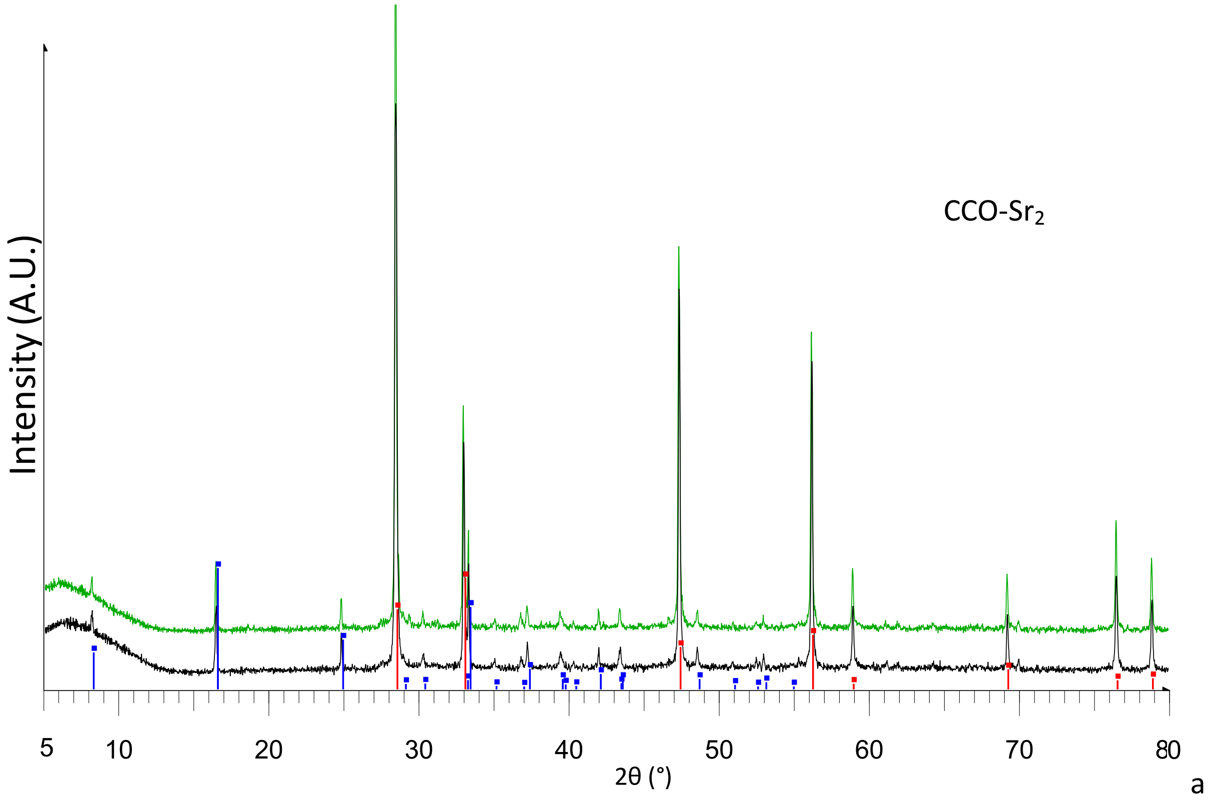

© 2014 Tous droits réservés.

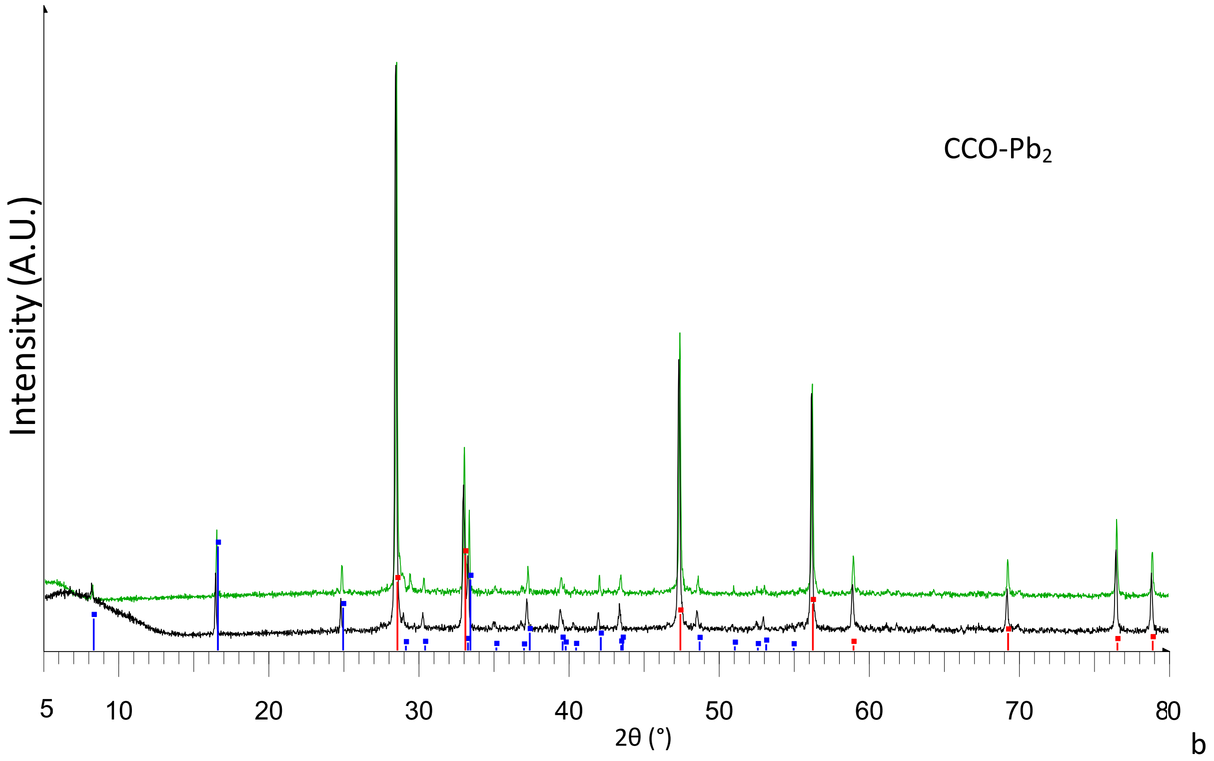

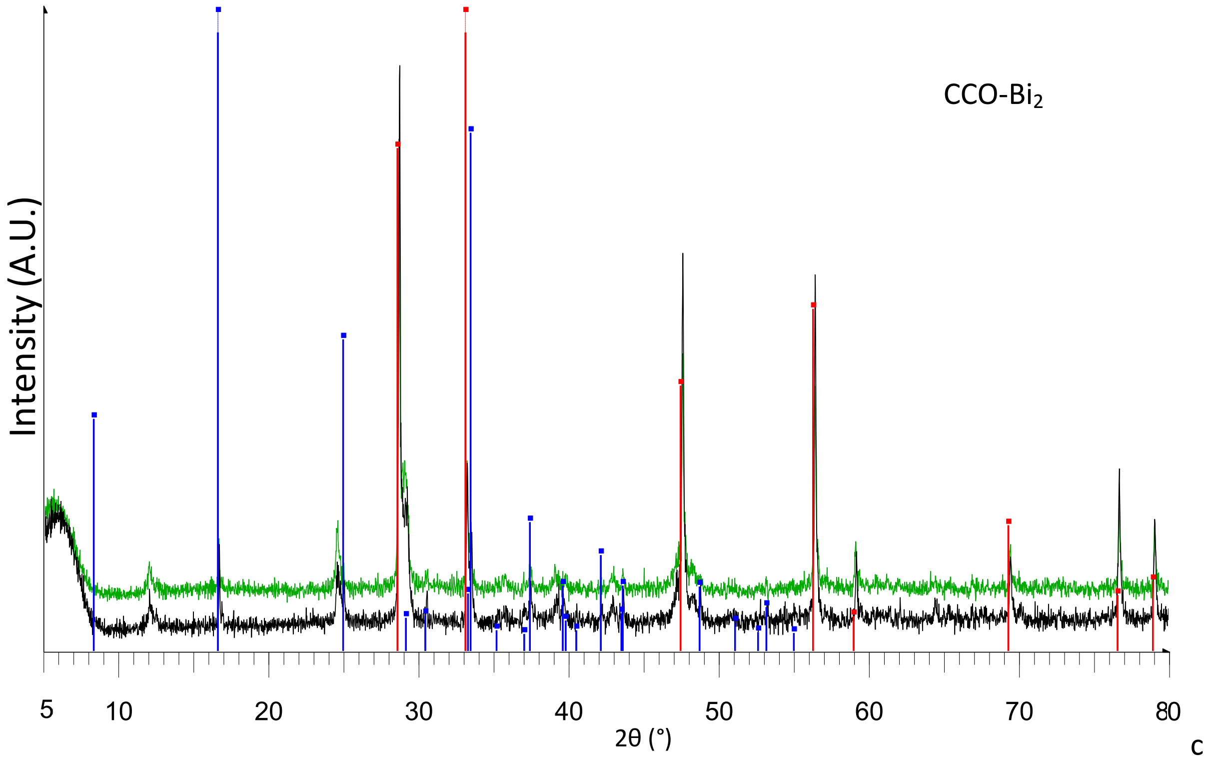

© 2014 Tous droits réservés.

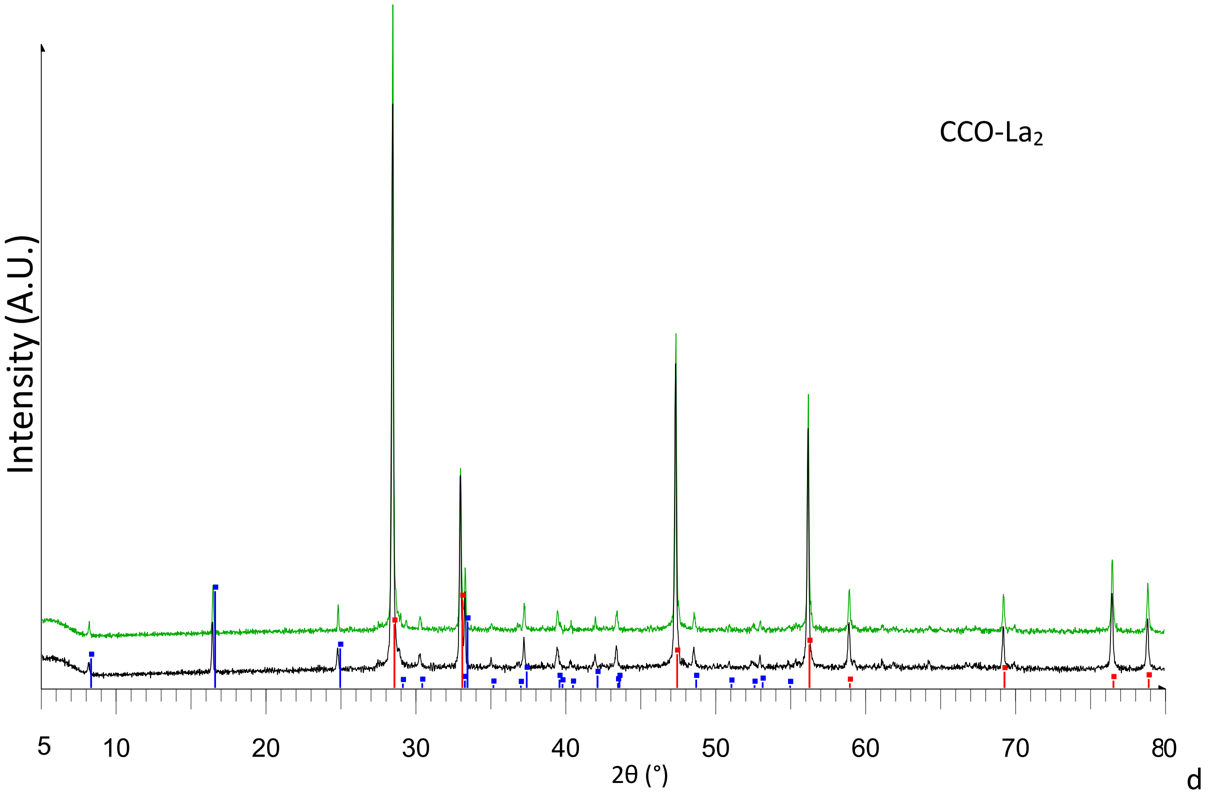

Fig. 4.2.10 - XRD spectra of screen printed 50/50-CGO/CCO-M_2 cathodes (M = Sr (a), Pb (b), Bi (c), La (d)) with .dif reference for CCO (blue bars) and standard PDF reference for CGO (red bars).

A distinctive feature is the lump on the low-angle part of the spectra. That is a normal feature of the instrument when running at such low angles. The steel cutting blade used to suppress this sort of artefacts limits greatly the intensity of the lump though it is still very pronounced.

Subsequently, EDS investigations were carried out at the Hitachi N5400 SEM microscope, equipped with an energy dispersion detector. The samples were irradiated with a 15 kV electronic beam with an intensity of 100-110 µA.

From the spectra were also calculated semi-quantitatively the amounts of each dopant (Table 4.6). The analyses confirmed the presence of the dopants, although their level is sometimes inferior to what expected (2%), especially in the case of bismuth for which a partial sublimation could be possible. However, these differences can also be explained by the fact that the very small rate of the substituents could fall below the detection limits of the detector and/or of the analytical technique.

Table 4.6 - Calculated atomic percentage with absolute error for CCO-M_2 (M = Sr, Pb, Bi, La)

Compound	Ca-K (%)	Co-K (%)	Sr-L/Pb-M/Bi-M/La-L (%)
CCO-Sr_2	38.7±3.6	60.0±11.8	1.2±0.8
CCO-Pb_2	62.1±13.5	37.6±22.2	1.8±2.0
CCO-Bi_2	51.1±3.5	45.4±9.0	0.5±0.7
CCO-La_2	34.0±1.0	64.6±3.9	1.4±1.6

© 2014 Tous droits réservés.

4.2.4. Calcium-site substitution by Sr, Pb, Bi and La: effect of the substituents on the performances of the material

Considering the very different electrochemical performances of the substituted calcium cobaltites it appears evident that the influence of the dopant is crucial.

The first factor is the impact of the substituents on the unit cell: from the X-Ray diffraction data the unit cell parameters of each doped compound were obtained by computer simulation to calculate the unit cell volume. It was always found an expansion of the unit cell in respect to the non-doped cell volume.

Another factor is the electronic shell filling of each metal ion. Ca^{2+} is in configuration $1s^2 2s^2 2p^6 3s^2 3p^6$ therefore it has neither 3d free orbitals nor any free electron pair.

Conversely, cobalt has free 3d orbitals ($[Ar]4s^2 3d^7$) and in the CoO_2 layers it was found to have a mixed valence 3+/4+ ($[Ar]3d^y$ y=5,6). This remarkable difference ensures the electronic conduction in the hexagonal sub-lattice of the CCO.

The electronic configurations of the dopants are: [Kr] for Sr^{2+}, $[Xe]3f^{14}5d^{10}6s^2$ for Pb^{2+} and Bi^{3+} and [Xe] for La^{3+}. Therefore, the main differences between Ca^{2+} and the substituents are the filling of more orbitals (Sr^{2+}), the charge (La^{3+}) or the availability of a $6s^2$ lonely electron pair (Pb^{2+} and Bi^{3+}). In the case of Bi^{3+}, additionally to the availability of a lone electron pair the charge is also different.

Whether this has a beneficial effect on the CCO electronic conduction is still debatable. In fact, the overall ASR and the R2 of 50/50-CGO/CCO-Bi_2 are bigger than those for 50/50-CCO/CGO. Additional confirmations come from the lead-doped CCO, for which the ASR is very close to that of the bismuth-doped CCO and much greater than the non-doped CCO.

Conversely, both strontium and lanthanum show less negative effect on ASR, W_S-R and R2 without having any electron lone-pair. Also in this case their ASR values are very close in magnitude but still quite higher than the non-doped CCO cathode's one.

The other difference between the five cations (Ca^{2+}, Sr^{2+}, Pb^{2+}, Bi^{3+} and La^{3+}), their valence, seems not to have much an important role to the overall performances. In fact Sr^{2+} and La^{3+} have close ASR to each other, just like Pb^{2+} and Bi^{3+}, even if in the two pairs of element the metals have different charge one another.

On the other hand, the morphologies of the cathodes, recorded by SEM imaging, do not show any macroscopic remarkable difference between the different compositions. Despite this, it is possible that other contributions to the morphology led to the obtained EIS results.

It has to be remembered that the cathode thickness is a key parameter: the optimum was found to be ~21 µm. Deviations from this value in both senses result in a bigger ASR.

© 2014 Tous droits réservés.

On the other hand, this value of thickness (21 µm) is the optimum condition for a 50/50-CCO/CGO cathode; this parameter was just kept constant for all the derived compositions assuming that the substitution has a mild effect on the geometry and microstructure of the cathode.

Nonetheless, if this assumption may be valid for strontium (for which the solid solution limits are 10 times larger than in the considered composition) it could not be the case for lead which is nearly at its solid solution limit ($3\%_{molar}$).

One last consideration on the optimum parameters touches the composition of the composite cathode. The best composition for non-doped CCO was found to be a $50\text{-}50\%_{w/w}$ blend of CCO and CGO. Also in this case the composition optimum was kept constant for the substituted compounds assuming they mimicked the non-doped CCO perfectly. While this hypothesis is much more likely than the previous one on the cathode thickness, because the non-doped and the doped phases are very closely related, it still cannot be taken for granted. Further experiments to assess the influence of the composition and of the cathode thickness on the electrochemical performances should be envisioned for each one of the doped compound, in order to deeper understand the impact of Ca-site doping.

Then, to go further in the understanding of the impact of such a doping on the CCO performances, oxygen diffusion was characterised by Isotope exchange.

© 2014 Tous droits réservés.

4.3. Oxygen transport in doped and non-doped $Ca_3Co_4O_{9+\delta}$

The electrochemical characterizations on the doped calcium cobaltites revealed that the influence of the dopant may vary according to a large number of factors. The analysed cathodes, also, had specific characteristics which influenced deeply the overall performances, such as the thickness. In the model of Adler, the extrinsic properties are just as important as the intrinsic ones.

Recalling equation 2.3.15, the polarisation resistance is given by:

$$R_{chem} = \frac{RT}{2F^2}\sqrt{\frac{\tau}{(1-\varepsilon)aC_0^2D^*k^*}} \qquad (2.3.15)$$

In this equation, other than the porosity ε and the tortuosity τ, also two important factors are present: the oxygen tracer diffusion coefficient D^* and the oxygen surface exchange coefficient k^*.

The ion transport properties of the material itself influence intimately the overall cell resistance; therefore a thorough study of the influence of the dopants on the oxygen ion transport properties of CCO was required.

Two main distinct mechanisms can be described, one at the surface and the other in the bulk of the material. The chemical equilibrium in between the molecular oxygen from the surrounding atmosphere and the oxide ions from the ceramic surface is a very complex phenomenon which involves a series of reaction steps (adsorption, dissociation, charge transfer, surface diffusion of intermediate species…). The kinetics of oxygen reduction at the gas/solid interface is given by the coefficient **k**, known as the surface diffusion coefficient or oxygen transfer coefficient. It is known that the surface exchange follows a first order kinetics though **k** cannot be measured directly. On the other hand it can be deduced from (or just replaced by) the *isotopic surface exchange coefficient* **k***, which expresses the same surface exchange kinetics but for ^{18}O.

Even though the exact mechanisms remain unclear, the occurrence of the ionic conductivity in solids depends on the presence of defects in the lattice. In particular, the species which are responsible for the ionic conductivity can be oxygen vacancies ($V_O^{\bullet\bullet}$), interstitial oxygen (O_i''), electrons (e^-) or electron holes ($h^\bullet$). At the air/material interface, the oxygen from air and from the ceramic can exchange according to the following reactions:

$$\frac{1}{2}O_2 + V_O^{\bullet\bullet} = 2h^\bullet + O_O^x$$

$$\frac{1}{2}O_2 + 2e^- = O_i''$$

In the material bulk, the oxygen ions are diffused by Brown atomic motion which, on the model of Wiener according to the random free path theory, follows the two Fick's laws.

© 2014 Tous droits réservés.

In the first law, inspired by Fourier's heat conduction law, Fick states that the diffusion of a species *i* in a medium M is proportional to its concentration's gradient C_i:

$$\vec{J_\imath} = -D_{i[M]} \cdot \overrightarrow{grad} C_i \tag{4.3.1}$$

In which $D_{i[M]}$ is the diffusion coefficient in the medium M.

The second law of Fick can be derived from the law of the conservation of the species. There, it is stated that the opposite of the variation by unit of time of the amount of particles *i* in a volume V is equal to the outgoing flux of the intensity vector for the particle current $\vec{J_\imath}$ through the closed surface *S* delimitating a volume *V*:

$$-\frac{\partial}{\partial t} ∯ C_i \cdot dV = ∰ div\,(\overrightarrow{J_\imath}) \cdot dV \tag{4.3.2}$$

By applying the Green-Ostrogradsky theorem the second law of Fick is established as it follows:

$$\frac{\partial C_i}{\partial t} - div(\overrightarrow{J_\imath}) = 0 \tag{4.3.3}$$

The ionic conductivity is related to the diffusion coefficient by the Einstein-Nernst relation:

$$\sigma_i = \frac{z_i^2 F^2 f D_i C_i}{RT} \tag{4.3.4}$$

being:

- z_i^2 the molar electric charge of the species *I*;
- D_i the self-diffusion coefficient;
- *f* the correlation factor.

The *k** and *D** values of the most typical solid oxide ionic conductors are reported in Table 4.7.

Table 4.7 - k* and D* values of the most common SOFC cathode and electrolyte materials

Material	T (°C)	pO_2 (mbar)	k* (cm s^{-1})	D* ($cm^2\ s^{-1}$)	Reference
$La_2NiO_{4\pm\delta}$	703	200	$1.75\cdot10^{-7}$	$3.38\cdot10^{-8}$	[140]
$La_{0.8}Sr_{0.2}MnO_3$	700	1000	$1.0\cdot10^{-9}$	$3.1\cdot10^{-16}$	[141]
$(La_{0.75}Sr_{0.25})_{0.95}Mn_{0.5}Cr_{0.5}O_{3+\delta}$	716	200	$3.6\cdot10^{-10}$	$7.0\cdot10^{-11}$	[142]
$La_{0.8}Sr_{0.2}Cr_{0.2}Fe_{0.8}O_3$	716	200	$2.7\cdot10^{-8}$	$7.6\cdot10^{-12}$	[143]
$La_{0.6}Sr_{0.4}CoO_3$	700	200	$1.3\cdot10^{-7}$	$1.6\cdot10^{-9}$	[144]
$GdBaCo_2O_{5+\delta}$	686	200	$1.3\cdot10^{-7}$	$1.3\cdot10^{-9}$	[145]
$La_{0.6}Sr_{0.4}Co_{0.2}Fe_{0.8}O_{3-\delta}$	800	880	$5.5\cdot10^{-6}$	$4.2\cdot10^{-8}$	[146]

The study of the oxygen transport makes the object of a large set of dedicated techniques. The oxygen transport properties may be investigated by oxygen permeation measurement,

© 2014 Tous droits réservés.

relaxation experiments (thermogravimetric relaxation or electrical conductivity relaxation) or oxygen exchange experiments.

This last kind of techniques is the object of this section. The oxygen transport parameters of doped CCO phases were investigated by the Isotope Exchange Depth Profiling (IEDP) method established at the Imperial College by B.C.H. Steele and J.A. Kilner in 1975 [147] and by the Pulse Isotopic Exchange (PIE) method more recently set up by H.J.M. Bouwmeester at the University of Twente.

The Isotopic Exchange Depth Profiling technique measures the transport coefficient by marking isotopically a very dense ceramic pellet. The specimen is then analysed by mass spectroscopy all over its depth to go back to the values of the transport coefficients.

More recently, Prof. H.J.M. Bouwmeester of the University of Twente, established a protocol for a new technique called Pulsed Isotopic Exchange (PIE) [148]. Here, the sample powder is put in a furnace and an isotopically marked atmosphere is sent by pulse. By measuring the amount of ^{18}O before and after passage over the sample it is possible to retrace the exchange properties while simultaneously providing insight into the mechanism of the oxygen exchange reaction.

Here, in a first step, the transport parameters of the 2%$_{\text{molar}}$ doped compounds were investigated by IEDP. For this purpose, pellets with a relative density higher than 95% were prepared. In a second step, to go further in the understanding of the oxygen molecule at the sample surface, PIE was carried out on the 10%$_{\text{molar}}$ Sr-doped CCO by PIE in the frame of an international cooperation between the universities of Lille and of Twente.

4.3.1. Isotopic Exchange Depth Profiling

The IEDP method was established by B.C.H Steele and J.A. Kilner at the Imperial College in the eighties [147] and it constitutes nowadays one of the most widely used techniques to reach the oxygen transport parameters of oxide materials. As previously stated, the oxide ions diffuse within the bulk of the dense ceramic pellet and are exchanged at the surface of it. These two distinct phenomena determine the ionic transport property of any ceramic material. Their kinetics are symbolised by the exchange coefficient **k** and by the diffusion coefficient **D***. Since the first of the two mechanisms is extremely complex and way far to be understood, it is replaced by its isotopic equivalent: namely, the isotopic exchange coefficient (**k***). The tracer diffusion coefficient **D*** is derived from the self-diffusion coefficient **D** through the following equation:

$$\mathbf{D^*} = f\mathbf{D} \qquad (4.3.5)$$

Where the coefficient f characterises the deviation from the random walk and its value is usually comprised in between 0.5 and 1.

© 2014 Tous droits réservés.

The basic principle of IEDP involves the annealing of a dense pellet of the oxide in ^{18}O-enriched atmosphere and subsequently the measurement of the isotopic profile using secondary Ion Mass Spectroscopy (SIMS). This principle is schematised in Fig. 4.3.1. It is worth saying that to make the sample reach the equilibrium, a pre-annealing is necessary to equilibrate the sample at the annealing temperature and oxygen pressure in natural oxygen prior to the isotopic exchange.

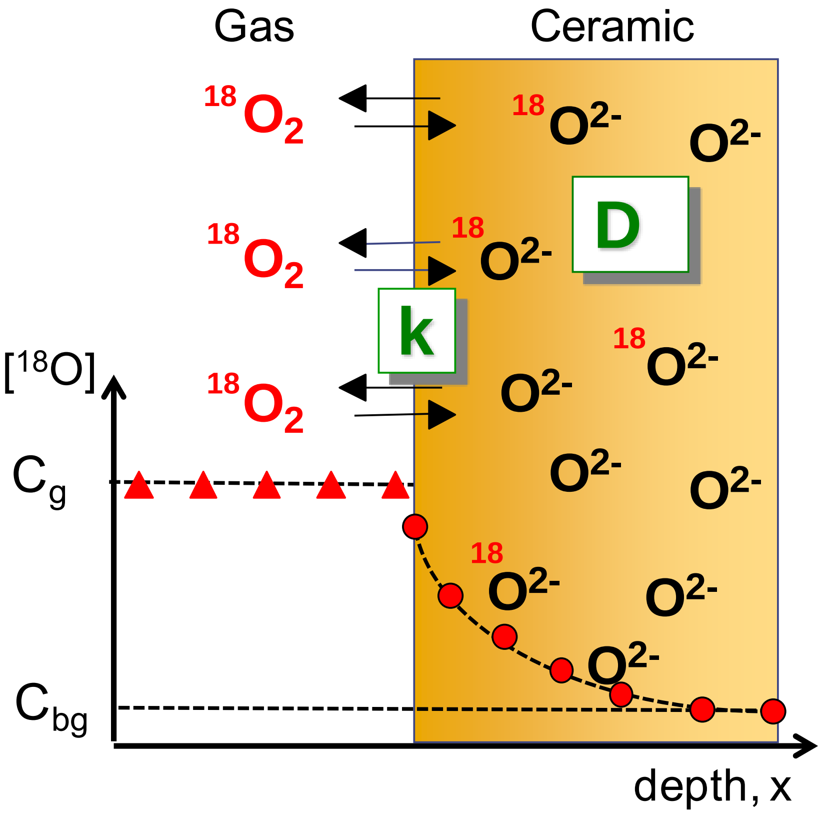

Fig. 4.3.1 - Principle of the oxigen exchange and diffusion in ceramics

Recalling the second Fick's law (eq. 4.3.2), the solution to diffusion equations was derived by Crank [149]. Considering the assumption that the rate of exchange is proportional to the difference between the concentration in the gas and the concentration in the surface at any time, the following equation is set as:

$$k\left(C_g - C_s\right) = -D\frac{\partial C(x)}{\partial x} = -D\overrightarrow{grad}(C) \qquad (4.3.6)$$

Where C_g and C_s are the ^{18}O ratio in the enriched exchange atmosphere and the solid surface respectively.

This boundary condition led to the following solution of the diffusion equation given by Crank is [149] that can be applied to the oxygen exchange in a solid:

$$\frac{C(x)-C_{bg}}{C_g-C_{bg}} = erfc\left\{\frac{x}{2\sqrt{D^*t}}\right\} - e^{\left(hx+h^2D^*t\right)}erfc\left\{\frac{x}{2\sqrt{D^*t}} + h\sqrt{D^*t}\right\} \qquad (4.3.7)$$

© 2014 Tous droits réservés.

Where C(x) is the ^{18}O ratio at depth x, C_{bg} the natural ^{18}O ratio, D* the ^{18}O tracer diffusion coefficient, k* the surface exchange coefficient, t the diffusion time and h = k*/D*. Oxygen tracer diffusion (D^*, cm^2/s) and surface exchange coefficients (k^*, cm/s) were determined by fitting the experimental data measured by Secondary Ion Mass Spectrometry (SIMS) to this equation.

For SIMS analysis, there are two modes of analysis: for materials with low diffusivity penetration depth at the chosen anneal temperature, the SIMS analysis may be performed by simply digging the ceramic within its thickness perpendicular to its surface, which is called the sputter depth profiling approach and is schematised in Fig. 4.3.2-a. In the case of oxides of higher diffusivity penetration depth, the SIMS acquisition is realized on a cross-section of the sample cut perpendicular to its surface, which is called the line scan approach and is schematised in Fig. 4.3.2.

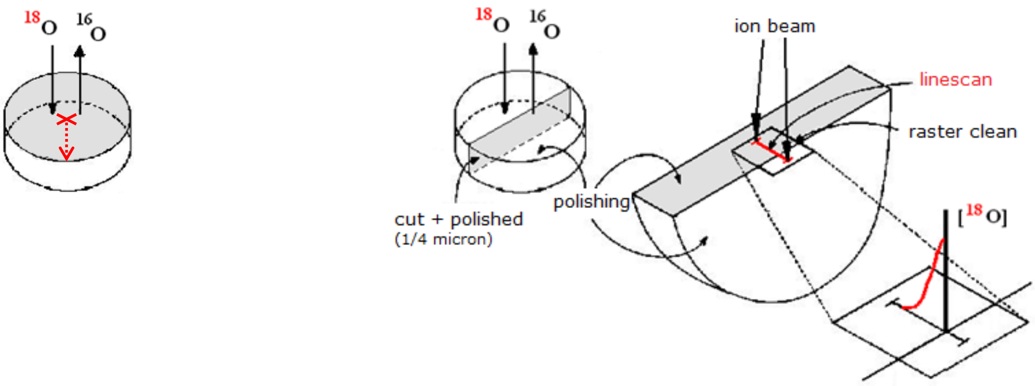

a) Sputter depth profiling SIMS
(low diffusion depth)

b) SIMS line scaning
(high diffusion depth)

Fig. 4.3.2 - Principle of functioning of a IEDP analysis (adapted from [150]

4.3.2. Isotopic exchange rig

Isotopic exchanges were carried out in a specific rig which allows inserting the sample in a closed environment, heating and quenching quickly and controlling both temperature and pressure.

Generally speaking, the isotopic exchange rig consists of a quartz tube connected, through a series of valves, to vacuum pumps and a sliding oven that can be put and removed from around the tube rapidly. A schematised representation of the isotopic exchange rig we used is given in Fig. 4.3.3.

© 2014 Tous droits réservés.

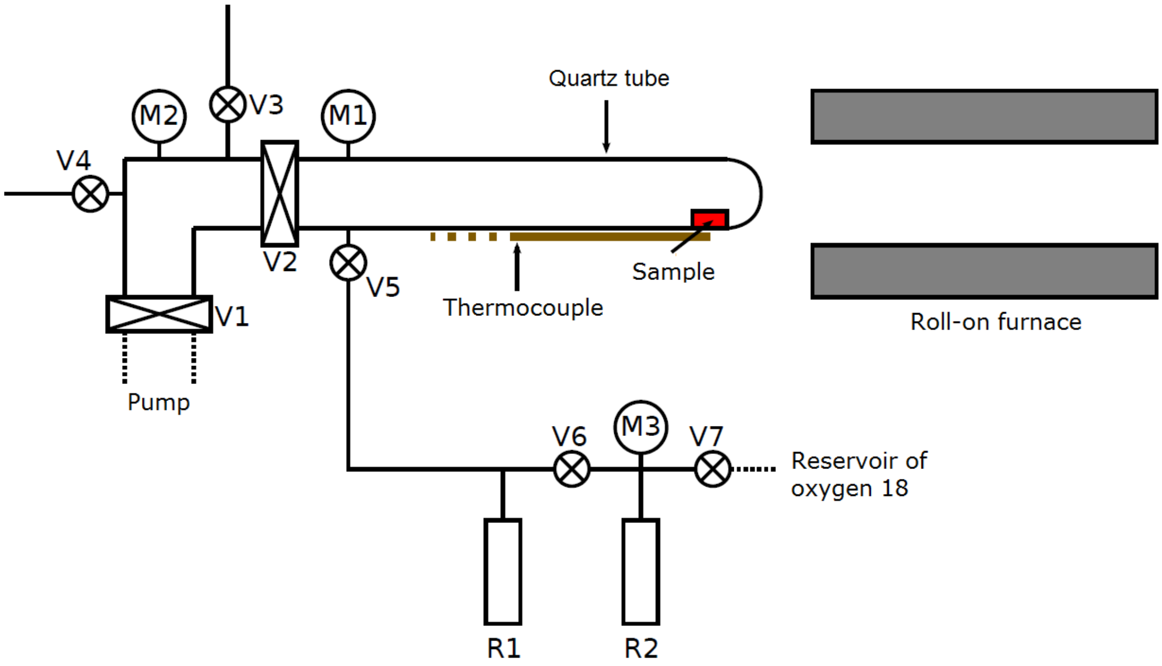

Fig. 4.3.3 - Schema of an isotopic exchange bench

The sample (the red rectangle in the scheme) is placed at the far end of the quartz tube in correspondence to the end of the thermocouple's sensor. This additional thermocouple (another one is integrated in the oven) serves to ensure the correctness of the temperature's measurement.

Initially, the sample in the quartz tube is evacuated of the atmosphere (air). Successively, normal oxygen (research grade oxygen 99.995% ALPHAGAZ™ 1, normal isotopic abundance) is introduced in the tube and, to condition the ceramic, the pre-heated oven is slid over the tube and the sample is annealed for a time approximatively 10 times larger than for the envisioned exchange time. This passage is necessary as it prepares the ceramic for the actual exchange by putting it under the thermodynamic equilibrium in the conditions of the exchange (temperature and oxygen partial pressure).

After the pre-treatment, the oven is removed and the tube quenched with a fan. Finally, the previous atmosphere is evacuated and replaced by a $^{36}O_2$ atmosphere (CortecNet research grade 97.1%); then, the oven is slid again around the tube and the sample is left exchanging. After the appropriate time, the oven is rolled off, the sample quenched with a fan and recovered. The ^{18}O-enriched atmosphere is recovered and stored in two side-reservoirs for further uses. The recovery is achieved by repeatedly cooling and heating the side-reservoirs (cryo-pumping) to the maximum possible extent (usually up to leaving 0.68 atm in the tube).

To measure the $^{18}O_2$ content in the gas phase, a piece of silicon is annealed at 1075°C for 3 h prior to the experiment.

© 2014 Tous droits réservés.

This procedure is quite time consuming and also very delicate. The montage requires several specific features and precautions, resulting in a large construction. A visual picture of the exchange rig available at the UCCS is provided in Fig. 4.3.4.

Fig. 4.3.4 - Isotopic exchange rig at the UCCS laboratory of the University of Lille

As was previously stated, the ceramic pellet exchanges the oxygen across its surface. Irregularities in the shape or in the structure would prevent the gas to follow the right pathway. For instance, the presence of holes would play the role of a local reservoir of $^{36}O_2$ thus rendering a microscopic area of the pellet more concentrated in ^{18}O than the rest of the bulk. Therefore, samples with relative density higher than 95% are required and good care must be taken to verify that their density is high enough to allow a controlled diffusion in the sample

4.3.3. Sample preparation for IEDP

As the surface adsorption occurs at any gas/solid interface it is extremely important that this exchange is limited to a very narrowly controlled zone. For instance, a highly porous pellet would have too many uncontrollable spots favourable for the surface exchange, namely every square centimetre from both the pellet's surfaces (upper, lower and lateral) and the pores' surfaces. Thence, a very dense pellet is required to successfully obtain a correct isotopic exchange experiment. Specifically, the relative density (ρ_{rel}) of the specimen has to be greater than 95% and possibly as close as to 100%.

© 2014 Tous droits réservés.

The two main ways to play on the relative density of a pellet are the casting (moulding) and the sintering. The mould casting is usually done with an appropriate die which has a circular hole inside which the powder is pressed into a cylindrical pellet. Subsequently the pellets can be further densified by sintering it under air at an appropriate temperature and time, which both depend on the powder. Nevertheless, this conventional method was not suited for the calcium cobaltite CCO.

Due to the limited condition of phase stability the sintering temperature has to be limited to a maximum of 900°C, leaving only the sintering time as a variable. In fact the $Ca_3Co_4O_{9+\delta}$ tends to decompose irreversibly into $Ca_3Co_2O_6$ at temperatures above 950-1000°C. The impossibility to play on the sintering temperature resulted in the very bad relative densities by conventional sintering (70-80%).

Alternatively, Spark Plasma Sintering (SPS) technique was chosen to obtain very dense calcium cobaltite's pellets. The two main advantages of this technique are that the powders are casted and sintered directly in a low oxygen atmosphere, under pressure and at an imposed current. This allows carrying out a thermal treatment at lower temperature (750°C).

The powders were put in a graphite crucible under an applied pressure of 50 MPa, and then fastly heated at 750°C in 10 minutes. These conditions were maintained for a few minutes (10-20 minutes) in order to obtain very compact pellets, then quenched and recovered.

As a matter of fact, the SPS is often alternatively called “flash” sintering because the powders are instantly sintered.

The obtained pellets have usually relative densities fairly higher than 95%. For the specimens used in this work, the SPS technique gave pellets with relative densities equal to 98.3% for $(Ca_{0.98}Sr_{0.02})_3Co_4O_{9+\delta}$, 99.4% for $(Ca_{0.98}Pb_{0.02})_3Co_4O_{9+\delta}$, 97.2% for $(Ca_{0.98}Bi_{0.02})_3Co_4O_{9+\delta}$ and 97.5% for $(Ca_{0.98}La_{0.02})_3Co_4O_{9+\delta}$.

These pellets were subsequently characterized by X-Ray diffraction which confirmed the purity of the phase and the absence of any parasitic composition. Additionally, unit cell parameters were refined using the FullProf Suite, on all the compositions and compared with the results of the as-synthesized powders to assess if the compounds kept their structure after all the manipulations.

The calculations showed that the pellets did not undergo any phase transition after the sintering procedure, as both the pellet and powder's X-Ray diffraction patterns were fully assigned to the reference lines.

The pellets were then further thermally treated to relieve the inter-grain constraint stress and remove all traces of graphite from the surfaces according to the procedure set up by V. Thoréthon during his PhD [107], in which it was evidenced that the inter-grain stress led to lose the surface smoothness after the exchange. Therefore, the specimens were heated at

© 2014 Tous droits réservés.

900°C for 12 hours before proceeding further with the sample preparation. In this way, the leftovers of the carbon deposit coming from the SPS procedure were also completely removed.

The pellets retrieved so far respond to one principal prerequisite, namely a very high relative density as close as possible to 100%. This requirement is necessary to control the oxygen exchange by limiting diffusion pathways to only the shown surfaces of the pellet. In fact, indents, fissures, pores etcetera cause the gas/solid interfaces to multiply thus letting oxygen to diffuse anywhere within the sample.

Another fundamental prerequisite of a good isotopic exchange specimen is that it has to have a very smooth surface (mirror polished). The depth profiling reconstructs the oxygen diffusion inside the material starting from the surface. If the surface is uneven, errors on the positioning of the zero will occur making the results unexploitable. Therefore the mirror polishing is an absolute requirement of the sample formatting. The polishing of the sample was iteratively done using successively sandpaper discs of smaller and smaller grit and, in the end, diamond paste.

The increase cannot be too abrupt because the sandpaper may leave scratches or stripe-like patterns on the pellet. The usual procedure foresaw at least four subsequent polishing, starting from a P1200 grit (15.3 µm) through P2400 (8 µm) and P4000 (3 µm) sandpapers. The values in brackets are the corresponding particle sizes of the ISO/FEPA grit values of the polishing discs. Finally, the last passage was done with a polishing cloth impregnated with a diamond polishing paste which has a particle size of 1 µm. At this level, the polished surface of the specimen had already the adequate quality for the ToF-SIMS analysis. Visually, the sample looked brilliant and reflected images like a mirror, which is why it is said to be mirror-polished. Fig. 4.3.5 shows the appearance of a mirror polished pellet with a copper rod reflecting into it.

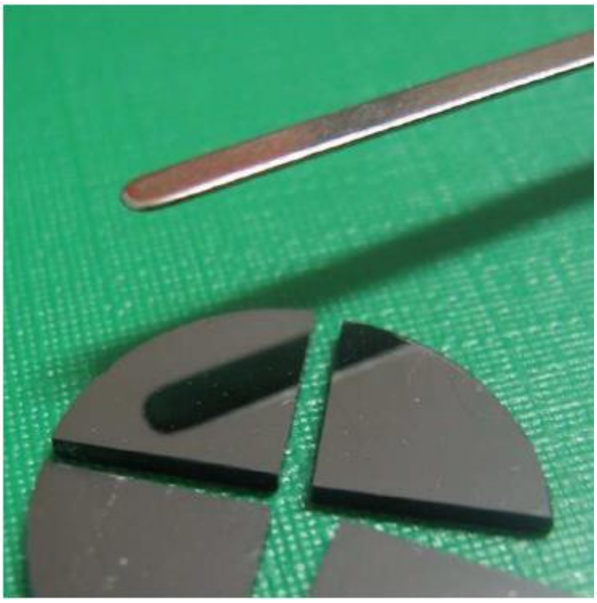

Fig. 4.3.5 - Aspect of a mirror-polished pellet with a roughness of about 1 µm

© 2014 Tous droits réservés.

A last optional polishing at 0.25 μm grit can be done on the sample prior to start the isotopic exchange experiment, although the improvement is scarcely visible. In Fig. 4.3.6 is shown the aspect of the surface of a not yet polished SPS dense pellet at different magnifications: 1000 X (a) and 5000 X (b). The images revealed a highly uneven surface with a lot of strokes running all along the pellet. This rough aspect was completely smoothened by polishing as it is shown in Fig. 4.3.7 which presents the aspect of a SPS dense pellet after the polishing procedure under secondary electron SEM imaging (a) and backscattered SEM imaging (b). Unlike the previous case, the surface is utterly smooth and no stroke is revealed. Even though the SEM images seem to reveal minor hollowness in a limited number of spots around the surface, those voids are negligible in size in comparison to the rest of the pellet's surface.

Finally, the mirror-polished pellets were cleaned in acetone and ethanol baths to remove any trace of polishing material (SiC) that may come from both the sandpaper discs and the polishing diamond paste. The pellets were put in small beakers and covered with acetone, then placed in an ultrasonic tank for increasing time (3, 5 and 10 minutes). Lastly, the pellets were placed in another beaker, covered in ethanol and sunk in an ultrasonic tank again for 10 minutes.

The polished pellets were subsequently recovered from the last beaker, rinsed with fresh ethanol and swiftly dried with a compressed air stream. Finally, the samples were carefully placed in small plastic boxes and classified.

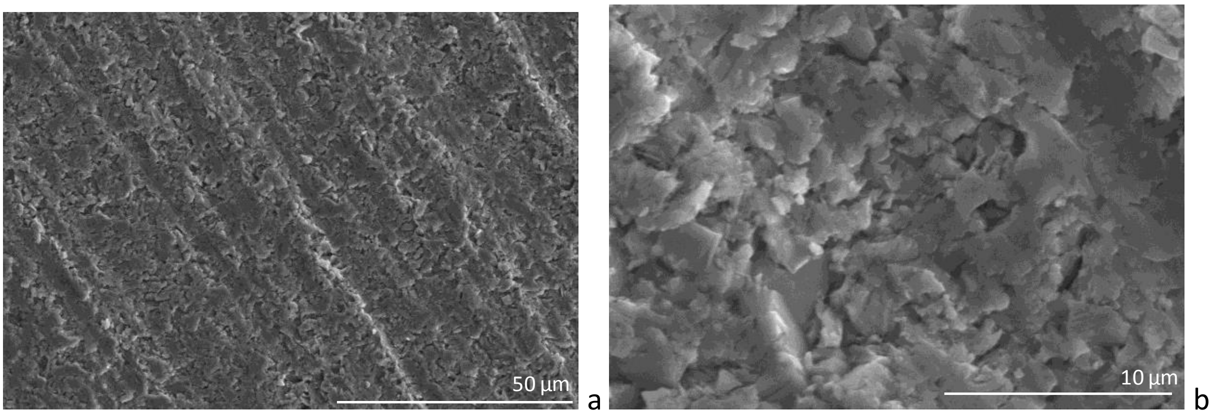

Fig. 4.3.6 - SEM images of a non-polished SPS pellet at 100X (a) and 500X (b) magnificaiton

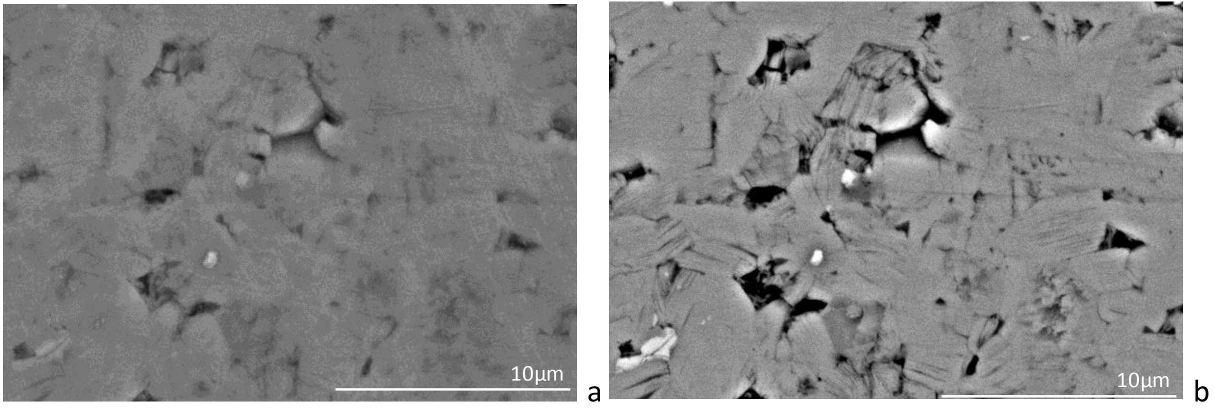

Fig. 4.3.7 - SEM imaging on a polished SPS pellet by secondary electrons (a) and by backscattered electrons (b)

© 2014 Tous droits réservés.

4.3.4. Post-exchange sample preparation for line scan and depth profiling analyses by SIMS

The specimens that have been exchanged with the procedure described previously need to be prepared for the SIMS analysis. In particular, there are two main analyses that are carried out on each sample: the depth profiling and the line scan.

The first one is carried out on the pellet’s surface while for the second the pellet’s quarter is cut in very thin slices. Both experiments will be further detailed later.

No sample preparation is actually required for the depth profiling (DP); the pellet has to be recovered carefully from the quartz tube and avoided to get contaminated from dust particles or skin grease of the operator.

Instead, for the line scan (LS) profiling the sample preparation plays a key role on the success of the experiment. Since the ToF detector is very sensitive to any unevenness of the sample, therefore the samples need to be perfectly flat and smooth.

In the very first instance, from the pellet’s quarter two narrow slices have to be cut with a diamond edged blade equipped with a micrometric screw that displaces the sample holder. The ceramic is glued on a copper rod by means of wax. The support metallic rod was purposedly chosen to be in copper to speed up the heating of the scaffold. The very fast heat transfer both in heating and in cooling is extremely important to minimize any possible thermally induced parasitic phenomena on the exchanged ceramic.

In between the ceramic and the copper rod is positioned a glass lamina serving to protect both the metallic rod and the saw blade: the glass interlayer acts as a soft buffer amid the two metallic parts.

Afterwards, the remainder of the pellet’s quarter was recovered from the copper rod and cleaned in acetone. Instead, the slices were recovered and glued on a stainless steel heavy-duty support and mirror polished in the same fashion as described in §4.3.3.

Lastly, the polished flat slices (roughness = 1 μm) were unglued from the steel support and carefully cleaned in acetone and ethanol with the aid of ultrasonic tank cleaner. The so-obtained ceramic slices were attached on a piece of bi-adhesive copper tape acting as support and electric current conductor.

4.3.5. Secondary Ion Mass Spectroscopy with Time of Flight detector for exchange profile tracing on ceramic samples

SIMS analyses were carried out on a TOF.SIMS[5] spectrometer of the ION-TOF company installed in the Regional Platform of Surface Analysis of the *Institut des Molécules et de la Matière Condensée de Lille (IMMCL, Fédération Chevreul).* Acquisitions were performed by Dr. Nicolas Nuns, *Ingénieur d’études*, in charge of this facility.

© 2014 Tous droits réservés.

The SIMS instrument is equipped with a Time of Flight (ToF) detector that combines a remarkable sensitivity and compactness. The analyses done at the ToF-SIMS instrument consisted of depth profiling (DP) and line scan (LS). Both provide fundamental information concerning the ion exchange profile of the dense ceramic specimens.

Principles of the Secondary Ion Mass Spectroscopy (SIMS) analysis

Mass spectroscopy is a well-established analytical technique in which the sample is eroded by an ion beam. Then, the charged fragments are accelerated in an electric field attaining different final velocities according to their mass-to-charge ratio $\frac{m}{q}$.

The particularity of secondary ion mass spectroscopy is that the source is represented by an ionic beam. These ions are said “primary” ions and are distinguished from the fragments which are denoted as “secondary” ions. The most common ionic generators for SIMS are highly brilliant gun of noble gases (Ar^+ or Kr^+ and Xe^+ in lesser amount), oxygen (O_2^+ or O^-), low melting point metals (Ga^+, Bi^+ etcetera) or caesium (Cs^+). While the gas sources are generated by formation of plasma, the metal ions may come from thermal decomposition (caesium) or field emission (“liquid” metals).

Fig. 4.3.8 represents a schematic view of the TOF.SIMS[5] machine with the main components which are housed in an ultra-high vacuum chamber

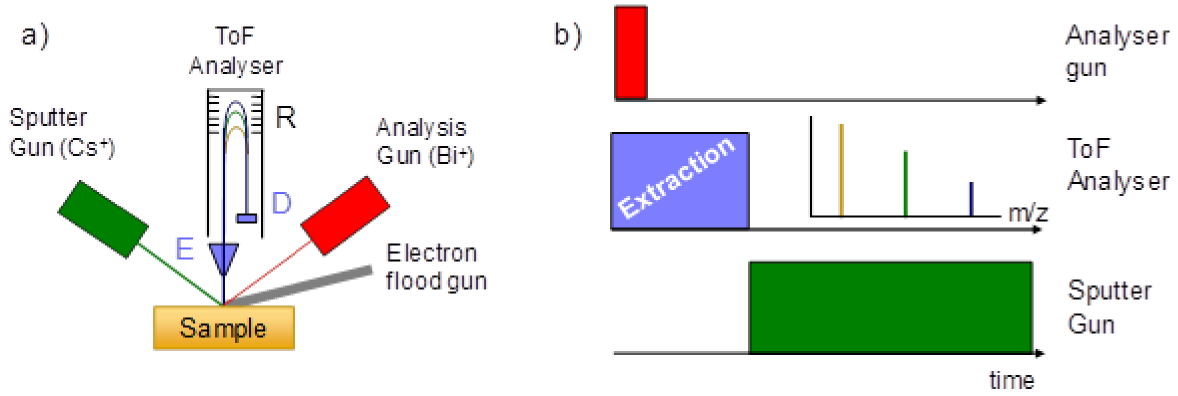

Fig. 4.3.8 – Schematic view of the TOF.SIMS[5] machine, R: reflectron, E: extraction electrode, D: detector (a); schematic diagram of a sputter depth profiling accomplished by interlacing the timing cycles of the analysis and sputtering ion beams (b)

Here, a Bi^+ (primary ion) gun was used for the analyses. This primary ion beam excavates a squared-shape well on the surface of the sample. The fragments are analysed in the ToF detector and the absolute amount of ^{16}O and ^{18}O coming from the extracted material is determined. The information from this first layer gives one point on the graphic of $^{16}O/^{18}O$ against the depth. After the analysis of the first layer, a more powerful ion beam is sent on the square well. The additional ion beam is called erosion beam or “secondary” primary ion gun. This gun shoots low energy heavy ions (Cs^+) that dig the specimen’s surface. The shape of the additional ion beam is squared too, but its size is much larger than the primary ion beam. This is necessary to produce a larger, deeper squared-shaped hole on the surface to

© 2014 Tous droits réservés.

be analysed. The hole has to be larger than the well to avoid border effect, which negatively affect the analysis. The hole is also deeper to allow the analysis of the layers just below the one which was just analysed.

After the erosion, another bismuth ion beam is shot from the primary gun to excavate another layer from the ceramic. The subsequent alternation between excavation with Bi^+ ions (analysis step) and surface digging by Cs^+ ions (profiling step) constitutes the core of the depth profiling analysis.

In the case of insulating samples, in which the charge misbalance induced by the fragmentation may be hold locally, the charge is compensated by sending, through a food gun, an electron stream to the bulk of the irradiated sample. Nevertheless, since the calcium cobaltite samples are electronic conductors, the use of the electron flood gun was not necessary.

There exist a large variety of MS detectors, from the oldest and extremely accurate magnetic sectors, to more modern quadrupoles. Each detector has unique specific advantages allowing to choose according to the needs. Specifically, the SIMS analyses performed on the isotopic exchanged calcium cobaltites have profited of the Time of Flight detector, which principles are described in the next section.

Principles of the Time of Flight detector

The secondary ions, generated by a pulse of bismuth ions, are extracted perpendicular to the sample surface with an electrical potential and enter the drift tube. Here, ions of given mass/charge ratio are separated according to their velocity following the second law of Newton and the law of conservation of energy.

However, secondary ions, even of the same type, are emitted with a distribution of energies, and hence, after extraction, they possess a distribution of velocities. The reflectron (an electrostatic mirror) compensates, at the outset, for this spread of velocities: ions with slightly higher velocities penetrate further into the field than the slower ions, with the result that ions of the same mass but different energies arrive at the detector at the same time. Arriving at the detector, the secondary ions are counted and have their arrival times recorded. In this way a complete mass spectrum is acquired for every scan. The acquisition of mass spectra can be repeated at a rate that depends on the flight time of the heaviest secondary ion to be monitored.

Also, as the time of flight is recorded very precisely by the instrument’s detector, the achievable mass resolution is excellent, up to the point of distinguishing between two of the isotopes of oxygen, notably ^{16}O and ^{18}O. As described by De Souza et al. [151] there are two main modes of analysis insuring the production of primary ion pulses of sufficiently short duration for high mass resolution but containing a large number of ions. The two main modes which were used for the ToF-SIMS analyses were the bunch and the burst modes, which are schematised in Fig. 4.3.9.

© 2014 Tous droits réservés.

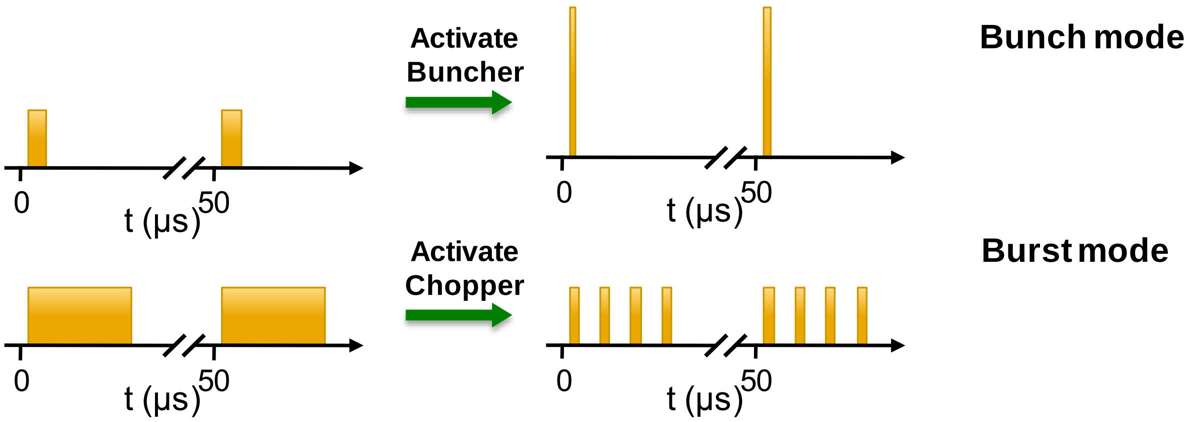

Fig. 4.3.9 - Scheme of the bunch and of the burst modes

The **bunch mode** gives the best mass resolution and sensitivity. The classic pulsed system produces pulses of 10-20 ns by cutting a continuous beam. By mean of an electrodynamic device, called buncher, each ionic packet is compressed to a durations lesser than 700 ps without almost any ionic loss. This allows having very short and intense pulses which maximises the mass resolution although, to avoid damaging the specimen's surface, the beam has to be defocused. This defocusing comes with a non-negligible loss of lateral resolution.

In the **burst mode**, instead, a 100 ns pulse is additionally cut in a series of pulses (from 1 to 10) by mean of a chopper (burst blanker). Each pulse is typically 1.5 ns long. This mode gives the best compromise in term of lateral and mass resolution, but at the price of a certain loss in sensitivity.

Table 4.8 - Summary of the specifics for bunch and burst modes

	Bunch Mode	Burst Mode
Lateral resolution	2 µm	< 350 nm
Mass resolution ($\mathcal{M}/\Delta$)	> 8000	5000
Ions per pulse	250-1000	40
Pulse duration	< 0.7 ns	1.5 ns

4.3.6. Sputter depth profiling analyses on dense ceramic samples

The sputter depth profiling mode may be considered as the absolute reference for the profiling of an isotopic exchanged sample, the analysed layers starting from the very surface (depth = 0) and proceeding further. However, because of its highly time consuming nature, the depth profiling mode is generally limited to the first few micrometres (usually up to 5 µm) of the specimen.

As already mentioned, the analysis in sputter depth profiling mode does not require particular preparation of the sample after exchange. Depth profiling is accomplished by interlacing the timing cycles of the analysis and sputtering ion beams. The analysis with the Bi^+ beam is realized on a reduced zone (75 µm x75 µm) centered on the zone eroded by the 2 keV Cs^+ ion beam (250 µm x 250 µm). In our case an 8 pulses burst mode is used, applying

© 2014 Tous droits réservés.

Poisson correction. In case of too high intensity, the detector may not recover from the high number of secondary ions in the first burst before ions from the second burst arrive. In this case, only the first burst was used in the quantification with Poisson correction on the 1st peak as explained by De Souza [151]. When no saturation was observed, all the bursts were used.

After analysis, the obtained profile is retrieved as a function of erosion time. The conversion of this erosion time in depth is simply obtained by measuring the total depth of the erosion crater, considering the erosion speed as a constant.

The crater depth was measured with a KLA Tencor Alpha-Step IQ Surface Profiler (resolution in the order of the nanometer). An example of crater depth measurement is reported in Fig. 4.3.10. The depth profile measurements were carried out for slightly less than 3 hours which resulted in craters with a depth of about 5 µm.

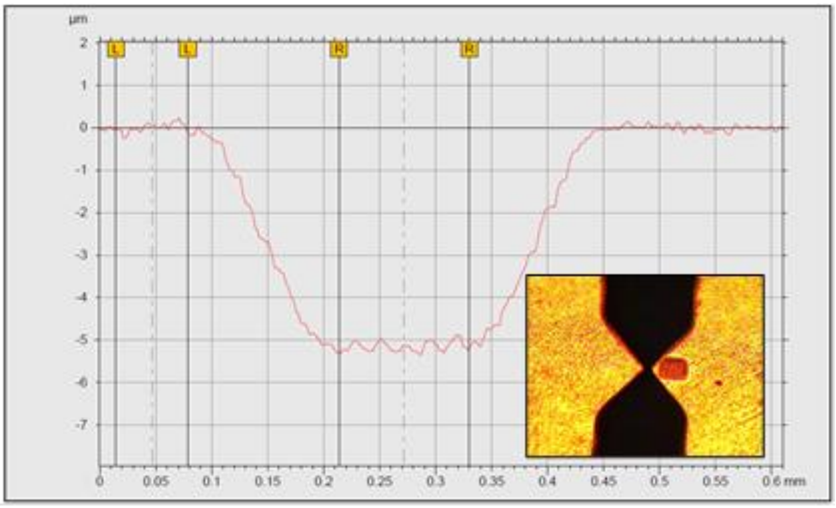

Fig. 4.3.10 - Depth profile example recorded with the mechanical profilometer KLA Tencor Alpha-Step IQ. In frame: erosion crater (250µm x250µm) placed on the side of the profilometre tip

4.3.7. Line scan analysis on polished slices of a dense ceramic pellet

The depth profiling analysis is highly time-consuming and often the results report only the profile of the first few micrometres of the ceramic sample. To go deeper in the sample, a complementary analysis is necessary to recover the overall exchange profile of the specimen, namely the line scan (LS) profiling. Also in this case a Bi^+ ionic beam is shot on the surface of the slice, but the main difference resides in the nature of the specimen. Unlike the previous case, in which the sample was attacked from the outermost surface, here the entire depth is analysed at once.

Prior to the analysis a cleaning of the surface was carried out. In case of line scan mode analysis, typically the Bi^+ beam rasters over 200 µmx 200 µm and the Cs^+ beam rasters 650 µm x 650 µm for sputtering. The zone of analysis was sampled on 512x512 pixels and 30 scans were successively recorded. As previously, an 8 pulses burst mode was used, the Poisson correction was applied to the whole spectra and the same procedure was used in case of a too high intensity by ignoring the burst mode in case of saturation of the detector.

© 2014 Tous droits réservés.

To derive the line scan, the images were integrated along the diffusion axis. To avoid border effect, two slices of a same sample were usually analysed side to side.

An example of surface imaging is reported in Fig. 4.3.11.

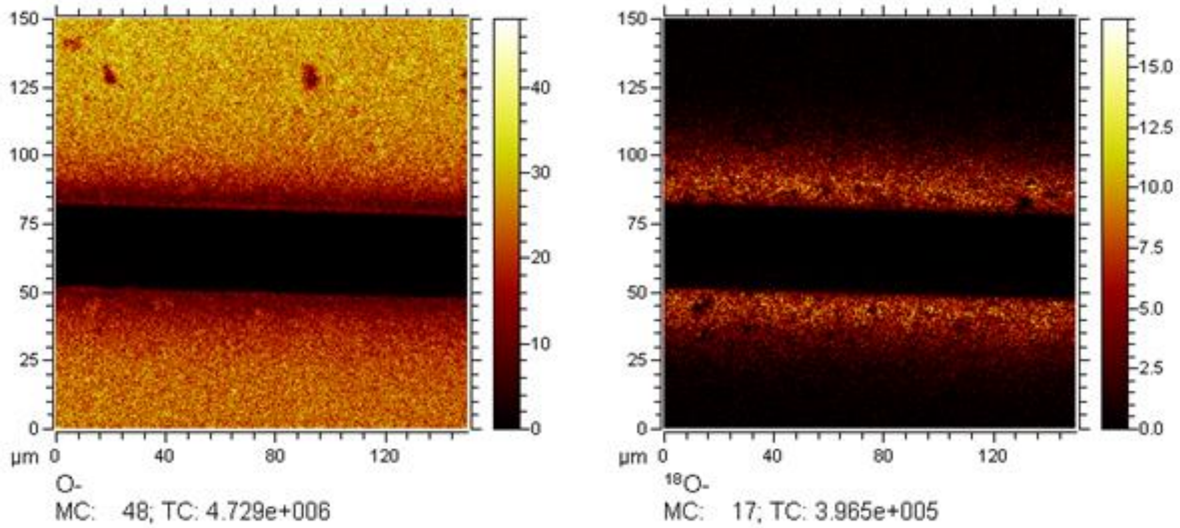

Fig. 4.3.11 - Surface imaging for $^{16}O^-$ (left) and $^{18}O^-$ (right) secondary ions for $(Ca_{0.98}Pb_{0.02})_3Co_4O_{9+\delta}$ exchanged at 700°C for 2h.

4.3.8. Results of the DP and LS analyses on the isotopic exchanged $(Ca_{0.98}M_{0.02})_3Co_4O_{9+\delta}$ dense pellets

The experimental conditions used for the isotopic exchanges performed on the $(Ca_{0.98}M_{0.02})_3Co_4O_{9+\delta}$ (M=Sr, Pb, La) ceramics are reported in Table 4.9. Due to a lack of time, the experiments were not carried out on the Bi compound.

Table 4.9 - Exchange conditions on the CCO-M_2 set of samples (M = Sr, La, Pb)

Sample	Temperature (°C)	Pressure (mbar)	Pre-annealing time (h)	Annealing time (h)	^{18}O ratio in gas phase
CCO-Sr_2	638	182	10	1	0.89
CCO-Sr_2	693	167	10	1	0.87
CCO-Sr_2	740	157	10	1	0.85
CCO-Pb_2	650	176	20	2	0.79
CCO-Pb_2	700	168	20	2	0.78
CCO-Pb_2	742	157	20	2	0.92
CCO-La_2	652	175	20	2	0.77
CCO-La_2	690	174	20	2	0.86

An example of a normalised ^{18}O diffusion profile is reported in Fig. 4.3.12. The graphs show the exchange profile of $(Ca_{0.98}Pb_{0.02})_3Co_4O_{9+\delta}$ as a plot of the $^{16}O/^{18}O$ ratio against the sample's depth. Both data recorded in depth profile (black dots) and line scan (blue dots) modes are shown.

© 2014 Tous droits réservés.

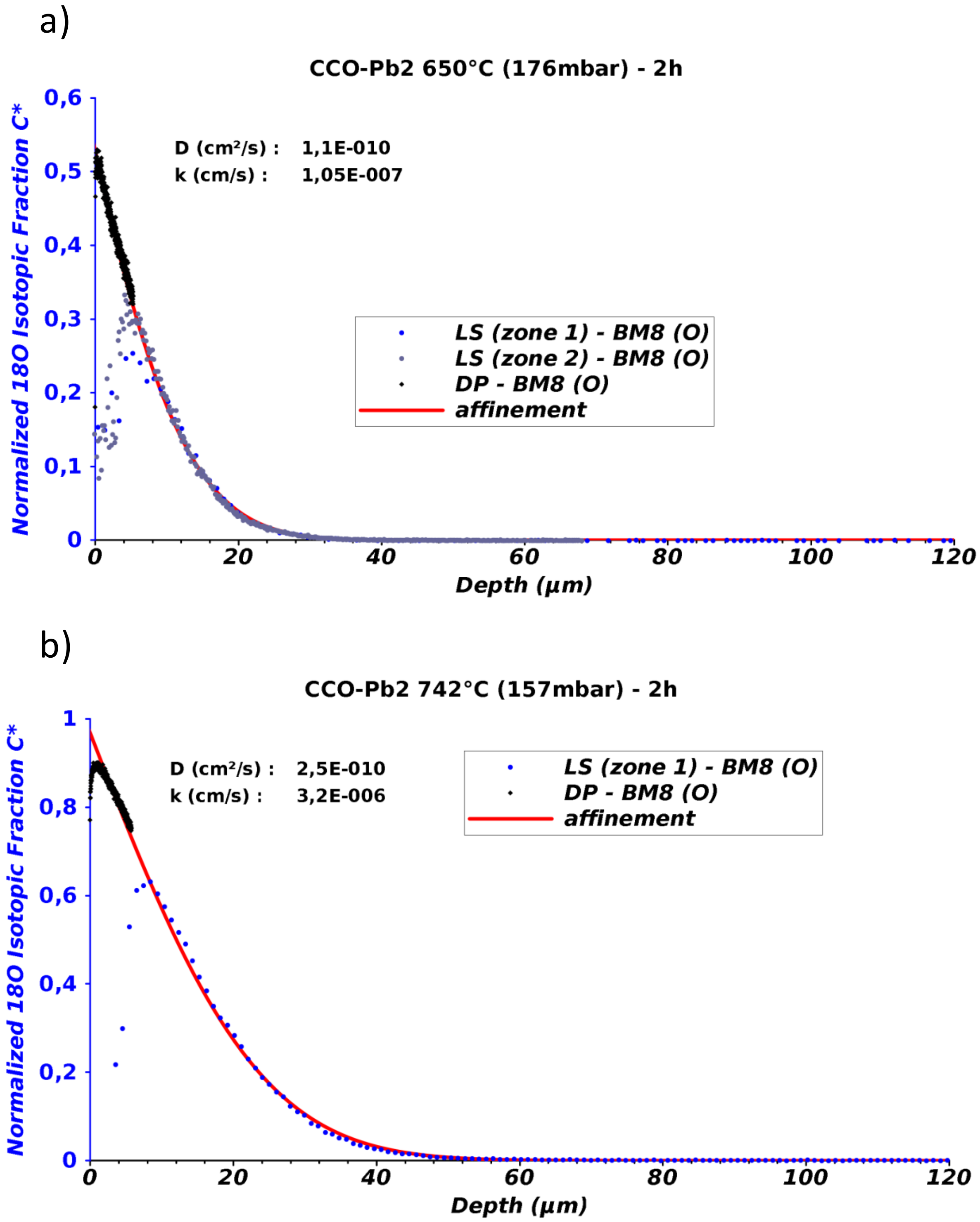

Fig. 4.3.12 - Normalised ^{18}O diffusion profile on $(Ca_{0.98}Pb_{0.02})_3Co_4O_{9+\delta}$ a) after diffusion for 2hours at 650°C under 176 mbar of dry $_{18}O$ oxygen and b) after diffusion for 2hours at 742°C under 157 mbar of dry $_{18}O$ oxygen. (LS refers to line scan and DP to depth profile)

In some cases, as illustrated in Fig. 4.3.12 (b), a particular profile was observed at the border of the sample where a decrease of the isotopic fraction was noticed over the first few µm. The same behaviour was observed for the pure $Ca_3Co_4O_{9+\delta}$ samples studied by Vincent Thoréton during his PhD [118].The possibility of a decrease of the ^{18}O in the gas phase was

© 2014 Tous droits réservés.

excluded since the variation of ^{18}O in the gas phase was estimated at a maximum of 2%, calculated by taking into account the volume of the tube used for the exchange and integrating the diffusion profile on the whole surface of the pellet to derive the amount of ^{18}O in the ceramic. The possibility of oxygen diffusion at room temperature was also excluded by a second analysis of one sample, one year later. However, higher concentrations of carbon and hydroxyls were noticed at the near surface thus carbonation or hydroxylation cannot be excluded. Nonetheless these phenomena were only observed for a depth of 100 to 200 nm, which is shorter than the ^{18}O surface depletion. To confirm the presence of carbonate or hydroxyl group, FTIR and Raman spectroscopy were carried out but did not lead to any clear evidence of these two species.

Oxygen tracer diffusion and surface exchange determined for the doped cobaltites $(Ca_{0.98}M_{0.02})_3Co_4O_{9+\delta}$ (M = Sr, Pb, La) are reported in Table 4.10 and compared to the oxygen transport kinetics of pure $Ca_3Co_4O_{9+\delta}$ [118]. The diffusion length ($2\sqrt{D^*.At}$), the extrapolated surface isotopic ratio (C_0), and the dimensionless parameter ($\eta = k.\sqrt{\frac{At}{D*}}$) are also included.

Table 4.10 - Results of the IEDP experiments on the pure [118] and doped calcium cobaltite

Sample	Temperature (°C)	Pressure (mbar)	k* $(cm.s^{-1})$	D* $(cm^2.s^{-1})$	$2\sqrt{D^*.At}$ (µm)	η	C_0 (extrapolated)
CCO	653	209	$8.0x10^{-08}$	$3.0x10^{-10}$	66	0.78	0.54
	700	230	$1.6x10^{-07}$	$2.7x10^{-10}$	50	1.5	0.68
	753	232	$5.0x10^{-06}$	$6.5x10^{-10}$	61	23	0.98
$CCO\text{-}Sr_2$	638	182	$1.35x10^{-07}$	$1.6x10^{-10}$	15.2	0.64	0.45
	693	167	$3.9x10^{-07}$	$2.8x10^{-10}$	20.1	1.4	0.65
	740	157	*$2.5x10^{-06}$*	*$4.0x10^{-10}$*	24.0	7.5	0.96
$CCO\text{-}Pb_2$	650	176	$1.05x10^{-07}$	$1.1x10^{-10}$	17.8	0.85	0.50
	700	168	$4.0x10^{-07}$	$1.6x10^{-10}$	21.5	2.68	0.80
	742	157	$3.2x10^{-06}$	$2.55x10^{-10}$	27.1	17	0.97
$CCO\text{-}La_2$	652	175	$9.9\cdot10^{-08}$	$1.6\cdot10^{-10}$	21.5	0.66	0.46
	688	174	$2.5\cdot10^{-07}$	$2.8\cdot10^{-10}$	28.4	1.26	0.63

The η and C_0 parameters may be related to the level of confidence in the measured values of D* and k*. A C_0 value close to 1 and a η value higher than 10 indicate high surface kinetics compared to oxide ion diffusion. Under these conditions, the confidence in D* is high but the confidence in k* is low. Conversely, when C_0 is far lower than the unity and η lower than 0.1, this indicates that surface exchange is slow in comparison with diffusion and under these conditions, the confidence in k* is high, but the confidence in D* is low [143]. For accurate measurement of D* and k* from a given profile, C_0 should ideally be approximately 0.5 and η approximately 1. For most of the values reported in the Table 4.10 these conditions are almost filled except at high temperature (~750°C) where high values of η indicate a high surface kinetics and therefore a good reliability on D* but a low confidence in k*.

© 2014 Tous droits réservés.

At the surface of the solid, x = 0, the solution to the diffusion equation given by Crank (eq. 4.3.7) is reduced to [150]:

$$C_0 = 1 - e^{(h^2 Dt)} erfc(h\sqrt{Dt}) \quad (4.3.7)$$

This function is plotted in Fig. 4.3.13 and compared to the experimental values of C_0 as a function of η. This illustrates that almost all the profiles obtained on the doped $Ca_3Co_4O_{9+\delta}$ are in good agreement with this theory except that for $(Ca_{0.98}Sr_{0.02})_3Co_4O_{9+\delta}$ at 740°C which moves a little bit away from the theoretical equation.

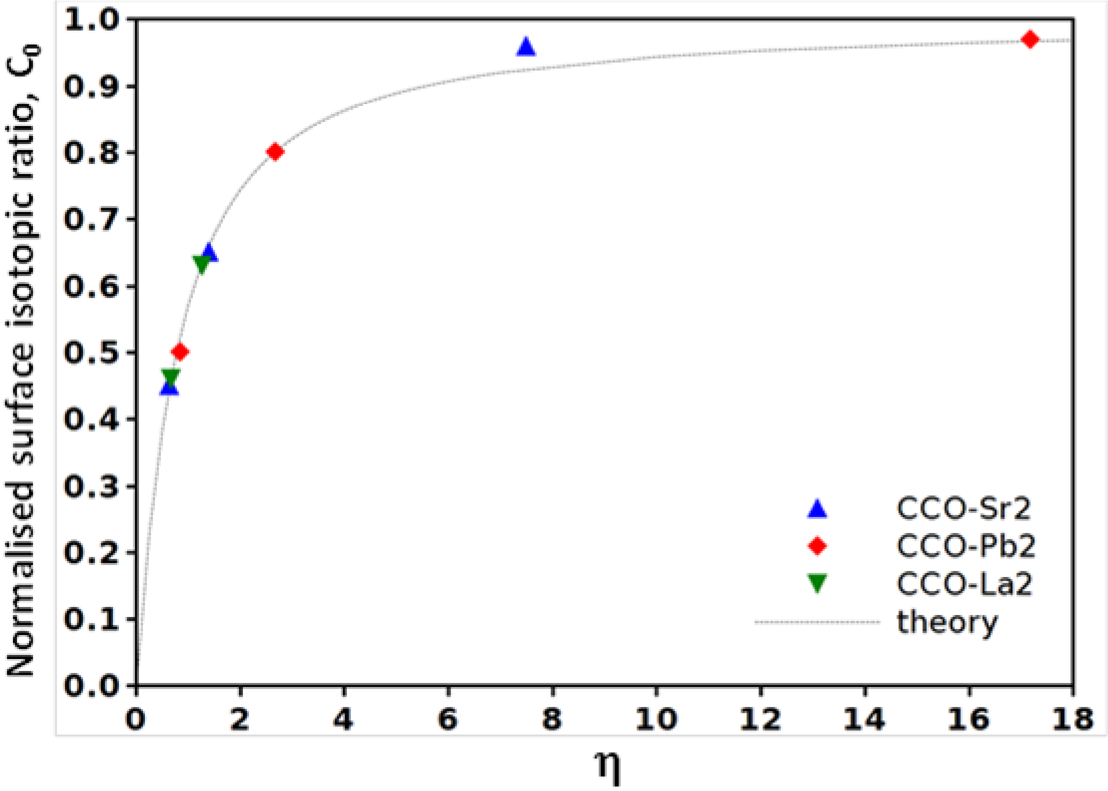

Fig. 4.3.13 - Normalised surface isotopic ratio, C_0, as a function of η

Because of the low substitution ratio, close oxygen transport parameters were derived for all samples with similar activation energies as shown in Fig. 4.3.14. This indicates that intrinsic properties may not be the limiting parameters in the electrochemical performances and further experiments will have to be carried out to clarify the higher ASR measured for the CCO-Pb_2 samples.

© 2014 Tous droits réservés.

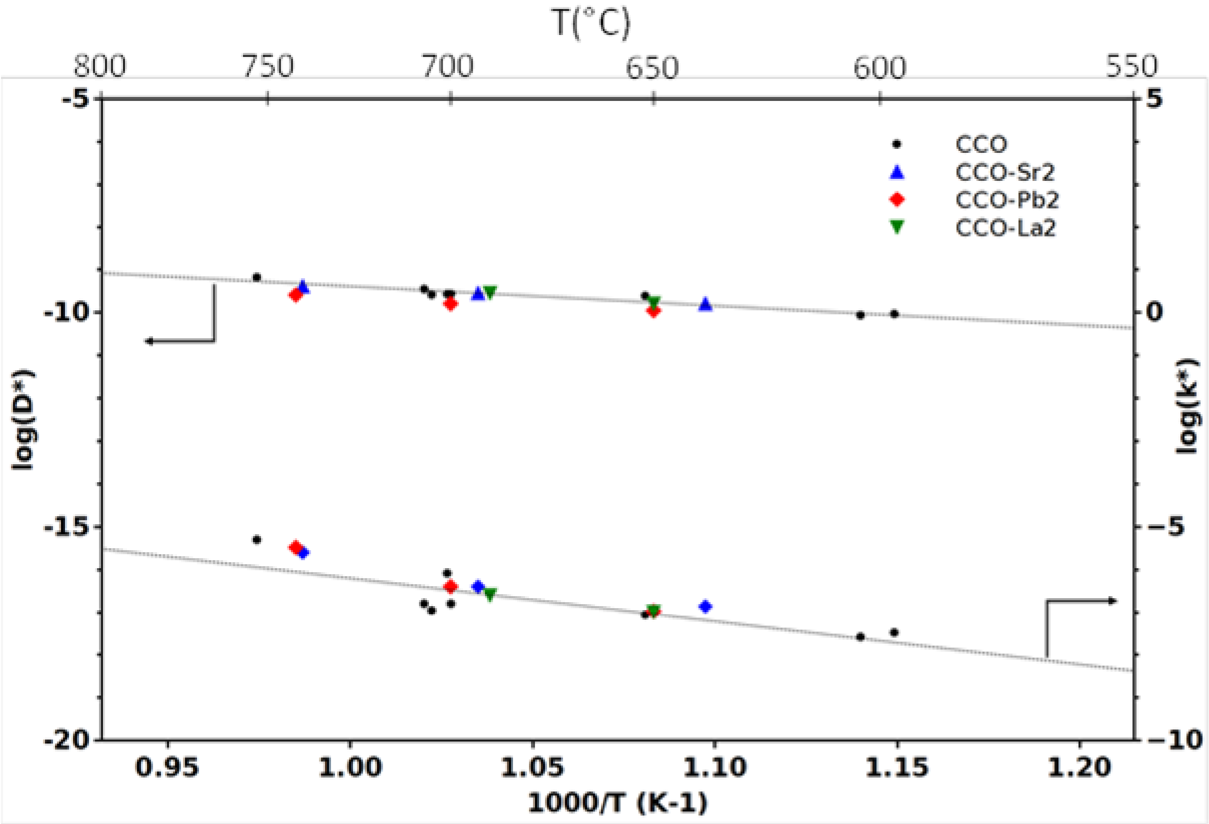

Fig. 4.3.14 - Arrhenius plot of the transport coefficients k*(cm·s^{-1}) and D* (cm²·s^{-1}). Values obtained for the doped CCO are compared to those obtained for pure CCO [118]. Dotted lines are the linear regression for pure CCO from which activation energies of 0.9 eV and 2 eV were derived for D* and k* respectively.

Generally speaking, it is difficult to draw a conclusion on the effect of the substitution on the transport parameters. In the case of the substitution by Pb^{2+}, which electrochemical performances were clearly lower in comparison to pure CCO (§4.2.3.1), a decrease of the diffusion coefficient values is revealed, although moderated and still seemingly within the experimental error. For the other dopants, Sr^{2+} and La^{3+}, the values of D* remain very similar to those obtained for pure CCO. Concerning the k* values, it is even more difficult to trace a tendency: whatever the dopant, the obtained values remain very close to those obtained for the non-doped compound, even if a slight increase may be observed in the case of the Sr substitution. Also, the confidence on the k* value is limited, as it can be seen on the repeated measurements on non-doped CCO at any temperature.

Nevertheless, for doped and non-doped calcium cobaltites, the D* is about two order of magnitudes lower than the acknowledged reference materials (~10^{-10} against ~10^{-08} for $La_2NiO_{4+\delta}$) at 700°C which confirms the necessity to blend the CCO with CGO for the application. Conversely, the value of k* has the same magnitude of the most used references, such as $La_2NiO_{4+\delta}$ (10^{-7}), revealing that the surface exchange kinetics are very interesting for this kind of material.

To study the influence of calcium site doping on the oxygen transport properties and proceed further in the understanding of the oxygen exchange at the sample surface, it would

© 2014 Tous droits réservés.

be necessary to repeat such experiments with higher substitution rates when this is allowed by the domain of solid solution, as it is the case for strontium which will be evaluated in the following section.

4.3.9. Evaluation of the substitution rate: strontium doping on the calcium site of $Ca_3Co_4O_{9+\delta}$

The previous study seems to confirm that the substitution on the calcium site by a cation having a bigger ionic radius like strontium greatly improves the CCO transport coefficients. The mere doping by 2% in Sr leads to an increment on the k* and D* coefficients by 60% and 4% at 700°C, respectively. This seems to confirm better kinetics towards oxygen dissociation when calcium is substituted by a bigger cation with the same valence, even if we have to be careful due to the slight difference over the whole range of temperature. The strontium substitution was chosen because the solid solution limit in CCO of this element is as high as $25\%_{mol}$. Therefore, a study on the effect of the composition, namely the substitution rate, was carried out on the $(Ca_{1-x}Sr_x)_{3.}Co_4O_{9+\delta}$ solid solution (see Table 4.1). To go further in the understanding of the reactions at the sample surface, pulse isotope exchange experiments were carried out on the $(Ca_{0.90}Sr_{0.10})_3Co_4O_{9+\delta}$ composition.

The technique of the Pulsed Isotopic Exchange (PIE) has the advantage of allowing to determine easily and quickly the surface diffusion coefficient. Moreover, the experiments can be performed directly on polycrystalline specimens which eliminates all the shaping and formatting necessary for the DP and LS procedure. The drawback is that only the surface exchange coefficient is accessible and not the diffusion coefficient.

For the PIE, the powder is loaded in a packed bed micro-reactor and allowed to equilibrate at a chosen oxygen partial pressure and temperature for a selected time. While maintaining the conditions of chemical equilibrium, the response to an ^{18}O-enriched pulse fed through the reactor under continuous flow conditions is measured by mass spectroscopy analysis of the gas phase fractions of oxygen isotopomers ($^{18}O_2$, $^{16}O^{18}O$ and $^{16}O_2$) at the exit of the reactor (see Fig. 4.3.15-a). From this measurement, the overall surface exchange rate $\Re_0$ at the given experimental conditions is calculated from the mean residence time and the uptake of ^{18}O by the sample and it can be connected to k* through the following relation:

$$\Re_0 = k^* \times [C_O]$$

The PIE experiments were carried out at the University of Twente, The Netherlands, thanks to the help of PhD student S. Saher and under the direction of Prof. H.J.M. Bouwmeester, during two different stays in June and July 2013 (funding retrieved from a EOLE Scholarship french-dutch exchange program).

4.3.9.1. PIE measurement experimental protocol

Prior to the measurements, the powders of CCO have to be sieved to homogenise the grain size, by eliminating the too big and the too small ones. The ideal interval of particles' size was in between 60 and 120 µm. The sieved powder was first submitted to B.E.T.

© 2014 Tous droits réservés.

measurement (Micromeritics Gemini VII) to assess the specific area surface of the sample. This value is fundamental in the subsequent determination of the k* coefficient (0.7291 m²/g for $(Ca_{0.90}Sr_{0.10})_3Co_4O_{9+\delta}$).

After the B.E.T. experiment, the powder is redirected to the PIE analysis. The powder is put in a fixed bed glass reactor which is then put in a tubular furnace (see Fig. 4.3.15 b, c, d). 0.0685 g of the sieved powder were inserted in the fixed bed reactor and put into furnace to heat and, finally, to exchange.

Finally, the furnace is closed with quartz wool to isolate the system and the temperature is increased by step of 200°C per hour until 850°C. The reactor was then flushed with the carrier gas for 2 hours to remove possible adsorbates such as CO_2. Once this pre-treatment finished, the reactor was reset at the desired temperature and left stabilising for 2 hours before taking any measurement. The temperature was initially set to 50°C to have a fixed "low temperature" reference, then it was increased to 400°C by steps of 200°C/h. Afterwards, the temperature was increased by steps of 50°C until 500°C, after which the step size was decreased to 25°C up to 600°C. The experiment was stopped at 600°C as it was considered concluded. Per each temperature (50, 400, 450, 500, 525, 550, 570 and 600 °C) at least 3 acquisitions were recorded, in order to have statistically significant data. From the mass spectra were calculated the relative fractions of $^{34}O_2$ and $^{36}O_2$ which were divided by the amount of $^{28}N_2$ to have a constant reference.

The volume of inlet oxygen in the calibrated loop was fixed at 500 µL per each exchange trial; the outlet oxygen was measured with a quadrupole-equipped Mass Spectrometer, and the results were recorded in an Excel® spreadsheet. A $^{32}O_2$/Ar gas mixture was used as carrier gas with a 50 $mL\cdot min^{-1}$ flow rate and a 0.21 atm oxygen partial pressure in the case of our measurements, then the $^{36}O_2$-marked oxygen was let in the calibrating fluid-dynamic steel circuit. This way, the contact time τ was surely comprised in between 4 and 40 ms. The marked oxygen was blended with nitrogen-28 to have an internal standard reference.

The parameter τ, which is the contact time, is also fundamental for the subsequent calculations so it has to be carefully calculated. Here the calculated contact time τ was approximately 11 ms.

The $^{36}O_2$ oxygen inlet, contained in the steel circuit, was impulse in the hot glass reactor and the response to the $^{18}O_2$–N_2 pulse was analysed at the outlet by on-line quadrupole mass spectrometry (OmniStarTM GSD 301, Pfeiffer-Vacuum). The mass analysis recorded the relative values of the $^{28}N_2$, $^{36}O_2$ and $^{34}O_2$ of the gas outlet. The $^{32}O_2$ fraction was calculated as

$$f_{32_{O_2}} = 1 - f_{36_{O_2}} - f_{34_{O_2}} \tag{4.3.8}$$

The $^{32}O_2$ fraction was not directly measured to avoid the oversaturation of the detector and the risk of leaks from air. The values of the $^{36}O_2$ and $^{34}O_2$ fractions were reported in

© 2014 Tous droits réservés.

proportion to the $^{28}N_2$ in order to make the measurements independent from the temperature or avoid errors coming from oscillations on the gas inlet amount.

The PIE measurement can be repeated a few times per each temperature. The mass detection is very fast and in less than 5 minutes the acquisition is complete. Therefore, a certain amount of acquisition points can be acquired for each temperature, thus making the measurement more statistically valid.

The average of the mass-detection measurement was used as the molar fraction for the subsequent calculations.

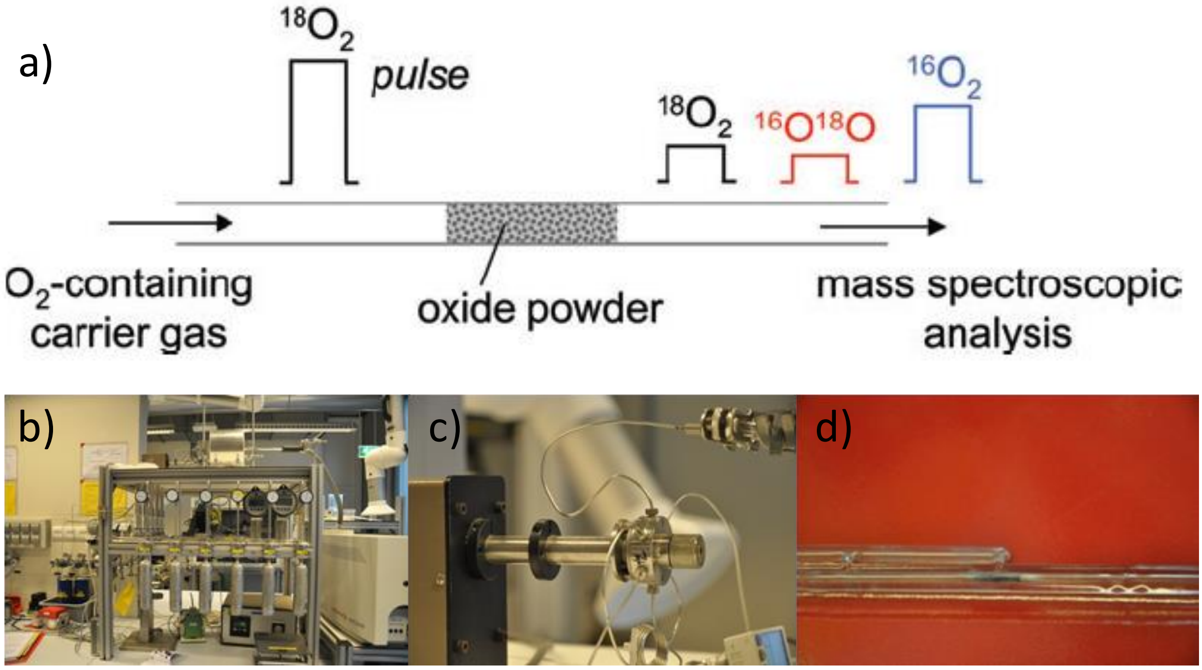

Fig. 4.3.15 - Schematic principle of the transient isotopic pulse technique [148] **(a), Pulse isotopic Exchange apparatus at University of Twente (b), detail of the 6-way valve for the pulse injection (c), detail of the micro-reactor (d)**

4.3.9.2. Mathematical models for PIE experiments

The aim of the PIE experiment is to provide a determination of the oxygen surface exchange rate of oxide ion conductors (and as a consequence k*) and to lead to a deeper understanding of the surface kinetics by yielding insight into the mechanism of the oxygen exchange reaction.

Considering that the isotopic fraction of ^{18}O in the solid is negligible in comparison to the fraction in the gas flux, the overall surface exchange coefficient, $\mathfrak{R}_0$, can be calculated according to the following equation:

$$\Re_0 = \frac{n}{\tau_s S} ln\left(\frac{f_{g,o}^{18}}{f_{g,i}^{18}}\right) \qquad (4.3.9)$$

© 2014 Tous droits réservés.

Where n is the total number of oxygen atoms in the gas phase, $f_{g,o}^{18}$ is the ^{18}O fraction in the gas outlet, $f_{g,i}^{18}$ the ^{18}O fraction in the gas inlet, τ_s is the average contact time and S is the specific area surface. These last two parameters, S and τ_s, were already defined as key parameters. While S is retrieved from the B.E.T. experiment, τ_s is calculated per each temperature.

Unlike the DP and LS experiments, which gave directly the values of k* and D*, the PIE gives the $\Re_0$ value, which is connected to k* only through the following relation:

$$\Re_0 = k^* \times [C_O] \tag{4.3.10}$$

Where $[C_O]$ represents the known value of the oxygen concentration in the gas phase.

The coefficient $\Re_0$ can be seen as the simultaneous contribution of $\Re_{ins}$ and $\Re_{ads}$ which are the insertion and adsorption coefficients, respectively. These two parameters account for the two main phenomena occurring during a pulsed isotopic exchange: the adsorption on the powder's surface and the insertion of marked oxygen from the surface through the material.

These two events are described by a first order's kinetics, hence their Arrhenius-like plot against temperature is described by a straight line. Nevertheless, the two lines can be very close or very far from each other. In fact, the insertion and the adsorption processes are concurrent as they both enter the overall $\Re_0$ exchange parameter as it follows:

$$\frac{1}{\Re_0} = \frac{1}{\Re_{ins}} + \frac{1}{\Re_{ads}} \tag{4.3.11}$$

Needless to say, there is not an analytical solution for the separation of the contribution knowing the $\Re_0$ parameter only. And as in the PIE experiments the only measured parameter is $\Re_0$, the two contribution cannot be separated. Therefore, mathematical models are needed to retrieve this information. Unfortunately, a unique model for all the ceramic oxides does not exist, and each one needs separate treatment for the best understanding of the occurring phenomena.

Nevertheless, there is one model equation that relates the molar fractions of the ^{18}O in the gas phase with the adsorption and insertion coefficients.

$$f_{g,i}^{36} = \left(\frac{(1-p)}{(1-2p)^{1/2}} \times f_{g,i}^{18}\right) \times e^{-\left(\frac{2\tau_r}{\tau_u}\right)} + \left(f_{g,i}^{36} - \left(\frac{(1-p)}{(1-2p)^{1/2}} \times f_{g,i}^{18}\right)^2\right) \times e^{-\left(\frac{\tau_s}{\tau_u p}\right)} \tag{4.3.12}$$

Where $p = \frac{\Re_{ins}}{\Re_{ads}+\Re_{ins}}$ and $\tau_u = \frac{n}{\Re_0 S}$. The parameter *p* reflects the probability of incorporation into the oxide lattice during its residence time at the oxide surface. This shows how an analytical solution to the determination of the insertion and adsorption coefficients is not possible. Instead, numerical solutions or iterative calculations can be tried in order to match

© 2014 Tous droits réservés.

the prevision of the equation with the experimental results, although this possibility requires highly time consuming simulations.

On the other hand, there are two cases in which the general equation (4.3.11) can be more easily solved. In case one of the two coefficients is negligible in comparison to the other, the smaller one can be cancelled and the overall $\mathfrak{R}_0$ coefficient becomes equipollent to one parameter only. The effect of the cancellation of one coefficient rather than another has a substantial effect on the aspect of the PIE experimental spectrum.

In case the adsorption kinetic is much faster than the insertion one, the ^{18}O from the gas phase has a stronger tendency to stay on the surface of the oxide rather than combining with the ^{16}O from the material itself. This results in a development of $^{32}O_2$ without the formation of $^{34}O_2$.

Conversely, when the insertion takes over the adsorption, the exchange rate with the ^{16}O of the oxide is extremely fast. Hence, all the ^{18}O from the gas phase, which is minoritary in comparison to the amount of ^{16}O from the ceramic, can react and form $^{34}O_2$ molecules. In the gas outlet there'll be only $^{34}O_2$ without the contributions of any other species ($^{36}O_2$ and $^{32}O_2$).

Of course those two extreme cases are not often encountered, and the insertion and adsorption kinetics are most of the times close to each other. This results in a spectrum which shows the progressive depletion of $^{36}O_2$ in favour of both $^{34}O_2$ and $^{32}O_2$. The trend line of the former one initially increases, then reaches a plateau or a summit and goes to zero again. The latter one, instead, shows a constant exponential growth from the initial exchange temperature until the end of the experiment.

In any case, the solution of the equation to retrieve the $\mathfrak{R}_{ins}$ and $\mathfrak{R}_{ads}$ coefficients was not part of the current work and only a qualitative analysis will be carried at this stage, Prof. Bouwmeester being currently working on the establishment of a model.

4.3.9.3. Results of the PIE experiments on the strontium doped calcium cobaltite

10 g of the raw powders of $(Ca_{0.90}Sr_{0.10})_3Co_4O_{9+\delta}$ were sieved to separate the grains with a size comprised in between 60 and 120 µm. Only about 3 g passed the selection and then, they were submitted to B.E.T. experiment to measure the specific area surface (S) of the specimen. It was found that for the $(Ca_{0.90}Sr_{0.10})_3Co_4O_{9+\delta}$ the specific area surface was 0.7291 m²/g.

The data points of the oxygen gas outlets as $f_{g,o}^{36}$, $f_{g,o}^{34}$ and $f_{g,o}^{32}$ were plotted against the temperature T in Celsius degrees. The plot is reported in Fig. 4.3.16. The aspect of the graphic is very typical, with the $^{34}O_2$ fraction drawing a summit at about 550°C and then decreasing to zero. This feature is typical of materials in which the adsorption and the insertion processes have kinetics very close to each other, and therefore no contribution can

© 2014 Tous droits réservés.

be neglected in the general model equation represented in eq. 4.3.11. Neither the adsorption nor the incorporation in the solid is the limiting step in the surface exchange process.

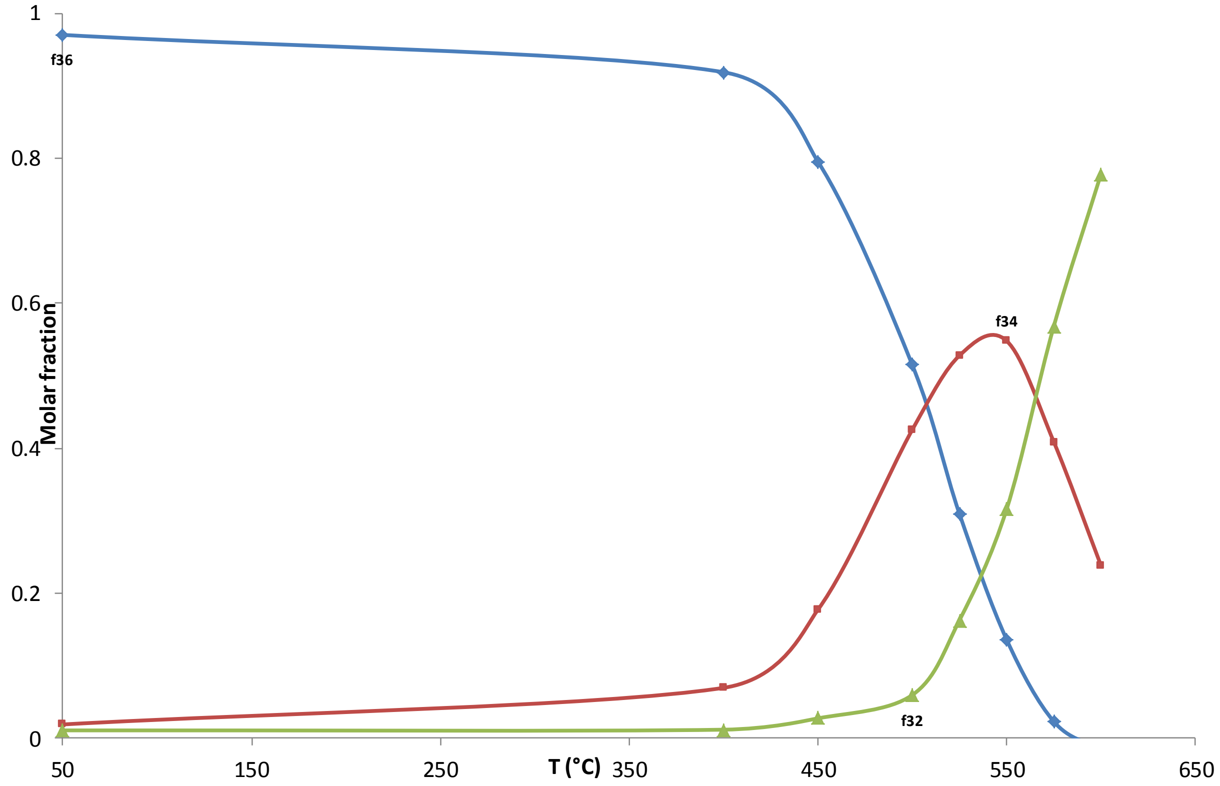

Fig. 4.3.16 - Temperature dependent trend of the 32, 34 and 36 oxygen molar fraction of the PIE on $(Ca_{0.90}Sr_{0.10})_3Co_4O_{9+\delta}$

Successively, the data on the oxygen fractions were converted in term of $\Re_0$ and k_s* and plotted as Log[k*] against $1000{\cdot}T^{-1}$ (in Kelvin) to have the Arrhenius-like plot for $(Ca_{0.9}Sr_{0.1})_3Co_4O_{9+\delta}$, reported in Fig. 4.3.17.

© 2014 Tous droits réservés.

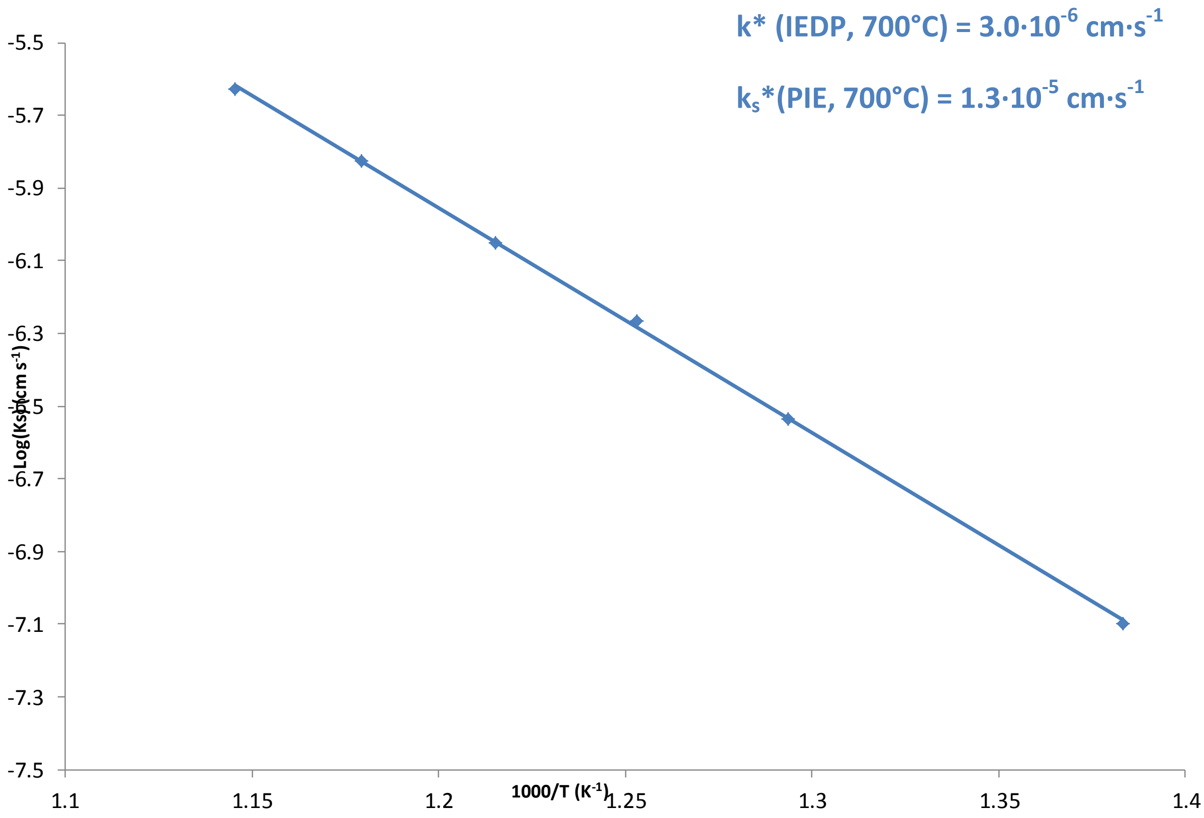

Fig. 4.3.17 - Temperature dependent trend of the Log[k_s] of $(Ca_{0.90}Sr_{0.10})_3Co_4O_{9+\delta}$

By extrapolation, it resulted that at 700°C the $\Re_0$ and k_s* for $(Ca_{0.9}Sr_{0.1})_3Co_4O_{9+\delta}$ equals to $5.64\cdot10^{-3}$ mol·g^{-1}s^{-1} and $1.30\cdot10^{-5}$ cm·s^{-1} respectively. This value is slightly higher than the one which was derived by IEDP (3.10^{-6} cm.s^{-1}). For the non-doped compound, PIE led also to a higher value when compared with IEDP experiments (8.10^{-7} cm.s^{-1} against $1,6.10^{-7}$ cm.s^{-1}) at 700°C [107]. It confirmed the higher kinetics of strontium doped compared for the oxygen surface exchange than the non-doped compound. An activation energy of 1.4 eV (between 400°C and 600°C) was derived, against 1.6 eV for the non-doped compound [107].

4.4.Conclusions

The impact of partial substitution on the electrochemical performances was tentatively studied with a wide range of dopant. It was difficult to draw conclusions on the impact of partial substitution on the calcium site on the electrochemical performances since these performances are strongly dependent on the sample preparation. Moreover, due to the low dopant concentration, imposed by the scarce solubility of lead in the calcium site, it was not possible to derive a clear tendency of the substituents' influence on the oxygen transport properties. Other experiments on samples bearing higher substitution rate are to be intended. However, by PIE, high surface exchange kinetics were confirmed for the $(Ca_{0.90}Sr_{0.10})_3Co_4O_{9+\delta}$ composition and it was shown that neither the oxygen adsorption of the surface nor the oxygen incorporation in the solid were the limiting step in the oxygen transfer. Even though the lower value of D* (e.g. $2.8\cdot10^{-10}$ cm²·s^{-1} for CCO-Sr$_2$ at 700°C) makes necessary the blending with CGO for the application of the calcium cobaltite as

© 2014 Tous droits réservés.

cathode material for SOFC, the high value of k* ($3.9 \cdot 10^{-7}$ cm·s^{-1} for CCO-Sr$_2$ at 700°C) places the calcium cobaltites amongst the good oxygen ionic conductors such as $La_2NiO_{4+\delta}$ ($3.38 \cdot 10^{-8}$ cm²·s^{-1} and $1.75 \cdot 10^{-7}$ cm·s^{-1} for D* and k* respectively).

© 2014 Tous droits réservés.

Conclusion

This PhD thesis presented the electrochemical and ionic transport properties of the misfit layered oxide $Ca_3Co_4O_{9+\delta}$ and of a few Ca-substituted compounds. The study dealt with the synthesis and characterisation of the powders, the preparation of inks for screen printing and the optimisation of this coating technique, the modification of the cathode microstructure by implementing the coating techniques and the evaluation of oxygen ion transport properties by two different techniques (IEDP and PIE).

All along the current investigation, the shaping and formatting of the specimens represented a big part of the work. For instance, for a screen-printed CCO cathode it was necessary to prepare an ink from the powder, whose preparation is quite time-consuming.

Nevertheless, the initial inks suffered from long-term instability and spoiled quite quickly. Hence it was developed a new methodology of preparation which solved the concerns about the stability of the pastes. With the newly obtained inks were prepared samples for the EIS investigation of the electrochemical properties of the CCO.

The calcium cobaltite showed quite good electrochemical properties, with an ASR as low as 0.5 Ωcm² for a composite $Ca_3Co_4O_{9+\delta}/Ce_{0.9}Gd_{0.1}O_{1.95}$ in a 1:1 mass ratio. This result is, unfortunately, still quite far from the goal set by Steele at 0.15 Ωcm² [152]. Making reference to the model of Adler, Lane and Steele, the cathode's microstructure plays a key role on the overall performances.

The modification of the microstructure was achieved by two different approaches: on the one hand by adopting completely new coating techniques (ESD and SC), and on the other hand by mimicking the experience of Hildenbrand thus intercalating a dense nanometric layer of CCO between the electrode and the electrolyte.

The first approach is still at the earliest stage, especially for the spin coating. As a matter of fact the templating of the cathode gave the best result but with an ASR of ~70 Ωcm², which is way too far from the goal (0.5 – 0.15 Ωcm²). Nevertheless it was shown that the scaffolding of the CCO cathode by polystyrene spheres decreases by a factor of two the overall ASR. The results from the ESD, instead, showed a much more interesting result, with an ASR of 3.32 Ωcm² for a 100%-CCO cathode.

This result, which is extremely encouraging in comparison with the one of a CCO screen printed cathode (4.5 Ωcm²), could be further improved with a survey on the effects of the composition and the thickness.

The second microstructural modification, namely the insertion of a dense layer of CCO did also provided promising results. Although the ASR of all the symmetric cells increased to about 1 Ωcm² (either with or without a dense CCO interlayer) this increase in the ASR has to be imputed to the lower than optimum value of the cathode thickness (about 16 μm). For the intercalation with a 2Hz-deposited CCO interlayer no major improvements were found,

© 2014 Tous droits réservés.

while for the one with a 3Hz interlayer the ASR was divided by a factor of 2. The simulations carried out by Z-View confirmed that the intercalation of a dense CCO nanometric layer has a beneficial effect on the overall conductivity, and causes the shift to higher frequency of the electrode/electrolyte contact associated phenomenon. Still, further characterisations of the interlayer deposit are envisioned (FIB, MET, ellipsometry).

Another aspect which was considered as very interesting is the doping on the calcium site by other elements. Starting from the results on the oxygen ion transport properties by PhD V. Thoréton [118], also the electrochemical properties of the 10% and 20% doped CCO were investigated. The survey revealed that the substitution of calcium by strontium may lead to a decrease of the ASR although the optimal conditions for the cathode were not matched.

Additionally, four different substitutions (strontium, lead, bismuth and lanthanum) were achieved for a substitution rate of $2\%_{\mathrm{molar}}$. This limit was determined by the low solubility of lead in CCO ($3\%_{\mathrm{molar}}$). The obtained compounds were evaluated both for their electrochemical and for the oxygen ion transport properties.

While the results from the EIS showed that the substitution of calcium by other metals has a rather negative effect on the overall ASR (+20 – 180% according to the dopant), the transport of the oxygen was very similar to those of the non-doped compound or slightly increased in some cases.

To evaluate the ionic exchange coefficients (k* and D*) two different techniques were used: the classical Isotopic Exchange Depth Profiling and Line Scanning, and the more recent and versatile Pulsed Isotopic Exchange.

Due to the low doping rate, it was not possible to draw a clear tendency of the effect of the substitution on the oxygen ion transport properties. Further experiments on samples bearing a higher substitution rate have to be carried out. However, pursuing the line traced in V. Thoréton's work [107], in the outlook of an international collaboration with Prof. H.J.M. Bouwmeester, PIE analyses were carried out to assess the *k** values by this novel technique. The $10\%_{\mathrm{molar}}$ Sr-doped CCO was chosen to perform this survey because the IE-DP/LS investigation showed that increasing the strontium content, the k* and D* coefficients increase nearly linearly. The PIE results confirmed the improved kinetics towards oxygen dissociation for the strontium doped compound. Interestingly nor the oxygen adsorption, nor its incorporation in the solid are limiting step to the oxygen surface exchange.

The calcium cobaltite, as a candidate for SOFC's cathode material, still has a few restraints and limitations. Which is the impact of the microstructure? How to optimise the coating technique? Would a substitution, rather than another, decrease the overall ASR value? The evaluation of the different aspects, such as coating technique, effect of composition and scaffolding of the microstructure, deserve further and more detailed investigation.

© 2014 Tous droits réservés.

Annex A. Ion transport in solids

Often, when considering the ionic conductivity the depicted model is the aqueous solution. Water, in fact, hydrolyses the ions making them free to move in a fluid medium. This model can be ascribed to the Daniell battery: two metallic electrodes (copper and zinc) and a copper sulphate solution to carry the electric charge.

This model is only apparently easy to describe: the interactions between the charge bearers are multiple, the electrical potential is influenced by the dielectric constant of water and so on.

Nevertheless, one fundamental concept is found in the aqueous solution model: the mobility. The charge, in fact, has to be transferred from the anode to the cathode. In this case the responsible for the charge transfer are the Cu^{2+} ions in solution.

The removal or depletion of the Cu^{2+} ions reduces the electrochemical performances of the battery, until it reaches the equilibrium and stops working.

Similarly, the charge can be transported by other species, either positively or negatively charged. In §§1.2.3 and 1.2.4 were presented, respectively, the alkaline and the molten carbonate fuel cells. In both the charge is transferred by a charge bearer throughout an aqueous solution within the fuel cell's membrane.

Unlike in Daniell's battery, in both cells the charge transfer is carried out by a negative species: in the first case the ionic species is the OH^- ion, while in the second it is the $(CO_3)^{2-}$ ion. The two ionic species cross the membrane bringing the charge from the anode to the cathode. Also here, the mobility is granted by the fluidity of the medium (water) which solvates and stabilizes the ions.

On the other hand, having a liquid medium causes problems of corrosion and leaks out of the membrane. This problem greatly limits the possibilities of improvement and large distribution of such devices.

Switching to solid membranes was the proposed solution. The PEM and SO fuel cells presented in §§1.2.1 and 1.2.5 exploit this concept. Unlike in the previous examples, the membrane is solid: polymeric in the first type of cells, ceramic in the second.

Also here, the charge transfer is the key point for the operation of the two fuel cells, but while in the PEM the charge is transferred by positively charged ions (H^+), in the SO the charge bearers are negatively charged (O^{2-}). Not only, the ionic radii of the two species are deeply different (~$1\cdot10^{-5}$Å for H^+ against ~1.2Å for O^{2-}) hence their relative mobility in a solid medium follows very different paths.

© 2014 Tous droits réservés.

All these characteristics make the ionic conductivity in solids more difficult to model and much less universal than in aqueous solution. Not all polymers can conduct protons, and not all ceramics can conduct oxide ions because of their very structure.

In this section will be presented the most important characteristics required for the ionic conductivity in a solid and the transport mechanisms.

Evidences of ionic conduction in crystalline or vitreous phases were found back in the end of 19th century by E. Warburg [153], [154] and Haber [155]. Nowadays, we are investigating ionic conductivity in solids for a wide variety of application (stock, energy, electrochromism, detectors, membranes, etcetera). The vast majority of solids shows an electrical conductivity at room temperature ranging in between 10^{-17} S/cm and 10^{5} S/cm, according to which we discriminate amongst isolators and conductors.

It is possible to distinguish three kinds of conductivity according to the nature of the charge bearer:

- Electronic conductors wherein electrons bring the charge (typical for metals, semiconductors and superconductors);
- Ionic conductors, wherein an ionic species brings the charge (often the case of ceramics, polymers and semimetals);
- Mixed conductors, wherein both charge bearers (electrons and ions) are responsible for the conductivity.

If a perfect crystal is considered, all atoms would be in their ideal positions in the lattice with 100% occupancy of all sites. This situation, nevertheless, cannot be obtained but at 0K while at any other temperature defects and imperfections take place modifying the lattice. Not only but also the composition of the ideal crystal should be perfectly homogeneous.

In fact, the entropy is defined by the Boltzmann equation as

$$S = k_B ln\Omega$$

Where k_B is the Boltzmann constant and Ω is the microscopic number of states. Being Ω dependent on the geometry too (namely, the molecule $^{16}O–^{18}O$ is not the same as $^{18}O–^{16}O$ in a condensed state), the only isotopic distribution of an element is enough to have $\Omega > 1$ and $\ln(\Omega) > 0$.

Hence S would not be equal to 0 even at 0K, making a hypothetical oxygen's perfect crystal still not ideally perfect (but equally not conductive).

It is this imperfect situation that allows the ionic conduction within the solids.

Recalling the model of the Daniell's battery, in which the fluid medium ensures the mobility of the charge barer, it is obvious that such settings are not possible to reproduce in a crystal:

© 2014 Tous droits réservés.

there is not the same freedom of movement in a solid than in a liquid. Still, the atoms are not statically motionless on the lattice nodes, but are granted a certain degree of freedom.

Nonetheless, this motion is local and can be translated into microscopic displacements of the atoms inside the lattice. The atoms are free to rock, scissor and vibrate and, in some limited extent, to rotate. In fact the solids are also IR and Raman active, due to the interactions of the atoms with the IR waves caused by the local modification of the electromagnetic environment by the atomic movements.

This disordered situation generates defects and defaults. There exist two main classes of defects: punctual and extended. The latter comprises grain boundaries and dislocations whereas the former accounts for Schottky and Frenkel defects.

Extended defects are regarded as the causes of failures and breakings of the solids. It is known that fissures tend to proceed along the planes of the dislocations. Therefore, extended defects are normally considered as problems in the crystal and tend to be avoided.

Conversely, punctual defects often influence greatly the physicochemical properties of solids. For instance, it is the case of ionic conduction in solids. To assure an ionic stream, the charge bearer must be able to migrate through vicinal sites inside the crystal. Namely, the charge bearer needs to jump from one vacancy to the next one throughout the whole lattice.

The presence of vacancies is ensured by Schottky and Frenkel defects which are induced by thermal agitation over the lattice. They belong to the very structure of the crystal and do not modify the stoichiometry of the material.

Frenkel defect

In a perfect crystal the atom occupancy is modified by thermal agitation by temperature increase. Frenkel's model of crystal interstitial disorder was the first one proposed [156] in 1926. Frenkel hypothesized that ions migrated from their proper position into an interstitial one, thus creating vacancies in the ion's sub-lattice.

This kind of defect is often found in fluorite-type structures such as CaF_2 or in rock-salt crystal (NaCl) and concerns rather cations than anions. The latter, in fact, are much bigger than the former therefore they would enter difficultly in interstitial sites. Nevertheless, especially in fluorine-type structure, the anionic Frenkel defects are encountered.

Schottky defect

The formation of Frenkel's defects is not acceptable to explain the ionic conduction in solids and crystals unless one species only contributes to it. In crystals like for example NaCl, where both Na^+ and Cl^- have conductivity activities, both sub-lattices present vacancies and interstitial sites. Therefore, in 1935, Schottky proposed a different model [157] in which both the anionic and cationic networks presented vacancies with the casted ions segregated on the solid's surface.

© 2014 Tous droits réservés.

The number of anionic and cationic vacancies is evened out to preserve electrical neutrality. An elevated ionic conductivity is possible as for each ion the occupancy level is locally lower than 1, like in β-alumina (Na_2O-11Al_2O_3) where Na^+ ions between the spinel blocks assure the ionic conductivity.

Other than the extended and the punctual (Schottky and Frenkel) defects, which are considered as *intrinsic* defects, also *extrinsic* defects exist.

These latter are often “induced” in a crystal, as for example by substitution of an n-valent cation with an m-valent one, and for which m ≠ n (either bigger or smaller). The changing in the positive charges account is compensated by a loss (or an incorporation, in case m>n) of counter anions, which creates, globally, vacancies or interstitial defects.

This modification of the lattice allows intense ionic conduction, as it is the case of $Zr_{0.96}Y_{0.04}O_{1.98}$ (YSZ) which is one of the most used current electrolytes for SOFC. The dilution of ZrO_2 with Y_2O_3, in which the cation valence is lower, induces vacancies in the obtained YSZ crystal thus enabling a strong anionic conduction.

On the other hand, the charge compensation can be achieved differently. If the replaced cation has two near and stable oxidation states (e.g. 3+ and 4+) the substitution induces a mixed valence of the element within the structure rather than an ionic over- (or sub-) stoichiometry.

It is the case of cerium orthovanadates in which Ce has oxidation state equal to +3. The replacement of Ce with an alkaline earth element such as strontium (Sr^{2+}) induces a charge disequilibrium which is balanced by partial oxidation of Ce^{3+} to Ce^{4+}. Unfortunately, this type of charge compensation has a much smaller effect on the ionic conductivity of a material than the creation of vacancies.

In the real situation both mechanisms usually concur to the re-equilibration of the system. Of course, one process may overwhelm the other thus the visible result is an almost exclusive contribution of a single one.

For this reason too the ionic conduction mechanisms are difficult to identify and categorize. In the following section the current available models will be discussed to the fullest extent of the present knowledges.

In the beginning of the 20th century, W.H. Nernst evidenced the electric properties of the zirconium oxide when mixed with other rare earths oxides in a determined proportion (85:15). This discovery led to the patent of several novel materials for power glowers [158] amongst which was $Zr_{0.85}Y_{0.15}O_{1.85}$, one of the electrolyte materials currently used in SOFCs. Unfortunately, the filament had to be pre-heated in order to work. This first example of applied ionic conduction reveals two main characteristics of the conduction mechanism.

© 2014 Tous droits réservés.

First is the effect of temperature. Although it was found that the yttrium-zirconium oxide is actually conducing and glowing, the pre-heating indicates that the mechanism is thermally activated.

In second instance, the composition of the glowing material: the glower is a double oxide, with both zirconium and yttrium in the crystal lattice coordinated with oxygen. It is currently well known that the stabilization of ZrO_2, which is monoclinic at room temperature, can be done partly (3YSZ, 8YSZ) of fully (10YSZ and 15YSZ) by changing the proportions of yttrium oxide and zirconium oxide.

The structure is the one of the zirconia at high temperature and unlike ZrO_2, which has very poor ionic conductivity, the YSZ is an excellent ionic conductor since it is the stabilized cubic form of the other phase at room temperature.

In fact, the transition to the cubic form of the YSZ comes with the formation of oxygen vacancies in the lattice. These vacancies grant the charge transfer within the crystal, given that the charge carriers have enough mobility (or energy) to travel inside the solid.

These two aspects (thermal activation and point defects) regulate the so-called bulk diffusion, namely the charge transfer within the crystal from one site to the next one. But another contribution to the overall ionic conductivity exists for every material and renders technologically applicable this phenomenon.

Other than with the neighbouring oxygen vacancies, the ions at the surface can interact with the molecular oxygen in the surrounding atmosphere. The transport mechanism is therefore regulated by two different kinetics: the surface exchange, which determines the *surface exchange coefficient* **k** ($cm \cdot s^{-1}$), and the bulk diffusion, which is represented by the *diffusion coefficient* **D*** ($cm^2 \cdot cm^{-1}$).

The chemical equilibrium in between the molecular oxygen from the surrounding atmosphere and the oxide ions from the ceramic surface is a very complex phenomenon. Even though the exact mechanisms remain unclear, the occurrence of the ionic conductivity in solids depends on the presence of defects in the lattice.

In particular, the species which are responsible for the ionic conductivity can be oxygen vacancies ($V_O^{\bullet\bullet}$), interstitial oxygen (O_i''), electrons (e^-) or electron holes ($h^\bullet$). At the air/material interface the oxygen from the air and from the ceramic can exchange according to the following reactions:

$$\frac{1}{2}O_2 + V_O^{\bullet\bullet} = 2h^\bullet + O_O^x$$

$$\frac{1}{2}O_2 + 2e^- = O_i''$$

© 2014 Tous droits réservés.

It is known that the surface exchange follows a first order kinetics though the surface diffusion coefficient **k** cannot be measured directly. On the other hand it can be deduced from (or just replaced by) the *isotopic surface exchange coefficient* **k***, which expresses the same surface exchange kinetics but for ^{18}O.

In the material bulk, the oxygen ions are diffused by Brown atomic motion which, on the model of Wiener according to the random free path theory, follows the two laws of Fick.

In the first law, inspired by Fourier's heat conduction law, Fick states that the diffusion of a species *i* in a medium M is proportional to its concentration's gradient C_i:

$$\vec{J_i} = -D_{i[M]} \cdot \overrightarrow{grad} C_i \tag{5.2.1}$$

In which $D_{i[M]}$ is the diffusion coefficient in the medium M.

The second law of Fick can be derived from the law of the conservation of the species. There it is stated that the opposite of the variation by unit of time of the amount of particles *i* in a volume V is equal to the outgoing flux of the intensity vector for the particle current $\vec{J_i}$ through the closed surface *S* delimitating a volume *V*:

$$-\frac{\partial}{\partial t} \oiint C_i \cdot dV = \oiiint div\,\overrightarrow{(J_i)} \cdot dV \tag{5.2.2}$$

By applying the Green-Ostrogradsky theorem the second law of Fick is established as it follows:

$$\frac{\partial C_i}{\partial t} - div\overrightarrow{(J_i)} = 0 \tag{5.2.3}$$

The ionic conductivity is related to the diffusion coefficient by the Einstein-Nernst relation:

$$\sigma_i = \frac{z_i^2 F^2 f D_i C_i}{RT} \tag{5.2.4}$$

being:

- z_i^2 the molar electric charge of the species *I*;
- D_i the self-diffusion coefficient;
- *f* the correlation factor.

The evolution of the ionic conductivity as a function of the temperature follows an Arrhenius-type trend which can be summed up with the following equation:

$$\sigma T = A \times e^{\left(\frac{-E_a}{kT}\right)} \tag{5.2.5}$$

Which is the typical Arrhenius relationship of a dimension (σ) with the temperature (T). The Arrhenius plot of the most common SOFC electrolyte material is shown in Fig. 1.4.1, the

© 2014 Tous droits réservés.

activation energy E_a is represented by the slope of the straight-line. The activation energy is the energy required to extract the ionic species from its potential well and make it migrate.

Noteworthy, as the y-scale is logarithmic, each unit represents one order of magnitude in the ionic conductivity. Hence, the increase of the slope means a very quick uptake of the activation energy of a material, therefore any compound having a flatter Arrhenius profile is more likely conducting (more or less well) in any temperature range.

© 2014 Tous droits réservés.

Bibliography

[1] J. Leslie, "Dawn of the Hydrogen Age," *Wired*, 1997.

[2] S. H. Jensen, X. Sun, S. D. Ebbesen, R. Knibbe, and M. Mogensen, "Hydrogen and synthetic fuel production using pressurized solid oxide electrolysis cells," *Int. J. Hydrogen Energy*, vol. 35, no. 18, pp. 9544–9549, Sep. 2010.

[3] O. Yamamoto, "Solid oxide fuel cells: fundamental aspects and prospects," *Electrochim. Acta*, vol. 45, no. 15–16, pp. 2423–2435, May 2000.

[4] K. Nagasawa, S. Daviero-Minaud, N. Preux, A. Rolle, P. Roussel, H. Nakatsugawa, and O. Mentré, "$Ca_3Co_4O_{9-\delta}$: A Thermoelectric Material for SOFC Cathode," *Chem. Mater.*, vol. 21, no. 19, pp. 4738–4745, Oct. 2009.

[5] A. Rolle, S. Boulfrad, K. Nagasawa, H. Nakatsugawa, O. Mentré, J. Irvine, and S. Daviero-Minaud, "Optimisation of the Solid Oxide Fuel Cell (SOFC) cathode material $Ca_3Co_4O_{9+\delta}$," *J. Power Sources*, vol. 196, no. 17, pp. 7328–7332, Sep. 2011.

[6] A. Rolle, V. Thoréton, P. Rozier, E. Capoen, O. Mentré, B. Boukamp, and S. Daviero-Minaud, "Evidence of the Current Collector Effect: Study of the SOFC Cathode Material $Ca_3Co_4O_{9+\delta}$," *Fuel Cells*, vol. 12, no. 2, pp. 288–301, Apr. 2012.

[7] A. J. Samson, M. Søgaard, N. Van Nong, N. Pryds, and N. Bonanos, "Enhanced electrochemical performance of the solid oxide fuel cell cathode using $Ca_3Co_4O_{9+\delta}$," *J. Power Sources*, vol. 196, no. 24, pp. 10606–10610, Dec. 2011.

[8] J. Zou, J. Park, H. Yoon, T. Kim, and J. Chung, "Preparation and evaluation of $Ca_{3-x}Bi_xCo_4O_{9-\delta}$ ($0< x \leq 0.5$) as novel cathodes for intermediate temperature-solid oxide fuel cells," *Int. J. Hydrogen Energy*, vol. 37, no. 10, pp. 8592–8602, May 2012.

[9] N. Hildenbrand, B. A. Boukamp, P. Nammensma, and D. H. A. Blank, "Improved cathode/electrolyte interface of SOFC," *Solid State Ionics*, vol. 192, no. 1, pp. 12–15, Jun. 2011.

[10] *Fuel Cell Handbook*, 7th ed., no. November. Morgantown, West Virginia: EG&G Technical Services, Inc., 2004, p. 427.

[11] P. W. Atkins, *Physical Chemistry*, 3rd ed. New York: W.H. Freeman & Co, 1986.

[12] S. Gottesfeld, "Polymer Electrolyte Fuel Cells: Transportation and Stationary Application." Stonehart Associated, Madison, Connecticut, 1993.

[13] D. Lousenberg, "Diferentiated Membranes and Dispersions for Commercial PEM Fuel Cell and Electrolysis Systems," 2003.

© 2014 Tous droits réservés.

[14] R. F. Savinell, J. S. Wainright, and M. Litt, “High Temperature Polymer Electrolyte Fuel Cells,” *Electrochem. Soc.*, vol. 98, no. 27, p. 81, 1951.

[15] J. M. King and IshikawaN., “Phosphoric Acid Fuel Cell Power Plant Improvements and Commercial Fleet Experience,” in *Fuel Cell Seminar*, 1996.

[16] V. Hacker, P. Enzinger, M. Muhr, K. Kordesh, J. Gsellman, M. Cifrain, P. Prenninger, K. Meitz, and R. Aronsson, “Advantages of Alkaline Fuel Cell Systems for Mobile Applications,” in *Fuel Cell Seminar Program and Abstracts*, 2000.

[17] A. Yuh and M. Farooque, “Carbonate Fuel Cell Materials,” *Adv. Mater. Process.*, 2002.

[18] P. V. Hendriksen, S. Koch, M. Mogensen, Y. L. Liu, and P. H. Larsen, “Solid Oxide Fuel Cells VIII,” in *The Electrochemical Socety Proceedings*, 2003, p. 1147.

[19] W. R. Grove, “XXIV. On voltaic series and the combination of gases by platinum,” *Philos. Mag. Ser. 3*, vol. 14, no. 86, pp. 127–130, 1839.

[20] W. R. Grove, “XLII. On a small voltaic battery of great energy; some observations on voltaic combinations and forms of arrangement; and on the inactivity of a copper positive electrode in nitro-sulphuric acid,” *Philos. Mag. Ser. 3*, vol. 15, no. 96, pp. 287–293, 1839.

[21] N. U. Pujare, K. W. Semkow, and A. F. Sammells, “A Direct H_2S / Air Solid Oxide Fuel Cell,” Aurora, Illinois, 1987.

[22] W. Vielstich, H. A. Gasteiger, and A. Lamm, “Handbook of fuel cells : fundamentals, technology and applications. Vol. 4,” in *Handbook of fuel cells : fundamentals, technology and applications*, T. Kawada and J. Mizusaki, Eds. Wiley, 2003.

[23] O. Yamamoto, Y. Arati, Y. Takeda, N. Imanishi, Y. Mizutani, M. Kawai, and Y. Nakamura, “Electrical conductivity of stabilized zirconia with ytterbia and scandia,” *Solid State Ionics*, vol. 79, pp. 137–142, Jul. 1995.

[24] R. L. Jones, R. F. Reidy, and D. Mess, “Scandia, yttria-stabilized zirconia for thermal barrier coatings,” *Surf. Coatings Technol.*, vol. 82, no. 1–2, pp. 70–76, Jul. 1996.

[25] H. Sumi, K. Ukai, Y. Mizutani, H. Mori, C. Wen, H. Takahashi, and O. Yamamoto, “Performance of nickel/scandia-stabilized zirconia cermet anodes for SOFCs in 3% H_2O/CH_4,” *Solid State Ionics*, vol. 174, no. 1–4, pp. 151–156, Oct. 2004.

[26] M. A. Laguna-Bercero, S. J. Skinner, and J. A. Kilner, “Performance of solid oxide electrolysis cells based on scandia stabilised zirconia,” *J. Power Sources*, vol. 192, no. 1, pp. 126–131, Jul. 2009.

[27] H. A. Abbas, C. Argirusis, M. Kilo, H.-D. Wiemhöfer, F. F. Hammad, and Z. M. Hanafi, “Preparation and conductivity of ternary scandia-stabilised zirconia,” *Solid State Ionics*, vol. 184, no. 1, pp. 6–9, Mar. 2011.

© 2014 Tous droits réservés.

[28] Y.-H. Choi, S.-H. Lee, J. Wackerl, D.-H. Jung, D.-S. Suhr, S.-Y. Choi, and D.-H. Peck, "Fabrication of scandia-stabilized zirconia electrolyte with a porous and dense composite layer for solid oxide fuel cells," *Ceram. Int.*, vol. 38, pp. S485–S488, Jan. 2012.

[29] S. P. Miller, B. I. Dunlap, and A. S. Fleischer, "Effects of dopant clustering in cubic zirconia stabilized by yttria and scandia from molecular dynamics," *Solid State Ionics*, vol. 253, pp. 130–136, Dec. 2013.

[30] S. P. S. Badwal, "Effect of dopant concentration on electrical conductivity in the Sc_2O_3-ZrO_2 system," *J. Mater. Sci.*, vol. 22, pp. 4125–4132, 1987.

[31] O. Bellon, N. M. Sammes, and J. Staniforth, "Mechanical properties and electrochemical characterisation of extruded doped cerium oxide for use as an electrolyte for solid oxide fuel cells," *J. Power Sources*, vol. 75, no. 1, pp. 116–121, Sep. 1998.

[32] C. Hatchwell, "Fabrication and properties of $Ce_{0.8}Gd_{0.2}O_{1.9}$ electrolyte-based tubular solid oxide fuel cells," *Solid State Ionics*, vol. 126, no. 3–4, pp. 201–208, Nov. 1999.

[33] C. . Hatchwell, N. Sammes, G. Tompsett, and I. W. Brown, "Chemical compatibility of chromium-based interconnect related materials with doped cerium oxide electrolyte," *J. Eur. Ceram. Soc.*, vol. 19, no. 9, pp. 1697–1703, Jul. 1999.

[34] M. Mogensen, "Physical, chemical and electrochemical properties of pure and doped ceria," *Solid State Ionics*, vol. 129, no. 1–4, pp. 63–94, Apr. 2000.

[35] B. Steele, "Appraisal of $Ce_{1-y}Gd_yO_{2-y/2}$ electrolytes for IT-SOFC operation at 500°C," *Solid State Ionics*, vol. 129, no. 1–4, pp. 95–110, Apr. 2000.

[36] K. Wincewicz and J. Cooper, "Taxonomies of SOFC material and manufacturing alternatives," *J. Power Sources*, vol. 140, no. 2, pp. 280–296, Feb. 2005.

[37] T. Ishihara, H. Matsuda, and Y. Takita, "Effects of rare earth cations doped for La site on the oxide ionic conductivity of $LaGaO_3$-based perovskite type oxide," *Solid State Ionics*, vol. 79, pp. 147–151, 1995.

[38] K. Huang, M. Feng, and J. B. Goodenough, "Sol-Gel Synthesis of a New Oxide-Ion Conductor Sr- and Mg-Doped $LaGaO_3$ Perovskite," *J. Am. Ceram. Soc.*, vol. 79, no. 4, pp. 1100–1104, 1996.

[39] K. Huang and J. B. Goodenough, "Wet Chemical Synthesis of Sr- and Mg-Doped $LaGaO_3$, a Perovskite-Type Oxide-Ion Conductor," *J. Solid State Chem.*, vol. 283, no. 136, pp. 274–283, 1998.

[40] K. Yamagi, T. Horita, M. Ishikawa, N. Sakai, and H. Yokohawa, "Chemical stability of the $La_{0.9}Sr_{0.1}Ga_{0.8}Mg_{0.2}O_{2.85}$ electrolyte in a reducing atmosphere," *Solid State Ionics*, vol. 121, pp. 217–224, 1999.

© 2014 Tous droits réservés.

[41] S. P. S. Badawal, “Stability of solid oxide fuel cell components,” *Solid State Ionics*, vol. 143, pp. 39–46, 2001.

[42] J. Goodenough, “Oxide-ion conduction in $Ba_2In_2O_5$ and $Ba_3In_2MO_8$ (M=Ce, Hf, or Zr),” *Solid State Ionics*, vol. 44, no. 1–2, pp. 21–31, Dec. 1990.

[43] J. B. Goodenough, A. Manthiram, and J.-F. Kuo, “Oxygen diffusion in perovskite-related oxides,” *Mater. Chem. Phys.*, vol. 35, no. 3–4, pp. 221–224, Oct. 1993.

[44] P. K. Moon and H. L. Tuller, “Evaluation of the $Gd_2(Zr_xTi_{1-x})_2O_7$ pyrochlore system as an oxygen gas sensor,” *Sensors Actuators B Chem.*, vol. 1, no. 1–6, pp. 199–202, Jan. 1990.

[45] H. Tuller, “Mixed ionic-electronic conduction in a number of fluorite and pyrochlore compounds,” *Solid State Ionics*, vol. 52, no. 1–3, pp. 135–146, May 1992.

[46] S. Kramer, “A novel titanate-based oxygen ion conductor: $Gd_2Ti_2O_7$,” *Solid State Ionics*, vol. 82, no. 1–2, pp. 15–23, Nov. 1995.

[47] T.-H. Yu and H. L. Tuller, “Ionic conduction and disorder in the $Gd_2Sn_2O_7$ pyrochlore system,” *Solid State Ionics*, vol. 86–88, pp. 177–182, Jul. 1996.

[48] O. Porat, “Stability and mixed ionic electronic conduction in $Gd_2(Ti_{1-x}Mo_x)_2O_7$ under anodic conditions,” *Solid State Ionics*, vol. 94, no. 1–4, pp. 75–83, Feb. 1997.

[49] H. Takamura, “Ionic conductivity of Gd_2GaSbO_7–$Gd_2Zr_2O_7$ solid solutions with structural disorder,” *Solid State Ionics*, vol. 134, no. 1–2, pp. 67–73, Oct. 2000.

[50] E. Kendric, M. Islam, and P. Slater, “Investigation of the structural changes on Zn doping in the apatite-type oxide ion conductor $La_{9.33}Si_6O_{26}$: A combined neutron diffraction and atomistic simulation study,” *Solid State Ionics*, vol. 177, no. 39–40, pp. 3411–3416, Jan. 2007.

[51] J. Sansom, “A powder neutron diffraction study of the oxide-ion-conducting apatite-type phases, $La_{9.33}Si_6O_{26}$ and $La_8Sr_2Si_6O_{26}$,” *Solid State Ionics*, vol. 139, no. 3–4, pp. 205–210, Feb. 2001.

[52] H. Arikawa, “Oxide ion conductivity in Sr-doped $La_{10}Ge_6O_{27}$ apatite oxide,” *Solid State Ionics*, vol. 136–137, no. 1–2, pp. 31–37, Nov. 2000.

[53] J. Sansom, “Synthesis and structural characterisation of the apatite-type phases $La_{10-x}Si_6O2_{6+z}$ doped with Ga,” *Solid State Ionics*, vol. 167, no. 1–2, pp. 17–22, Feb. 2004.

[54] P. Berastegui, S. Hull, F. J. Garcı Garcı, and J. Grins, “A Structural Investigation of $La_2(GeO_4)O$ and Alkaline-Earth-Doped $La_{9.33}(GeO_4)_6O_2$,” *J. Solid State Chem.*, vol. 168, no. 1, pp. 294–305, Oct. 2002.

© 2014 Tous droits réservés.

[55] C. Guo, T. Cai, W. Zhang, C. Tian, and Y. Zeng, “Synthesis and characterization of Al^{3+}-doped $La_{9.33}Ge_6O_{26}$ intermediate temperature electrolyte for SOFCs,” *Mater. Sci. Eng. B*, vol. 171, no. 1–3, pp. 50–55, Jul. 2010.

[56] J. SANSOM, “Oxide ion conductivity in mixed Si/Ge-based apatite-type systems,” *Solid State Ionics*, vol. 175, no. 1–4, pp. 353–355, Nov. 2004.

[57] A. J. Jacobson, “Materials for Solid Oxide Fuel Cells,” *Chem. Mater.*, vol. 22, no. 3, pp. 660–674, Feb. 2010.

[58] C. Périllat-merceroz, “Titanates de structures pérovskite et dérivées: influence des éléments constitutifs et de la dimensionnalité sur les propriétés d’anode SOFC,” Université Lille 1, 2009.

[59] H. S. Spacil, “Electrical device including nickel-containing stabilized zirconia electrode.” Google Patents, 31-Mar-1970.

[60] W. E. Tragert, “Fuel cell with stabilized zirconia electrolyte and nickel-silver alloy anode.” Google Patents, 03-Jan-1967.

[61] J. F. B. Rasmussen and A. Hagen, “The effect of H_2S on the performance of Ni–YSZ anodes in solid oxide fuel cells,” *J. Power Sources*, vol. 191, no. 2, pp. 534–541, Jun. 2009.

[62] M. Cassidy, G. Lindsay, and K. Kendall, “The reduction of nickel/zirconia cermet anodes and the effects on supported thin electrolytes,” *J. Power Sources*, vol. 61, no. 1–2, pp. 189–192, Jul. 1996.

[63] T. Iwata, “Characterization of Ni/YSZ Anode Degradation for Substrate-Type Solid Oxide Fuel Cells,” *J. Electrochem. Soc.*, vol. 143, no. 5, pp. 1521–1525, May 1996.

[64] K. Nikooyeh, R. Clemmer, V. Alzate-Restrepo, and J. M. Hill, “Effect of hydrogen on carbon formation on Ni/YSZ composites exposed to methane,” *Appl. Catal. A Gen.*, vol. 347, no. 1, pp. 106–111, Sep. 2008.

[65] J. Van herle, T. Horita, T. Kawada, N. Sakai, H. Yokokawa, and M. Dokiya, “Sintering behaviour and ionic conductivity of yttria-doped ceria,” *J. Eur. Ceram. Soc.*, vol. 16, no. 9, pp. 961–973, Jan. 1996.

[66] J. B. Wang, J.-C. Jang, and T.-J. Huang, “Study of Ni-samaria-doped ceria anode for direct oxidation of methane in solid oxide fuel cells,” *J. Power Sources*, vol. 122, no. 2, pp. 122–131, Jul. 2003.

[67] X. Xu, C. Xia, G. Xiao, and D. Peng, “Fabrication and performance of functionally graded cathodes for IT-SOFCs based on doped ceria electrolytes,” *Solid State Ionics*, vol. 176, no. 17–18, pp. 1513–1520, May 2005.

© 2014 Tous droits réservés.

[68] F.-Y. Wang, B.-Z. Wan, and S. Cheng, “Study on Gd^{3+} and Sm^{3+} co-doped ceria-based electrolytes,” *J. Solid State Electrochem.*, vol. 9, no. 3, pp. 168–173, 2005.

[69] M. Cimenti and J. M. Hill, “Direct utilization of ethanol on ceria-based anodes for solid oxide fuel cells,” *Asia-Pacific J. Chem. Eng.*, vol. 4, no. 1, pp. 45–54, Jan. 2009.

[70] X.-F. Ye, S. R. Wang, Q. Hu, J. Y. Chen, T. L. Wen, and Z. Y. Wen, “Improvement of Cu–CeO_2 anodes for SOFCs running on ethanol fuels,” *Solid State Ionics*, vol. 180, no. 2–3, pp. 276–281, Mar. 2009.

[71] N. Q. Minh, “Ceramic fuel cells,” *J. Am. Ceram. Soc.*, vol. 76, no. 3, pp. 563–588, 1993.

[72] S. Tao and J. T. S. Irvine, “A redox-stable efficient anode for solid-oxide fuel cells,” *Nat Mater*, vol. 2, no. 5, pp. 320–323, May 2003.

[73] B. Huang, S. R. Wang, R. Z. Liu, X. F. Ye, H. W. Nie, X. F. Sun, and T. L. Wen, “Performance of $La_{0.75}Sr_{0.25}Cr_{0.5}Mn_{0.5}O_{3-\delta}$ perovskite-structure anode material at lanthanum gallate electrolyte for IT-SOFC running on ethanol fuel,” *J. Power Sources*, vol. 167, no. 1, pp. 39–46.

[74] T. Jardiel, M. T. Caldes, F. Moser, J. Hamon, G. Gauthier, and O. Joubert, “New SOFC electrode materials: The Ni-substituted LSCM-based compounds $(La_{0.75}Sr_{0.25})(Cr_{0.5}Mn_{0.5-x}Ni_x)O_{3-\delta}$ and $(La_{0.75}Sr_{0.25})(Cr_{0.5-x}Ni_xMn_{0.5})O_{3-\delta}$,” *Solid State Ionics*, vol. 181, no. 19–20, pp. 894–901, Jul. 2010.

[75] O. Marina, “Thermal, electrical, and electrocatalytical properties of lanthanum-doped strontium titanate,” *Solid State Ionics*, vol. 149, no. 1–2, pp. 21–28, Jul. 2002.

[76] P. Blennow, K. K. Hansen, L. R. Wallenberg, and M. Mogensen, “Electrochemical characterization and redox behavior of Nb-doped $SrTiO_3$,” *Solid State Ionics*, vol. 180, no. 1, pp. 63–70, Feb. 2009.

[77] P. Blennow, K. K. Hansen, L. Reine Wallenberg, and M. Mogensen, “Effects of Sr/Ti-ratio in $SrTiO_3$-based SOFC anodes investigated by the use of cone-shaped electrodes,” *Electrochim. Acta*, vol. 52, no. 4, pp. 1651–1661, Dec. 2006.

[78] P. R. Slater, D. P. Fagg, and J. T. S. Irvine, “Synthesis and electrical characterisation of doped perovskite titanates as potential anode materials for solid oxide fuel cells,” *J. Mater. Chem.*, vol. 7, no. 12, pp. 2495–2498, 1997.

[79] J. C. Grenier, J.-M. Bassat, and F. Mauvy, “Novel cathodes for solid oxide fuel cells,” in *Functional Materials*, Woodhead Publishing, 2012.

[80] K. Kordesch and G. Simader, “Fuel Cells and their Applications,” in *Fuel Cells and their Applications*, Wiley, 1996.

[81] R. Koc and H. U. Anderson, “Effect of cation substitution on the thermal expansion coefficient of $LaCrO_3$,” *J. Mater. Sci. Lett.*, vol. 11, no. 17, pp. 1191–1192, 1992.

© 2014 Tous droits réservés.

[82] K. Sasaki, J. -P. Wurth, R. Gschwend, M. Gödickemeier, and L. J. Gauckler, “Microstructure: Property Relations of Solid Oxide Fuel Cell Cathodes and Current Collectors: Cathodic Polarization and Ohmic Resistance,” *J. Electrochem. Soc.*, vol. 143, no. 2, pp. 530–543, Feb. 1996.

[83] H. Nishiyama, M. Aizawa, H. Yokokawa, T. Horita, N. Sakai, M. Dokiya, and T. Kawada, “Stability of Lanthanum Calcium Chromite/Lanthanum Strontium Manganite Interfaces in Solid Oxide Fuel Cells,” *J. Electrochem. Soc.*, vol. 143, no. 7, pp. 2332–2341, Jul. 1996.

[84] B. Fan, J. Yan, and X. Yan, “The ionic conductivity, thermal expansion behavior, and chemical compatibility of $La_{0.54}Sr_{0.44}Co_{0.2}Fe_{0.8}O_{3-\delta}$ as SOFC cathode material,” *Solid State Sci.*, vol. 13, no. 10, pp. 1835–1839, Oct. 2011.

[85] D. Marinha, J. Hayd, L. Dessemond, E. Ivers-Tiffée, and E. Djurado, “Performance of $(La,Sr)(Co,Fe)O_{3-x}$ double-layer cathode films for intermediate temperature solid oxide fuel cell,” *J. Power Sources*, vol. 196, no. 11, pp. 5084–5090, Jun. 2011.

[86] Z. Shao and S. M. Haile, “A high-performance cathode for the next generation of solid-oxide fuel cells.,” *Nature*, vol. 431, no. 7005, pp. 170–3, Sep. 2004.

[87] K. Wang, R. Ran, W. Zhou, H. Gu, Z. Shao, and J. Ahn, “Properties and performance of $Ba_{0.5}Sr_{0.5}Co_{0.8}Fe_{0.2}O_{3-\delta}$-$Sm_{0.2}Ce_{0.8}O_{1.9}$ composite cathode,” *J. Power Sources*, vol. 179, no. 1, pp. 60–68, Apr. 2008.

[88] Z. Shao, J. Mederos, W. C. Chueh, and S. M. Haile, “High power-density single-chamber fuel cells operated on methane,” *J. Power Sources*, vol. 162, no. 1, pp. 589–596, Nov. 2006.

[89] R. N. Basu, F. Tietz, O. Teller, E. Wessel, H. P. Buchkremer, and D. Stöver, “$LaNi_{0.6}Fe_{0.4}O_3$ as a cathode contact material for solid oxide fuel cells,” *J. Solid State Electrochem.*, vol. 7, no. 7, pp. 416–420, 2003.

[90] E. Bucher, A. Egger, P. Ried, W. Sitte, and P. Holtappels, “Oxygen nonstoichiometry and exchange kinetics of $Ba_{0.5}Sr_{0.5}Co_{0.8}Fe_{0.2}O_{3-\delta}$,” *Solid State Ionics*, vol. 179, no. 21–26, pp. 1032–1035, Sep. 2008.

[91] A. Maignan, B. Raveau, C. Martin, and M. Hervieu, “Large Intragrain Magnetoresistance above Room Temperature in the Double Perovskite Ba_2FeMoO_6,” *J. Solid State Chem.*, vol. 144, no. 1, pp. 224–227, Apr. 1999.

[92] Borges, R. P. Thomas, R. M. Cullinan, C. Coey, J. M. D. Suryanarayanan, R. Ben-Dor, L. Pinsard-Gaudart, L. Revcolevschi, A., “Magnetic properties of the double perovskites A_2FeMoO_6; A = Ca, Sr, Ba,” *J. Phys. Condens. Matter*, vol. 11, no. 40, p. L445, 1999.

[93] Rubi, D. Frontera, C. Roig, A. Nogues, J. Munoz, J. S. Fontcuberta, J., “Increasing the Curie temperature of Ca_2FeMoO_6 double perovskite by introducing near-neighbour

© 2014 Tous droits réservés.

antiferromagnetic interactions," *J. Phys. Condens. Matter*, vol. 17, no. 50, p. 8037, 2005.

[94] A. A. Taskin, A. N. Lavrov, and Y. Ando, "Achieving fast oxygen diffusion in perovskites by cation ordering," *Appl. Phys. Lett.*, vol. 86, no. 9, p. 91910, 2005.

[95] G. Kim, S. Wang, A. J. Jacobson, L. Reimus, P. Brodersen, and C. A. Mims, "Rapid oxygen ion diffusion and surface exchange kinetics in $PrBaCo_2O_{5+x}$ with a perovskite related structure and ordered A cations," *J. Mater. Chem.*, vol. 17, no. 24, pp. 2500–2505, 2007.

[96] A. Tarancon, S. J. Skinner, R. J. Chater, F. Hernandez-Ramirez, and J. A. Kilner, "Layered perovskites as promising cathodes for intermediate temperature solid oxide fuel cells," *J. Mater. Chem.*, vol. 17, no. 30, pp. 3175–3181, 2007.

[97] M.-B. Choi, S.-Y. Jeon, J.-S. Lee, H.-J. Hwang, and S.-J. Song, "Chemical diffusivity and ionic conductivity of $GdBaCo_2O_{5+\delta}$," *J. Power Sources*, vol. 195, no. 4, pp. 1059–1064, Feb. 2010.

[98] J.-C. Grenier, M. Pouchard, and P. Hagenmuller, "Vacancy ordering in oxygen-deficient perovskite-related ferrites," in *Ferrites · Transitions Elements Luminescence SE - 1*, vol. 47, Springer Berlin Heidelberg, 1981, pp. 1–25.

[99] P. Berastegui, S.-G. Eriksson, and S. Hull, "A neutron diffraction study of the temperature dependence of $Ca_2Fe_2O_5$," *Mater. Res. Bull.*, vol. 34, no. 2, pp. 303–314, Jan. 1999.

[100] J. Vente, S. McIntosh, W. Haije, and H. M. Bouwmeester, "Properties and performance of $Ba_xSr_{1-x}Co_{0.8}Fe_{0.2}O_{3-\delta}$ materials for oxygen transport membranes," *J. Solid State Electrochem.*, vol. 10, no. 8, pp. 581–588, 2006.

[101] A. Shaula, Y. Pivak, J. Waerenbogh, P. Gaczynski, A. Yaremchenko, and V. Kharton, "Ionic conductivity of brownmillerite-type calcium ferrite under oxidizing conditions," *Solid State Ionics*, vol. 177, no. 33–34, pp. 2923–2930, Nov. 2006.

[102] V. V. Kharton, I. P. Marozau, N. P. Vyshatko, A. L. Shaula, A. P. Viskup, E. N. Naumovich, and F. M. B. Marques, "Oxygen ionic conduction in brownmillerite $CaAl_{0.5}Fe_{0.5}O_{2.5+\delta}$," *Mater. Res. Bull.*, vol. 38, no. 5, pp. 773–782, Apr. 2003.

[103] Q. Li, L. Sun, L. Huo, H. Zhao, and J.-C. Grenier, "Electrode properties of Co-doped $Ca_2Fe_2O_5$ as new cathode materials for intermediate-temperature SOFCs," *Int. J. Hydrogen Energy*, vol. 35, no. 17, pp. 9151–9157, Sep. 2010.

[104] S. N. Ruddlesden and P. Popper, "The compound $Sr_3Ti_2O_7$ and its structure," *Acta Crystallogr.*, vol. 11, no. 1, pp. 54–55, 1958.

© 2014 Tous droits réservés.

[105] X. Weng, P. Boldrin, I. Abrahams, S. J. Skinner, and J. A. Darr, "Direct Syntheses of Mixed Ion and Electronic $La_4Ni_3O_{10}$ and $La_3Ni_2O_7$ from Nanosized Coprecipitates," *Chem. Mater.*, vol. 19, no. 6, pp. 4382–4384, 2007.

[106] G. Amow, I. Davidson, and S. Skinner, "A comparative study of the Ruddlesden-Popper series, $La_{n+1}Ni_nO_{3n+1}$ (n=1, 2 and 3), for solid-oxide fuel-cell cathode applications," *Solid State Ionics*, vol. 177, no. 13–14, pp. 1205–1210, May 2006.

[107] V. Thoréton, "Propriétés de transport de l 'oxygène dans les cobaltites $Ba_2Co_9O_{14}$ et $Ca_3Co_4O_{9+\delta}$: apport du SIMS et du LEIS," UST Lille1, 2012.

[108] S. Li, R. Funahashi, I. Matsubara, K. Ueno, S. Sodeoka, and H. Yamada, "Synthesis and Thermoelectric Properties of the New Oxide Materials $Ca_{3-x}Bi_xCo_4O_{9+\delta}$ (0.0<x<0.75)," *Chem. Mater.*, vol. 12, no. 8, pp. 2424–2427, 2000.

[109] S. Lambert, H. Leligny, and D. Grebille, "Three Forms of the Misfit Layered Cobaltite $[Ca_2CoO_3]$ $[CoO_2]_{1.62}$: A 4D Structural Investigation," *J. Solid State Chem.*, vol. 160, no. 2, pp. 322–331, Sep. 2001.

[110] a. Masset, C. Michel, A. Maignan, M. Hervieu, O. Toulemonde, F. Studer, B. Raveau, and J. Hejtmanek, "Misfit-layered cobaltite with an anisotropic giant magnetoresistance: Ca3Co4O9," *Phys. Rev. B*, vol. 62, no. 1, pp. 166–175, Jul. 2000.

[111] P. Boullay, R. Seshadri, F. Studer, M. Hervieu, D. Groult, and B. Raveau, "Chemical and Physical Aspects of the Misfit Layer Oxides $Tl_\alpha[(Sr_{1-y}Ca_y)O]_{1+x}(CoO_2)$," *Chem. Mater.*, vol. 10, no. 1, pp. 92–102, 1998.

[112] M. Hervieu, P. Boullay, C. Michel, A. Maignan, and B. Raveau, "A New Family of Misfit Layered Oxides with Double Rock Salt Layers Bi_α $(A_{0.75\pm\varepsilon}Bi_{0.25\pm\varepsilon}O)_{(3+3x)/2}MO_2$ (A = Ca, Sr and M= Co, Cr)," *J. Solid State Chem.*, vol. 142, no. 2, pp. 305–318, 1999.

[113] E. Makovicky and B. G. Hyde, "Non-commensurate (misfit) layer structures," in *Inorganic Chemistry*, Springer, 1981, pp. 101–170.

[114] C. Brisi and P. Rolando, "The calcium oxide-cobalt (II) oxide-oxygen system," *Ann. Chim.*, vol. 58, 1968.

[115] H. Muguerra and D. Grebille, "Original disorder-order transition related to electronic and magnetic properties in the thermoelectric misfit phase $[Ca_2CoO_3][CoO2]_{1.62}$," *Acta Crystallogr. B.*, vol. 64, no. Pt 6, pp. 676–683, Dec. 2008.

[116] S. Li, R. Funahashi, I. Matsubara, K. Ueno, and H. Yamada, "High temperature thermoelectric properties of oxide Ca9Co12O28," *J. Mater. Chem.*, vol. 9, pp. 1659–1660, 1999.

[117] Y. Wakisaka, S. Hirata, T. Mizokawa, Y. Suzuki, Y. Miyazaki, and T. Kajitani, "Electronic structure of $Ca_3Co_4O_9$ studied by photoemission spectroscopy: Phase separation and charge localization," *Phys. Rev. B*, vol. 78, no. 23, p. 235107, Dec. 2008.

© 2014 Tous droits réservés.

[118] V. Thoréton, Y. Hu, C. Pirovano, E. Capoen, N. Nuns, A. S. Mamede, G. Dezeanneau, C. Y. Yoo, H. J. M. Bouwmeester, and R. N. Vannier, "Oxygen transport kinetics of the misfit layer oxide $Ca_3Co_4O_{9+\delta}$" *Chem. Mater.*, 2014.

[119] Y. M. Iyazaki, M. O. Noda, T. O. Ku, M. K. Ikuchi, and Y. I. Shii, "Modulated Structure of the Thermoelectric Compound [Ca2CoO3]0.62 CoO2," *J. Phys. Soc. Japan*, vol. 71, no. 2, pp. 491–497, 2002.

[120] H. Leligni, D. Grebille, O. Pérez, A.-C. Masset, M. Hervieu, C. Michel, and B. Raveau, "A bismuth cobaltite with an intrinsically modulated misfit layer structure: $[Bi_{0.87}SrO_2]_2[CoO_2]_{1.82}$," *C. R. Acad. Sci. Paris*, no. figure 2. Editions scientifiques et médicales Elsevier SAS, pp. 409–414, 1999.

[121] P. Limelette, V. Hardy, P. Auban-Senzier, D. Jérome, D. Flahaut, S. Hébert, R. Frésard, C. Simon, J. Noudem, and a. Maignan, "Strongly correlated properties of the thermoelectric cobalt oxide $Ca_3Co_4O_9$," *Phys. Rev. B*, vol. 71, no. 23, p. 233108, Jun. 2005.

[122] S. Adler, "Limitations of charge-transfer models for mixed-conducting oxygen electrodes," *Solid State Ionics*, vol. 135, no. 1–4, pp. 603–612, Nov. 2000.

[123] D. Johnson, "Z View." Schribner Associates Inc.

[124] M. J. Jørgensen and M. Mogensen, "Impedance of solid oxide fuel cell LSM/YSZ composite cathodes," *J. Electrochem. Soc.*, vol. 148, no. 5, pp. A433–A442, 2001.

[125] "Chemistry of Materials," *Chem. Mater.*, vol. 20, no. 3, pp. 599–1190, 2008.

[126] G. I. N. Waterhouse, J. B. Metson, H. Idriss, and D. Sun-Waterhouse, "Physical and Optical Properties of Inverse Opal CeO2 Photonic Crystals†," *Chem. Mater.*, vol. 20, no. 3, pp. 1183–1190, 2008.

[127] J. Hierso, P. Boy, K. Vallé, J. Vulliet, F. Blein, C. Laberty-Robert, and C. Sanchez, "Nanostructured ceria based thin films (≤1µm) As cathode/electrolyte interfaces," *J. Solid State Chem.*, vol. 197, pp. 113–119, Jan. 2013.

[128] G. Muller, R. N. Vannier, and A. Ringuedé, "Laberty− Robert, C.; Sanchez, C., Microstructure and Electrical Properties of Nanocrystalline, Mesoporous $NiO/Ce_{0.9}Gd_{0.1}O_{2-\delta}$ Thin Films: In situ Characterization of Electrical Properties During the Reduction of NiO," *J. Mater. Chem. A*, 2013.

[129] G. Muller, C. Boissiere, D. Grosso, A. Ringuede, C. Laberty-Robert, and C. Sanchez, "Understanding crystallization processes of $NiO/Ce_{0.9}Gd_{0.1}O_{2-\delta}$ sol–gel processed thin films for the design of efficient electrodes: an in situ thermal ellipsometry analysis," *J Mater Chem*, vol. 22, no. 18, pp. 9368–9373, 2012.

[130] G. Muller, R.-N. Vannier, A. Ringuede, and C. Laberty-Robert, "Reduction of NiO to Ni in Nanocrystalline Composite $NiO/Ce_{0.9}Gd_{0.1}O_{2-\delta}$ Porous Thin Films: Microstructure

© 2014 Tous droits réservés.

Evolution Through in Situ Impedance Spectroscopy," *J. Phys. Chem. C*, vol. 117, no. 32, pp. 16297–16305, 2013.

[131] G. Muller, A. Ringuedé, and C. Laberty-Robert, "Discussion on a Percolating Conducting Network of a Composite Thin-Film Electrode (≤ 1 µm) for Micro-Solid Oxide Fuel Cell Application," *Langmuir*, vol. 30, no. 29, pp. 8889–8897, 2014.

[132] A. Stein, F. Li, and N. R. Denny, "Morphological Control in Colloidal Crystal Templating of Inverse Opals, Hierarchical Structures, and Shaped Particles," *Chem. Mater.*, vol. 20, no. 3, pp. 649–666, Dec. 2007.

[133] T. Nguyen, "Deposition and characterization of nanocrystalline tetragonal zirconia films using electrostatic spray deposition," *Solid State Ionics*, vol. 138, no. 3–4, pp. 191–197, Jan. 2001.

[134] A. Princivalle and E. Djurado, "Nanostructured LSM/YSZ composite cathodes for IT-SOFC: A comprehensive microstructural study by electrostatic spray deposition," *Solid State Ionics*, vol. 179, no. 33–34, pp. 1921–1928, Oct. 2008.

[135] T. Sun, J. Ma, Q. Y. Yan, Y. Z. Huang, J. L. Wang, and H. H. Hng, "Influence of pulsed laser deposition rate on the microstructure and thermoelectric properties of $Ca_3Co_4O_9$ thin films," *J. Cryst. Growth*, vol. 311, no. 16, pp. 4123–4128, Aug. 2009.

[136] R. D. T. Shannon, "Revised effective ionic radii and systematic studies of interatomic distances in halides and chalcogenides," *Acta Crystallogr. Sect. A Cryst. Physics, Diffraction, Theor. Gen. Crystallogr.*, vol. 32, no. 5, pp. 751–767, 1976.

[137] L. B. Wang, A. Maignan, D. Pelloquin, S. Hébert, and B. Raveau, "Transport and magnetic properties of $Ca_{3-x}Sr_xCo_4O_9$," *J. Appl. Phys.*, vol. 92, no. 1, p. 124, 2002.

[138] H. Nakatsugawa, H. M. Jeong, R. H. Kim, and N. Gomi, "Thermoelectric and Magnetic Properties of $[(Ca_{1-x}Pb_x)_2CoO_{3.1}]_{0.62}CoO_2$ ($0 \le x \le 0.03$)," *Jpn. J. Appl. Phys.*, vol. 46, no. 5A, pp. 3004–3012, May 2007.

[139] J. Nan, J. Wu, Y. Deng, and C.-W. Nan, "Thermoelectric properties of La-doped Ca–Co–O misfit cobaltites," *Solid State Commun.*, vol. 124, no. 7, pp. 243–246, Nov. 2002.

[140] S. Skinner, "Oxygen diffusion and surface exchange in La2−xSrxNiO4+δ," *Solid State Ionics*, vol. 135, no. 1–4, pp. 709–712, Nov. 2000.

[141] R. A. De Souza, J. A. Kilner, and J. F. Walker, "A SIMS study of oxygen tracer diffusion and surface exchange in $La_{0.8}Sr_{0.2}MnO_{3+\delta}$," *Mater. Lett.*, vol. 43, no. March, pp. 43–52, 2000.

[142] E. Raj, J. Kilner, and J. Irvine, "Oxygen diffusion and surface exchange studies on $(La_{0.75}Sr_{0.25})_{0.95}Cr_{0.5}Mn_{0.5}O_{3-\delta}$," *Solid State Ionics*, vol. 177, no. 19–25, pp. 1747–1752, Oct. 2006.

© 2014 Tous droits réservés.

[143] A. Atkinson, R. J. Chater, and R. Rudkin, "Oxygen diffusion and surface exchange in $La_{0.8}Sr_{0.2}Fe_{0.8}Cr_{0.2}O_{3-\delta}$ under reducing conditions," *Solid State Ionics*, vol. 139, no. 3–4, pp. 233–240, Feb. 2001.

[144] A. V Berenov, A. Atkinson, J. A. Kilner, E. Bucher, and W. Sitte, "Oxygen tracer diffusion and surface exchange kinetics in $La_{0.6}Sr_{0.4}CoO_{3-\delta}$," *Solid State Ionics*, vol. 181, no. 17, pp. 819–826, 2010.

[145] A. Tarancón, S. J. Skinner, R. J. Chater, F. Hernandez-Ramirez, and J. A. Kilner, "Layered perovskites as promising cathodes for intermediate temperature solid oxide fuel cells," *J. Mater. Chem.*, vol. 17, no. 30, pp. 3175–3181, 2007.

[146] A. Esquirol, N. P. Brandon, J. A. Kilner, and M. Mogensen, "Electrochemical Characterization of $La_{0.6}Sr_{0.4}Co_{0.2}Fe_{0.8}O_3$ Cathodes for Intermediate-Temperature SOFCs," *J. Electrochem. Soc.*, vol. 151, no. 11, pp. A1847–A1855, 2004.

[147] J. A. Kilner, J. Drennan, P. Dennis, and B. C. H. Steele, "A study of anion transport in bismuth based oxide systems by electrical conductivity and secondary ion mass spectroscopy (SIMS)," *Solid State Ionics*, vol. 5, pp. 527–530, 1981.

[148] H. J. M. Bouwmeester, C. Song, J. Zhu, J. Yi, M. van Sint Annaland, and B. a Boukamp, "A novel pulse isotopic exchange technique for rapid determination of the oxygen surface exchange rate of oxide ion conductors.," *Phys. Chem. Chem. Phys.*, vol. 11, no. 42, pp. 9640–3, Nov. 2009.

[149] J. Cranck, "The mathematics of diffusion, 1975." Clarendon Press, Oxford.

[150] R. J. Chater, S. Carter, J. A. Kilner, and B. C. H. Steele, "Development of a novel SIMS technique for oxygen self-diffusion and surface exchange coefficient measurements in oxides of high diffusivity," *Solid State Ionics*, vol. 53–56, pp. 859–867, 1992.

[151] R. Desouza, J. Zehnpfenning, M. Martin, and J. Maier, "Determining oxygen isotope profiles in oxides with Time-of-Flight SIMS," *Solid State Ionics*, vol. 176, no. 15–16, pp. 1465–1471, May 2005.

[152] B. C. H. Steele, "Survey of materials selection for ceramic fuel cells: II. Cathodes and anodes," *Solid State Ionics*, vol. 88, pp. 1223–1234, 1996.

[153] E. Warburg, "Über das Verhalten sogenannter unpolarisirbarer Elektroden gegen Wechselstrom," *Ann. der Phys. und Chemie*, vol. 67, no. 3, pp. 493–499, 1899.

[154] E. Warburg, "Über die Electrolyse des festen Glases," *Ann. Phys.*, vol. 257, no. 4, pp. 622–646, 1884.

[155] F. Haber and S. Tołłoczko, "Über die Reduktion der gebundenen, festen Kohlensäure zu Kohlenstoff und über elektrochemische Veränderungen bei festen Stoffen," *Zeitschrift für Anorg. Chemie*, vol. 41, no. 1, pp. 407–441, 1904.

© 2014 Tous droits réservés.

[156] J. Frenkel, “Zur Theorie der Elastizitätsgrenze und der Festigkeit kristallinischer Körper,” *Z. Phys.*, vol. 37, pp. 572–609, 1926.

[157] W. Schottky, “Zur Theorie der thermischen Fehlordnung in Kristallen,” *Naturwissenschaften*, vol. 23, no. 38, pp. 656–657, 1935.

[158] W. Nernst, “Material for electric-lamp glowers,” US685730 A, 29-Oct-1901.

© 2014 Tous droits réservés.

Abstract

In this PhD thesis, the electrochemical performances of the misfit layered oxide $Ca_3Co_4O_{9+\delta}$ used as a cathode for Solid Oxide Fuel Cell were tentatively optimised by optimisation of the electrode microstructure and composition. Using screen printing as a deposition technique, the Area Specific Resistance was decreased to 0.5 Ωcm^2 at 700°C for a composite made of 50% in weight of cerium gadolinium doped oxide and $Ca_3Co_4O_{9+\delta}$. Spin coating and electrostatic deposition were also tested as promising technique to improve the performances. The impact of partial substitution of the calcium site on the electrochemical performances was tentatively studied with a wide range of dopant (Sr, Pb, Bi, La). It was difficult to draw conclusions since their performances depend strongly on the sample preparation. Moreover, due to the low amount of the dopant, imposed by the low solubility of lead in the calcium site, it was not possible to derive a clear tendency of the substituent's impact on the oxygen transport properties. However, by pulse isotopic exchange, high surface exchange kinetics were confirmed for the $(Ca_{0.90}Sr_{0.10})_3Co_4O_{9+\delta}$ composition and it was shown that neither the oxygen adsorption of the surface nor the oxygen incorporation in the solid were the limiting step in the oxygen transfer.

Key words: Solid Oxide Fuel Cells, cobaltite, mixed ionic/electronic conductor, doping, microstructure, impedance spectroscopy, isotopic exchange.

Cette thèse porte sur l'optimisation en termes de microstructure et de composition des propriétés électrochimiques du composé $Ca_3Co_4O_{9+\delta}$ pour une application comme cathode pour Pile à Combustible à Oxyde. En utilisant la sérigraphie comme technique de dépôt, la Résistance Surfacique Spécifique a été diminuée jusqu'à 0.5 Ωcm^2 à 700°C pour un matériau composé de 50% en masse d'oxyde de cérium dopé au gadolinium et $Ca_3Co_4O_{9+\delta.}$ Par ailleurs, des techniques telles que le spin-coating et l'électro-spray apparaissent comme prometteuses pour l'amélioration des performances. Nous avons tenté d'étudier l'impact de la substitution partielle sur le site calcium sur les performances électrochimiques pour différents dopants (Sr, Pb, Bi, La). Du fait que les performances électrochimiques dépendent fortement de la préparation et de la faible concentration en dopant contrainte par la faible solubilité du plomb en site calcium, il n'a pas été possible de tirer des conclusions claires sur l'impact d'un tel dopage, de même pour les propriétés de transport de l'oxygène. Par contre, l'analyse par Echange Isotopique Pulsé de la composition $(Ca_{0.90}Sr_{0.10})_3Co_4O_{9+\delta}$ a permis de confirmer les très bonnes cinétiques d'échange de l'oxygène pour les composés partiellement substitués par du strontium, montrant par ailleurs que ni l'adsorption en surface de l'oxygène ni son incorporation dans le solide sont des étapes limitantes dans le mécanisme d'échange en surface.

Mots clef : Pile à Combustible à Oxydes Solides, cobaltite, conducteur ionique/électronique mixte, dopage, spectroscopie d'impédance, échange isotopique.

© 2014 Tous droits réservés.